

# Synthetic Applications of Vortex Thin Film Microfluidics

By  
Scott J. Pye

*Thesis  
Submitted to Flinders University  
for the completion of Ph. D. candidature*

Ph. D. (Chemistry)  
College of Science and Engineering  
26<sup>th</sup> of June, 2020

---

# Contents

<b>List of Figures</b>	<b>iv</b>
<b>List of Tables</b>	<b>ix</b>
<b>Summary</b>	<b>x</b>
<b>Declaration</b>	<b>xi</b>
<b>Acknowledgements</b>	<b>xii</b>
<b>Chapter 1 - Introduction</b>	<b>1</b>
1.1 - Flow Chemistry	1
1.1.1 - Improved Reaction Outcome	2
1.1.2 - Automation	4
1.1.3 - Safety	5
1.2 - The Vortex Fluidic Device (VFD)	7
1.2.1 - Description of the VFD	8
1.2.2 - Chemical Transformations in the VFD	9
<b>Chapter 2 - Organic Oxidations</b>	<b>11</b>
2.1 - Aerobic Oxidation of <i>N</i> -acetyl-L-cysteine	12
2.1.1 - Discussion on Aerobic Oxidation in the VFD	13
2.1.2 - Summary and Outlook on Aerobic Oxidation in the VFD	15
2.2 - Bleach Oxidations Beyond the Aqueous Phase	16
2.2.1 - Discussion on Bleach Oxidations in the VFD	17
2.2.2 - Summary and Outlook on Bleach Oxidations in the VFD	19
2.3 - Hydrogen Peroxide Oxidations, Avoiding Run-Away Exotherms	20
2.3.1 - Discussion on Hydrogen Peroxide Oxidations in the VFD	20
2.3.2 - Summary and Outlook on Hydrogen Peroxide Oxidations in the VFD	24
2.4 - Conclusions on Organic Oxidations in the VFD	25
2.5 - Experimental Details and Spectra	26
2.5.1 - Obtaining reference sample of disulphide 2	26
2.5.2 - Small Scale Batch and Confined Mode VFD Processing.	27
2.5.3 - Large Scale VFD Processing with Atmosphere of O <sub>2</sub> vs Air	29
2.5.4 - Large Scale Batch Aerobic Oxidation	31
2.5.5 - Continuous Flow VFD Aerobic Oxidation at pH 11	33
2.5.6 - Synthesis of allyl phenyl sulphide 3	34
2.5.7 - Batch vs VFD Bleach Oxidations	35
2.5.8 - VFD synthesis and Isolation of compound 22	37
2.5.9 - Epoxidation of 25 with Hydrogen Peroxide	39
2.5.10 - Batch vs VFD Epoxidation with Hydrogen Peroxide	42
2.5.11 - Continuous flow VFD Epoxidation with Hydrogen Peroxide	43
2.5.12 - X-Ray Structure determination of 27a	44
2.5.13 - Thermal monitoring of Batch vs VFD Epoxidation	47
2.5.14 - NaOH Recycling in the Epoxidation with Hydrogen Peroxide	48
<b>Chapter 3 - Olefin Metathesis</b>	<b>49</b>
3.1 - Ethenolysis	51

3.1.1 - Discussion on Ethenolysis in the VFD	52
3.2 - <i>N</i> -Acetyl-L-cysteine Quench	54
3.2.1 - Discussion on <i>N</i> -Acetyl-L-cysteine as a Quenching agent	54
3.3 - In-Line Catalyst Separation	63
3.3.1 - In-Line Catalyst Separation in the VFD	63
3.3.2 - Summary and Outlook of In-Line Catalyst Separation in VFD Flow	69
3.4 - Exploring VFD Enhancement of OM	70
3.4.1 - Discussion on Exploring VFD Enhancement of OM	71
3.4.2 - Summary and Outlook of Exploring the VFD Enhancement	78
3.5 - Experimental Details and Spectra	79
3.5.1 - Esterification of Oleic Acid to Form Methyl Oleate	79
3.5.2 - Ethenolysis of Methyl Oleate	82
3.5.3 - Continuous Flow Ethenolysis	84
3.5.4 - CM of 34, Establishing Quench of 18 + MeCN	85
3.5.5 - Monitoring Conversion of 34 CM Over Time, Quench vs No-Quench	86
3.5.6 - Biphasic CM of Allyl Alcohol	87
3.5.7 - Synthesis of Substrate 45 from 1-thio- $\beta$ -D-glucose tetraacetate (39)	88
3.5.8 - Synthesis of Substrate 45 from $\beta$ -D-glucose pentaacetate (41)	90
3.5.9 - Synthesis of Catalyst HGII-NH <sub>3</sub> <sup>+</sup>	94
3.5.10 - Synthesis of Fe <sub>3</sub> O <sub>4</sub> @SiO <sub>2</sub>	103
3.5.11 - 5 minute CM of 20 in Batch vs VFD Under O <sub>2</sub> , With N <sub>2</sub> Control	104
3.5.12 - 1 hour CM of 20 in VFD, comparing O <sub>2</sub> vs N <sub>2</sub> Atmospheres	105
3.5.13 - 1 Hour CM of 20, Replacing Atmosphere N <sub>2</sub> After 10 Minutes	106
3.5.14 - Monitoring the GI Catalysed CM of 34 over 10 Minutes in Batch	108
3.5.15 - Monitoring the GI catalysed RCM of 59 Over 10 Minutes	109
3.5.16 - Monitoring the GII Catalysed CM of 20 Over 10 Minutes	110
3.5.17 - Monitoring the GII Catalysed CM of 34 Over 10 Minutes	111
3.5.18 - Monitoring the GII Catalysed RCM of 61 in Toluene Over 10 Minutes	112
3.5.19 - Monitoring the GII Catalysed RCM of 59 in Toluene Over 10 Minutes	113
3.5.20 - Monitoring the GII Catalysed Metathesis in Various Solvents	114
3.5.21 - Monitoring the GII Catalysed RCM of 61 in DMF vs DMC over 25 Minutes	115
3.5.22 - Monitoring the GI Catalysed RCM of 61 Over 25 Minutes in Batch vs VFD	116
<b>Chapter 4 - Polymer Synthesis in the VFD</b>	<b>117</b>
4.1 - Polyurethane and Polythiourethane Synthesis	118
4.1.1 - Discussion on Polyurethane and Polythiourethane Synthesis in VFD	119
4.1.2 - Conclusion for Synthesis of Polyurethane & Polythiourethane in VFD	125
4.2 - Polycarbonate Synthesis in the VFD	126
4.2.1 - Discussion on Polycarbonate Synthesis in the VFD	126
4.2.2 - Conclusions and outlook for Polycarbonate Synthesis in VFD	128
4.3 - Polystyrene Synthesis	129
4.3.1 - Discussion on Polystyrene Synthesis in VFD	129
4.3.2 - Summary and outlook for Polystyrene Synthesis in VFD	131
4.4 - Conclusions and Outlook on Polymer Synthesis in the VFD	132

4.5 - Experimental Details and Spectra	135
4.5.1 - Controls for the Formation of Urea	69 135
4.5.2 - Polyurethane and Polyallophinate Formation in Batch vs VFD	137
4.5.3 - Polyurethane and Polyallophinate Selectivity by <sup>1</sup> H-NMR	139
4.5.4 - Polythiourthane Procedure for Batch vs VFD	140
4.5.5 - Polycarbonate Synthesis From 65 and CO <sub>2</sub> in Batch vs VFD	142
4.5.6 - Polycarbonate Formation from 72 and CO <sub>2</sub> in Batch vs VFD	143
4.5.7 - Thermally Initiated Polystyrene Synthesis, at 280 Equivalents of BPO	144
4.5.8 - Thermally Initiated Polystyrene Synthesis, at 140 Equivalents of BPO	146
4.5.9 - Photo-initiated Polystyrene Synthesis with Benzophenone and Benzoyl Peroxide	147
4.5.10 - Photo-initiated Polystyrene Synthesis with Irgacure-2959	148
<b>Chapter 5 - Oxidative Sulphitolysis (OS)</b>	<b>149</b>
5.1 - Oxidative Sulphitolysis in the VFD	149
5.1.1 - Discussion on the OS of L-Cystine	151
5.1.2 - Discussion on the OS of Oxytocin	153
5.1.3 - Discussion on the OS of Insulin	155
5.2 - Summary and Outlook of Oxidative Sulphitolysis in the VFD	157
5.3 - Experimental Details and Spectra	158
5.3.1 - Cystine OS at pH 11.3, Batch versus VFD	158
5.3.2 - Cystine OS at pH 9, Batch vs VFD	159
5.3.3 - Oxytocin OS Batch versus VFD	160
<b>Chapter 6 - Vortex Fluid Behaviour</b>	<b>162</b>
6.1 - Vortexed Liquid Film Shape	162
6.1.1 - Confined Mode Liquid Film Shape	163
6.1.2 - Continuous Flow by Dripping Liquid Delivery	165
6.1.3 - Summary and Outlook on the Vortexed Liquid Film Shape	169
6.2 - Biphasic Systems	170
6.2.1 - Discussion on Biphasic Systems	170
6.2.2 - Summary and Outlook on Biphasic Systems in the VFD	175
<b>Chapter 7 - Future Works</b>	<b>176</b>
7.1 - Ferrocene Processing in the VFD	176
7.2 - Oscillation Reactions	183
7.3 - Oil degumming	187
7.4 - Experimental Details and Spectra	188
7.4.1 - VFD One-Pot Synthesis of Ferrocene	188
7.4.2 - Attempted Cracking of Dicyclopentadiene in VFD with Carrier Gas	189
7.4.3 - Attempted Cracking of Dicyclopentadiene in VFD (Sealed)	190
7.4.4 - Oscillation Details	191
7.4.5 - Oil Degumming Details	192
<b>Chapter 8 - Summary and Outlook</b>	<b>193</b>
<b>Bibliography</b>	<b>195</b>

## List of Figures

- Figure 1.** Documents published by year featuring "flow chemistry" or "flow synthesis" in the title, abstract or key-words, between the years of 1971 – 2018. Generated from SCOPUS, accessed March 2019. .... 1
- Figure 2.** General pathway for the Swern-Moffat oxidation of an alcohol (**3**), showing possible Pummerer rearrangements of intermediates **2** & **4**. .... 3
- Figure 3.** Cross sectional schematics of common ways of achieving multiphase continuous flow across (A) liquid-gas, (B) liquid-liquid and (C) liquid-solid phase boundaries.<sup>29</sup> ..... 3
- Figure 4.** Flow synthesis and optimisation of **12**.<sup>66</sup> IR detection was used to monitor the deprotonation of **8** to form enolate **9**. <sup>1</sup>H-NMR detection monitored the formation of **11** from reacting enolate **9** with aldehyde **10**. Finally, HPLC-UV was able to monitor the formation of, and resulting stereochemistry of **12**. .... 5
- Figure 5.** Biphasic & photochemical flow 1,2-bromoazidation of alkenes, as reported by Cantillo *et.al.*<sup>81</sup> ..... 6
- Figure 6.** The Vortex Fluidic Device (VFD). (A) Schematic showing a flow process in the VFD, where reagents are delivered to the base of the rotating tube. Expansion represents the liquid thin film against the glass tubing as it flows up the length of the tube. (B) Photograph of a VFD, with a tube partly inserted.<sup>82, 83</sup> ..... 7
- Figure 7.** Examples of synthetic applications reported in the VFD. (A) Outcome of cross-coupling reactions in the VFD, controlling for tilt angle and rotational speed.<sup>100</sup> (B) Enzymatic activity is rotational speed dependant.<sup>99</sup> ..... 9
- Figure 8.** Examples of materials processing applications reported in the VFD. (A) The controlled cutting of carbon nanotubes.<sup>89</sup> (B) SEM images of conical C<sub>60</sub> fullerene crystals formed under specific conditions.<sup>101</sup> ..... 10
- Figure 9.** Large-volume (≥100 mL) aerobic oxidation of **18** to **19** is limited by inefficient mass transfer of oxygen to the reaction mixture, but this is more efficient using VFD processing (rotational speed 7 krpm, 45°)..... 14
- Figure 10.** An optimised continuous flow oxidation of **18** to **19** provides full conversion of the disulphide over a short residence time ..... 14
- Figure 11.** Photograph of allyl phenyl sulphide (**20**) and bleach (HOCl + NaOCl, aq.). Clearly indicating the immiscibility thereof. .... 17
- Figure 12.** (A) Allyl phenyl sulphide (**20**) is immiscible in bleach. Inefficient mixing in stirred batch reactions results in minimal oxidation. (B) VFD processing promotes the bleach oxidation of **20**, providing dichlorinated sulphone **23** as the major product..... 17
- Figure 13.** Demonstration of the VFD providing sulphone **23** in useful isolated yields..... 18
- Figure 14.** Asymmetric unit found in the crystal structure of purified **23**. .... 18
- Figure 15.** (A) To determine the relative stereochemistry in **26**, the epoxide was opened by the stereo- and region-specific reaction with thiophenol. The product of this reaction was suitably crystalline for single crystal diffraction studies. (B) Symmetry expanded crystal structure of **27**, confirming the relative stereochemistry and showing a hydrogen-bonded dimer (H-bonds shown as dotted red lines). .... 21
- Figure 16.** The VFD is efficient at dissipating the heat associated with the exothermic epoxidation. When the reaction was simply stirred (bottom left image), IR thermal imaging revealed temperature spikes to over 90 °C after just 3 minutes. The same reaction in the thin film of the VFD was maintained at 23 °C (bottom right image)..... 22
- Figure 17.** (A) Epoxidation of **25** with H<sub>2</sub>O<sub>2</sub>, catalysed by NaOH. The aqueous phase was re-used for multiple cycles successfully, demonstrating the ability to recycle the aqueous phase. (B) Conversion in increasing re-use cycles. Also shown is the corresponding reduction in concentration of NaOH in the aqueous layer with each cycle, from the addition of aqueous H<sub>2</sub>O<sub>2</sub>. (C) Repeated experiment adding extra H<sub>2</sub>O<sub>2</sub> and NaOH to maintain original concentrations. .... 23
- Figure 18.** (A) General schemes of common olefin metathesis reactions CM, RCM and ROMP. (B) Mechanism of the ruthenium based methylidene active species, showing the 4-membered ring transition state. This methylidene is formed from the initial catalyst going through the same process shown here.<sup>149, 150</sup> ..... 49
- Figure 19.** Grubbs-type ruthenium OM catalysts used in this work. These were purchased as a kit from Sigma-Aldrich. 50
- Figure 20.** Schematic of a general ethenolysis type olefin metathesis (OM) reaction..... 51
- Figure 21.** Metathesis equilibrium of methyl oleate (**28**)..... 52
- Figure 22.** The compositional distribution of the reaction mixture after 20 minutes is shown, comparing VFD and batch processing for catalysts (B) **G1**, (C) **GII** and (D) **HGI** including results from continuous flow processing with 20-minute residence time. Compositional distributions determined by GCMS. (see Figure 21 for reaction scheme) ..... 53
- Figure 23.** Monitoring the conversion of **34** (**34**) CM with catalyst **G1** over 10 minutes. Adding the quenching solution at 1 minute halts the reaction. The quenching solution consisted of *N*-acetyl-L-cysteine (**18**) in MeCN (20 mg/mL, 0.12 M). Conversions were determined by GCMS..... 54

- Figure 24.** (A) Super imposed  $^1\text{H-NMR}$  spectra of catalyst **GI** titrated against **18** (20mg/mL in MeCN). Contains an internal standard of trimethoxybenzene (1 eq. wrt. **GI**). Added at equivalents of, from left to right, 0 eq. (red), 0.2 eq. (yellow), 0.4 eq. (green), 0.6 eq. (cyan), 0.8 eq. (blue), 1 eq. (purple). Note the convenient down-field shift at each addition, likely due to the increasing concentration of MeCN. This allows visualization without shifting the spectra relative to each-other. (B) Consumption of **GI** after addition of **18** solution (20 mg/mL in MeCN) to **GI**. Determined from the alkylidene  $^1\text{H-NMR}$  peak relative to internal standard (TMB). ..... 55
- Figure 25.** (A) Super imposed  $^1\text{H-NMR}$  spectra of catalyst **GI** titrated against **18** (20mg/mL in MeCN). Contains an internal standard of trimethoxybenzene (1 eq. wrt. **GI**). Shown are the new peaks formed after addition of the **18** solution. Added at equivalents of, from left to right, 0 eq. (red), 0.2 eq. (yellow), 0.4 eq. (green), 0.6 eq. (cyan), 0.8 eq. (blue), 1 eq. (purple). (B) Formation of new singlet at 10.05 ppm after additions of **18** solution (20 mg/mL in MeCN) to **GI**. Determined from the new  $^1\text{H-NMR}$  singlet at 10 ppm. Integral relative to internal standard (TMB). Note that the TMB integral is a result of three  $^1\text{H}$  nuclei and has been adjusted as such..... 57
- Figure 26.** HRMS (+ve) of crude mixture after reacting **GI** with **18** / MeCN solution (1 eq., 20 mg/mL). ..... 57
- Figure 27.** HRMS (-ve) of crude mixture after reacting **GI** with **18** / MeCN solution (1 eq., 20 mg/mL). ..... 58
- Figure 28.** Quenching activity of both MeCN and a MeCN + **18** solution for three different Grubbs-type Ru-based OM catalysts. .... 60
- Figure 29.** Chromatographic retention of the four different Ru-based OM catalysts, **GI**, **GII**, **HGI** and **HGII**. Mobile phase of 20% EtOAc in hexanes. Stationary phase of Silica coated aluminum plate. Visualized with UV light (256 nm). ..... 60
- Figure 30.** UV-Vis spectra in solutions of  $\text{CHCl}_3$ . Spectra for **GI**, **GI** with MeCN and finally the catalyst **GI** with the quenching solution of **18** in MeCN (0.12 M)..... 61
- Figure 31.** UV-Vis spectra and photographs of the **GI** catalyzed CM of **34** in solution ( $\text{CHCl}_3$ ), and also when quenched, both with MeCN and **18** + MeCN. .... 62
- Figure 32.** Diagram displaying the two different approaches to continuous flow catalyst separation in the VFD. On the left of the VFD is the proposed multiphase metathesis. On the right are the two methods for catalyst immobilisation. .... 63
- Figure 33.** Multiphase CM of allyl alcohol. (A) Comparison between batch vs VFD processing, and (B) the  $^1\text{H-NMR}$  analysis, highlighting the overlap observed in the starting material and product peaks when using  $\text{D}_2\text{O}$  solvent. .... 64
- Figure 34.** Two methods developed for the synthesis of **45**. (A) Synthesis in two steps (55 % yield) from 1-thio- $\beta$ -D-glucose tetraacetate (**39**), and (B) Synthesis in four steps (14 % yield) from  $\beta$ -D-glucose pentaacetate (**41**). ..... 65
- Figure 35.** Proposed tethering method using catalyst **HGII-NH<sub>3</sub><sup>+</sup>**. The Silane can be tethered to either the glass VFD tube or to  $\text{SiO}_2$  coated nanoparticles (Figure 32). ..... 65
- Figure 36.** Pathway for the synthesis of the NHC ligand **54** as a tetrafluoroborate salt. This synthesis was adopted from Robinson et.al.<sup>235</sup> ..... 66
- Figure 37.** Ligand exchange of the imidazolium salt with the  $\text{P}(\text{Cy})_3$  ligand of the catalyst **HGI**. Shown is (A) the literature method from Robinson et.al.,<sup>235</sup> and (B) the exchange facilitated by DBU. .... 67
- Figure 38.**  $^1\text{H-NMR}$  spectra of the imidazolium salt before and after ion exchange of the tetrafluoroborate (**54**) to the carbonate (**55**). This was performed in a column loaded with Amberlyst resin. Highlighted is the full consumption of the tetrafluoroborate salt proton peak. .... 67
- Figure 39.** Attempts to achieve ligand exchange of the imidazolium to replace the  $-\text{P}(\text{Cy})_3$  of catalyst **HGI**. Various bases trialled were (A) sodium carbonate, (B) triethylamine and (C) DBU. DBU being the only successful base trialled. .... 68
- Figure 40.** Method used for the preparation of  $\text{Fe}_3\text{O}_4@ \text{SiO}_2$ . This involves co-precipitation to form the  $\text{Fe}_3\text{O}_4$  and subsequent silane coating using a reverse-emulsion method..... 68
- Figure 41.** VFD and batch comparisons for 9 different catalysts, for the (A) CM of **20**, (B) CM of **34**, (C) RCM of **59** and (D) RCM of **61**. Conversions determined by  $^1\text{H-NMR}$ . For catalyst structures, see pg. 50. .... 70
- Figure 42.** The CM reaction of **20**, comparing both  $\text{N}_2$  and  $\text{O}_2$  atmospheres, in VFD at 7 krpm for (A) 5 minutes (also shown is batch control) and (B) for 1 hour..... 71
- Figure 43.** The CM reaction of **20**, in the VFD at 7 krpm. Atmosphere maintained for 10 minutes, before being replaced for the remaining 50 mins, for a total reaction time of 1 h. .... 72
- Figure 44.** E/Z ratio of the CM reaction of **20** in VFD at 7 krpm, after 1 h. Comparisons between various atmospheric compositions are shown. Arrow (->) indicates that at 10 minutes, the atmosphere was evacuated and replaced with a new atmosphere. .... 72
- Figure 45.** The RCM reaction of **61**. Plot showing the reaction conversions after an hour after maintaining atmospheric compositions of  $\text{O}_2$  and  $\text{N}_2$ , and reactions maintaining the initial atmosphere for 10 mins, then replacing the atmosphere with  $\text{N}_2$  for the remaining 50 mins of reaction..... 73

<b>Figure 46.</b> Monitoring the activity of catalyst <b>GI</b> in CH <sub>2</sub> Cl <sub>2</sub> for both the (A) CM of <b>34</b> and (B) RCM of <b>59</b> . Aliquots were taken at set time intervals and quenched in a solution of <b>18</b> in MeCN. Conversion determined by GCMS.....	74
<b>Figure 47.</b> Monitoring the activity of catalyst <b>GII</b> in toluene for the (A) CM of <b>20</b> , (B) CM of <b>34</b> , (C) RCM of <b>61</b> and (D) RCM of <b>59</b> . Aliquots were taken at set time intervals and quenched in a solution of <b>18</b> in MeCN before GCMS analysis. ....	75
<b>Figure 48.</b> The activity of catalyst <b>GII</b> after 10 minutes in various solvents for two examples of CM ( <b>20</b> and <b>34</b> ) and two examples of RCM ( <b>61</b> and <b>59</b> ). Reactions were quenched with <b>18</b> in MeCN and conversions were determined by GCMS. ....	76
<b>Figure 49.</b> Monitoring the activity of <b>GII</b> in the catalysis of the RCM of <b>61</b> , in solvents of (A) dimethyl formamide (DMF) and (B) dimethyl carbonate (DMC). Comparisons were drawn between batch and VFD 7 krpm processing. Aliquots were taken at set time intervals and quenched in a solution of <b>18</b> in MeCN before GCMS analysis. ....	76
<b>Figure 50.</b> Activity of catalyst <b>GI</b> in the RCM of <b>61</b> in toluene, in VFD and batch. Comparisons were drawn between batch and VFD 7 krpm processing. Aliquots were taken at set time intervals and quenched in a solution of <b>18</b> in MeCN before GCMS analysis. ....	77
<b>Figure 51.</b> Activity of catalyst <b>GI</b> in the RCM of <b>61</b> in toluene, in VFD at 7 krpm compared to batch. Aliquots were taken at set time intervals and quenched in a solution of <b>18</b> in MeCN before GCMS analysis. Note that there was a 1 hour gap between collecting the data points for the 4-minute and 4.5-minute points for the VFD processed reaction. There was also a 1.8 °C drop in outside room temperature recorded in this time.....	78
<b>Figure 52.</b> General schematics showing the formation of polyurethane from (A) conventional method using di-alcohols and di-isocyanate, and (B) from an epoxide and an isocyanate. ....	118
<b>Figure 53.</b> (A) The salen based catalyst, either the Mg or the Zn variant. (B) The <b>64-Mg</b> catalysed reaction of phenyl isocyanate ( <b>66</b> ) with cyclohexene oxide ( <b>65</b> ), producing the polyurethane, polyallophinate and the isocyanurate ( <b>67</b> ). (C) the <b>64-Mg</b> catalysed reaction of cyclohexene oxide with phenyl isothiocyanate ( <b>68</b> ), which does not form the allophinate or the cyanurate. Note that a Newman-Kwart re-arrangement of the thiol is taking place. ....	118
<b>Figure 54.</b> (A) Formation of di-phenyl urea ( <b>69</b> ) in the VFD, (B) evident from the small crystals that form on the VFD tube. (C) the speculative mechanism for the production of <b>69</b> from <b>66</b> and water. (D) none of the urea <b>69</b> is formed when performed under inert atmosphere with flame-dried glassware.....	120
<b>Figure 55.</b> Stability of both the polyurethane and the polyallophinate was established in the VFD before undertaking further any synthesis of polyurethanes or polyallophinates. This shows that after 12 h processing in the VFD at 7 krpm, dissolved in dioxane, there is no degradation of the polymers.....	121
<b>Figure 56.</b> Comparisons of batch vs VFD processing for the <b>64-Mg</b> (7 mg, 0.2 mol %) catalysed polymerisation of <b>65</b> (0.5 mL, 4.9 mmol) and <b>66</b> (0.54 mL, 4.9 mmol). The recovered yields are reported as the weight (mg) due to the M <sub>w</sub> not being possible to determine. Composition of the polymers were determined by <sup>1</sup> H-NMR analysis (80 °C, D <sub>6</sub> -DMSO - see pg. 138). ....	123
<b>Figure 57.</b> Comparisons of the conversions to the polythiourethane in batch vs VFD processing for the <b>64-Mg</b> (7 mg, 0.2 mol %) catalysed polymerisation of <b>65</b> (0.5 mL, 4.9 mmol) and <b>68</b> (0.59 mL, 4.9 mmol). Conversions determined by <sup>1</sup> H-NMR analysis (CDCl <sub>3</sub> ). ....	124
<b>Figure 58.</b> Comparisons of the M <sub>w</sub> of polymers produced in batch vs VFD processing for the <b>64-Mg</b> (7 mg, 0.2 mol %) catalysed polymerisation of <b>65</b> (0.5 mL, 4.9 mmol) and <b>68</b> (0.59 mL, 4.9 mmol). M <sub>w</sub> determined by GPC... ..	125
<b>Figure 59.</b> Attempted <b>64-Mg</b> catalysed polymerisation of epoxide <b>65</b> with isothiocyanate ( <b>70</b> ). This was not found to occur with the stated conditions. Only recovered starting material was identified by <sup>1</sup> H-NMR analysis. ....	125
<b>Figure 60.</b> Stacked <sup>1</sup> H-NMR spectra of <b>72</b> operated in the both batch and the VFD@7 krpm for 12 hours at 100 °C. Also present is 0.01 equivalents of trimethoxy benzene ( <b>74</b> ). These were both performed in VFD tubes sealed with a rubber septum. This shows that the <b>72</b> permeates the rubber seal, and that more is lost in VFD processing compared to batch.....	127
<b>Figure 61.</b> Synthesis of nylon-6,6 – The famous nylon rope trick. <sup>264</sup> .....	133
<b>Figure 62.</b> SEM images of polyurethane / graphene oxide composites formed after continuous flow processing in VFD at 45° tilt angle. Two feeds were employed, one of polyurethane solution the other of the graphene oxide solution. The graphene oxide was dissolved in water, the polyurethane was dissolved in either DMF (A, C & E) or CHCl <sub>3</sub> (B, D & F)) as indicated in image annotation. Each feed was delivered by syringe pump to the base of the rotating tube at a rate of 0.5 mL/min for a total flow rate of 1 mL/min (≈ 20 minute residence). Rotational speeds used were 8 krpm (A & B), 6 krpm (C & D) and 4 krpm (E & F), as specified in image annotation. ....	134
<b>Figure 63.</b> <sup>1</sup> H-NMR (D <sub>6</sub> -DMSO, 90 °C) spectrum of the polymer produced from <b>65</b> and <b>66</b> in the VFD at 7 krpm, at 100 °C for 30 minutes (Figure 56). Highlighted are the Phenyl, methyne and methyl contributions from each of the polyurethane and polyallophinate fractions. ....	139
<b>Figure 64.</b> General scheme for the oxidative sulphitolysis (OS) reaction, cleaving a disulphide with sulphite and tetrathionate. This process results in sulphite protected thiols.....	149

<b>Figure 65.</b> Representation of insulin, highlighting the two chains that are linked through two disulphide bridges. These are the A-chain and the B-chain. There is also a disulphide bridge in the A-chain .....	150
<b>Figure 66.</b> OS of L-cystine ( <b>82</b> ) in a tris buffered D <sub>2</sub> O solution (pH 11.3). Conversions determined by <sup>1</sup> H-NMR analysis. Comparisons between batch and four VFD rotational speeds (4, 6, 7.5 and 9 krpm).....	151
<b>Figure 67.</b> OS of L-cystine in a carbonate buffered D <sub>2</sub> O solution (pH 9). Conversions determined by <sup>1</sup> H-NMR analysis. Comparisons between batch and three VFD rotational speeds (4.5, 7 & 9 krpm).....	152
<b>Figure 68.</b> OS of oxytocin ( <b>84</b> ) in carbonate buffer. Comparisons between batch vs three VFD operational speeds (4.5, 7 and 9 krpm) were performed in carbonate buffered to pH's of 9, 9.5, 10 and 10.5. The conversions were determined using HPLC. ....	154
<b>Figure 69.</b> HPLC-MS TIC trace for the insulin in a tris buffered (pH 9) urea solution (8 M aq.) with EDTA. Shown are ( <b>A</b> ) the freshly prepared solution and ( <b>B</b> ) the same solution after 24 hours. Peaks of interest are the five observed peaks between 12 – 15 minutes.....	155
<b>Figure 70.</b> HPLC-MS TIC trace of the reaction mixture following OS of the complex degraded insulin seen in Figure 69. The peak at 14.58 min retention can be identified as the B chain of insulin with both thiols capped with SO <sub>3</sub> <sup>-</sup> . The peak at 19.07 mins does not match expected masses for A chain with any possible combination of -SO <sub>3</sub> <sup>-</sup> capping on the possible four cysteine residues (Table 14). ....	156
<b>Figure 71.</b> Representative neutron images of the VFD with 1 mL H <sub>2</sub> O. ( <b>A</b> ) shows the raw image, and ( <b>B</b> ) shows the result of subtracting an image of the VFD with an empty tube. VFD was operated at 45° tilt angle. Images were taken at 50 rpm increments from 2-8 krpm. ....	163
<b>Figure 72.</b> Experimentally validating a theoretical model for predicting film thickness and maximum film height of water within the VFD. <sup>271</sup> .....	164
<b>Figure 73.</b> A) Cross sectional diagram and B) photograph of a typical single feed continuous flow VFD process. Shown is the lipped glass tube which is rotating independently of a stainless-steel jet feed. Liquid is injected into the steel jet feed, forms droplets and travels to the hemispherical base of the rotating tube. It then forms a vortex and moves up and out of the tube. The liquid then exits perpendicular to the rotating tube due to centrifugal forces. ....	165
<b>Figure 74.</b> Neutron images of a continuous flow process in the VFD, at 45° tilt. H <sub>2</sub> O is being delivered via stainless steel jet-feed to the base of the tube, rotating at 6.5 krpm. Shown are frames progressing as ( <b>A</b> ) the droplet of liquid forms within the jet-feed, ( <b>B</b> ) moves down the jet-feed and ( <b>C</b> ) enters the rotating tube. ( <b>D</b> ) After the droplet has been delivered, the increased volume within the tube is evident by the film reaching a higher point of the tube. ....	166
<b>Figure 75.</b> Photographs of the spatter patterns of red dye exiting the rotating VFD tube at rotational speeds of ( <b>A</b> ) 7 krpm, ( <b>B</b> ) 8 krpm and ( <b>C</b> ) 9 krpm. ....	166
<b>Figure 76.</b> Frequency distribution plots of the size (width, μm) of the droplets after exiting the rapidly rotating VFD tube. Droplets are shown in Figure 75. The size of the droplets in μm are graphed, for speeds of ( <b>A</b> ) 7 krpm, ( <b>B</b> ) 8 krpm and ( <b>C</b> ) 9 krpm. “n” indicates sample size of droplet spatters. ....	168
<b>Figure 77.</b> Stitched neutron images showing toluene (0.5 mL) and D <sub>2</sub> O (0.5 mL) in the VFD at various speeds. These speeds are ( <b>A</b> ) 1 krpm, ( <b>B</b> ) 2 krpm, ( <b>C</b> ) 3 krpm, ( <b>D</b> ), 4 krpm, ( <b>E</b> ) 5 krpm and ( <b>F</b> ) 6 krpm. ....	171
<b>Figure 78.</b> Neutron images of the base of rotating tube with 1:1 toluene to D <sub>2</sub> O. The top row ( <b>A-C</b> ) contains 1 mL total (0.5 mL of each liquid) and the bottom row ( <b>D-F</b> ) contain 4 mL total (2 mL of each). The resolution between layers, especially at high speeds is vastly improved with larger volumes. Image contrasts are adjusted to clearly show two phases where possible. ....	172
<b>Figure 79.</b> Representative neutron image from monitoring the phase separation of a pre-sonicated emulsion of toluene and D <sub>2</sub> O. Image from the combined exposure over the initial 30 seconds of rotating the emulsion at 8 krpm. ....	173
<b>Figure 80.</b> In-situ SANS pattern of D <sub>2</sub> O, and mixtures of D <sub>2</sub> O/toluene at various speeds in the VFD. This pattern is baseline – no structure can be elucidated. ....	174
<b>Figure 81.</b> Common procedure for the synthesis of ferrocene. ....	176
<b>Figure 82.</b> Attempts to achieve one-pot synthesis of ferrocene in the VFD. This involved room temperature in batch ( <b>A</b> ) and VFD @ 7 krpm ( <b>B</b> ), and also at 80 °C in batch ( <b>C</b> ) and VFD @ 7 Krpm ( <b>D</b> ). Reactions were performed in deuterated solvents and <sup>1</sup> H-NMR analysis was performed directly on crude reaction mixtures after 1 h. No ferrocene was detected in any case. ....	177
<b>Figure 83.</b> Attempted on-pot synthesis of ferrocene in the VFD with laser (1000 nm), with laser power at ( <b>A</b> ) 650 mJ and ( <b>B</b> ) 460 mJ. <sup>1</sup> H-NMR analysis revealed only starting materials remained. ....	177
<b>Figure 84.</b> ( <b>A</b> ) cross sectional schematic of the experimental set-up. A steady stream of N <sub>2</sub> gas is gently flowed over the vortex film ( <b>87</b> ), exits the VFD at passes through a cold trap (-180 °C). ( <b>B</b> ) photograph of the o-ring in the “upper bearing”, where leaks are occurring. ....	178



<b>Figure 85.</b> (A) $^1\text{H-NMR}$ spectra of <b>88</b> , and (B) superimposed $^1\text{H-NMR}$ spectra of attempts to crack <b>87</b> in the VFD at rotational speeds of 3, 4, 5, 6, 7, 8, & 9 krpm. Showing area of the spectrum where <b>88</b> is expected.....	179
<b>Figure 86.</b> The $\text{Fc}/\text{Fc}^+$ redox couple. Shown are the bond lengths. <sup>106</sup> .....	179
<b>Figure 87.</b> Ferrocene crystals obtained in the VFD. (A) Crystals typically obtained in the VFD are rods, with corresponding XRD pattern expected for ferrocene. (B) cubic crystals sometimes obtained at 9 krpm, with unique XRD pattern. ....	182
<b>Figure 88.</b> (A) The competing reactions in the cerium/malonic acid oscillator. (B) the pH indicator ferroin used to visualise this oscillation. ....	183
<b>Figure 89.</b> (A) Absorbance of the cerium/malonic acid oscillator upon reaching the resting state, highlighting the $\lambda$ max at 512 nm. (B) monitoring the wavelength 512 nm over time of the cerium/malonic acid oscillation in an unstirred cuvette – visualised by ferrocene pH indicator ( <b>92</b> ). Note that the instrument was only able to measure consecutively for 2 minutes. After this, it had to be manually reset ( $\approx$ 30 sec) This is indicated by breaks in the spectra and new colour shading.....	184
<b>Figure 90.</b> Plotting the (A) time intervals between each oscillation and the (B) maximum absorbance reached in each oscillation (Figure 89). Intervals indicate the 2-minute monitoring time. Shown are the linear trend-lines, their equations and the linear $R^2$ values.....	185

## List of Tables

<b>Table 1.</b>	Without external temperature regulation, epoxidation of $\alpha,\beta$ -unsaturated ketone <b>25</b> proceeds in higher yield and diastereoselectivity in the VFD (7 krpm). Both confined and continuous modes (entries 3 & 4, respectively) of operation provide higher conversions than batch (entry 2). .....	20
<b>Table 2.</b>	Possible molecular ions for ligand exchanges in (+ve) mode .....	58
<b>Table 3.</b>	Possible molecular ions for ligand exchanges in (-ve) mode .....	59
<b>Table 4.</b>	Chromatographic retention of the four different Ru-based OM catalysts, <b>GI</b> , <b>GII</b> , <b>HGI</b> and <b>HGII</b> . Mobile phase of 20% EtOAc in hexanes. Stationary phase of Silica coated aluminum plate. Visualized with UV light (256 nm). Table shows the retention factors ( $R_F$ ) of each catalyst, quenched and un-quenched. ....	61
<b>Table 5.</b>	Pre-liminary experiments for observing the effect of the VFD on the formation of isocyanurate ( <b>66</b> ). Comparisons between VFD @ 7 krpm vs batch are shown, entries 1 & 2 are 12 hour runs without catalyst ( <b>64-Mg</b> ), 3 & 4 are 0.5 hour runs with 2 mol % catalyst ( <b>64-Mg</b> ), followed by entries 5 & 6 which extend to 2 hours with the catalyst. Conversions were determined by $^1\text{H-NMR}$ analysis. ....	119
<b>Table 6.</b>	Reaction of phenyl isocyanate ( <b>66</b> ) in VFD at 7 krpm, vs batch. However, the temperature of VFD reaction was later proven un-reliable. ....	122
<b>Table 7.</b>	Comparisons of the <b>64-Mg</b> catalysed reaction of epoxide ( <b>65</b> ) with isocyanate ( <b>66</b> ) in batch vs VFD. Entries 1 & 2 and 3 & 4 are duplicates of the same conditions, entry 5 is a lone experiment in the VFD at 4 krpm. Entries 6 & 7 are both in batch, comparing different temperatures (80 & 95 °C). ....	122
<b>Table 8.</b>	Comparisons of the conversion to the polycarbonate and cyclic carbonate ( <b>71</b> ) in batch vs VFD for the <b>64-Mg</b> catalysed reaction of the epoxide ( <b>65</b> ) with $\text{CO}_2$ . Conversions were determined by $^1\text{H-NMR}$ analysis. ....	126
<b>Table 9.</b>	Comparisons of the conversion to the polycarbonate and cyclic carbonate ( <b>73</b> ) in batch versus VFD for the <b>64-Mg</b> catalysed reaction of the epoxide ( <b>72</b> ) with $\text{CO}_2$ . Entries 1 and 2 were performed at 100 °C, whilst entries 3 & 4 were at 115 °C. The conversion were determined by $^1\text{H-NMR}$ analysis. ....	127
<b>Table 10.</b>	Thermally initiated free radical polymerisation of styrene ( <b>75</b> ) with benzoyl peroxide ( <b>76</b> ). ....	129
<b>Table 11.</b>	Ability for benzoyl peroxide ( <b>76</b> ) to initiate the polymerisation of styrene ( <b>75</b> ) at room temperature. (n.r = no reaction). ....	130
<b>Table 12.</b>	Benzophenone ( <b>77</b> ) as a photosensitiser for <b>76</b> to be a radical initiator of the polymerisation of <b>75</b> . (n.r = no reaction). ....	130
<b>Table 13.</b>	The polymerisation of styrene initiated by irgacure-2959 ( <b>78</b> ). ....	131
<b>Table 14.</b>	Insulin A-chain expected (-) ve mode masses. Shown are the expected masses with increasing amount of charge in the columns, and the increasing amount of possible $-\text{SO}_3^-$ groups, capping the four possible cysteine thiol residues. Numbers calculated from native A-chain chemical formula of $\text{C}_{99}\text{H}_{155}\text{N}_{25}\text{O}_{35}\text{S}_4$ . ....	156
<b>Table 15.</b>	Insulin B-chain expected (-) ve mode masses. Shown are the expected masses with increasing amount of charge in the columns, and the increasing amount of possible $-\text{SO}_3^-$ groups, capping the two possible cysteine thiol residues. Numbers calculated from native B-chain chemical formula of $\text{C}_{158}\text{H}_{234}\text{N}_{40}\text{O}_{42}\text{S}_2$ . ....	156
<b>Table 16.</b>	Measurements of the thickness of the toluene and $\text{D}_2\text{O}$ phases in a pre-sonicated emulsion after operating in the VFD at various rotational speeds. Measurements are taken from images from the initial 30 seconds, and the final 30 seconds of a 15 minute spin time. Ratios of each layer are shown, and the change in the ratio is calculated. From this, positive values indicate increased mixing and negative values indicate phase separation. ....	173
<b>Table 17.</b>	Studying oxidation of Fc ( <b>90</b> ) to form $\text{Fc}^+$ ( <b>91</b> ) in the VFD vs batch. The biphasic system of <b>90</b> in toluene (1 M) and water was operated under various mixing conditions. Presence of <b>91</b> determined from blue colour in the aqueous phase. ....	180
<b>Table 18.</b>	Studying oxidation of Fc ( <b>90</b> ) to form $\text{Fc}^+$ ( <b>91</b> ) in the VFD vs batch. The biphasic system of <b>90</b> in toluene (1 M) and HCl (1 M, aq.) was operated under various mixing conditions. Presence of <b>91</b> determined from blue colour in the aqueous phase. ....	180
<b>Table 19.</b>	Studying oxidation of <b>90</b> to form <b>91</b> in the VFD vs batch. The biphasic system of <b>90</b> in toluene (1 M) and an oxidant ( $\text{Ox} = \text{Fe}^{\text{III}}$ or $[\text{Fe}^{\text{III}}(\text{CN})_6]^{3+}$ (1 M, aq.) was operated in batch and in the VFD at 7 krpm. Presence of <b>91</b> determined from blue colour in the aqueous phase. ....	181
<b>Table 20.</b>	Comparisons of the phosphorous content (P) in mustard seed oil (entry 1) to that of attempted de-gumming in batch and VFD processing. P determined by microwave assisted acid digestion for ICP-OES analysis. ....	187

## Summary

Sustainable chemistry is vital for the survival of the human race. If unsustainable methods continue, how will future generations continue producing the required foods, materials and medicines? Thus, it is vital to work towards a circular economy, in which everything is sustainably sourced and disposed. It has become apparent over the last decade that flow chemistry can offer a great deal in moving towards a circular economy, and this work seeks to expand on that. Specifically, what benefits can flow vortex microfluidics offer? To this goal, the work herein focuses on exploring a new flow chemistry platform, the Vortex Fluidic Device (VFD) – initially developed by Prof C. L Raston. It was clear in undertaking this Ph. D candidature, that the VFD offers unique benefits for chemical processing - but many questions remained un-answered. Such questions as “how do these benefits arise”, and “what can this device offer in moving towards a circular economy”. During the course of this work, collaborating with many diversely talented people, many questions have been answered - and many *more* questions have been uncovered.

Detailed in this thesis are the avenues that I explored, regarding the development of the VFD. Firstly, the complex fluid dynamics of how liquids behave in the vortex fluidic device, specifically how two immiscible liquids interact, drilling down on the extent of the interfacial area provided by the liquid vortex. Applying these fundamental understandings led to enhancing the heat and mass transfer capabilities of liquids, revealing the possibility to utilise cheap and green reagents where they are not traditionally viable. This was shown to provide scalable transformations whilst enhancing the safety aspects of working with toxic and exothermic reactions. This line of work led to the production of never-before seen compounds, and solved stereo-chemical questions on molecules reported nearly a century ago. Further work showed that the liquid-gas phase barrier is overcome, with mass-transfer achieved on scale in the VFD. This also prompted the development of cheap and novel quenching methods for post-VFD characterisation.

## Declaration

I certify that this thesis does not incorporate without acknowledgment any material previously submitted for a degree or diploma in any university; and that to the best of my knowledge and belief it does not contain any material previously published or written by another person except where due reference is made in the text.

Signed: Scott Pye

Date: 17/12/2019

## Acknowledgements

Throughout the duration of this work, I'd like to acknowledge the following funding that I have received:

- Funding for my Ph. D was provided by the Australian Government Research Training Program Scholarship (This stipend was named the Flinders University Research Scholarship (FURS) for the first year of candidature)
- Funds provided by the Australian Research Council, through discovery grants secured by my supervisors Prof C. L Raston and Dr J. M Chalker.
- Funds provided by the Government of South Australia to set up the Clean Technologies Laboratories.
- Funding for travel, accommodation and consumables relating to a collaborative project involving my visit to the University of Lincoln, UK was provided by The Royal Society (RS), through the International Exchanges scheme.
- Funding towards the travel and accommodation to the International Symposium on the relations between Homogenous and Heterogeneous Catalysis, 2018 (ISHHC18) was provided by Flinders University through a HDR Conference Travel Grant.
- Funding for the travel and accommodation in Lucas Heights, and access to the neutron instruments QUOKKA, BILBY and DINGO and supporting staff were provided in the form of Australian Nuclear Science and Technology Organisation (ANSTO) travel grants.

*I'd like to thank my family. Without their support, this Ph.D. would not have been possible.*

I'd also like to thank both my supervisors for their ongoing support and training. I feel I have learned immensely from them both. Their willingness to help, and for keeping my best interests in mind is greatly appreciated. The individual work of both of my supervisors has already changed the world for the better, and it was an honour to work with you both, especially at the time of your initial collaboration. I look forward to the insights and influences you both will have on facing future issues.

To Dr Louis Adriaenssens, for giving me the opportunity to perform research abroad. Your techniques and approach to life that you have shared are top-notch stuff. Both your mentorship and friendship are greatly appreciated. To Greg Weiss, the ongoing insights and support was greatly appreciated, and I'm very fortunate to have met with you and shared your passion for photography, wildlife and all things.

To all lab members I was fortunate enough to have as colleagues, past and present. The help and support I received in my early years was crucial, and the ability to aid in the development of new members brings me great joy. I look forward to following all your fruitful careers, and I cherish the friendships I have made.

# Chapter 1 - Introduction

## 1.1 - Flow Chemistry

Continuous flow chemistry is not an entirely new concept – early microfluidic devices have been reported as far back as 1940.<sup>1</sup> However, it wasn't until the late 2000's that interest in flow chemistry spiked (Figure 1). Flow chemistry serves as an alternative to traditional “batch” reactors – a term that refers to the typical stirred flask or vats used in chemical synthesis. Put simply, flow chemistry is chemistry that occurs in a fluid medium that is pumped along through a reaction vessel, typically tubing, into a collection vessel. There are a variety of ways to achieve this that vary from typical tube flows; such as falling film, or spinning disk processors. A number reasons have been identified for choosing continuous flow over batch processing. With the large spike in interest also came some exaggerated claims of what is possible – posing questions such as “*Will microreactors replace the round-bottomed flask to perform chemical reactions in the near future?*”<sup>2</sup> These have spurred counter claims such as “*Although they [flow processes] may have helped the academic scientist to produce papers, they have not yet changed the world of those with practical problems in microscale analysis or manipulation*”.<sup>3</sup> Modern consensus gives both flow and batch chemistry their place, and it is not doubted that flow chemistry has much to offer. This chapter highlights what flow chemistry is and what benefits have been described.

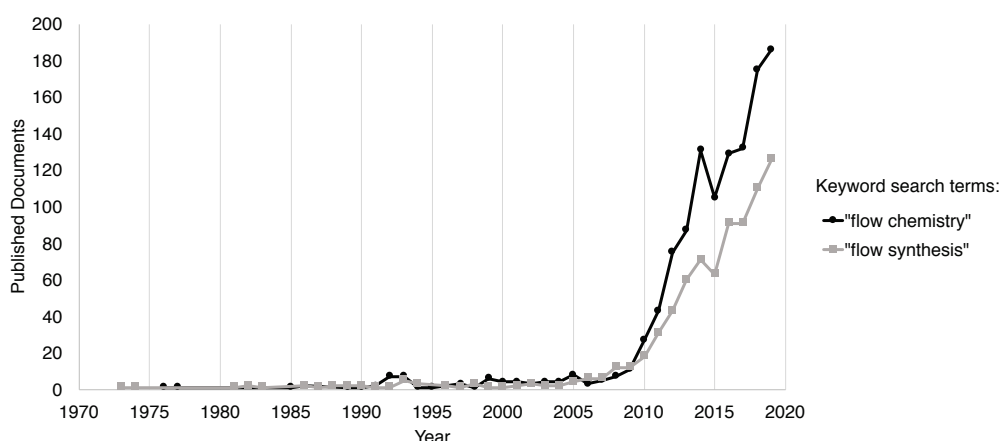


**Figure 1.** Documents published by year featuring "flow chemistry" or "flow synthesis" in the title, abstract or key-words, between the years of 1971 – 2018. Generated from SCOPUS, accessed March 2019.

There has been a great deal of research into flow chemistry, and many concepts have been identified and described in detail in recent reviews.<sup>4-7</sup> A broad approach to describing the benefits of flow chemistry is made here, by categorising in terms of improving the reaction outcome, by the ability to automate a flow process and also the added safety that flow can entail. These concepts are individually reviewed below.

### 1.1.1 – Improved Reaction Outcome

When mentioning a flow process, the first cited “selling-point” often highlights the improved efficiency of the flow process. Efficiency is referred to in terms of both energy usage and atom economy. The fact that flow processes can improve yields in both time and space are incredibly important to improving the green metrics, and cost-benefits of a process.<sup>8-11</sup> In fact, flow chemistry can improve the reaction outcome in many different ways, and what works for one process may not be applicable to another. Thus, when considering the implementation of a flow process, it is important to know the ways in which flow can be beneficial, and how it applies to the given process.<sup>6</sup> Keep in mind that continuous flow also enables allows tailoring of multiple requirements, simplifying multiple step processes.<sup>12, 13</sup>

Firstly, continuous flow devices can improve the surface-area-to-volume-ratios (SA:V). Liquid within a microfluidic flow platform experiences greater SA:V than bulk solutions seen in batch reactors. This in turn increases both the heat-transfer, and the mass-transfer capabilities. The ability to facilitate heat-transfer increases proportionally to the surface area,<sup>7</sup> thus smaller reaction volumes with a great surface area can vastly improve the heat-transfer capabilities. The enhanced ability to remove heat from the reaction has many implications, especially in increasing the safety aspects of exothermic reactions. Inversely, enhanced delivery of heat energy in to the reaction is also a major benefit. This is especially true in providing precise temperature control, optimal for a specific reaction to take place, minimising by-products and reducing waste energy. All of these aspects mentioned are highlighted by the combined research of several groups into continuous flow Swern-Moffatt oxidations. The Swern-Moffatt oxidation is a routinely used text-book reaction.<sup>14, 15</sup> It is employed to oxidise primary or secondary alcohols into the corresponding aldehydes or ketones (Figure 2).<sup>16</sup> Typically, a Swern-Moffatt oxidation is performed at, or below -50 °C for two main reasons. Firstly, to safely perform several key steps that are highly exothermic, and secondly, to slow the thermal degradation of several sensitive intermediates.<sup>17</sup> Recent reports have demonstrated efficient flow Swern-Moffatt oxidations at 0 °C,<sup>16, 18-21</sup> demonstrating how flow chemistry can obviate the need for energy intensive cooling.<sup>22</sup> The exothermic reactions are assisted by the ability to diffuse the heat to the environment as it is generated, before any run-away exotherms can manifest. This allows for a greater degree of temperature control that is not possible in batch reactors, especially on industrially relevant scales. The problem of temperature sensitive intermediates is overcome by the ability to rapidly react these intermediates directly with an input of the next reagent. In the case of Swern-Moffatt oxidations, two key intermediates are susceptible to Pummerer rearrangements (**2** & **4**), rendering them as a hindrance to the reaction efficiency. A stream of the alcohol (**3**) reacts directly with intermediate **2**, forming the second intermediate **4**, which is in turn directly reacted with a separate input stream of the base, forming the final carbonyl product (**5**). Reacting the intermediates directly when they form minimises the life-time of these intermediates, and thus lowers the chance of degradation.

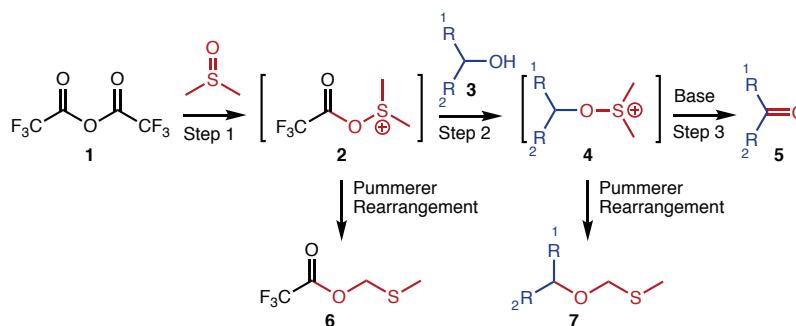


**Figure 2.** General pathway for the Swern-Moffat oxidation of an alcohol (**3**), showing possible Pummerer rearrangements of intermediates **2** & **4**.

Boosting the efficiency of a Swern-Moffat oxidation, by introducing the reagents where they are needed is a type of just-in-time production – another feature of flow chemistry for improving efficiency. This feature has also been demonstrated to allow for chemistry that is not viable in batch reactors, with further examples of controlling unstable intermediates, and also obviating the need for protecting groups.<sup>23</sup> Further examples where a just-in-time approach boosts efficiency are found in the radiochemical synthesis of radio-labelled tracer compounds for PET imaging (positron emission tomography).<sup>24-26</sup> Flow devices have shown promise in improving synthesis of such probes, especially those containing short half-life isotopes; such as <sup>18</sup>F ( $t_{1/2} = 109.7$  min), <sup>15</sup>O ( $t_{1/2} = 2.07$  min), <sup>13</sup>N ( $t_{1/2} = 9.9$  min) and <sup>11</sup>C ( $t_{1/2} = 20.4$  min).<sup>27, 28</sup> In these cases, as soon as the isotope is produced there is a count-down to synthetically incorporate it into the probe molecule, perform any necessary purification and/or validation and then deliver it to the patient. Flow chemistry allows for efficient delivery of the reagents, across multiple steps. In-line purification methods also ensure a pure drug, safe for consumption. The on-demand nature of these processes also can eliminate the requirements of transport, storage and handling of potentially dangerous compounds.<sup>17</sup>

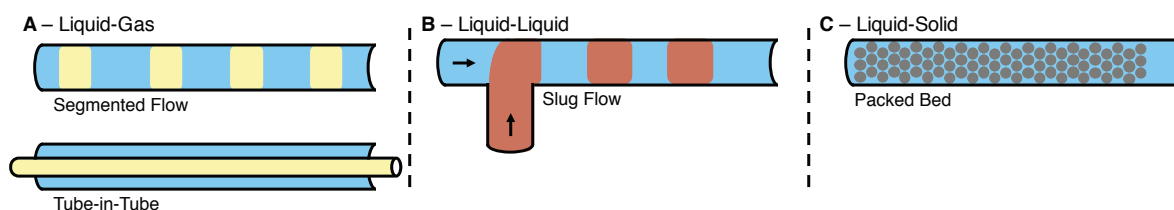


**Figure 3.** Cross sectional schematics of common ways of achieving multiphase continuous flow across (A) liquid-gas, (B) liquid-liquid and (C) liquid-solid phase boundaries.<sup>29</sup>

As previously mentioned, mass-transfer is also increased from greater SA:V ratios. This can be utilised for multiphase reactions limited by phase boundaries, whether it be liquid/gas, liquid/liquid, or liquid/solid. Flow devices have been shown to improve the efficiency of mixing, thus increasing the amount of reactive collisions between molecules.<sup>29</sup> Achieving reactivity across phase boundaries is an obstacle for both batch and flow, however they are able to be overcome with unique set-ups. The type of flow set-up depends on the phases involved. For liquid/gas reactions, various flow regimes have been reported such as bubble, slug and annular flow.<sup>30</sup> These flow regimes allow for interfacial areas 2 orders of magnitude in flow ( $3400 - 18000 \text{ m}^2/\text{m}^3$ ) compared to typical flasks ( $38 - 141 \text{ m}^2/\text{m}^3$ ).<sup>7, 30</sup> These are collectively referred to as segmented flow (Figure 3A). Another way to achieve liquid-gas mass-transfer are by tube-in-tube reactors. These consist of two tubes, a larger outer tube and a smaller inner tube. The inner tube being permeable to gasses, but not liquids. This allows the mass transfer of gas reagents into the liquid media.<sup>30</sup> Alternatively, gaseous by-products can be



removed by having one of the tubes at a reduced pressure. This is the case in the olefin metathesis reaction, where ethene gas build-up can limit reaction progress. A tube-in-tube reactor was shown to improve the reaction outcome by removal of this ethene, driving the equilibrium.<sup>31</sup>

Liquid-liquid phase boundaries are perhaps the most commonly encountered. Typical batch methods for overcoming this use intense mixers, which do not guarantee uniform processing. Another method is to use auxiliary compounds as phase transfer catalysts.<sup>32, 33</sup> These effectively ferry components from their preferred phase and temporarily dump them into the other phase.<sup>34</sup> However, these are often toxic and may involve themselves in the reaction. Flow methods simply combine two (or more) streams of the immiscible liquids.<sup>35</sup> Doing so through a pressure regulated T-junction can provide slug flow (Figure 3B). This is desirable, as the size of the slugs can be accurately controlled, and the interfacial area can be optimised.<sup>29</sup> Furthermore, the fluid within the slug experiences toroidal currents which enhance the mixing ability beyond diffusion limits.<sup>7</sup>

Flow processes across a liquid-solid phase boundary are also common. Typically, a solid supported catalyst will form the stationary phase of a packed bed reactor (Figure 3C).<sup>36, 37</sup> This allows a given transformation to occur, without the need to perform downstream removal of the catalyst. Immobilised catalysts can involve transition metals,<sup>38</sup> enzymes,<sup>39</sup> or magnetically retained nanoparticles<sup>40</sup> to name a few.

### 1.1.2 - Automation

Another feature of flow is the ability to allow automation of the entirety of a process. From planning the retro-synthetic pathway, controlling reaction conditions, detecting reaction progress to the final product purification. This also allows the high throughput generation of data for studying the fundamental kinetics, or optimisation of reaction parameters.

Many established monitoring techniques already exist, for example the commonplace gas chromatography (GC). This is essentially a flow device, commonly monitored by mass-spectrometry (MS) or flame ionization detectors (FIDs). Similarly, high performance liquid chromatography (HPLC) instruments often use the non-destructive U.V-Vis spectrometer detectors. Transferring these existing technologies into flow devices for monitoring reaction progress is therefore not a far-stretch. Thus, these methods for monitoring reaction outcomes in real time have been applied, along with many new methods that have been developed.<sup>41</sup> Because there can't be a single-method able to monitor all possible reaction outcomes, a suite of process analytical technologies have been reported.<sup>42-44</sup> Examples of monitoring by NMR,<sup>45-47</sup> UV-Vis,<sup>48, 49</sup> IR<sup>50-54</sup> and Raman<sup>55, 56</sup> are common, along with other promising techniques such as MS,<sup>57</sup> and cyclic-voltametry.<sup>58</sup> Methods that combine multiple detection methods are vital for a system with broad applicability.<sup>59-68</sup> An example of a modular flow platform combining NMR, IR and UPLC-UV detection was recently reported by the Kappe group (Figure 4).<sup>66</sup> This platform was designed around a multi-step reaction for a medically relevant compound.<sup>69</sup> The first step involves a deprotonation of the propionate **8** with LDA, generating the enolate **9**. This enolate is then reacted with aldehyde **10**, generating the intermediate lithium salt **11**. An input of water then quenched the intermediate **11**, giving the desired product **12**. Monitoring of each step individually allows for the systematic optimisation of the reaction parameters. In this study, the equivalents of LDA was varied between 1 – 1.2 eq. at each temperature of 0, 20 and 40 °C – a monumental task if performed by tradition batch chemistry. This

showed the optimal temperature was actually 20 °C, and not 40 °C as expected. Furthermore, increasing the relative amount of LDA proportionally increased the conversion, and was demonstrated to plateau at 1.1 equivalents. Traditionally, when planning this synthesis, a chemist could easily think “I’ll do it hot, with excess LDA”. Without the high-throughput data generation that automated flow allows, the subtleties of this reaction may not have been found, and the green metrics would be worse-off by comparison. Although the set-up used in this study is somewhat easier to assemble than other flow systems, it is still a limitation to have one set-up for one reaction, *ie.* having a 5 second reaction path before an IR detector, followed by a new input for a further 80 second residence reaction time before a NMR detector. This will not be compatible for studying other reactions. The use of a flow system in facilitating a diverse scope of chemical reactions has been largely addressed by the Jamison group. The use of removable flow modules is promising, allowing the required heating, cooling, light source, or more-whatever is required by the reaction. This is achieved by simply adding or removing the appropriate modules as needed,<sup>59</sup> and has been further explored by the use of retro-synthetic planning software to identify what is required for a reaction, coupled with robotic arms to automate the assembly & disassembly of required modules.<sup>62</sup>

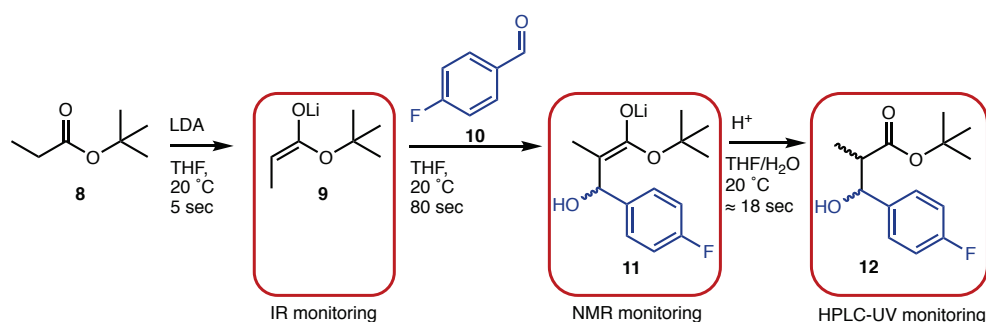


**Figure 4.** Flow synthesis and optimisation of **12**.<sup>66</sup> IR detection was used to monitor the deprotonation of **8** to form enolate **9**. <sup>1</sup>H-NMR detection monitored the formation of **11** from reacting enolate **9** with aldehyde **10**. Finally, HPLC-UV was able to monitor the formation of, and resulting stereochemistry of **12**.

Continuous flow offers ease of optimisation for multiple variables of a reaction.<sup>64</sup> There are an ever-expanding amount of methods developed for real-time monitoring of the reaction progress in flow.<sup>45, 49, 67, 68, 70, 71</sup> Variables such as reaction time, temperature, concentration, stoichiometry, solvent choice and reaction scope are traditionally tediously optimised. Flow allows for high throughput screening of individual parameters.<sup>59, 72, 73</sup> This has recently been demonstrated, and holds potential for vastly increasing the development of fundamental concepts in chemistry.<sup>63, 66</sup> On the other hand; sorting, identifying and then disseminating reaction outcomes from the database of human knowledge is now easier than ever, with the development of automated cataloguing and data-search methods.<sup>48, 74, 75</sup> Flow systems are fundamental to facilitate the automated, scalable synthesis demanded from industry-4.0, and subsequent synthesis-4.0 movement(s).<sup>62</sup> This is made possible by the ability to mix reagents from a hopper, perform desired reaction conditions (heat, light, catalysis *ect.*) and then purify the compound in a single pass.<sup>51, 65, 76</sup>

### 1.1.3 - Safety

Flow platforms can increase the safety aspects of chemical reactions.<sup>17</sup> As previously touched on, the ability to dissipate heat from exothermic reactions is a major boon to safety. Many deaths at chemical plants have arisen from explosions, caused by run-away isotherms in large volumes<sup>77</sup>. Continuous flow can mitigate this

by having smaller volumes within the tubing, and greater surface areas to dissipate the produced heat. This also allows for greater control of the reaction outcome and selectivity. In flow, all parcels of the liquid are treated in a more uniform manner, as opposed to large vessels that allow for heterogeneous heat distribution – *ie.* “hot-spots” in the bulk solution.<sup>17</sup> Flow also enables separating or quenching hazardous compounds in-line, without ever requiring human handling. Separating humans from toxic chemicals is inherently safer than the alternative. An example of harmful processes made safe by flow processing can be found in the handling of azides. Azides are particularly problematic as they pose a variety of hazards; they are typically highly toxic, highly reactive, extremely sensitive and also highly explosive. This aside, the synthetic power and versatility of azides make them a desirable reagent for a number of applications, particularly in cycloadditions forming tri-azole based heterocycles. A prominent example is the important azide click-chemistry reaction.<sup>78-80</sup> A flow processes that encapsulates the added safety, along with the utilisation of a biphasic photochemical process has been reported by Cantillo *et.al.* (Figure 5).<sup>81</sup> In this report, bromine azide (**15**) was generated and subsequently used in the selective 1,2-bromoazidation of olefins. with oxone as an oxidizer, sodium azide (**13**) and sodium bromide (**14**) were reacted to generate the bromine azide (**15**) in an aqueous phase. This is subsequently reacted across the phase boundary with an alkene (**16**) in a hydrophobic phase, generating the 1,2-bromine azide (**17**). For the hydrophobic phase, both CH<sub>2</sub>Cl<sub>2</sub> and EtOAc were demonstrated as effective solvents. Because sodium bromide (**15**) is highly water sensitive, the rapid extraction into the organic phase is reported to slow its decomposition to hydroazoic acid and hypobromous acid, which subsequently decompose into N<sub>2</sub> and HBr. The selectivity of the 1,2-bromoazidation is controlled by the competing ionic vs radical addition pathways. The chance of the radical pathway occurring is increased by the addition of the UV light, amongst other factors (solvent polarity, E.W.G ect.). Thus, the tubing was wrapped around a compact fluorescent lamp, exposing the reaction mixture to UV light. This enhances the radical addition, and subsequently the anti-Markovnikov selectivity. The reaction conversion eventually plateaus with the increasing the reaction time beyond 1 hour, due to the decomposition of the bromine azide. Thus, shorter residence times were employed, before exiting the flow and quenching in excess Na<sub>2</sub>S<sub>2</sub>O<sub>3</sub>. The scope of this reaction was demonstrated for a variety of styrenes, cinnamates and stilbenes, with great success. This demonstrates the power of flow to perform biphasic, photo-chemical processes on reagents that are otherwise too toxic and short-lived to consider using on a large scale.

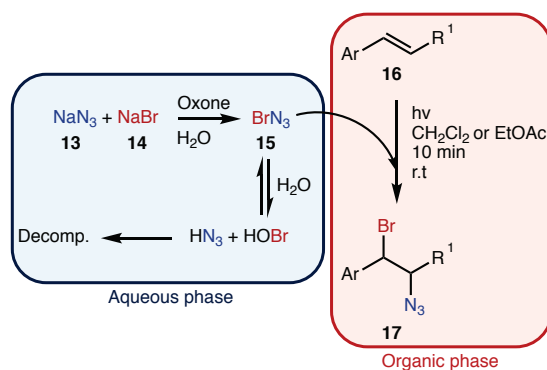
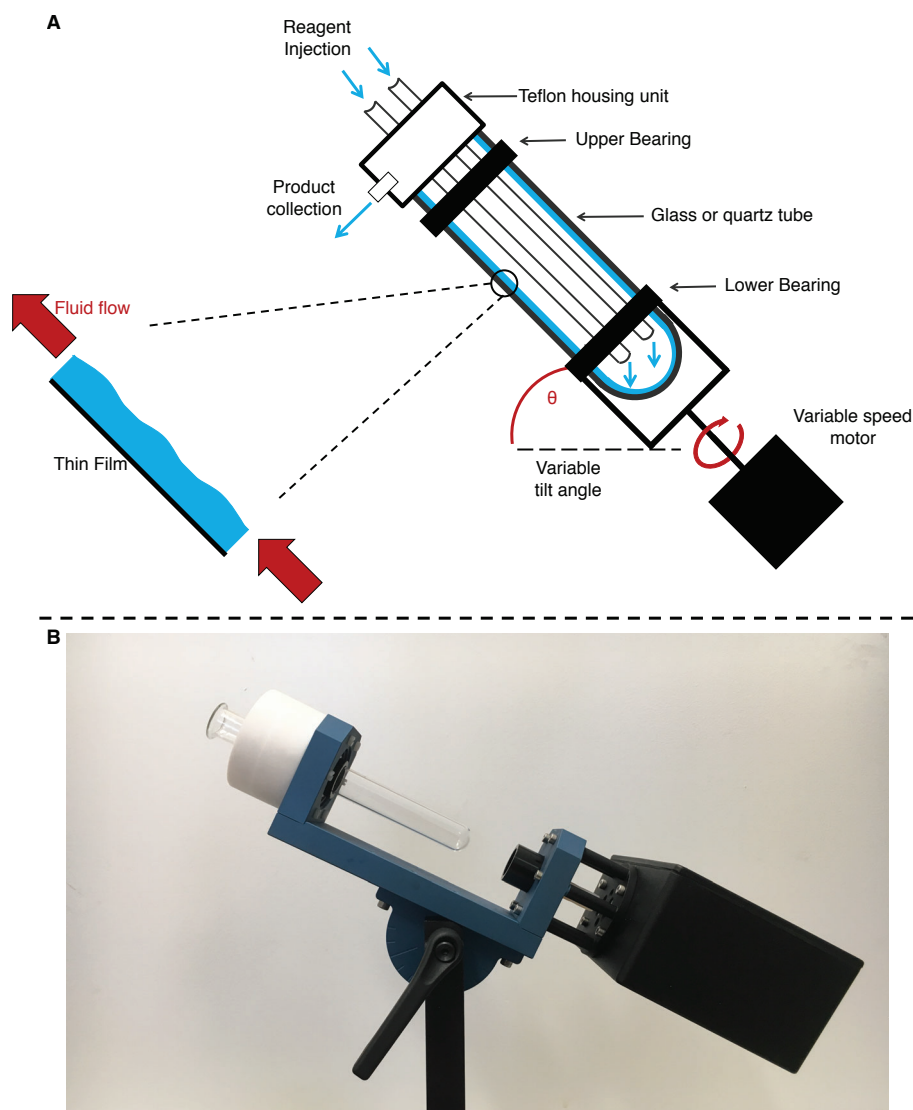


Figure 5. Biphasic & photochemical flow 1,2-bromoazidation of alkenes, as reported by Cantillo *et.al.*<sup>81</sup>

## 1.2 – The Vortex Fluidic Device (VFD)

The Vortex Fluidic Device (VFD, Figure 6) is a unique spin on flow chemistry. The VFD provides an intense vortex in any fluid, and the unique conditions experienced in such a vortex have proven to be extremely promising for a wide variety of applications, in a wide variety of sciences. The VFD also benefits from simplicity in design - simply plug-in and spin.



**Figure 6.** The Vortex Fluidic Device (VFD). (A) Schematic showing a flow process in the VFD, where reagents are delivered to the base of the rotating tube. Expansion represents the liquid thin film against the glass tubing as it flows up the length of the tube. (B) Photograph of a VFD, with a tube partly inserted.<sup>82, 83</sup>

In the VFD, reaction mixtures are rotated at high speeds (current models operate at 0 – 12 krpm), producing a large surface area as the liquid forms a thin film.<sup>84</sup> Highlighted in a recent review,<sup>82</sup> the unique conditions provide many benefits in organic,<sup>85</sup> biochemical<sup>86, 87</sup> and materials chemistry.<sup>88</sup> Previous work shows unique conditions such as shear<sup>86, 89-92</sup>, increased surface area,<sup>93-96</sup> vibrational induced wave effects,<sup>87, 97, 98</sup> of which all can provide many benefits for a wide variety of chemical processing. These are further discussed below. However, despite the progress, there is further research required, as made clear by the surprises that this device still produces.

### 1.2.1 – Description of the VFD

The VFD (Figure 6) was developed by C. Raston in 2011. It is an iteration of high-shear continuous flow devices, expanding upon spinning-disk and rotating-barrel processors. It consists of a variable speed motor, currently capable of selecting, and holding, any rotational speed between 0 – 12 krpm. Through a driveshaft, this rotation is imparted on a tube held between an upper and lower bearings. This tube is typically glass, although quartz variants are regularly used. The earliest models of the VFD housed 10 mm outer-diameter (OD) NMR tubes. Later generations that have become standard, house 20 mm (OD) NMR tubes. These glass tubes are  $\approx 1.5$  mm thick, resulting in internal diameters of  $\approx 17$  mm, depending on manufacturing variance. These tubes are typical NMR tube or test tube designs, but are altered at the open end by creating a lip, as can be seen in photograph in Figure 6B. This lip ensures the liquid leaves the tube, and does not run down the external side after exiting the tube. The two spin guide bearings hold the tube and allow for smooth rotation, and minimal lateral movements, which can cause failures in the glass tubing. The tube connects to the bearings by rubber o-rings, two of which are found in each bearing. These two bearings are held at a fixed distance by aluminium plates, anodised for chemical resistance. This section then sits on a weighted base, and is connected by a hinge. This hinge allows pivoting to set the tilt angle anywhere between  $0^\circ$  –  $90^\circ$ . The final component is the Teflon housing unit, which can house jet-feeds, typically stainless steel for reagent delivery. The liquid, when delivered to the base of the rotating tube will then whirl up and out of the tube. Upon exiting the tube, aided by the lips, it will spray into the housing unit, where it will collect and flow out of a channel for product collection.

Reagent delivery can be achieved by a number of means, peristaltic or HPLC pumps have been successfully employed, however syringe pumps are standard. These pumps allow a liquid reservoir from a syringe to be delivered at an accurate rate. The liquid is delivered from the syringe pump into a jet feed. These are typically 2 mm (OD) stainless steel tubes. The liquid flows through these to a set delivery-point on the tube, forming a droplet which then impacts on the rotating tube. Any fluid within the tube will form a vortex upon rotation, and depending on the rotational speed, will whirl up the length of the tube. Alternatively, the VFD can be operated in the so called “confined mode”. This does away with the liquid delivery apparatus, and is simply a finite amount of liquid within the tube. This liquid is confined within the tube for a certain volume of liquid and rotational speed so as that the liquid does not reach the exit of the tube. Alternatively, a cap can be used to seal the tube, preventing the liquid from escaping. Confined mode is typically used for small scale optimisation before moving to continuous flow, or where small volumes are manipulated, for example in accelerating enzymatic reactions.<sup>99</sup>

### 1.2.2 – Chemical Transformations in the VFD

The VFD has shown un-paralleled effects on chemical transformation that are not seen in batch or traditional flow platforms. These seemingly anomalous effects have been reported on all scales, from small molecule transformations, supramolecular chemistry, enzymatic activity and protein structure all the way through to materials processing. Many unique features are found within the vortex environment, including thin films, high shear regimes, vibrational induced pressure fluctuations amongst other unique fluid dynamics that are not yet fully described. These complex features are enigmatic, and vail each other in ways that are difficult to de-couple. As a result, predictive certainty is not yet achieved with this new technology, and more work is required to realise the potential of vortex flow processing. Nevertheless, these features result in a reaction platform that is truly a paradigm shift in chemical synthesis. Encapsulating the benefits of continuous flow alone is a revolutionary field, and expanding on this with the unique dynamics has seen the realisation of never before seen processing outcomes.

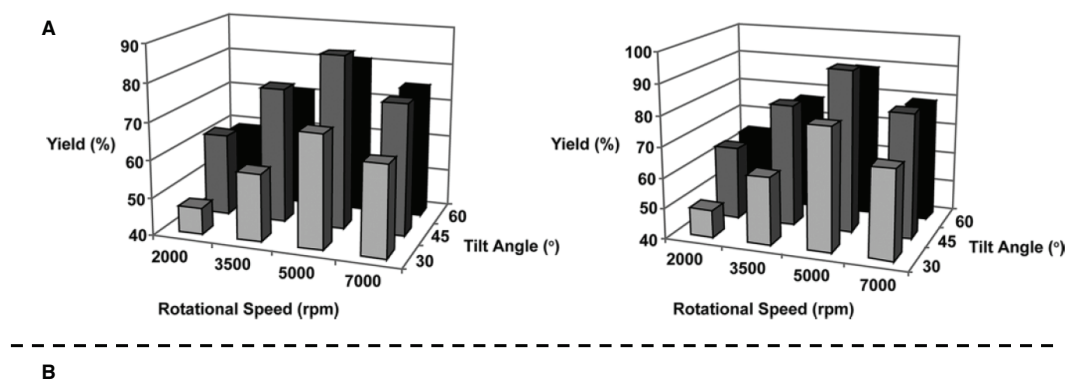


Image removed due to copyright restriction.

**Figure 7.** Examples of synthetic applications reported in the VFD. (A) Outcome of cross-coupling reactions in the VFD, controlling for tilt angle and rotational speed.<sup>100</sup> (B) Enzymatic activity is rotational speed dependant.<sup>99</sup>

A new parameter unique amongst flow devices is provided by the variable tilt angle. Changing the tilt angle has shown to affect the reaction outcome. This is demonstrated in the transition-metal free cross coupling reactions (Figure 7A).<sup>100</sup> Here the reaction outcome is effected by both the tilt angle, and the rotational speed. It was found in this work that a tilt angle of 45° is optimal for these cross-coupling reactions. The fundamental reasons behind these is still uncertain, but it is thought that the vibrational induced waves in the liquid film create pressure gradients, and that this is maximised at 45°. The resulting pressure gradients may then lower the activation energy of the reaction, favouring the productive collapse of the transition state. It is also observed here that the reaction outcome is similarly dependant on the rotational speed, where a rotational speed of 5 krpm was found to be optimal in both cases. This is extrapolated further in the exploration of enzymatic

enhancement (Figure 7B).<sup>99</sup> Here, the activity of 4 enzymes (Esterase,  $\beta$ -glucosidase, Alkaline phosphatase and DERA) were found to experience enhancement dependant on the rotational speed. The optimal rotational speed was found to be different between each enzyme, and also different to the 5 krpm optimal for the cross-coupling reactions. This indicates that the optimal conditions are highly reaction dependant, and there is no one-size fits all approach to vortex fluidics. Again, the fundamental underpinnings of this enzymatic enhancement is not well defined, but it is thought to again be attributed to the pressure fluctuations.

With regards to materials processing, the VFD has seen a plethora of unexpected outcomes. A fine example is the ability for the VFD to cut carbon nanotubes to lengths with un-precedent control (Figure 8A).<sup>89</sup> Here, the shear forces in the VFD will bend the nanotubes until a kink is formed. This alone is not enough strain to force carbon-carbon bond cleavage, however with the use of thermal energy delivered by a high powered NIR laser ( $\lambda = 1064$  nm, 260 mJ pulsed Nd:YAG crystal), enough energy can be imparted to facilitate the bond cleavage. The length of the tubes can then be controlled simply by adjusting the rotational speed. Another example is that of controlling the crystal growth of  $C_{60}$  fullerenes (Figure 8B).<sup>101</sup> Here, it was found that  $C_{60}$  fullerenes, when dissolved solvent mixture of o-xylene and DMF were found to crystallise into never-before seen conical shapes. These were highly specific to the conditions of 4 krpm, at  $45^\circ$  tilt. And also to the flow rate, where a 1 mL/min total flow rate was found to be crucial. These cones can't be justified by vibrations, or by shear stress alone and highlight the complex and mysterious fluid dynamics underpinning the VFD.

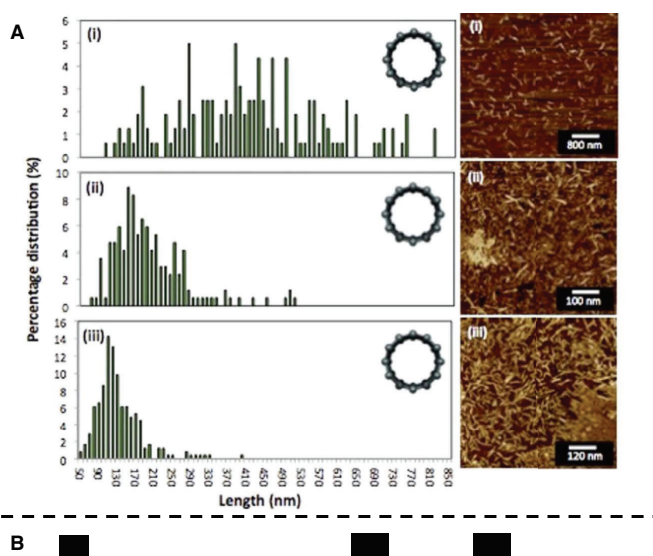


Image removed due to copyright restriction.

**Figure 8.** Examples of materials processing applications reported in the VFD. (A) The controlled cutting of carbon nanotubes.<sup>89</sup> (B) SEM images of conical  $C_{60}$  fullerene crystals formed under specific conditions.<sup>101</sup>

It is clear that the VFD has much to offer, but further work is required to understand the complexities of the fluid flow. Furthermore, developing predictable outcomes of processing using the device is necessary to fully realise the power of vortex fluidics.

## Chapter 2 – Organic Oxidations

*This work has been published in volume 20 of the RSC published journal “Green Chemistry”.  
(2018, page 118-124).*

*Titled “Organic Oxidations Promoted in Vortex Driven Thin Films Under Continuous Flow”<sup>102</sup>*

Environmentally benign chemical transformations are essential in organic synthesis and sustainable processes for the future.<sup>103, 104</sup> Rudimentary oxidations are among the most widely used reactions in synthesis, so efforts to improve their green chemistry profile are especially important.<sup>105-107</sup> However, many classic oxidations are still used routinely in both academic and industrial research despite their reliance on the stoichiometric use of toxic metals,<sup>108</sup> high molecular weight reagents<sup>109</sup> that suffer from poor atom economy,<sup>110, 111</sup> or highly energetic oxidants that present detonation risks.<sup>109, 112</sup> Alternative options such as air or molecular oxygen,<sup>113, 114</sup> hypochlorous acid and sodium hypochlorite (chlorine bleach),<sup>115</sup> and hydrogen peroxide<sup>116, 117</sup> have been identified as green oxidants because of their attractive safety profile, high atom economy, and the generation of innocuous by-products such as water or sodium chloride.<sup>118</sup> To this end, continuous flow reactors have been shown to address safety, scalability and efficiency of many transformations,<sup>12, 17</sup> including these oxidations.<sup>119, 120</sup> These advances notwithstanding, such continuous flow reactors often suffer from high overhead cost, complex operation, the use of organic solvents and channel blocking associated with the formation of emulsions, salts and other insoluble material.<sup>121-123</sup> This chapter examines how the previously mentioned green oxidants can be used ever more efficiently by pairing them with new methods of reaction processing that are efficient, safe, and operationally simple. Specifically, we studied these oxidations in the VFD, with an aim to identify practical benefits that would encourage increased consideration and uptake of green oxidations in chemical synthesis.

We designed our study around two key hypotheses. First, we posited that the thin film processing would improve gas exchange between the reaction medium and the atmosphere, perhaps improving the rate of aerobic oxidations and providing a simple and efficient method for deploying gaseous reagents in synthesis. Second, we suspected that the intense micro-mixing in the VFD that results from extremely rapid rotation of the inclined reaction tube, typically 45° for optimum processing,<sup>85-88</sup> would enable efficient mixing of immiscible materials such as non-polar organic substrates and oxidants in aqueous solution. The problem of immiscibility limits the use of these aqueous oxidants, even in conventional flow reactors, as evident by the use of phase transfer catalysis to promote such reactions.<sup>119, 124</sup> Overcoming this requirement for a catalyst, through intense mixing, could expand the scope of substrates for oxidation with aqueous hypochlorous acid or hydrogen peroxide. Pursuing these hypotheses, we examined three fundamental reactions in organic synthesis: aerobic oxidation of thiols, oxidation of sulphides with bleach, and epoxidation of alkenes with hydrogen peroxide, while eliminating the need for any added catalysts.



## 2.1 - Aerobic Oxidation of *N*-acetyl-L-cysteine

Given the versatility of the VFD and its ease of use, we were motivated to explore the ways in which it could be integrated into oxidations that align with the tenets of green chemistry.<sup>103</sup> Molecular oxygen (O<sub>2</sub>) is a ubiquitous and sustainable oxidant.<sup>113, 114</sup> Because the terminal product of aerobic oxidations is typically innocuous water, oxygen is commonly considered to be a desirable and benign reagent.<sup>125</sup> Its green chemistry credentials notwithstanding, oxygen (as a gas) is often difficult to handle and can present risks for fire when used with organic substrates and flammable solvents.<sup>126, 127, 32</sup> These risks are exacerbated at elevated temperatures and pressures - conditions that also introduce an energy penalty to the process. Therefore, it is useful to devise methods to carry out aerobic oxidations at atmospheric pressure, room temperature, and with non-flammable solvents. With this in mind, we examined the aerobic oxidation of *N*-acetyl-L-cysteine (**18**) in water. The conversion of thiols to disulphides is an important reaction in synthesis and biochemistry, with particular relevance to peptide and protein folding.<sup>128, 129</sup> Given that the VFD has been explored as a technology for folding proteins in-flow,<sup>86</sup> the study of aerobic oxidations of cysteine to cystine also has broader relevance to bioorganic chemistry.

### 2.1.1 – Discussion on Aerobic Oxidation in the VFD

As a starting point, a solution of **18** in D<sub>2</sub>O (1 mL) was buffered to a pH of 9.8 and processed under a stream of oxygen both in a vial with simple stirring and also in the VFD in the confined mode of operation where a defined volume of liquid is placed in the tube at 45° tilt and rapidly rotated. The oxygen flow rate was set at a slow rate (no more than 0.5 L/min) to maintain an oxygen atmosphere, and the pH was selected based on exploratory work that revealed an increase in the rate of oxidation with increasing pH. At pH 9.8, aerobic oxidation of **18** to **19** proceeded at a rate that was convenient for direct analysis of reaction conversion by <sup>1</sup>H NMR. For this small-scale reaction, modest rate enhancement was observed using VFD processing with 40 % conversion observed after 10 minutes in the VFD (7 krpm) and 25 % conversion observed in the vial batch reactor. Apparently at this scale, there is sufficient O<sub>2</sub> available to at least partially oxidise **18** using batch processing and mass transfer of the oxidant is not rate limiting. In contrast, when the batch processing was carried out at a 100 mL scale in a round bottom flask with stirring, very low levels of oxidation were observed (< 5% conversion) even after several hours of reaction time. The resistance to oxidation was observed even when the headspace of the reaction flask was saturated with oxygen, and even when oxygen was bubbled directly into the reaction mixture (Figure 9). This experiment illustrates the common challenge of translating a batch reaction that occurs at small scales to one at larger scales where mass transfer (of gas in this case) is simply not as efficient. The VFD, as a microfluidic platform that can operate under continuous flow, overcomes this problem of scalability by design. As with other microfluidic reactors, a reaction is run locally on a small-scale in the VFD, with up-scaling a matter of simply running the process in continuous mode for a longer time. Gratifyingly, the oxidation of **18** to **19** could be carried out in the VFD operating in continuous mode, with a flow rate of 0.5 mL/min and a stream of oxygen supplied to the reaction at no more than 0.5 L/min. The conversion was 55% (the average for product samples collected regularly from the reactor over a two-hour period). This conversion is slightly improved compared to that observed in confined mode, for the same rotational speed and tilt angle, indicating a reliable translation from small to large scale processing in the VFD.

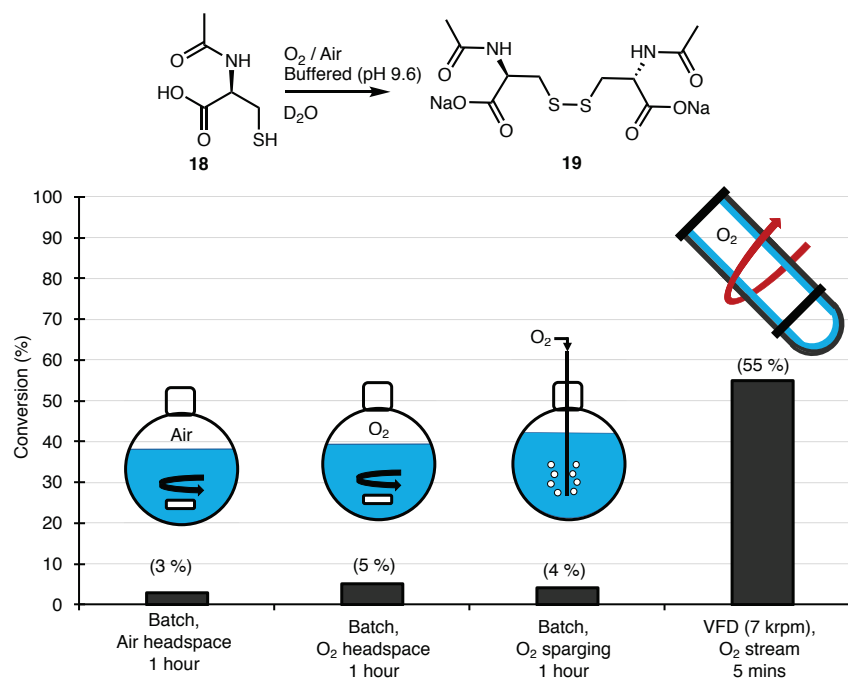


**Figure 9.** Large-volume ( $\geq 100$  mL) aerobic oxidation of **18** to **19** is limited by inefficient mass transfer of oxygen to the reaction mixture, but this is more efficient using VFD processing (rotational speed 7 krpm,  $45^\circ$ ).

Finally, the continuous process was modified to illustrate that synthetically useful conversions could be obtained with this method. Simply raising the pH to 11 allowed the full conversion of **18** to **19**, with 20 mL of reaction mixture processed in a mere 20 minutes (1 mL/min). Under these conditions, the residence time in the VFD (the time for a finite volume of liquid to enter the bottom of the tube and exit at the top) is  $\approx 2.5$  minutes, indicating a highly efficient aerobic oxidation (Figure 10).

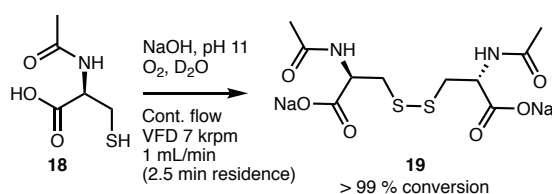


**Figure 10.** An optimised continuous flow oxidation of **18** to **19** provides full conversion of the disulphide over a short residence time

### 2.1.2 - Summary and Outlook on Aerobic Oxidation in the VFD

This series of experiments illustrated that gases such as oxygen can be delivered more efficiently to the thin film reaction mixtures in the VFD than they can to the bulk solutions in batch processing. Continuous processing in the VFD also revealed the ease at which reactions can be scaled relative to batch processing. More generally, the aerobic oxidation of thiols to disulphides is an important transformation in many areas such as organic synthesis<sup>130</sup> and peptide and protein chemistry<sup>129, 131</sup>

## 2.2 – Bleach Oxidations Beyond the Aqueous Phase

Aqueous hypochlorous acid and sodium hypochlorite (chlorine bleach) have long been used as non-flammable, non-explosive green oxidants.<sup>115</sup> However, their direct use in chlorinating or otherwise oxidising non-polar organic substrates is often confounded by the immiscibility of the starting material in water. Accordingly, various surfactants, emulsifiers and phase transfer catalysts have been used to mediate these reactions.<sup>132</sup> We were particularly intrigued by reports in which the non-polar substrate allyl phenyl sulphide (**20**) was resistant to oxidation with bleach.<sup>133, 134</sup> This outcome was quite reasonably attributed to the low miscibility of the polar hypochlorite salts and the hydrophobic (**20**), which prompted the development of various phase transfer catalysts to provoke this two phase reaction.<sup>133, 134</sup> As allyl sulphides and their corresponding sulphoxides and sulphones are highly useful in synthesis,<sup>135-140</sup> we were curious as to whether or not the intense micro-mixing in the VFD would enable oxidation of organic sulphides in bleach without recourse to organic solvents, surfactants or phase transfer catalysts.

### 2.2.1 – Discussion on Bleach Oxidations in the VFD

Firstly, Allyl phenyl sulphide (**20**) was chosen as a model substrate for the bleach oxidation. As seen in Figure 11, **20** is clearly immiscible in the aqueous bleach.

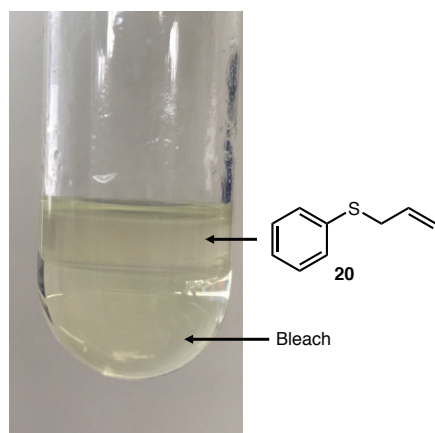


**Figure 11.** Photograph of allyl phenyl sulphide (**20**) and bleach (HOCl + NaOCl, aq.). Clearly indicating the immiscibility thereof.

Allyl phenyl sulphide (**20**) was reacted directly with 10 and then 20 equivalents of bleach oxidant in batch, where the mixture was simply stirred with a stirring bar for 40 minutes at room temperature. Perhaps not surprisingly, limited oxidation was observed in the batch, with less than 10 % total conversion to sulfoxide **21** and sulphone **22**. The major product in this control experiment was unreacted **20** (Figure 12A). In contrast, when these reaction mixtures were prepared in the same way and processed in the VFD operating at 7 krpm and using 20 equivalents of bleach, nearly all of the starting material was consumed within 40 minutes (Figure 12B). The major products of the reaction were allyl phenyl sulphone **22** and its dichlorinated derivative **23**. The formation of **23** was somewhat surprising, as this material has not been previously observed in the bleach oxidation of allyl phenyl sulphide.<sup>133, 134, 141</sup> It is likely that the chlorination results from deprotonation of the acidic  $\alpha$ -protons of **20** (the pH of the bleach was 12), followed by direct reaction with an electrophilic chlorine species such as hypochlorous acid. This pathway is consistent with that observed in the  $\alpha$ -chlorination of other aryl sulphones by reaction with hypochlorous acid,<sup>142</sup> but we note that, to the best of our knowledge, this is the first reported route to **23** using chlorine bleach. Furthermore, other reports of  $\alpha$ -chlorination of allyl aryl sulphones relied on phase-transfer catalysis and the toxic hexachloroethane as the electrophilic chlorine source.<sup>143</sup> Clearly the VFD process in Figure 12 is advantageous, as it requires only aqueous bleach.

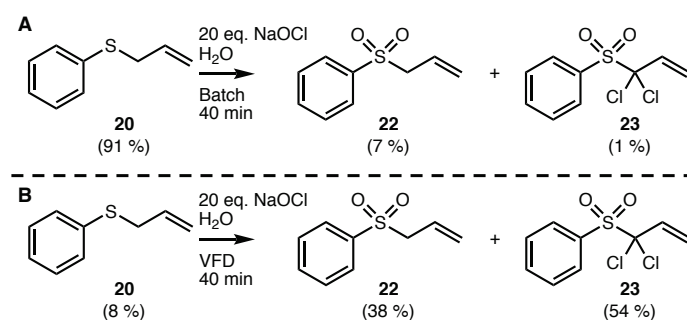


**Figure 12.** (A) Allyl phenyl sulphide (**20**) is immiscible in bleach. Inefficient mixing in stirred batch reactions results in minimal oxidation. (B) VFD processing promotes the bleach oxidation of **20**, providing dichlorinated sulphone **23** as the major product.

To prepare **23** in synthetically useful yields, the reaction was simply run in the VFD for 3 hours in the confined mode. <sup>1</sup>H-NMR analysis of the crude reaction mixture indicated approximately 71 % conversion to **23**, with purification by column chromatography providing this dichlorinated sulphone in a respectable 63 % isolated yield (Figure 13). The column chromatography was carried out primarily for analytical purposes as compound **23** has not been previously reported. Without the column chromatography purification, a pure compound can be achieved with much better green metrics (E-factor of 3 without chromatography, and E-factor of 715 with chromatography, see pg. 37)

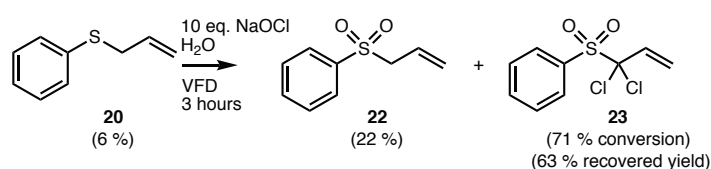


Figure 13. Demonstration of the VFD providing sulphone **23** in useful isolated yields.

To confirm the structure unambiguously, single crystals of **23** that were suitable for diffraction studies were obtained from hexane and dichloromethane. The crystals were found to be in a monoclinic cell and structural analysis was carried out in the space group *P*2<sub>1</sub>. Figure 14 shows the asymmetric unit that contains two molecules of **23**, unambiguously confirming the structure of this product.

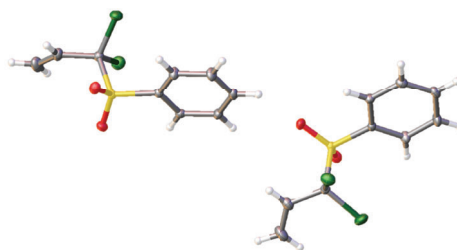


Figure 14. Asymmetric unit found in the crystal structure of purified **23**.

### 2.2.2 - Summary and Outlook on Bleach Oxidations in the VFD

This reaction illustrates that the intense micro-mixing of the VFD enables efficient reaction of substrates that are largely immiscible, and indeed the promotion of reactions that have otherwise not been observed. This capability means that the use of organic solvents, phase transfer catalysts and emulsifiers commonly used in such transformations can be circumvented when using a VFD. Eliminating these materials simplifies the procedure and improves the green chemistry metrics. Furthermore, immiscible liquids do not form emulsions in the VFD, thereby simplifying the processing.<sup>144</sup> From a selectivity perspective, the unexpected chlorination is interesting in that it occurs only at the  $\alpha$  position of the sulphone and not at the phenyl ring, so this can be considered a chemo- and regioselective oxidation. Importantly, this transformation is an exception to the rule that "the insolubility of hypochlorite salts in hydrocarbons and organic solvents has prevented the use of this material as a reagent for the selective oxidation of organic substrates."<sup>133</sup>



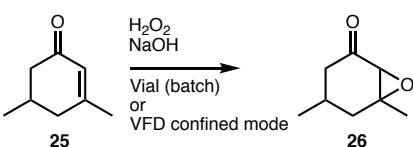
## 2.3 – Hydrogen Peroxide Oxidations, Avoiding Run-Away Exotherms

Aqueous hydrogen peroxide is a green oxidant that is relatively safe in comparison to organic peroxides and produces an innocuous water by-product after its reaction with reducing substrates.<sup>116</sup> To explore this oxidant in the VFD, we examined the Weitz-Scheffer epoxidation of  $\alpha,\beta$ -unsaturated ketones using hydrogen peroxide under basic conditions, without the addition of a phase transfer catalyst (Table 1).<sup>145</sup> Substrate **25** was selected because it is a hydrophobic liquid and insoluble in water at room temperature. Inspired by the efficient mixing of immiscible substrates observed in the VFD studies on bleach oxidations, we anticipated that the conversion of alkene **25** to epoxide **26** could be carried out without the need for organic solvents, surfactants, or phase-transfer catalysts.

### 2.3.1 – Discussion on Hydrogen Peroxide Oxidations in the VFD

Indeed, when **25** was reacted in the VFD in the confined mode with 5 equivalents of hydrogen peroxide in basic water, rapid consumption of starting material was observed. After a total of 1 hour of reaction time, epoxide **26** was isolated in 85 % yield after chromatographic purification (Table 1, entry 1). The epoxidation was also highly diastereoselective (d.r. = 22 : 1.0, as determined by both GC and <sup>1</sup>H NMR). To obtain a direct comparison between batch and VFD processing, the epoxidation was carried out simultaneously over 30 minutes in the VFD at 7 krpm and in a batch process with simple magnetic stirring (Table 1, entries 2 & 3). From this, slightly lower conversion was observed in batch (75 % compared to 90 % in VFD), with inferior d.r. (11 : 1.0 compared to 22 : 1 in VFD, as determined by GC). We attribute the eroded diastereoselectivity in batch processing to the uncontrolled exotherm that occurs. The conditions in the VFD result in high heat transfer and a more uniform heat dissipation.<sup>146</sup> This important feature of the microfluidic platform improves both safety and selectivity - important considerations in evaluating the green chemistry metrics and utility of a synthetic transformation.

**Table 1.** Without external temperature regulation, epoxidation of  $\alpha,\beta$ -unsaturated ketone **25** proceeds in higher yield and diastereoselectivity in the VFD (7 krpm). Both confined and continuous modes (entries 3 & 4, respectively) of operation provide higher conversions than batch (entry 2).



Reaction scheme showing the epoxidation of  $\alpha,\beta$ -unsaturated ketone **25** to epoxide **26** using  $\text{H}_2\text{O}_2$  and  $\text{NaOH}$ . The reaction is performed in either a vial (batch) or VFD confined mode.

Entry	Time (min)	Vessel	Conversion (%)	d.r. (9a:9b)	E-factor
1	60	VFD 7 krpm	99 (85 % yield)	22:1	0.05
2	30	Batch	75	11:1	0.38
3	30	VFD 7 krpm	90	22:1	0.14
4	30	Continuous flow VFD 7 krpm	84	20:1	0.22

To verify the relative stereochemistry in **26**, it was converted to thioether **27** by the stereo- and regio-specific ring opening of the epoxide by thiophenol (Figure 15A). Single crystals of **27** that were suitable for diffraction studies were obtained directly from this reaction mixture. The crystals were found to be in a monoclinic cell and structural analysis was carried out in the space group  $P2_1/n$ . The structure in Figure 15B confirms the

relative stereochemistry for the major diastereomer isolated upon opening of the epoxide with thiophenol and, by extension, the stereochemistry in epoxide **26**. Note that this reaction does not alter the enantiomeric ratio, and as can be seen in the crystal structure, a racemic mixture is present in the hydrogen bonded dimer.

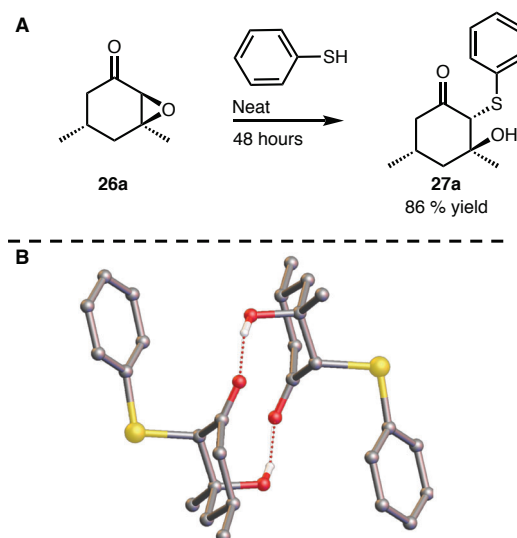


**Figure 15.** (A) To determine the relative stereochemistry in **26**, the epoxide was opened by the stereo- and region-specific reaction with thiophenol. The product of this reaction was suitably crystalline for single crystal diffraction studies. (B) Symmetry expanded crystal structure of **27**, confirming the relative stereochemistry and showing a hydrogen-bonded dimer (H-bonds shown as dotted red lines).

Examining the exotherm of the reaction further, it was revealed by infrared thermal imaging that the batch reaction reached temperatures over 90 °C (Figure 16), consistent with the original report of this reaction in which the liberation of heat was noted.<sup>145</sup> In contrast, the thin film processing in the VFD dissipated thermal energy of the same reaction very efficiently, resulting in an internal temperature that did not exceed the room temperature of 23 °C over the course of the reaction, as indicated by IR thermal imaging (Figure 16).

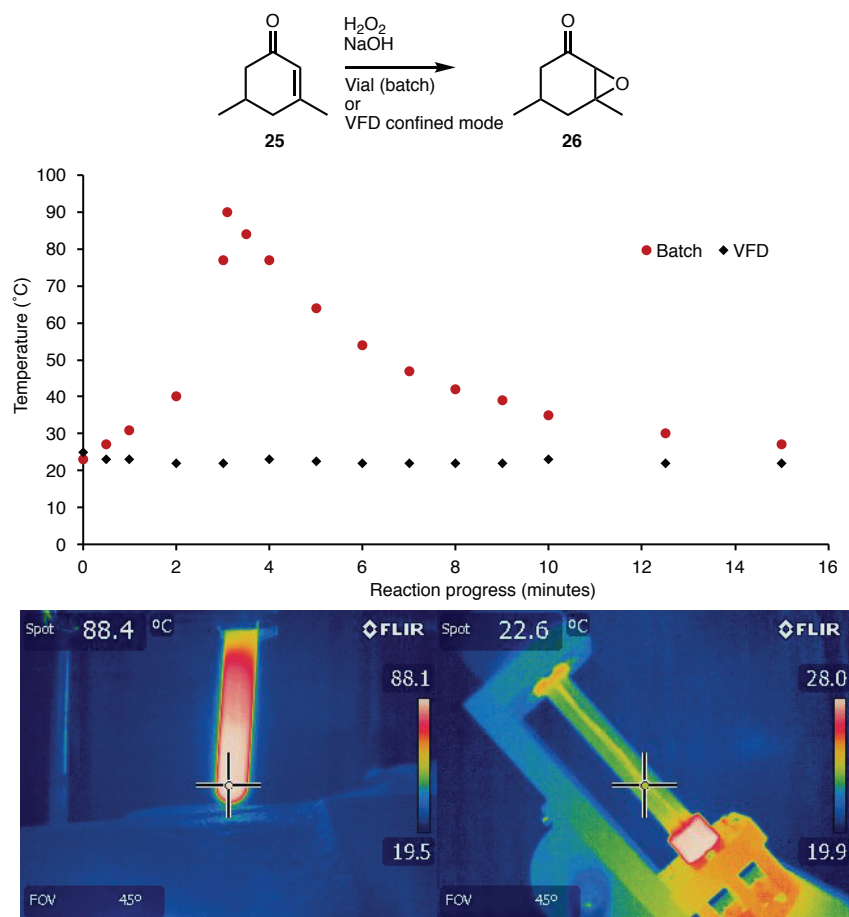


**Figure 16.** The VFD is efficient at dissipating the heat associated with the exothermic epoxidation. When the reaction was simply stirred (bottom left image), IR thermal imaging revealed temperature spikes to over 90 °C after just 3 minutes. The same reaction in the thin film of the VFD was maintained at 23 °C (bottom right image).

Since the NaOH in this process is catalytic, it was hypothesised that the green metric could be vastly improved by reusing this catalyst. This is made possible by simply re-using the aqueous phase (Figure 17). After 3 cycles (Figure 17A), the NaOH acts catalytically and remains active, with reduced conversion corresponding to the reduced concentration. The reduced concentration is a result from dilution of each subsequent reaction. This dilution occurs as H<sub>2</sub>O<sub>2</sub> is added to each reaction as a liquid, diluting the aqueous phase. Accounting for this by adding extra NaOH to maintain a consistent concentration throughout results in full conversion across all 3 cycles (Figure 17B).

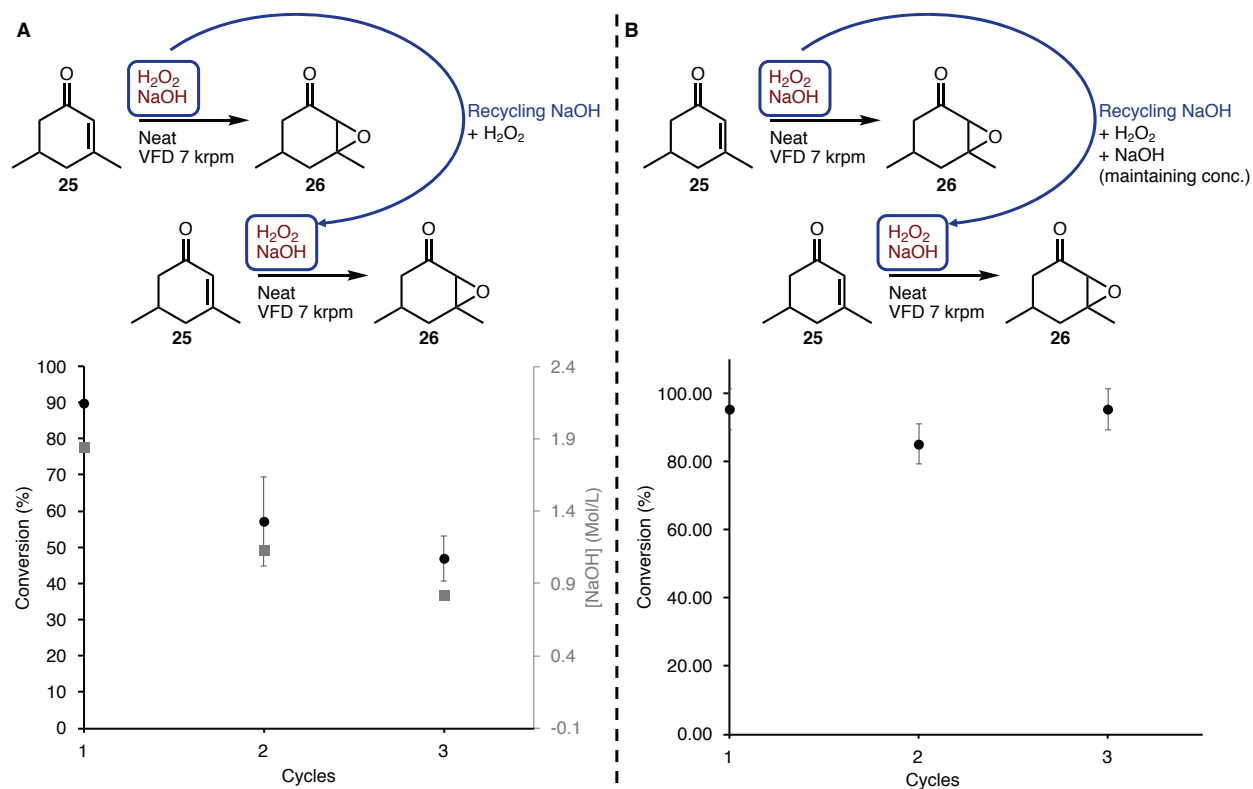


**Figure 17.** (A) Epoxidation of **25** with H<sub>2</sub>O<sub>2</sub>, catalysed by NaOH. The aqueous phase was re-used for multiple cycles successfully, demonstrating the ability to recycle the aqueous phase. (B) Conversion in increasing re-use cycles. Also shown is the corresponding reduction in concentration of NaOH in the aqueous layer with each cycle, from the addition of aqueous H<sub>2</sub>O<sub>2</sub>. (C) Repeated experiment adding extra H<sub>2</sub>O<sub>2</sub> and NaOH to maintain original concentrations.

### 2.3.2 – Summary and Outlook on Hydrogen Peroxide Oxidations in the VFD

While our initial interest in studying hydrogen peroxide oxidations in the VFD was centred on its ability to efficiently mix immiscible reagents, an additional benefit in exotherm control was revealed. Because peroxides present a detonation risk for runaway reactions,<sup>112</sup> the VFD dramatically improves the safety profile for these reactions. To expand on this capability, the conversion of **25** to **26** was adapted to a continuous process in which the epoxidation was easily scaled with high reaction efficiency (84 % conversion), while preventing runaway exotherms that would be associated with large scale batch process (Table 1, Entry 4). Isolation and purification of **26** (pg. 44) was performed purely for analytical purposes, as the stereochemical assignment of **26** has not been previously reported. The preparation of **27** as single crystals allowed the stereochemistry to be determined unambiguously using X-ray diffraction data.

## 2.4 - Conclusions on Organic Oxidations in the VFD

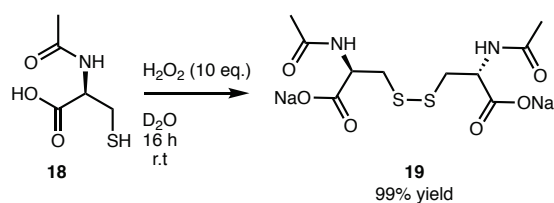
Three distinct types of oxidation were studied in the vortex fluidic device, with thin film processing shown to be beneficial in aerobic oxidations, in which mass transfer of oxygen gas to the reaction medium is rate-limiting, as illustrated by the efficient oxidation of *N*-acetyl-L-cysteine (**18**) to its disulphide (**19**) on a large volume. The intense mixing in the VFD also benefits oxidations in which non-polar organic substrates are reacted with polar oxidants in water without phase transfer catalysis, as demonstrated in the oxidation and unexpected chlorination of allyl phenyl sulphide (**20**). Finally, the VFD is well-positioned to dissipate heat generated in the microfluidic thin film during exothermic reactions such as the epoxidation of  $\alpha,\beta$ -unsaturated ketones using hydrogen peroxide, thereby making such reactions safer and more synthetically useful. Scaling up requirements using the VFD will depend on the product volume requirements, but for large volumes it is envisaged that a parallel array of VFDs will be effective, noting parallel processing features in conventional channel based microfluidics, albeit for much smaller volumes.

We note that while the bleach oxidation of the sulphide to the sulphone is effective and provided a novel compound (**23**). The results may heighten concern that using bleach as an oxidant may produce chlorinated organic impurities. Due to their potential toxicity, translating any findings using bleach into the market place should be accompanied by an analysis of the toxicity impact of such trace compounds, using assay systems such as TIPED.<sup>147</sup> Accordingly, care needs to be taken in classifying bleach as a green oxidant, and should be done so only with consideration of potential chlorinated by-products.

Importantly, all of the oxidants used in the featured reactions benefit from high atom economy, low toxicity, and safer processing - especially when compared to other oxidants commonly employed in chemical synthesis. The methods proposed herein also minimise or eliminate the need for any organic solvents. Demonstrating ways in which these green transformations can be exploited in the VFD flow chemistry platform is an advance in improving the green chemistry aspects of the chemical processing.

## 2.5 - Experimental Details and Spectra

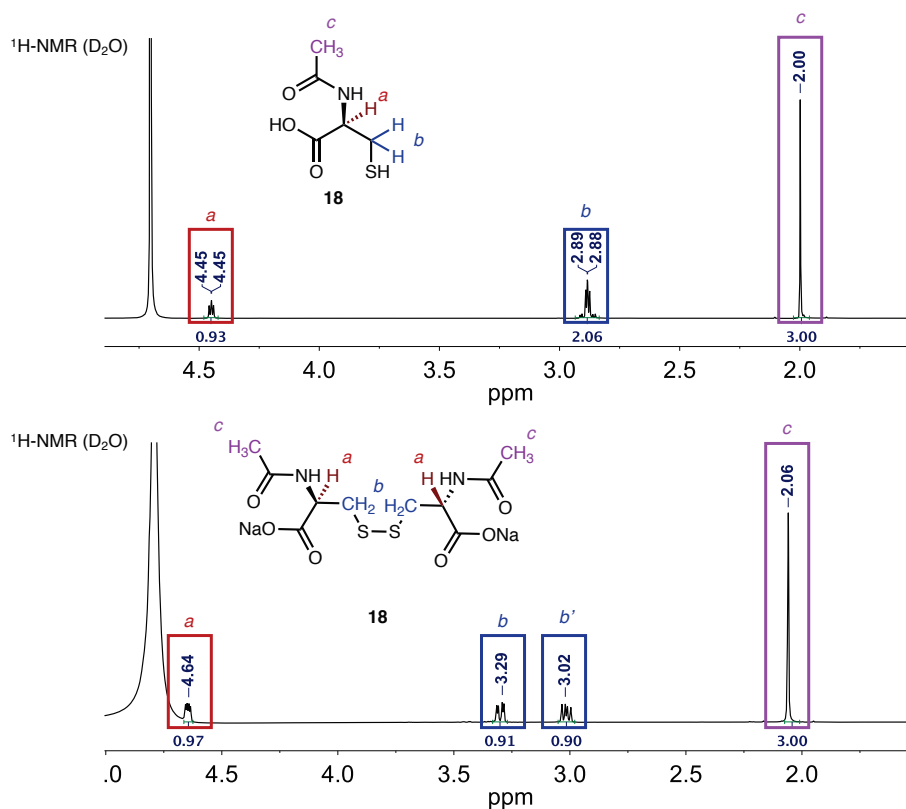
### 2.5.1 - Obtaining reference sample of disulphide 2



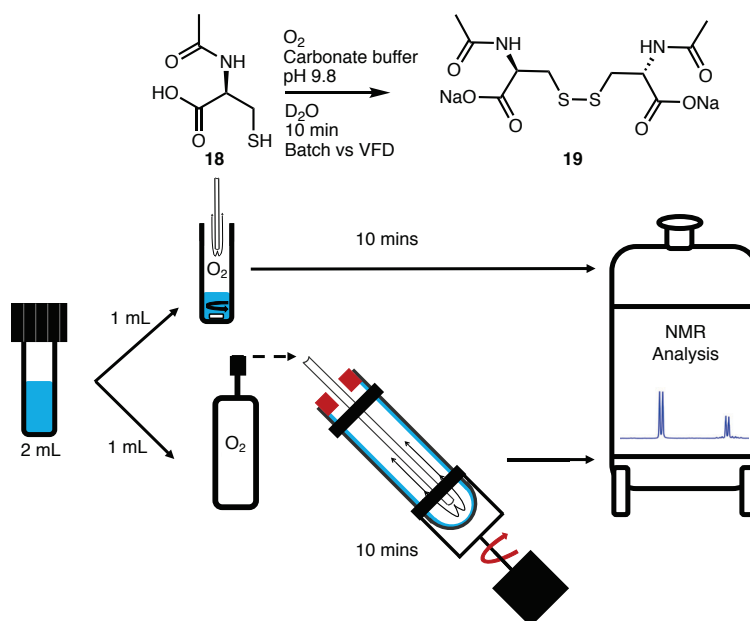
A reference sample of disulphide **19** was prepared by adding 30 % w/w  $\text{H}_2\text{O}_2$  (20  $\mu\text{L}$ , 1.2 mmol) to *N*-acetyl-L-cysteine (20 mg, 0.12 mmol) in  $\text{D}_2\text{O}$  (2 mL) in a small vial. Reaction took place over 16 hours,  $^1\text{H}$ -NMR and MS analysis showed disulphide **19** in high purity without need for further purification. The resulting spectra can be found on the following page.

$^1\text{H}$  NMR (600 MHz,  $\text{CDCl}_3$ ):  $\delta_{\text{H}}$  = 4.64 (2H, q,  $J$  = 3.95 Hz,  $\text{NHCH}$ ), 3.29 (2H, m,  $\text{S-SCHH}$ ), 3.02 (2H, m,  $\text{S-SCHH}$ ), 2.06 (6H, s,  $\text{O=CCH}_3$ ).

LRMS:  $[\text{M}+\text{H}]^+ = 325 \text{ m/z}$



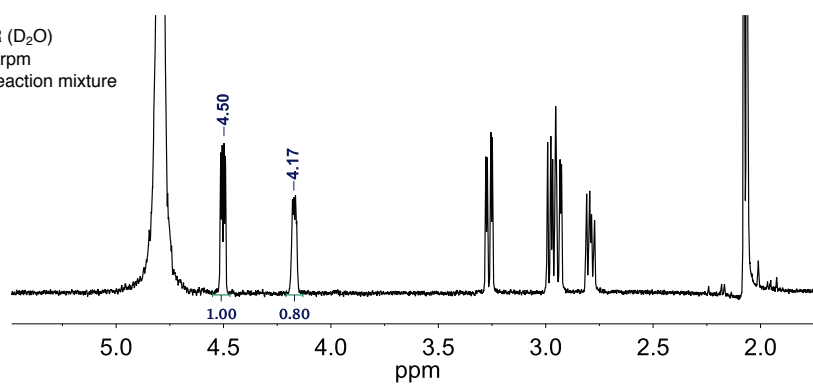
## 2.5.2 - Small Scale Batch and Confined Mode VFD Processing.



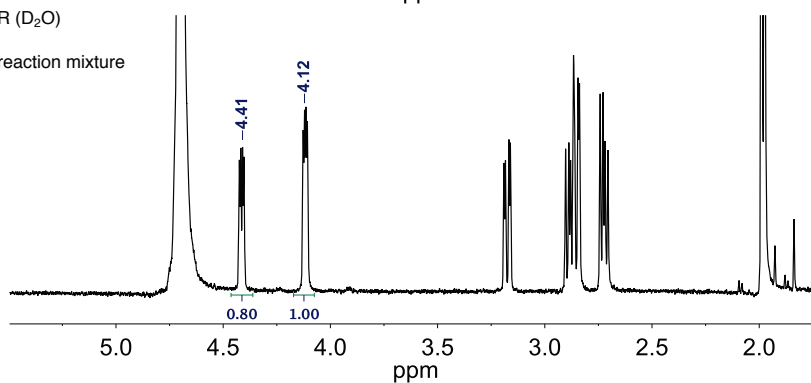
Comparisons between small scale confined mode VFD and batch were made. First a buffered stock solution of *N*-acetyl-L-cysteine in  $D_2O$  was prepared by addition of sodium carbonate (2.12 mg, 0.02mmol) and sodium bicarbonate (16.8 mg, 0.2 mmol) to 2 mL of  $D_2O$ , followed by the addition of *N*-acetyl-L-cysteine (3.28 mg, 0.02 mmol). The pH of this solution was measured to be 9.8. Then, 1 mL of this was transferred to a 20 mm VFD tube and operated at 7 krpm, whilst simultaneously the other 1 mL was transferred to a 20 mm VFD tube and stirred with a magnetic stirrer bar under a stream of  $O_2$  gas. After 10 minutes of elapsed reaction time these samples analysed by H NMR. This experiment was performed in duplicate. The batch sample was also then left in the NMR tube for 3 days and re-analyzed. This showed conversion times were moderately faster in the VFD on these 1 mL scale volumes and that the reaction will continue until completion if left for 3 days.



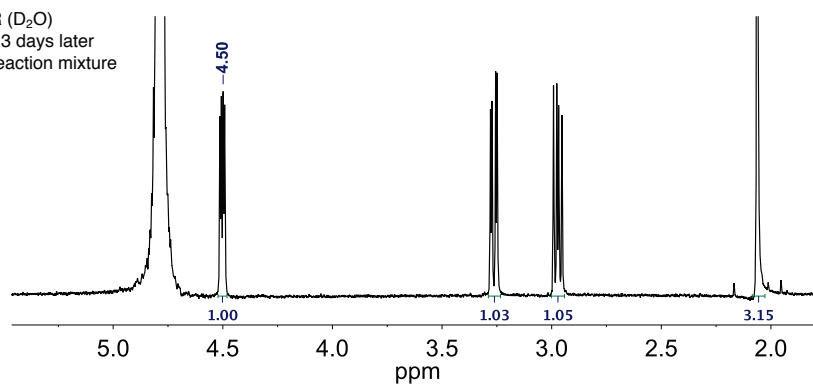
<sup>1</sup>H-NMR (D<sub>2</sub>O)  
VFD 7 krpm  
Crude reaction mixture



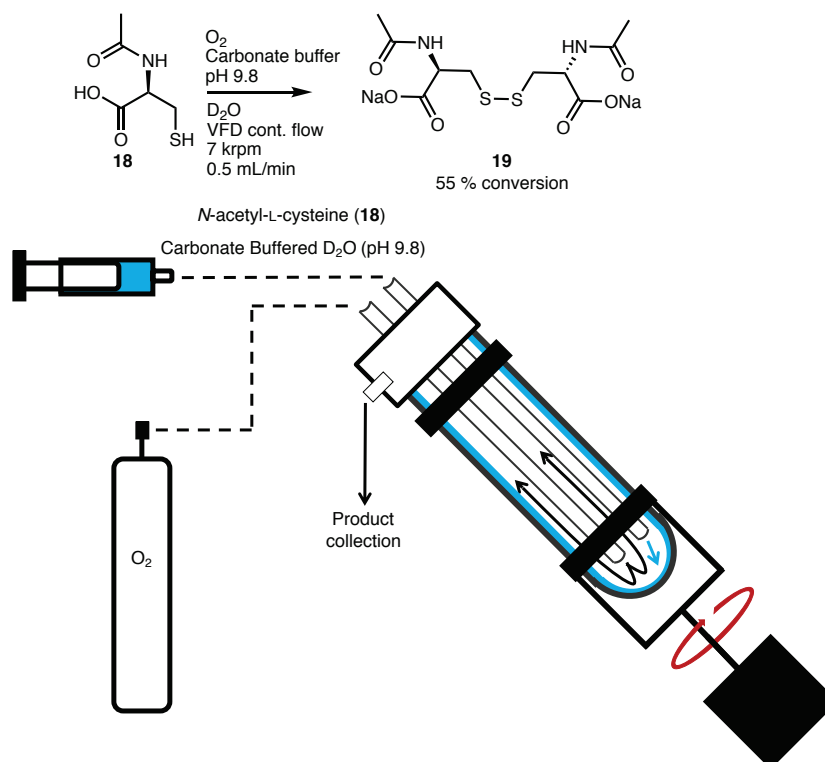
<sup>1</sup>H-NMR (D<sub>2</sub>O)  
Batch  
Crude reaction mixture



<sup>1</sup>H-NMR (D<sub>2</sub>O)  
Batch – 3 days later  
Crude reaction mixture

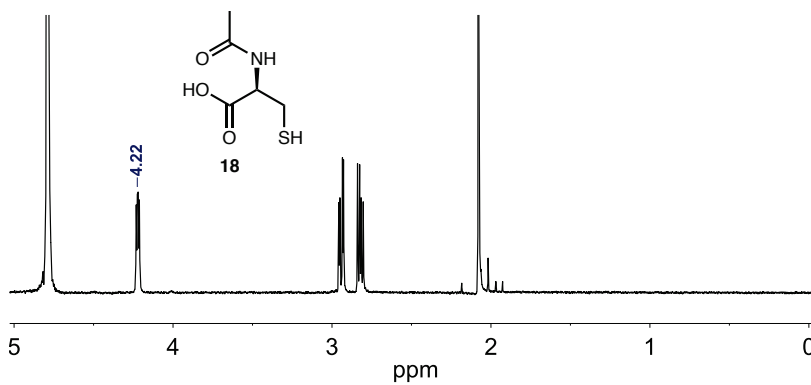


### 2.5.3 - Large Scale VFD Processing with Atmosphere of O<sub>2</sub> vs Air

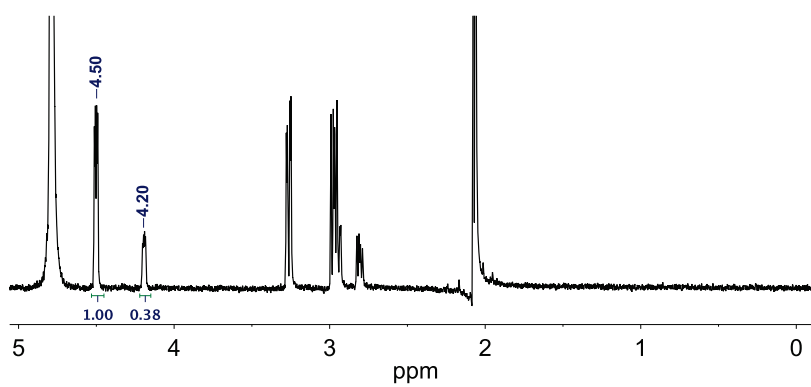


A buffered solution of D<sub>2</sub>O was prepared by the addition sodium carbonate (150 mg, 1.42 mmol) and sodium bicarbonate (420 mg, 5.00 mmol) to 50 mL of D<sub>2</sub>O. *N*-acetyl-L-cysteine (82 mg, 0.50 mmol) was then added to the buffered solution and the initial pH was 9.9, as measured using a pH meter. This solution was then injected via syringe pump at the desired 0.5 mL/min into the base of the VFD tube, operating at 7 krpm with a 45° tilt angle. In another jet feed of the VFD, a stream of O<sub>2</sub> gas was introduced so that flow rate was no more than 0.5 L/min. The device was operated for a total of 2 h, over which time the collection vessel was changed every 30 mins giving 4 fractions of reaction product. Fractions were analysed by <sup>1</sup>H-NMR upon collection. A final pH was also recorded for the fractions. A control experiment was also carried out where air was used instead of O<sub>2</sub> gas. Reaction conversions were calculated based on the relative integration of the alpha protons for the starting material (18) and product (19). It was found that the average conversion across the 3 fractions was 55% when O<sub>2</sub> gas was used, compared to 7 % when air was used, indicating O<sub>2</sub> is required for useful conversions. Representative NMR data for this set of experiments can be found below.

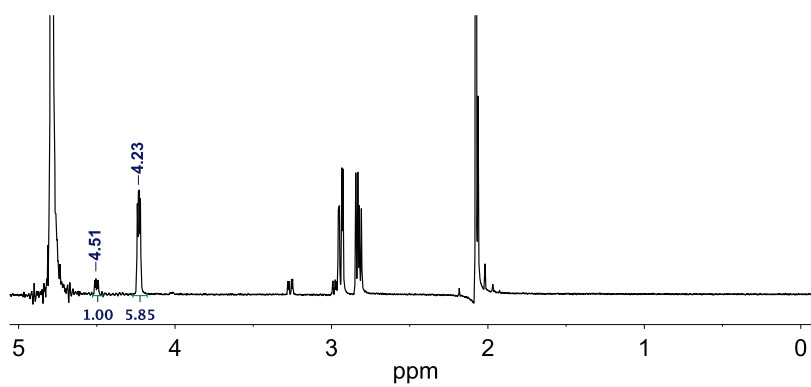
<sup>1</sup>H-NMR (D<sub>2</sub>O)  
Starting material  
(18)



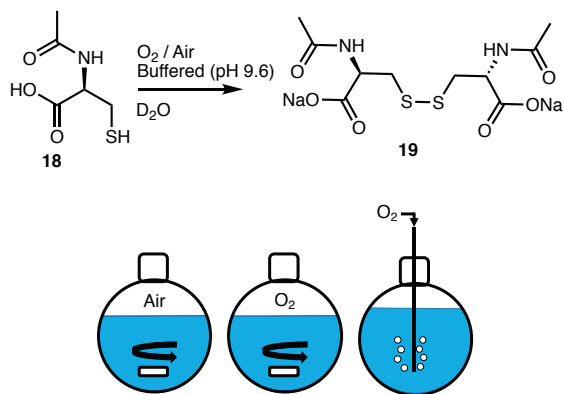
<sup>1</sup>H-NMR (D<sub>2</sub>O)  
VFD 7 krpm  
Cont flow with O<sub>2</sub>



<sup>1</sup>H-NMR (D<sub>2</sub>O)  
VFD 7 krpm  
Cont. flow with air



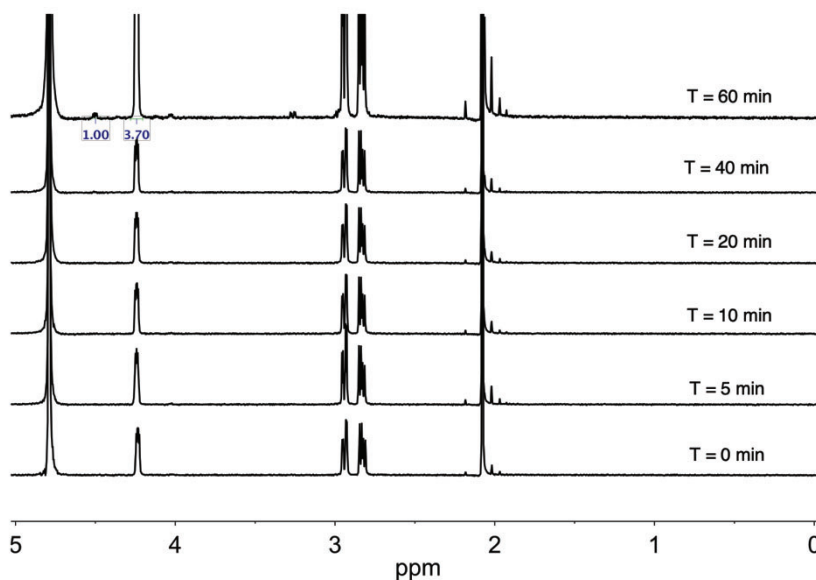
## 2.5.4 - Large Scale Batch Aerobic Oxidation



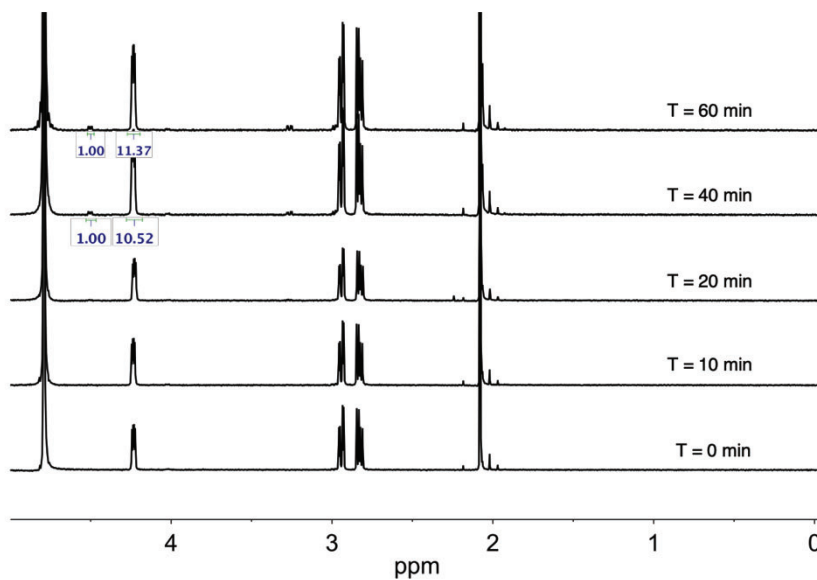
Three control experiments were carried out using batch conditions to determine if running the reaction in the VFD confers a benefit in reaction rate. A) A buffered *N*-acetyl-L-cysteine solution stirred with a with headspace of air. B) A buffered *N*-acetyl-L-cysteine solution stirred with a sealed headspace of O<sub>2</sub>. C) A buffered *N*-acetyl-L-cysteine solution with stream of O<sub>2</sub> gas bubbled through. Accordingly, a buffered solution of D<sub>2</sub>O was prepared by the addition sodium carbonate (300 mg, 2.84 mmol) and sodium bicarbonate (842 mg, 10.0 mmol) to 100 mL of D<sub>2</sub>O. *N*-acetyl-L-cysteine (164 mg, 1.00 mmol) was added to the buffered solution and the initial pH was 9.9, as measured using a pH meter. This solution was then stirred with either a headspace of air (open flask), O<sub>2</sub> (1 atm, sealed flask) or a stream of O<sub>2</sub> bubbling through continuously at no more than 0.5 L/min. NMR samples were taken at times of 0, 5, 10, 20, 40 and 60 minutes, with conversions determined directly by <sup>1</sup>H NMR analysis. The results are tabulated below, with NMR data on the following page. It is interesting to note that while only a small difference was observed in VFD vs batch processing for small scale processing, major differences in conversion were observed on up-scaling.

Elapsed Time (min)	Conversion (%)		
	Air	O <sub>2</sub>	O <sub>2</sub> (bubbling)
0	0	0	0
5	0	0	0
10	0	0	0
20	0	0	0
40	< 1	5	4
60	3	5	4
960	12	-	-

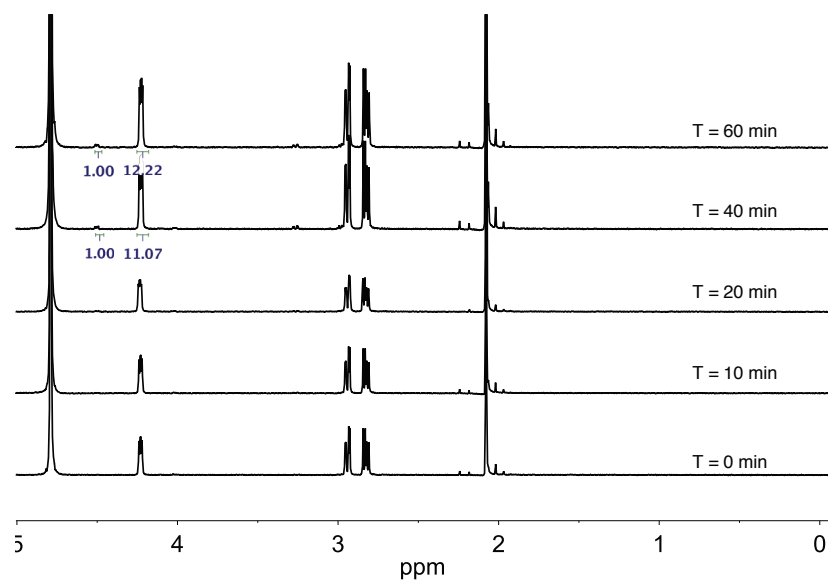
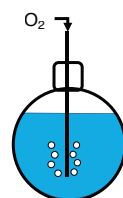
Batch, 100 mL  
air headspace



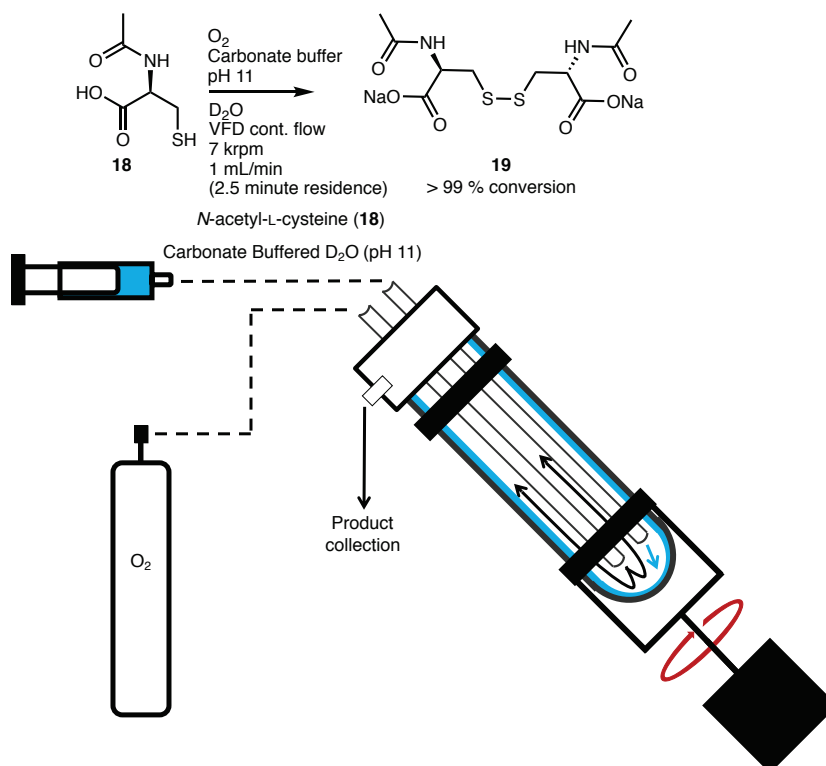
Batch, 100 mL  
O<sub>2</sub> headspace



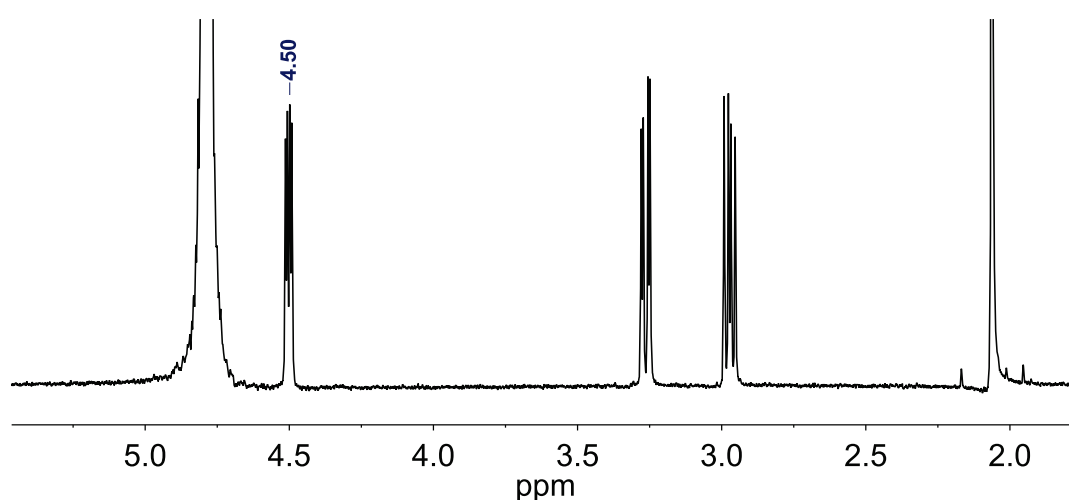
Batch, 100 mL  
O<sub>2</sub> Bubbling



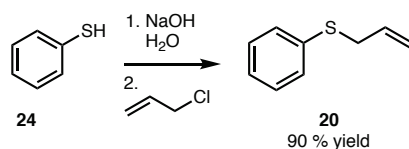
## 2.5.5 - Continuous Flow VFD Aerobic Oxidation at pH 11



A 5 M NaOH (0.5 mL, 2.5 mol) was added to 20 mL D<sub>2</sub>O. *N*-acetyl-L-cysteine (82 mg, 0.50 mmol) was then added to the solution. This solution was then injected via syringe pump at the 1 mL/min into the base of the VFD tube, operating at 7k rpm with a 45° tilt angle. In another jet feed of the VFD, a stream of O<sub>2</sub> gas was introduced so that the flow rate was no more than 0.5 L/min. The device was operated for a total of 20 mins, over which time the collection vessel was changed every 5 mins giving 4 fractions of reaction product. Fractions were analyzed by <sup>1</sup>H-NMR upon collection. Average conversion across all 4 fractions showed a conversion >99 % to the disulphide. Representative <sup>1</sup>H NMR spectra can be found below.

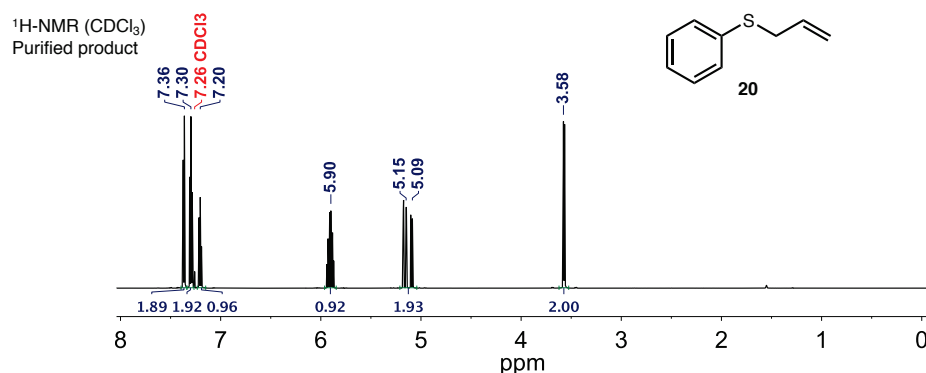


### 2.5.6 - Synthesis of allyl phenyl sulphide 3

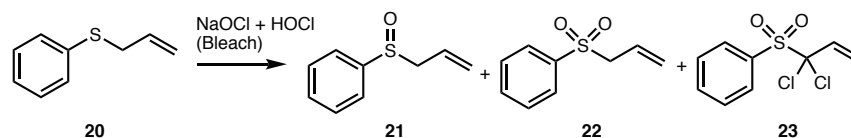


NaOH (1.56 g, 39.0 mmol) was added to a 100 mL round bottom flask and dissolved in 50 mL of deionized H<sub>2</sub>O. The stirred solution was cooled to 0 °C and thiophenol (4.0 mL, 39.0 mmol) was added. After 5 minutes of stirring, allyl chloride (3.3 mL, 42.9 mmol) was added. The resulting cloudy reaction mixture was stirred vigorously for 6 hours at room temperature. TLC (10% EtOAc in hexane) indicated the formation of a single product. The reaction was diluted with 250 mL Et<sub>2</sub>O and washed successively with 0.1 M NaOH (3 × 100 mL) and brine (200 mL). The organic layer was dried over MgSO<sub>4</sub>, filtered, and concentrated under reduced pressure to give **20** as a clear oil that required no purification. Reaction was performed to provide compound **20** as needed, resulting in a typical yield of 90 - 95 %.

<sup>1</sup>H NMR (600 MHz, CDCl<sub>3</sub>): δ<sub>H</sub> = 7.35-7.38 (2H, m, Ar), 7.28-7.32 (2H, m, Ar), 7.2 (1H, tt, J = 7 Hz, 1 Hz, Ar), 5.87-5.94 (1H, m, CH=CH<sub>2</sub>), 5.14-5.18 (1H, m, CH=CHH'), 5.08-5.11 (1H, m, CH=CHH''), 3.58 (2H, dt, J = 7 Hz, 1 Hz, PhSCH<sub>2</sub>).



### 2.5.7 – Batch vs VFD Bleach Oxidations



Allyl phenyl sulphide (20 mg, 0.067 mmol), and a solution of 4% active chlorine bleach (2.45 mL, 0.67 mmol NaOCl) were transferred into a 20 mm VFD tube. The reaction mixture appears as two phases. This tube was then placed into a VFD and operated in the confined mode at 7 krpm with a tilt angle of 45° for 40 minutes. After rotation had stopped, extraction was performed using CDCl<sub>3</sub> and <sup>1</sup>H-NMR analysis was undertaken on the crude extract. All experiments were all repeated where the VFD tube was not rotated, these are noted as “batch” controls. Experiments were also performed for 20 eq. of bleach, in which case the amount of allyl phenyl sulphide was halved (10 mg, 0.033 mmol). All experiments were performed in duplicate. Reaction conversions were determined by relative integration of the allylic protons for **20** and **21** and the CH=CH<sub>2</sub> peak for **22** (3.5 , 3.8, 6.3 δ<sub>H</sub> ppm shifts respectively).

Here, since the oxidative ability of bleach is the focus, the E-factor was calculated assuming all oxidation products are desired products. The waste is the generated NaCl (assuming 1:1 conversion from NaOCl) and the unreacted starting material. Note that since compounds are in separate phases, pipetting of the product is the only purification step required. Separation of the oxidation products requires further purification, such as the column chromatography reported on page 37 of this document.

#### Batch, 20 eq.

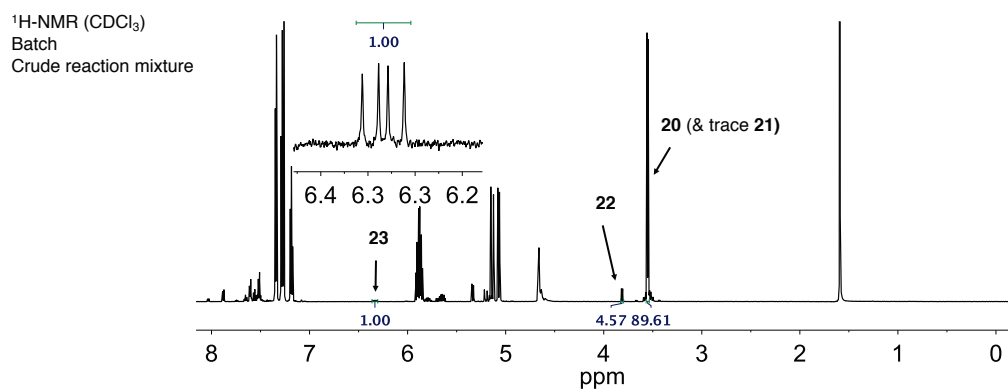
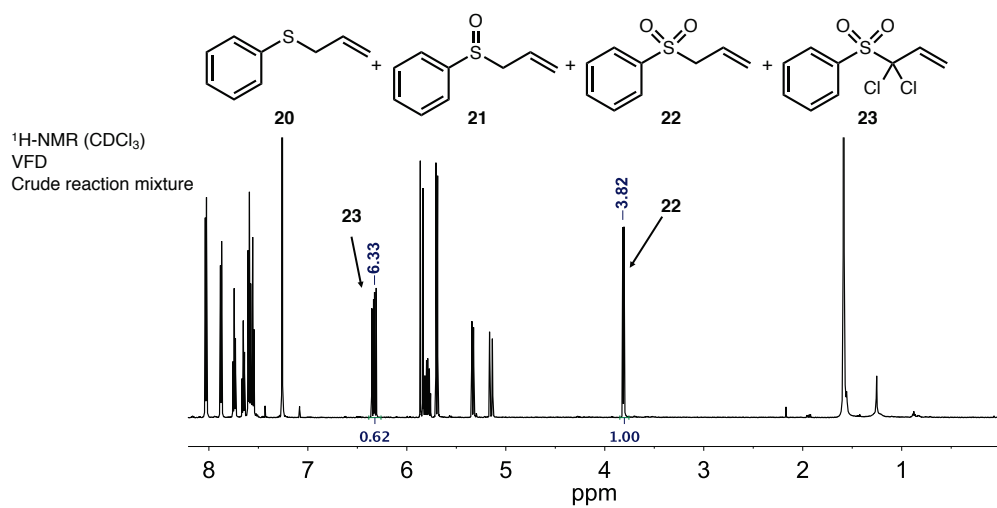
$$E_{(batch)} = \frac{390 \text{ mg}}{0.47 \text{ mg}} = 91$$

#### VFD, 20 eq.

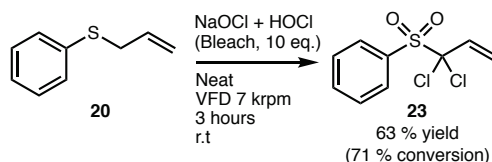
$$E_{(VFD)} = \frac{386 \text{ mg}}{6.8 \text{ mg}} = 6$$

Noting that the majority of waste in the VFD processing is innocuous NaCl.





### 2.5.8 - VFD synthesis and Isolation of compound 22



Allyl phenyl sulfide (60  $\mu\text{L}$ , 0.40 mmol), and a solution of 8-12 % active chlorine bleach (2.45 mL, 2.6 – 3.9 mmol, 6.5 - 10 eq.) were transferred into a 20 mm VFD tube. This tube was then placed into a VFD and operated in confined mode at 7 krpm for 3 h. NMR analysis of crude product showed 71 % conversion to compound **23**. Flash column chromatography was performed with a mobile phase of 30% EtOAc in hexane ( $\approx$  50 mL). This resulted in separation of compound **23** (63.3 mg) in yield of 63 %.  $^1\text{H}$  NMR,  $^{13}\text{C}$  NMR, IR and MS were performed on this isolated compound and spectra can be found below. The E-factor for the formation of compound **23** is calculated below, noting that the vast majority of waste is innocuous NaCl.

$$E_{(\text{crude})} = \frac{0.239 \text{ g}}{0.071 \text{ g}} = 3$$

$$E_{(\text{isolated})} = \frac{45 \text{ g}}{0.063 \text{ g}} = 715$$

Melting point: 64-68  $^{\circ}\text{C}$

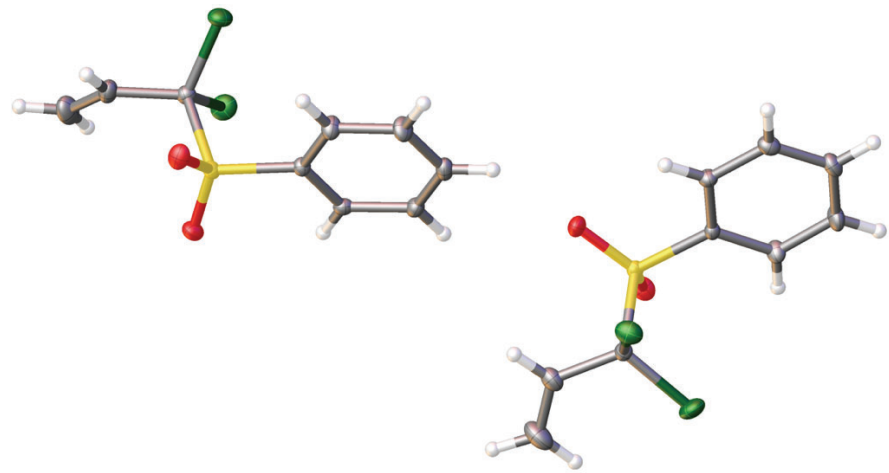
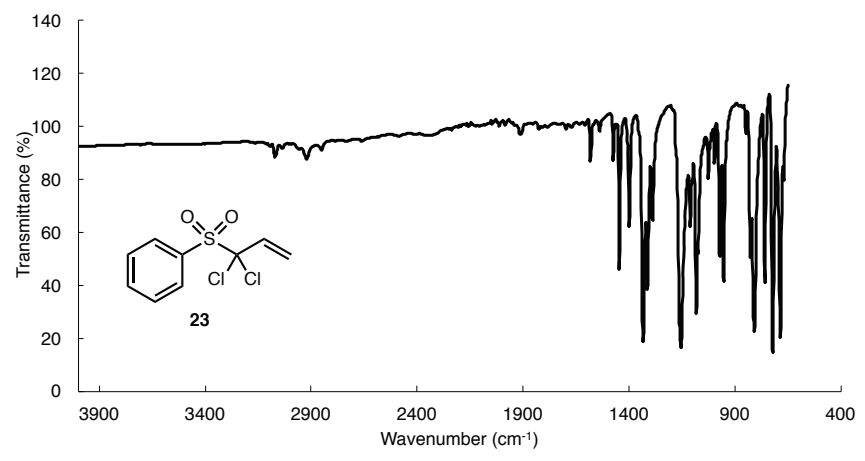
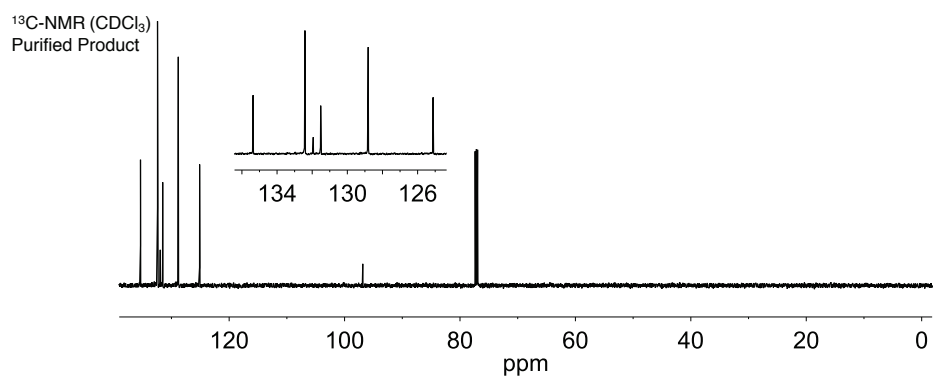
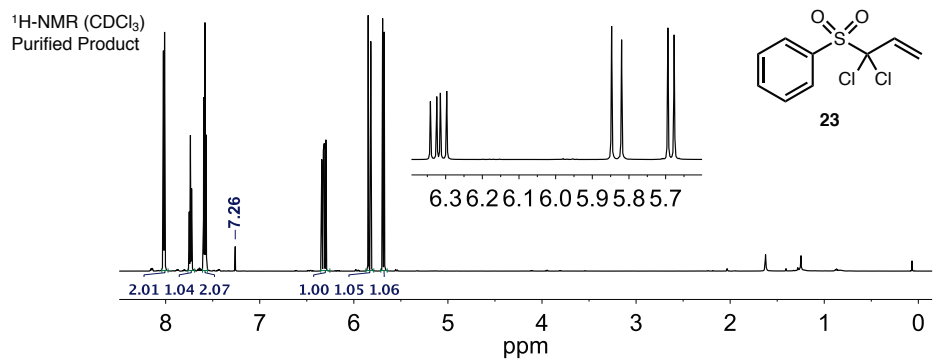
$^1\text{H}$  NMR (600 MHz,  $\text{CDCl}_3$ ):  $\delta_{\text{H}} = 8.01$  (2H, dd,  $J = 8, 1$  Hz, Ar), 7.73 (1H, tt,  $J = 8, 1$  Hz, Ar), 7.58, (2H, m, Ar), 6.3 (1 H, dd,  $J = 16, 10$  Hz,  $\text{CH}=\text{CH}_2$ ) 5.83 (1H, d,  $J = 16$  Hz,  $\text{CH}=\text{CHH}'$ ) , 5.68 (1H, d,  $J = 10$  Hz,  $\text{CH}=\text{CHH}'$ ).

$^{13}\text{C}$  NMR (600 MHz,  $\text{CDCl}_3$ ):  $\delta_{\text{C}} = 135.35$  (Ar), 132.32 (Ar), 131.91 ( $\text{CH}=\text{CH}_2$ ), 131.56 (Ar), 128.82 (Ar), 125.11 ( $\text{CH}=\text{CH}_2$ ), 96.84 ( $\text{PhSO}_2\text{C}$ ).

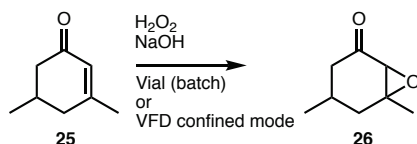
IR ( $\nu_{\text{max}}$ , crystals ATR): 1581, 1475, 1446, 1399, 1333, 1313, 1289, 1155, 1111, 1083, 1026, 998, 972, 953, 808, 759, 722, 687.

LR-MS: 251  $[\text{M}+\text{H}]^+$ .

**Crystal Data for 23 (CCDC 1552986):**  $\text{C}_9\text{H}_8\text{Cl}_2\text{O}_2\text{S}$ ,  $M = 251.11$  g/mol, monoclinic, space group  $P2_1$  (no. 4),  $a = 7.3712(4)$   $\text{\AA}$ ,  $b = 10.3338(6)$   $\text{\AA}$ ,  $c = 13.8683(8)$   $\text{\AA}$ ,  $\beta = 93.683(3)^{\circ}$ ,  $V = 1054.20(10)$   $\text{\AA}^3$ ,  $Z = 4$ ,  $T = 100(2)$  K,  $\mu(\text{MoK}\alpha) = 0.782$   $\text{mm}^{-1}$ ,  $D_{\text{calc}} = 1.582$   $\text{g/cm}^3$ , 4177 reflections measured ( $2.94^{\circ} \leq 2\theta \leq 66.48^{\circ}$ ), 4177 unique ( $R_{\text{int}} = 0.0000$ , merged due to twin refinement,  $R_{\text{sigma}} = 0.0204$ ) which were used in all calculations. The final  $R_1$  was 0.0239 ( $>2\text{sigma}(I)$ ) and  $wR_2$  was 0.0580 (all data).



### 2.5.9 – Epoxidation of 25 with Hydrogen Peroxide



First, a NaOH solution (5 M, 0.7 mL, 3.5 mmol) was mixed with a H<sub>2</sub>O<sub>2</sub> solution (30% aq. v/v, 1.2 mL, 17.5 mmol) over an ice bath and cooled for 15 minutes. This was then removed from ice and transferred to a 20 mm VFD tube. Following this, Compound **25** (0.5 mL, 3.5 mmol) was added to the reaction mixture and was operated at 7k rpm in a VFD for 1 hour. Crude NMR in CDCl<sub>3</sub> at this point revealed a conversion of 99 %. Further purification of this compound was performed for analytical purposes, since the structure of the respective minor and major diastereomers have not been previously reported. The organic material was extracted from the aqueous hydrogen peroxide using chloroform (3 x 10 mL extractions). This extract was then combined with the NMR sample and dried (magnesium sulphate, ≈ 3 g), filtered and concentrated under a stream of compressed air. Flash column chromatography was then performed using a mobile phase of 20% EtOAc in toluene (≈50 mL), giving compound **26** (417 mg) as a yellow/clear oil in 85 % yield (d.r 22:1). NMR, GC-MS, and IR analysis were performed on this extract as reported below, with spectra found on the following page. E-factor calculations, are shown below. Since the terminal products are water, and the NaOH is catalytic, no purification is required in cases where full conversion is observed. Also shown is the E-factor of the purification process that was performed for analytical purposes.

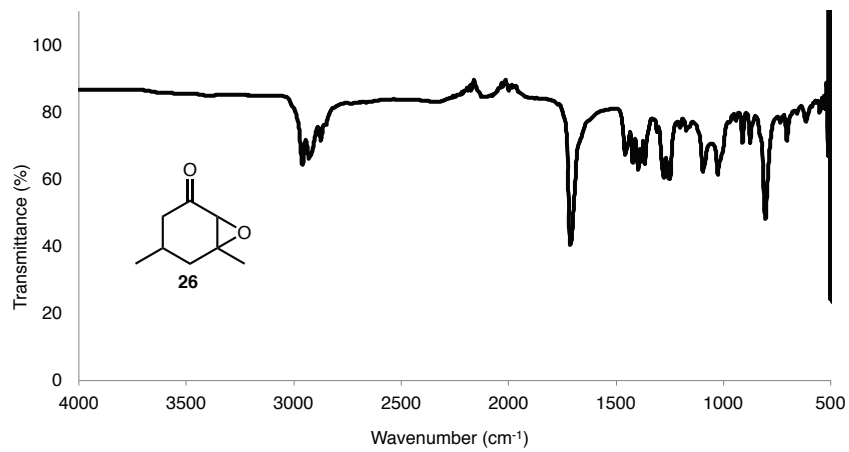
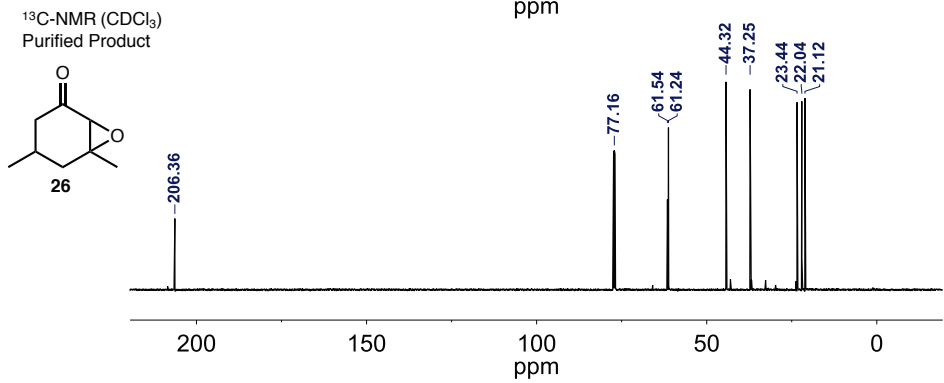
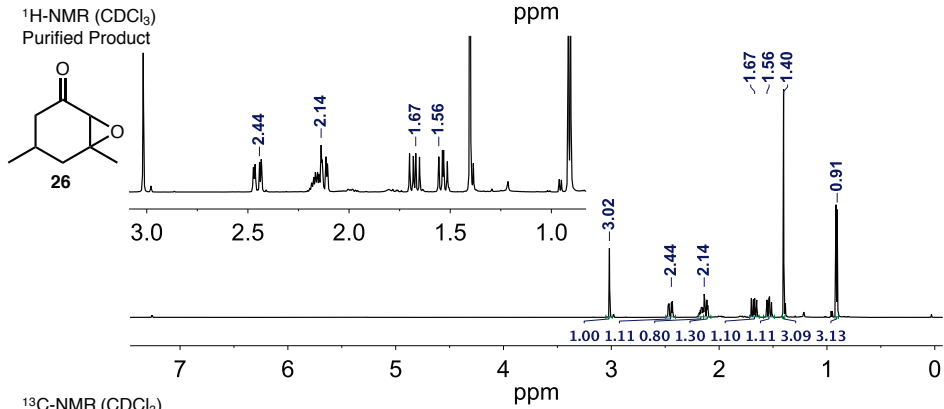
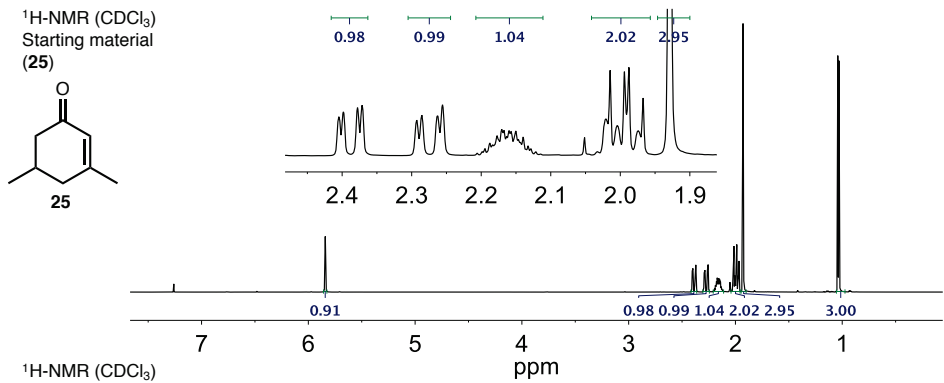
$$E = \frac{0.026 \text{ g}}{0.486 \text{ g}} = 0.05$$

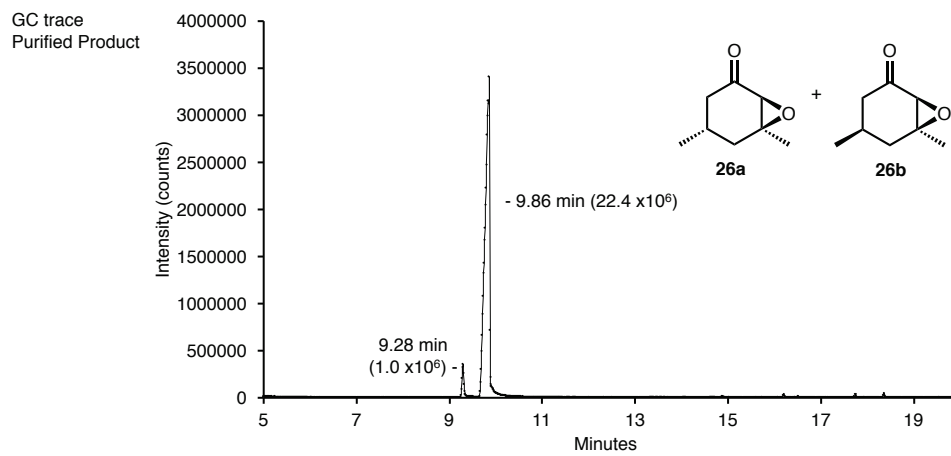
$$E_{(\text{isolated})} = \frac{95.68 \text{ g}}{0.417 \text{ g}} = 229$$

<sup>1</sup>H NMR (600 MHz, CDCl<sub>3</sub>): δ<sub>H</sub> = 3.02 (1H, s), 2.44 (1H, dd, J = 5.2 Hz, 18.1 Hz, CHH'C=O), 2.16-2.24 (m, 1H, CHCH<sub>3</sub>), 2.14 (1H, dd, J = 4.1 Hz, 18.4 Hz, CHH'), 1.67 (1H, dd, J = 11.0 Hz, 18.3 Hz, CHH'), 1.56 (1H, dd, J = 10.5 Hz, 14.2 Hz, CHH'), 1.40 (s, 3H, CH<sub>3</sub>), 0.94 (3H, d, J = 6.7 Hz, HC-CH<sub>3</sub>).

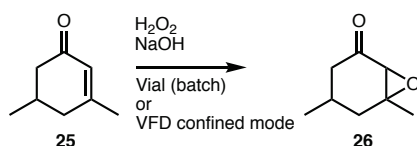
<sup>13</sup>C NMR (600 MHz, CDCl<sub>3</sub>): δ<sub>C</sub> = 206.3 (C=O), 61.5 (O-CH), 61.2 (O-CCH<sub>3</sub>), 44.3 (CH<sub>2</sub>C=O), 37.2 (CH<sub>2</sub>CCH<sub>3</sub>), 23.4 (CHCH<sub>3</sub>), 22.0 (CH<sub>3</sub>C-O), 21.1 (CH<sub>3</sub>CH).  
 IR (u<sub>max</sub>, liquid ATR): 2963, 2933, 2877, 1713, 1461, 1425, 1400, 1366, 1281, 1260, 1097, 1029, 913, 877, 807, 707.

LR-MS: 141 [M+H]<sup>+</sup>.





## 2.5.10 - Batch vs VFD Epoxidation with Hydrogen Peroxide



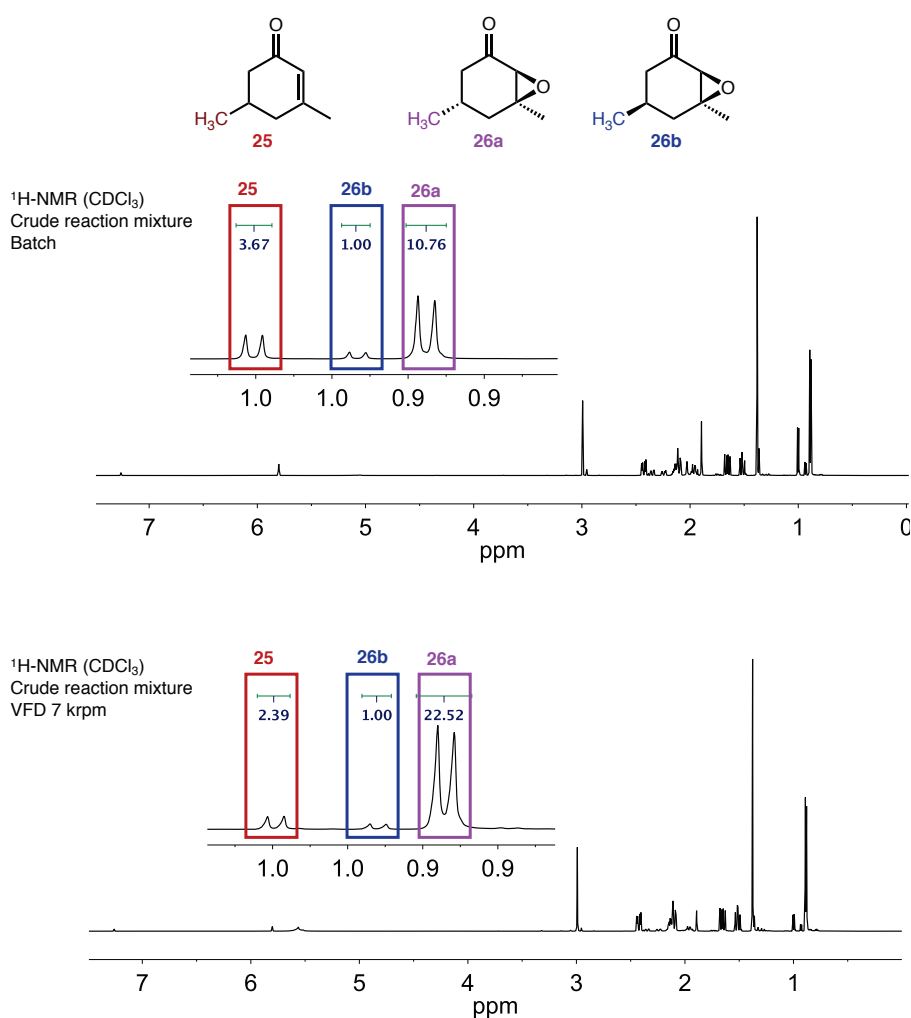
For both VFD and batch experiments, a NaOH solution (5 M, 0.7 mL, 3.5 mmol) was mixed with a H<sub>2</sub>O<sub>2</sub> solution (30% aq. v/v, 1.2 mL, 17.5 mmol) over an ice bath and cooled for 15 minutes. This vial was then removed from ice and allowed to return to room temperature. Following this, compound **8** (0.5 mL, 3.5 mmol) was added to the reaction mixture. Stirring was then begun (7 krpm in VFD, and 500 rpm for the magnetic stirrer bead batch control). After 15 minutes of reaction time CDCl<sub>3</sub> (≈ 1.5 mL) was used to extract the crude reaction mixture for NMR and GC-MS analysis. The experiment was performed in duplicate for each the batch and VFD processing. Conversions and d.r were determined by comparing the integration of the CHCH<sub>3</sub> in the <sup>1</sup>H NMR spectrum for the starting material and the product isomers. Representative spectra and the E-factor calculations are shown below.

### Batch

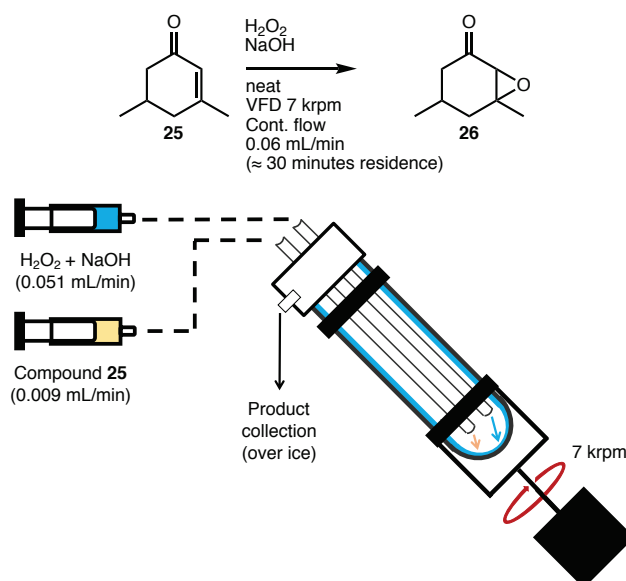
$$E_{(batch)} = \frac{0.14 \text{ g}}{0.368 \text{ g}} = 0.38$$

### VFD

$$E_{(VFD)} = \frac{0.06 \text{ g}}{0.442 \text{ g}} = 0.14$$

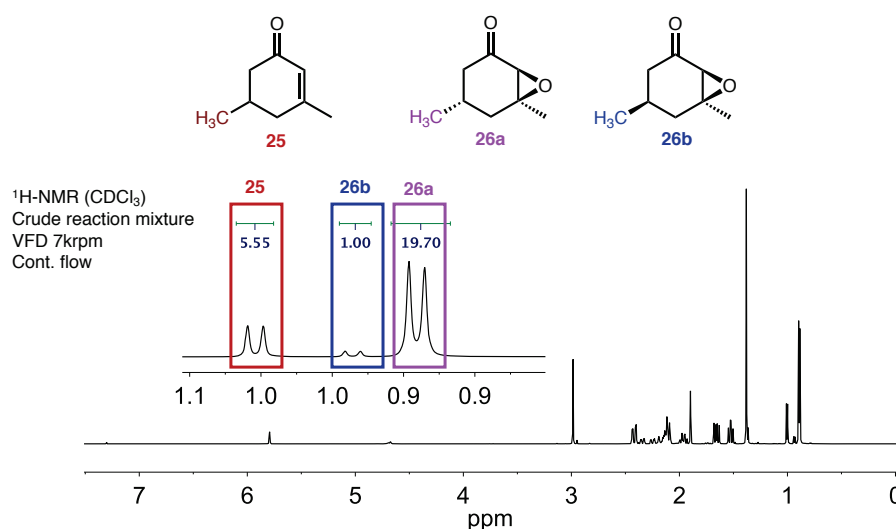


## 2.5.11 - Continuous flow VFD Epoxidation with Hydrogen Peroxide



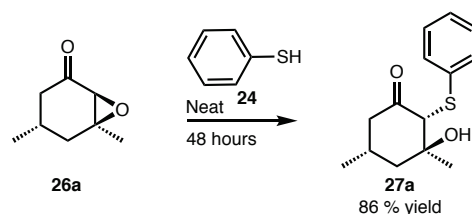
Two syringe pumps were used to pump the liquid reagents through the continuous flow set up. A solution of NaOH (5 M, 3.6 mL, 18.3 mmol) and aqueous  $\text{H}_2\text{O}_2$  (30% v/v, 7.14 mL, 91.4 mmol) was prepared and cooled to 0 °C over ice for 15 minutes. This solution was then removed from ice and transferred into 1 of the 2 syringes. This syringe was set to deliver contents at 0.051 mL/min. The other syringe contained compound **25** (2 mL, 18.3 mmol) and was set to deliver contents at 0.009 mL/min. This resulted in a total flow rate of 0.06 mL/min, which relates to  $\approx$  30-minute residence time (time for the liquid delivered to the base of the rotating tube to leave the top). Once exiting from the vortex, the reaction mixture was collected over ice. The total reaction time was 3.5 hours, over which time the collection vessel was changed every 30 mins giving 7 fractions of reaction product. The organic material was extracted from these fractions with  $\text{CDCl}_3$  and analyzed by  $^1\text{H}$ -NMR upon collection. Averaging these fraction gave a conversion of 84 % and a d.r of 20 : 1. A representative  $^1\text{H}$  NMR can be found below. The E-Factor calculation for this experiment is shown below.

$$E = \frac{0.471 \text{ g}}{2.15 \text{ g}} = 0.219$$





### 2.5.12 – X-Ray Structure determination of 27a



Epoxide **26** is an oil and standard NMR analysis was not sufficient for determining the relative stereochemistry for the major diastereomer **26a**. Epoxide **26** was therefore converted to crystalline derivative **27** using a regio- and stereo-specific ring-opening reaction. The major diastereomer, **27a** crystallised directly from the mixture and X-ray crystallographic analysis confirmed the relative stereochemistry. Protocol for conversion of **26** to **27**: Epoxide **26** (0.36 mmol, 50  $\mu\text{L}$ ) was reacted directly with thiophenol **24** (0.36 mmol, 37  $\mu\text{L}$ ) (neat reaction, no solvent). Over 48 hours, the product crystallised directly from the mixture. The crystals were isolated by filtration and then washed with water (3 x 5 mL) and hexane (3 x 5 mL), providing compound **27** in 86% yield (76 mg, 0.307 mmol).

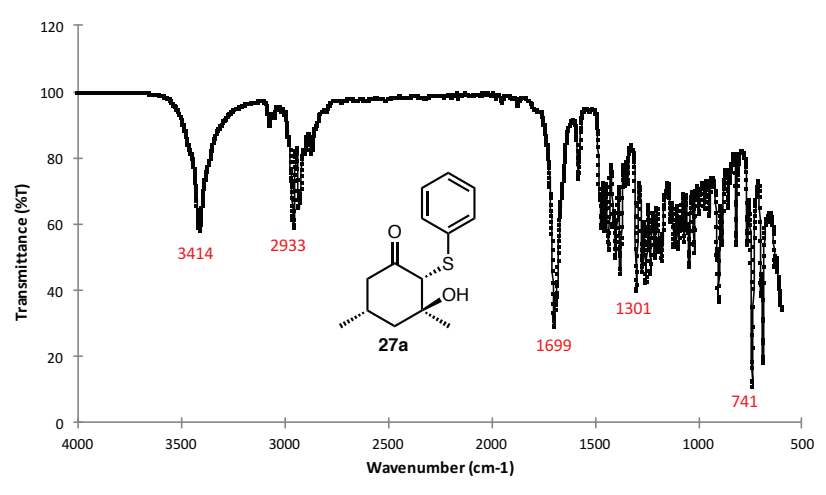
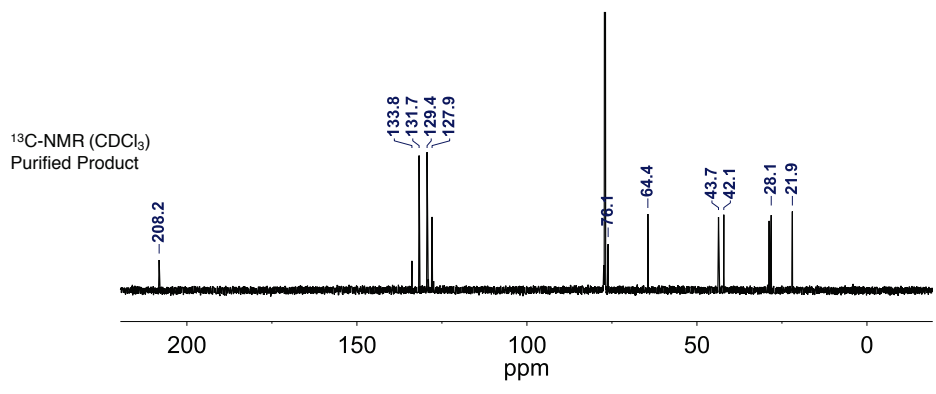
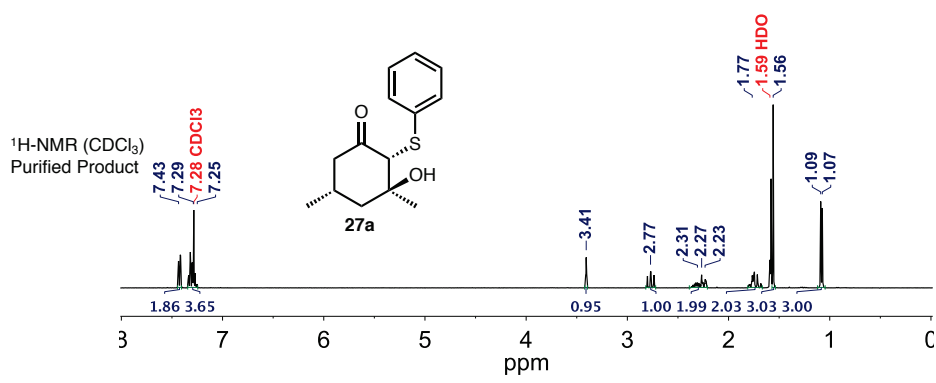
Melting point: 74  $^{\circ}\text{C}$

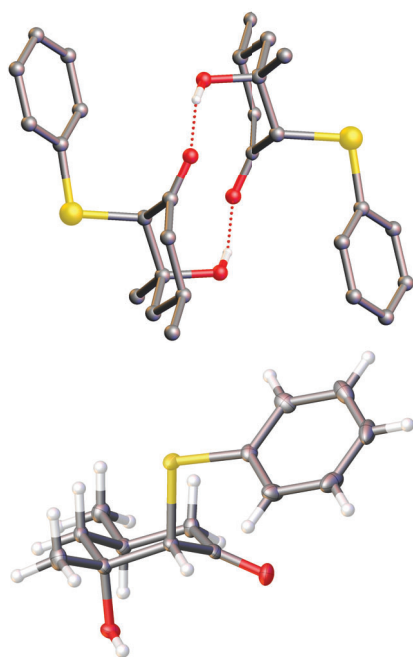
$^1\text{H}$  NMR (600 MHz,  $\text{CDCl}_3$ ):  $\delta_{\text{H}} = 7.44 - 7.40$  (2H, m, Ar), 7.34 - 7.24 (3H, m, Ar), 3.41 (1H, s,  $\text{CH}_2\text{S}$ ), 2.77 (1H, t,  $J = 12.4$  & 14 Hz,  $\text{CHHC}=\text{O}$ ), 2.26-2.17 (1H, m,  $\text{CHCH}_3$ ), 2.14 (1H, dd  $J = 14, 4.7$  Hz,  $\text{CHHC}=\text{O}$ ), 1.8-1.7 (3H, m,  $\text{CH}_2\text{COH}$ ), 1.56 (3H, s,  $\text{HOCCH}_3$ ), 1.08 (3H, d, 6.4 Hz,  $\text{HCCH}_3$ )

$^{13}\text{C}$  NMR (600 MHz,  $\text{CDCl}_3$ ):  $\delta_{\text{C}} = 208.2$  ( $\text{C}=\text{O}$ ), 133.8 (Ar  $4^{\circ}$ ), 131.7, 129.4, 127.9 (Ar,  $\text{CHx3}$ ), 76.1 ( $\text{COH}$ ), 64.4 ( $\text{CSPH}$ ), 43.7 ( $\text{CH}_2\text{C}=\text{O}$ ), 42.1 ( $\text{CH}_2\text{COH}$ ), 28.1 ( $\text{CH}_3\text{COH}$ ), 21.9 ( $\text{CH}_3\text{CH}$ )

IR ( $u_{\text{max}}$ , crystals ATR): 3414, 2958, 2933, 1699, 1455, 1441, 1435, 1401, 1379, 1300, 1254, 1233, 1177, 1117, 1096, 1045, 1021, 948, 856, 819, 765, 741, 696

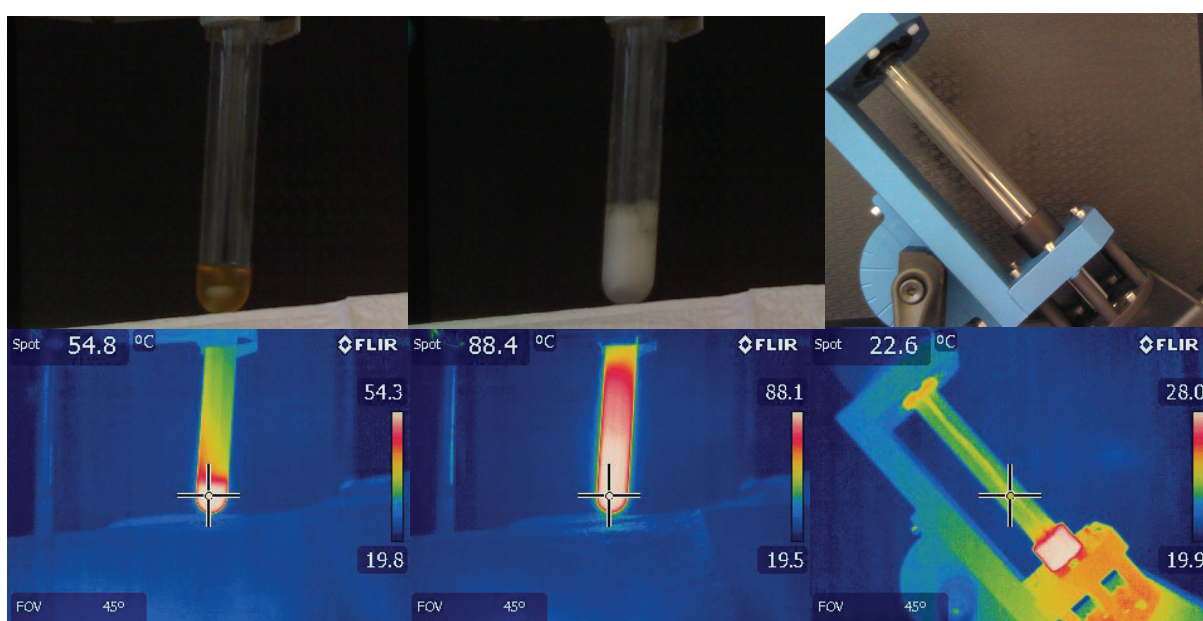
**Crystal Data for 27 (CCDC 1552987):**  $\text{C}_{14}\text{H}_{18}\text{O}_2\text{S}$ ,  $M = 250.34$  g/mol, monoclinic, space group  $P2_1/n$  (no. 14),  $a = 7.8477(5)$   $\text{\AA}$ ,  $b = 7.9550(5)$   $\text{\AA}$ ,  $c = 20.8582(11)$   $\text{\AA}$ ,  $\beta = 96.801(2)^{\circ}$ ,  $V = 1292.98(13)$   $\text{\AA}^3$ ,  $Z = 4$ ,  $T = 100(2)$  K,  $\mu(\text{MoK}\alpha) = 0.238$   $\text{mm}^{-1}$ ,  $D_{\text{calc}} = 1.286$   $\text{g/cm}^3$ , 11046 reflections measured ( $5.36^{\circ} \leq 2\theta \leq 53.46^{\circ}$ ), 2733 unique ( $R_{\text{int}} = 0.0211$ ,  $R_{\text{sigma}} = 0.0188$ ) which were used in all calculations. The final  $R_1$  was 0.0283 ( $I > 2\sigma(I)$ ) and  $wR_2$  was 0.0755 (all data).



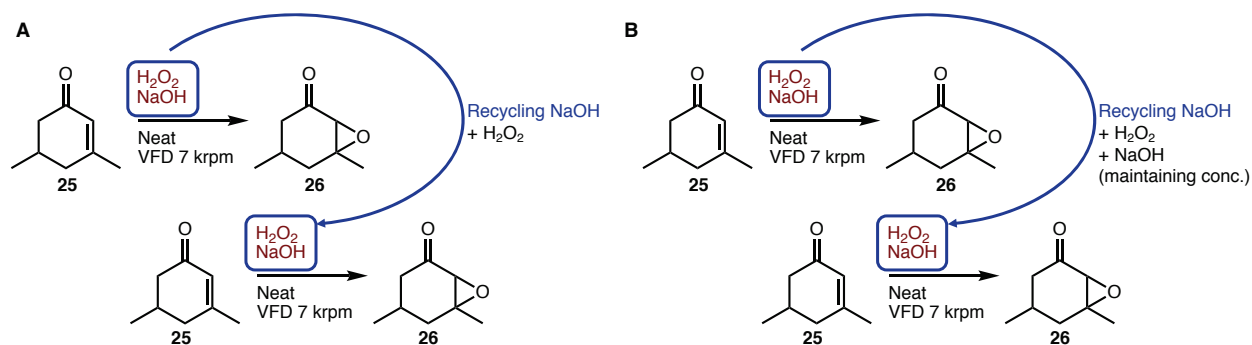


### 2.5.13 - Thermal monitoring of Batch vs VFD Epoxidation

For both VFD and batch experiments, a NaOH solution (5 M, 0.7 mL, 3.5 mmol) was mixed with a H<sub>2</sub>O<sub>2</sub> solution (30% aq. v/v, 1.2 mL, 17.5 mmol) over an ice bath and cooled for 15 minutes. This vial was then removed from ice and allowed to return to room temperature. Following this, Compound **25** (0.5 mL, 3.5 mmol) was added to the reaction mixture. Stirring was then begun (7 krpm in VFD, and 500 rpm for the magnetic stirrer bead batch control). During this time, thermal imaging of the reaction mixture was performed at set intervals (see below images). After 15 minutes of reaction time CDCl<sub>3</sub> was used to extract the crude reaction mixture for NMR and GC-MS analysis. Interestingly, comparing the integration of the CHCH<sub>3</sub> in the <sup>1</sup>H NMR spectrum for the starting material and the product isomers, it was still observed that the reaction progressed further in the VFD at 7 krpm compared to the batch sample in 15 minutes, despite not reaching temperatures over 23 °C.



## 2.5.14 - NaOH Recycling in the Epoxidation with Hydrogen Peroxide



A NaOH solution (5 M, 0.7 mL, 3.5 mmol) was mixed with a  $\text{H}_2\text{O}_2$  solution (30% aq. v/v, 1.2 mL, 17.5 mmol) over an ice bath and cooled for 15 minutes. This was then removed from ice and returned to room temperature. Following this, compound **25** (0.5 mL, 3.5 mmol) was added to the reaction mixture, followed by operation at 7 krpm in the VFD for 30 minutes. Upon completion, the aqueous layer was separated by pipette, and the organic layer was collected for crude NMR analysis. The aqueous layer, containing the NaOH was then re-used, mixing with fresh  $\text{H}_2\text{O}_2$  solution over ice, followed by the addition of compound **25**, and then operated in the VFD at 7 krpm for 30 mins. This was repeated for a total of 3 cycles, with the organic layer being analysed by  $^1\text{H-NMR}$  for conversion. Because the addition of  $\text{H}_2\text{O}_2$  dilutes the reaction mixture with each cycle, the conversion decreases under the same time frame. To ensure the same molar ratio of reagents, 0.7 mL of the aqueous layer was re-used each cycle, using reduced amounts of  $\text{H}_2\text{O}_2$  and compound **25**.

Another experiment was performed where the recycled aqueous layer (1.9 mL) was mixed with solid NaOH (160 mg, 4 mmol) and  $\text{H}_2\text{O}_2$  (30% aq. v/v, 1.2 mL, 17.5 mmol) and compound **25** (0.5 mL, 3.5 mmol). This was repeated for a total of 3 cycles.

## Chapter 3 – Olefin Metathesis

The olefin metathesis (OM) reaction is an established versatile and robust tool in synthesis (Figure 18A).<sup>148-153</sup> Highlighting the impact of this reaction, Robert H. Grubbs, Yves Chauvin and Richard. R Schrock shared the 2005 Nobel prize in chemistry for their efforts in developing and describing this OM. As described in the name, “meta” meaning to change, and “thesis” referring to position. The result of this reaction is to effectively swap partners across the double bond. This is achieved through the formation of and subsequent collapse of a 4-membered transition state at the metal centre (Figure 18B).

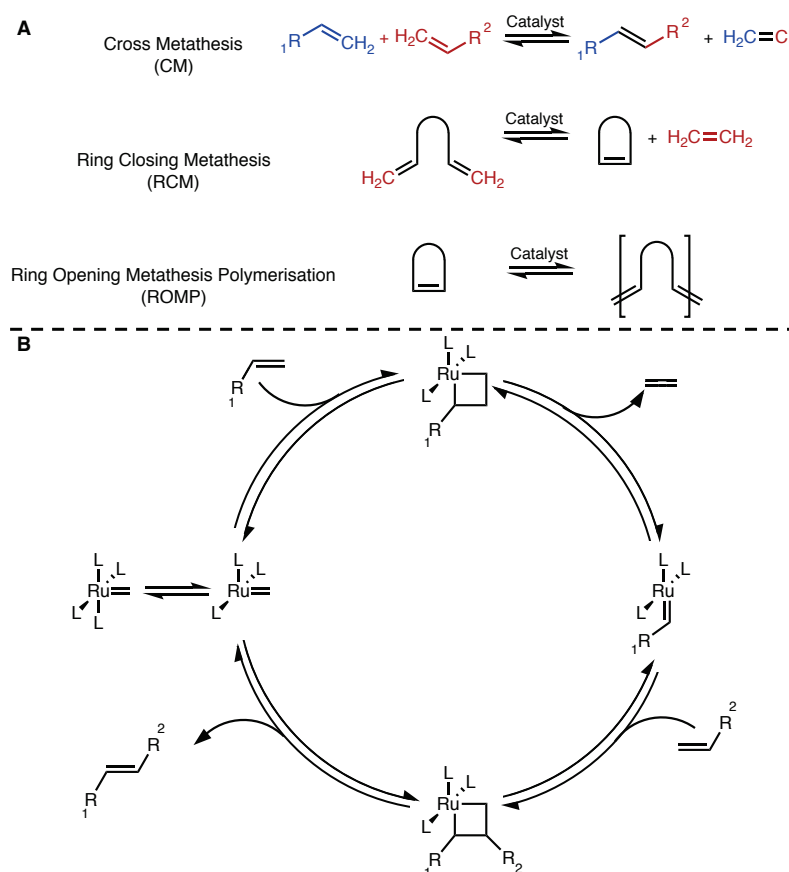


**Figure 18.** (A) General schemes of common olefin metathesis reactions CM, RCM and ROMP. (B) Mechanism of the ruthenium based methylidene active species, showing the 4-membered ring transition state. This methylidene is formed from the initial catalyst going through the same process shown here.<sup>149, 150</sup>

There are a large number of catalysts available for this reaction. Common catalysts are based on those developed by Grubbs (Figure 19). These contain a ruthenium centre. The first of which was Grubbs 1<sup>st</sup> generation catalyst (**GI**). The activity of these catalysts is largely controlled by the ligands, be it controlled sterically or by electronic effects. Due to this, a large number of ruthenium based catalysts are commercially available. Other catalysts containing different metal centres have been developed, based on metals such as tungsten or molybdenum.

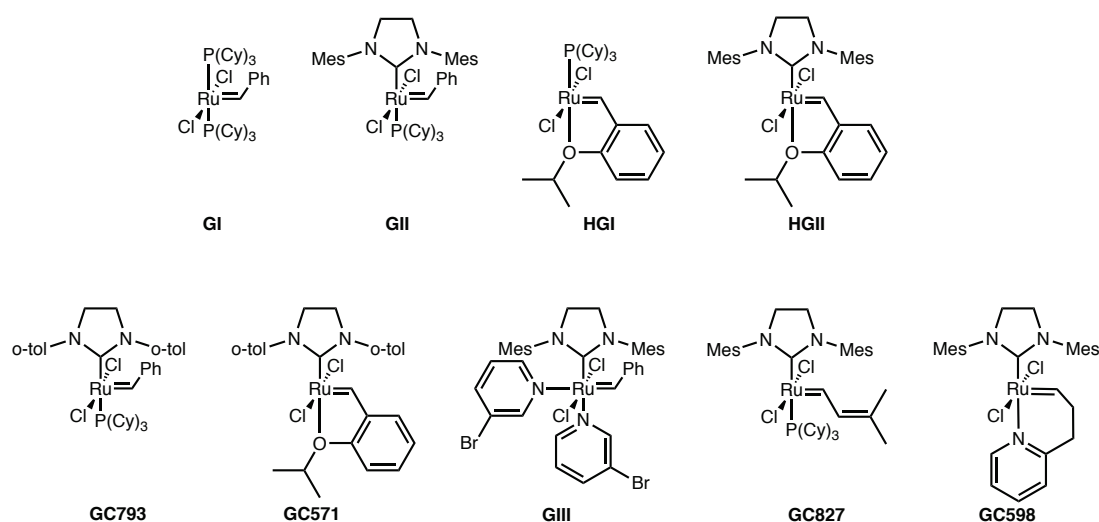


**Figure 19.** Grubbs-type ruthenium OM catalysts used in this work. These were purchased as a kit from Sigma-Aldrich.

Due to the inherent utility of OM, this reaction has seen a great deal of use in synthesis.<sup>154-157</sup> Although originally developed as a carbon-carbon double bond forming reaction, it has recently evolved to include carbon-carbon triple bonds and carbon-oxygen double bonds.<sup>158, 159</sup> This recent expansion of applicability has seen an even greater impetus for applying this reaction.

However, industry uptake of OM is limited by several key factors. Overcoming these limitations will allow incorporation OM into industrial processes, realising the waste-eliminating potential. A key problem encountered when employing OM, is the need to remove the ruthenium catalyst from the final product. Typical removal methods are chromatographic. Another limiting factor is the reactivity of the catalysts. There are some functionalities that, when adjacent to the target olefin, will slow or halt the OM reaction.

### 3.1 - Ethenolysis

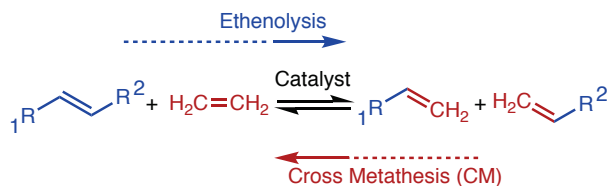


Figure 20. Schematic of a general ethenolysis type olefin metathesis (OM) reaction.

Transition metal catalysed olefin metathesis (OM) is a versatile and robust tool in chemical synthesis.<sup>150-152</sup> One specific application of OM of increasing interest is ethenolysis. Typically, this reaction transforms an internal alkene into two separate terminal alkenes (Figure 20).<sup>160, 161</sup> Ethenolysis has applications in synthesis,<sup>162-165</sup> and has been lauded for its potential in the valorisation of renewably sourced unsaturated materials from plants or microbes.<sup>166-174</sup> Indeed, producing fine chemicals from renewable sources is important for reducing the reliance on petroleum feedstocks.<sup>175-177</sup> In ethenolysis, the distribution of products is highly dependent on the catalyst and alkene substrate.<sup>178-184</sup> A major focus of work in this area has been to develop catalysts that will produce high conversions.<sup>165, 185, 186</sup> As a result, many catalysts have been reported.<sup>184-194</sup> Despite catalyst activity being largely addressed, several issues currently hinder industrial applications of ethenolysis. For example, there are safety concerns associated with the use of large volumes of flammable gasses, the removal of the catalyst from the product is a challenge, and the large-scale mass transfer of gaseous reagents into the liquid reaction media is a non-trivial problem. Continuous flow technology is well-suited to the scalability,<sup>7</sup> mass-transfer<sup>6, 29, 119</sup> and safety<sup>17, 195</sup> issues of many chemical reactions. Accordingly, there have been several reports of continuous flow ethenolysis.<sup>196-200</sup> These methods mostly use liquid/gas plug flow regimes.

A common substrate used to study the ethenolysis reaction is methyl oleate (**28**).<sup>166, 196, 201</sup> **28** is sourced from renewable plant oils, such as canola oil, olive oil and related sources of triglycerides - increasingly important feedstocks in the synthesis of organic building blocks, polymers and composites.<sup>170, 202-204</sup> Indeed, direct ethenolysis of **28** produces the terminal alkenes 1-decene and methyl-9-decenoate, which are important feedstocks for polymer and fine chemical synthesis (Figure 21 – group 2). The work herein reports on the ethenolysis of **28** in a VFD.



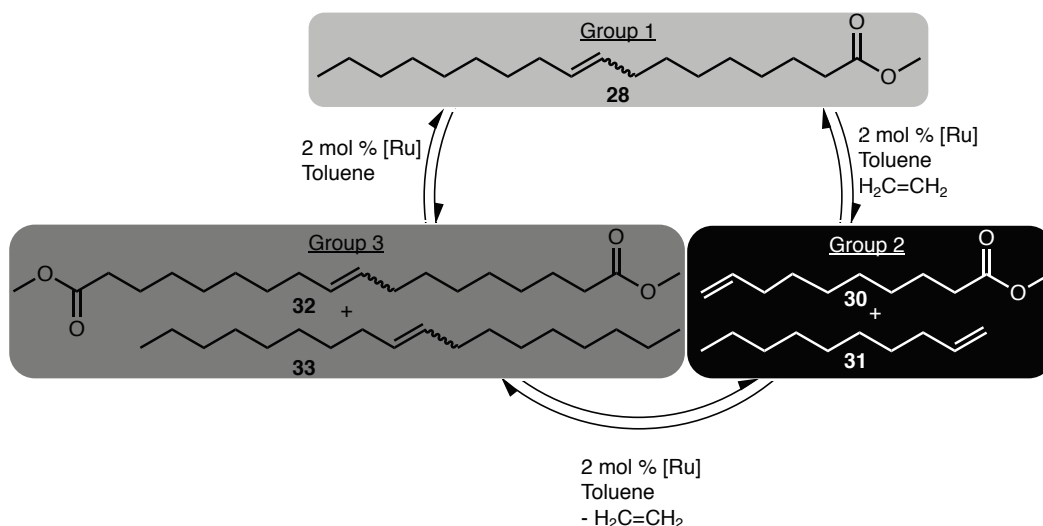


Figure 21. Metathesis equilibrium of methyl oleate (28).

### 3.1.1 - Discussion on Ethenolysis in the VFD

Recent work in our laboratories demonstrated the ability to safely deliver gaseous reagents such as air or oxygen to the reaction film for aerobic oxidations,<sup>102</sup> and also the extraction and processing of plant and microbial oils.<sup>205, 206</sup>

A common issue when employing ethenolysis or any liquid-gas reaction is that of mass transfer. At low surface area to volume ratios, the mass transfer of the gaseous reagent into the solution can become a rate-limiting factor.<sup>207</sup> It was hypothesised that the VFD would be a useful flow platform for providing a scalable and consistent method for delivering gaseous reagents such as ethene, avoiding mass transfer limitations. Furthermore, the reaction volume at any given time in the VFD is small ( $\approx 1$  mL), so reactions are typically safer than the corresponding batch processes - especially for large scale preparations.

In order to compare batch and VFD processing, the compositional distribution at equilibrium was compared for both processing methods. To achieve this, firstly a tube was prepared with an atmosphere of ethene by replacing with ethene (balloon). **28** in toluene (1 mL, 0.24 mM) was then added followed by a homogenous catalyst solution in toluene (1 mL,  $4.86 \times 10^{-3}$  mM). After 20 minutes, these reactions were quenched with a solution of **18** in MeCN (1 mL, 0.12 M).

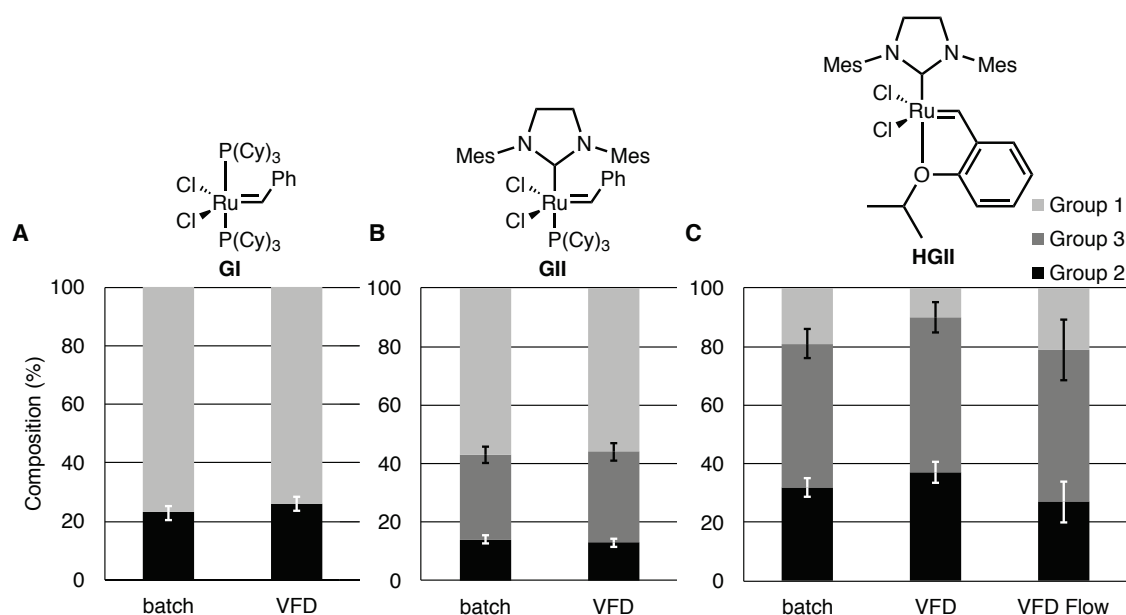


**Figure 22.** The compositional distribution of the reaction mixture after 20 minutes is shown, comparing VFD and batch processing for catalysts **(B) GI**, **(C) GII** and **(D) HGI** including results from continuous flow processing with 20-minute residence time. Compositional distributions determined by GCMS. (see Figure 21 for reaction scheme)

The compositional distribution of the established equilibrium was then analysed via GC-MS. The results of this are found in Figure 22 which demonstrate that the VFD does not alter the equilibrium in the ethenolysis of **28**, for any of the Grubbs-type catalysts trialled. It also appears for these small reaction volumes that the gas transfer is not rate limiting - hence the same conversions in batch and VFD processing. However, these experiments are important for several reasons. Firstly, other studies have revealed that flow platforms can alter the reaction rates and product distributions, and it is important to know how the VFD compares to these reactors.<sup>196-200</sup> Secondly, as the VFD has shown many unexpected influences on the outcome of other reactions, its utility is warranted, understood and validated for any new reaction. Thirdly, Figure 22C also highlights that the outcome is not affected by continuous flow operation, therefore establishing a safe method for scale-up. This continuous flow comparison was performed in a VFD, maintaining an atmosphere of ethene by continuously delivery of reactants to the base of the VFD tube, **28** in toluene (9 mL, 79.2 mM) and HGII catalyst in toluene (9 mL, 1.59 mM) using separate jet feeds with flow rates of 0.05 mL/min, total flow rate 0.1 mL/min (20 minutes residence time). Upscaling in batch processing, in contrast, would require separate optimisation and accommodations for heat and mass transfer. The slight reduction in the “group 2” terminal alkenes observed is likely due to the increased evaporation of these volatile compounds when they are processed in a thin film in an open tube.

### 3.2 – N-Acetyl-L-cysteine Quench

There are a variety of reported compounds that quench removal of ruthenium based OM catalysts.<sup>208-215</sup> However, this work sought to employ simple cysteine derivatives for the quenching role. Cysteine is known to bind to transition metals,<sup>216-218</sup> including ruthenium metathesis catalysts.<sup>219-223</sup> The high affinity of the sulphur for these catalysts,<sup>219, 224</sup> and the possibility of chelation,<sup>218</sup> led to the hypothesis that cysteine or its derivatives would be efficient reagents for binding and quenching these Ru-based catalysts. There are some clues in the literature that support this hypothesis, such as the use of a basic solution of cysteine to extract residual ruthenium into water.<sup>225</sup> The ability for N-Acetyl-L-cysteine to affect the chromatographic retention of ruthenium catalyst complexes (as discussed below) has promise for catalyst removal – a major drawback for OM. N-Acetyl-L-cysteine may be added to solutions containing unwanted catalyst prior to chromatographic separations, allowing for a greater degree of control of retentions.

#### 3.2.1 – Discussion on N-Acetyl-L-cysteine as a Quenching agent

For the VFD reactions of **28** (Figure 21), in order to decouple the reactivity imparted by the VFD from any reaction in the collection vessel, a quenching method was necessary. We found here, that the addition of **18** with MeCN as a co-solvent binds to the ruthenium catalysts and arrests metathesis activity (Figure 23). The co-solvent is present to allow miscibility of the quenching agent in solvents commonly used in OM, such as CH<sub>2</sub>Cl<sub>2</sub> and toluene, none of which fully dissolve **18**. Additionally, it is noted that there were no signs of double bond migration isomerisation after quenching the catalyst in this way.

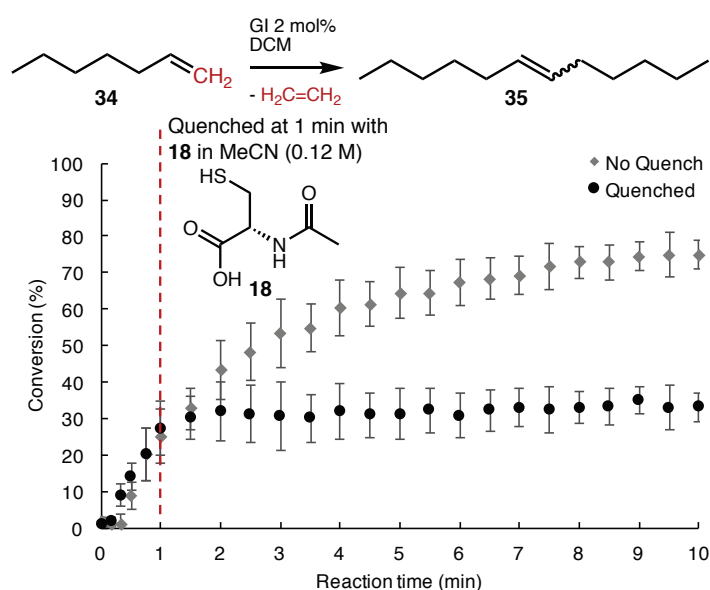


**Figure 23.** Monitoring the conversion of **34** (**34**) CM with catalyst **GI** over 10 minutes. Adding the quenching solution at 1 minute halts the reaction. The quenching solution consisted of N-acetyl-L-cysteine (**18**) in MeCN (20 mg/mL, 0.12 M). Conversions were determined by GCMS.

This is a major issue when selecting a quenching method, as external factors can result in a isomerisation catalyst from the metathesis catalyst,<sup>226</sup> for example, in generating a ruthenium-hydride species.<sup>227-229</sup> This was encountered here when both methanol and tertiary-butanol were trailed as co-solvents for **18**. Both of which were found to cause migrations of the double bond within the product olefin.

Whilst the structure of the quenched complex was not determined unambiguously, it can be seen by  $^1\text{H}$  NMR spectroscopy that catalyst **GI** is consumed rapidly in the presence of **18** (Figure 24A). Unfortunately, attempts to grow crystals of the resulting product(s) were unsuccessful. Nevertheless, this spectroscopic evidence is consistent with rapid binding of **18** to the ruthenium, converting the complex to an inactive catalyst.

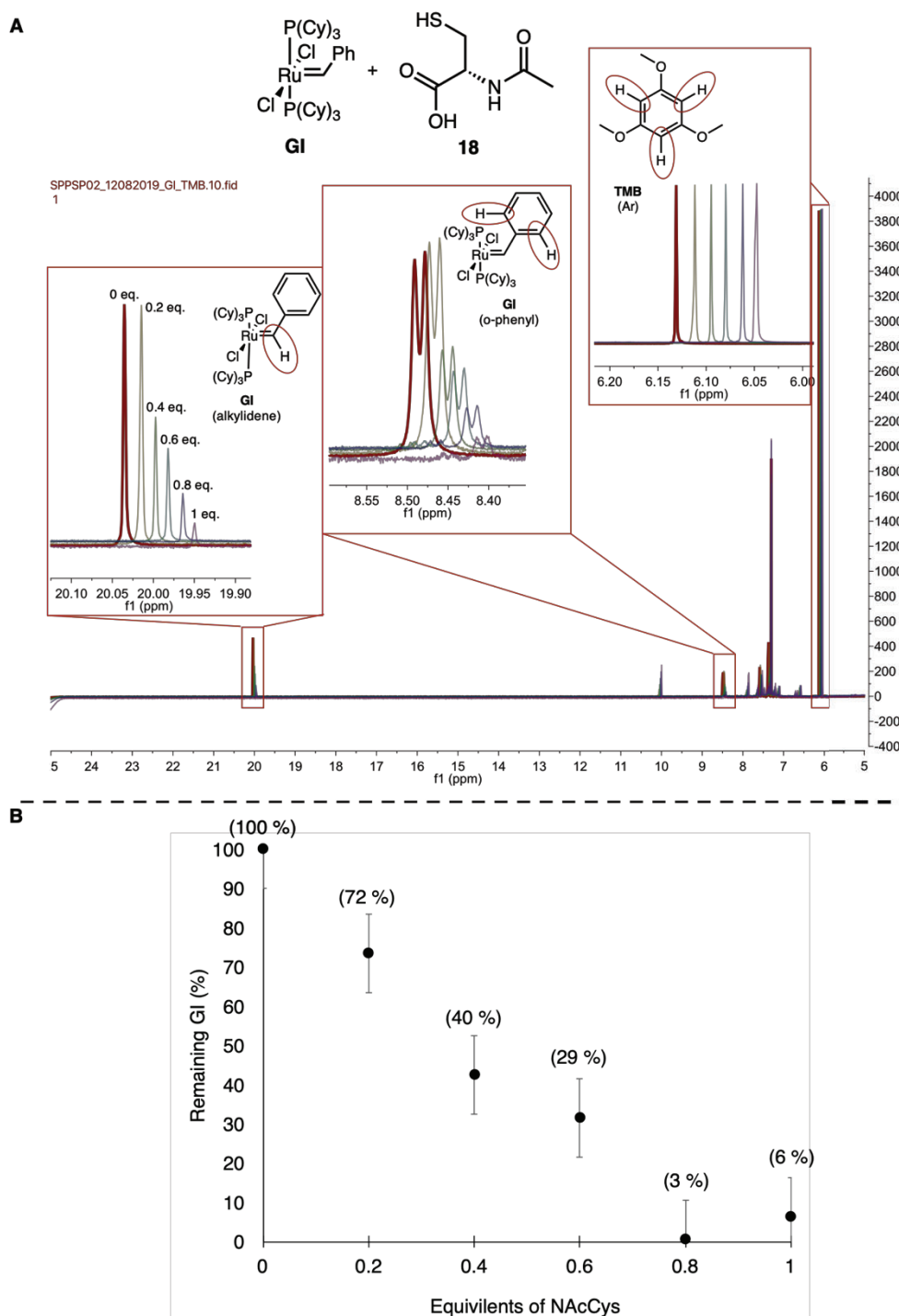


**Figure 24.** (A) Super imposed  $^1\text{H}$ -NMR spectra of catalyst **GI** titrated against **18** (20mg/mL in MeCN). Contains an internal standard of trimethoxybenzene (1 eq. wrt. **GI**). Added at equivalents of, from left to right, 0 eq. (red), 0.2 eq. (yellow), 0.4 eq. (green), 0.6 eq. (cyan), 0.8 eq. (blue), 1 eq. (purple). Note the convenient down-field shift at each addition, likely due to the increasing concentration of MeCN. This allows visualization without shifting the spectra relative to each-other. (B) Consumption of **GI** after addition of **18** solution (20 mg/mL in MeCN) to **GI**. Determined from the alkylidene  $^1\text{H}$ -NMR peak relative to internal standard (TMB).

In order to monitor the interaction of the catalyst with the quenching agent, a solution of **GI** (10 mg, 0.012 mmol) was titrated against a solution of **18** in MeCN (20 mg/mL, 0.12 M). An internal standard of trimethoxybenzene (4 mg, 0.012 mmol) was used for qualitative analysis of peak integrals. A focus was placed on the alkylidene (Ru=CHPh) proton, and also on the 5 phenyl protons. Note the higher field scan range (between 25 – 5 ppm), necessary to observe the high field alkylidene. Spectra are shown below, qualitatively showing the consumption of **GI** (Figure 24) and the formation of a new compound (Figure 25). Peak integrals were used to quantify the degradation of **GI** and the formation of the new compound. Note that the formation of the new alkylidene suggests only  $\approx 15\%$  conversion, whereas  $\approx 96\%$  of the original **GI** has been consumed. This suggests that multiple compounds are produced after reacting with the **18** / MeCN solution.

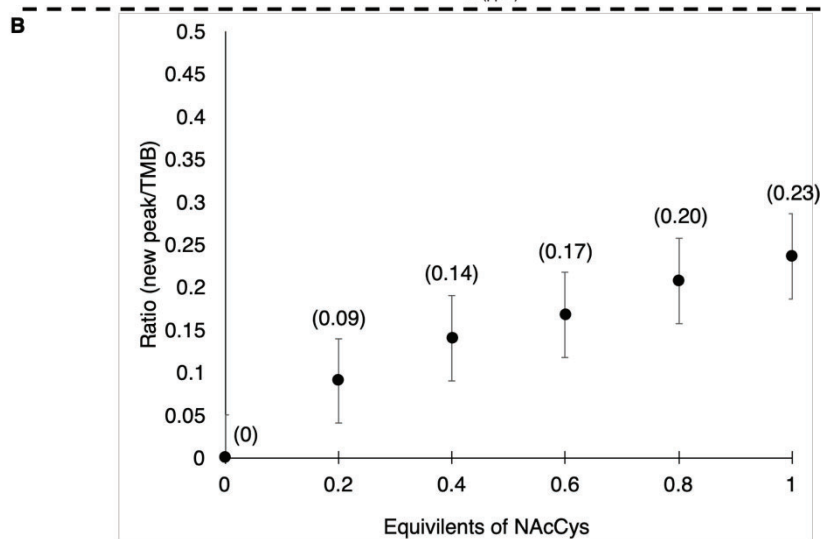
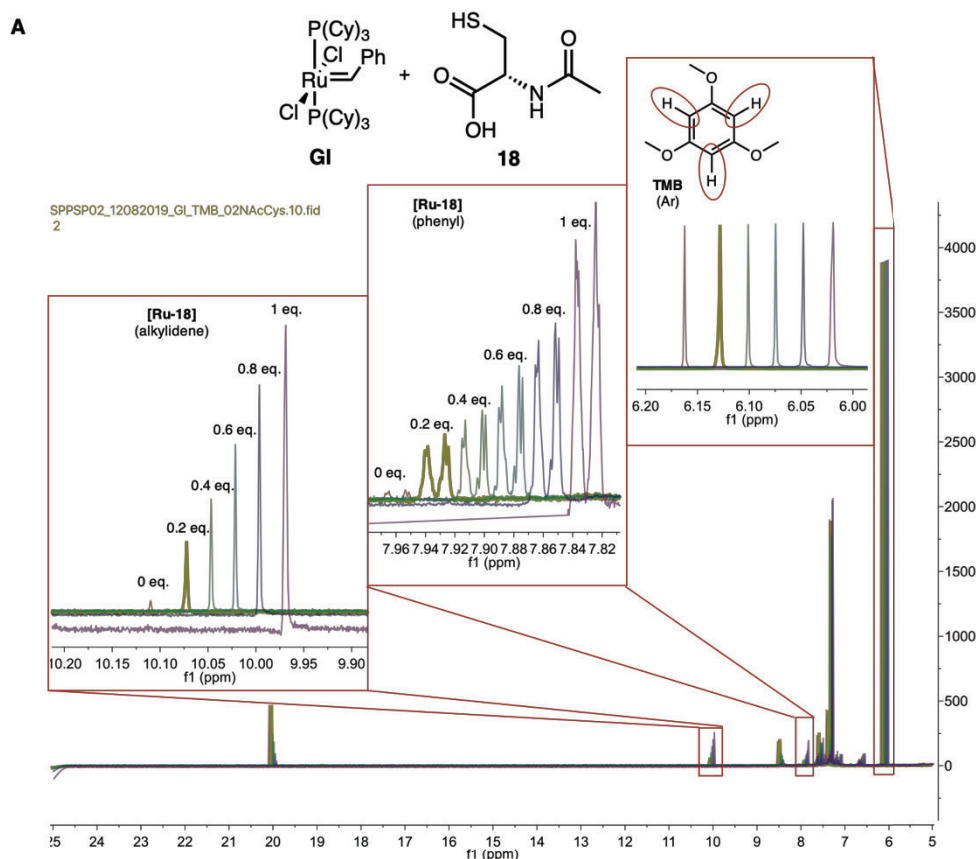


**Figure 25. (A)** Super imposed  $^1\text{H-NMR}$  spectra of catalyst **GI** titrated against **18** (20mg/mL in MeCN). Contains an internal standard of trimethoxybenzene (1 eq. wrt. **GI**). Shown are the new peaks formed after addition of the **18** solution. Added at equivalents of, from left to right, 0 eq. (red), 0.2 eq. (yellow), 0.4 eq. (green), 0.6 eq. (cyan), 0.8 eq. (blue), 1 eq. (purple). **(B)** Formation of new singlet at 10.05 ppm after additions of **18** solution (20 mg/mL in MeCN) to **GI**. Determined from the new  $^1\text{H-NMR}$  singlet at 10 ppm. Integral relative to internal standard (TMB). Note that the TMB integral is a result of three  $^1\text{H}$  nuclei and has been adjusted as such.

The following MS (Figure 26 (+ve mode) & Figure 27 (-ve mode)), although being inconclusive, shows that there is no simple ligand exchange occurring between **GI** and the **18** in MeCN. Table 2 & Table 3 show the possible masses that would result from ligand exchanges, and cannot be found in the MS.

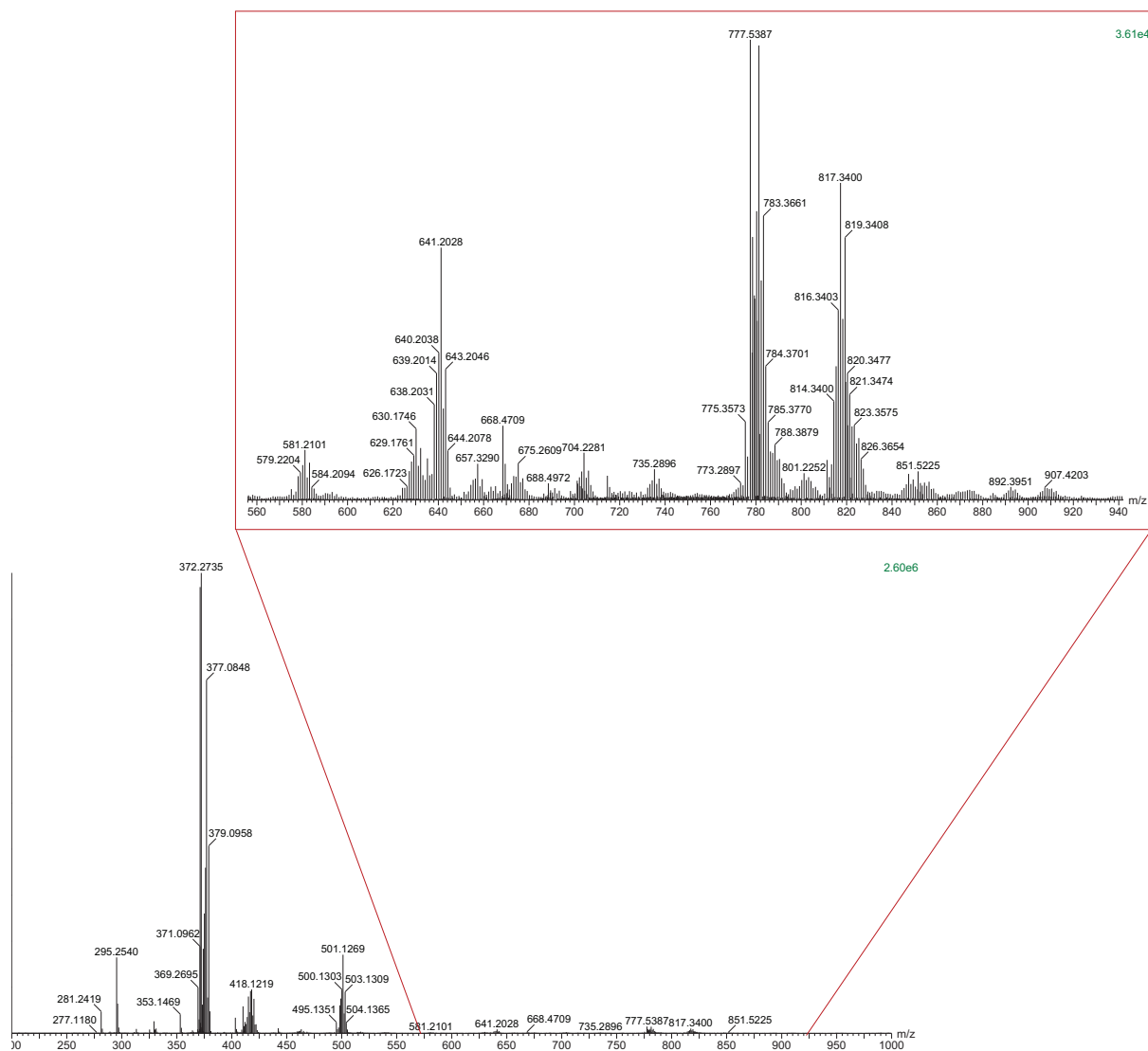
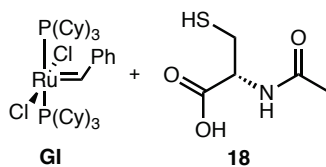
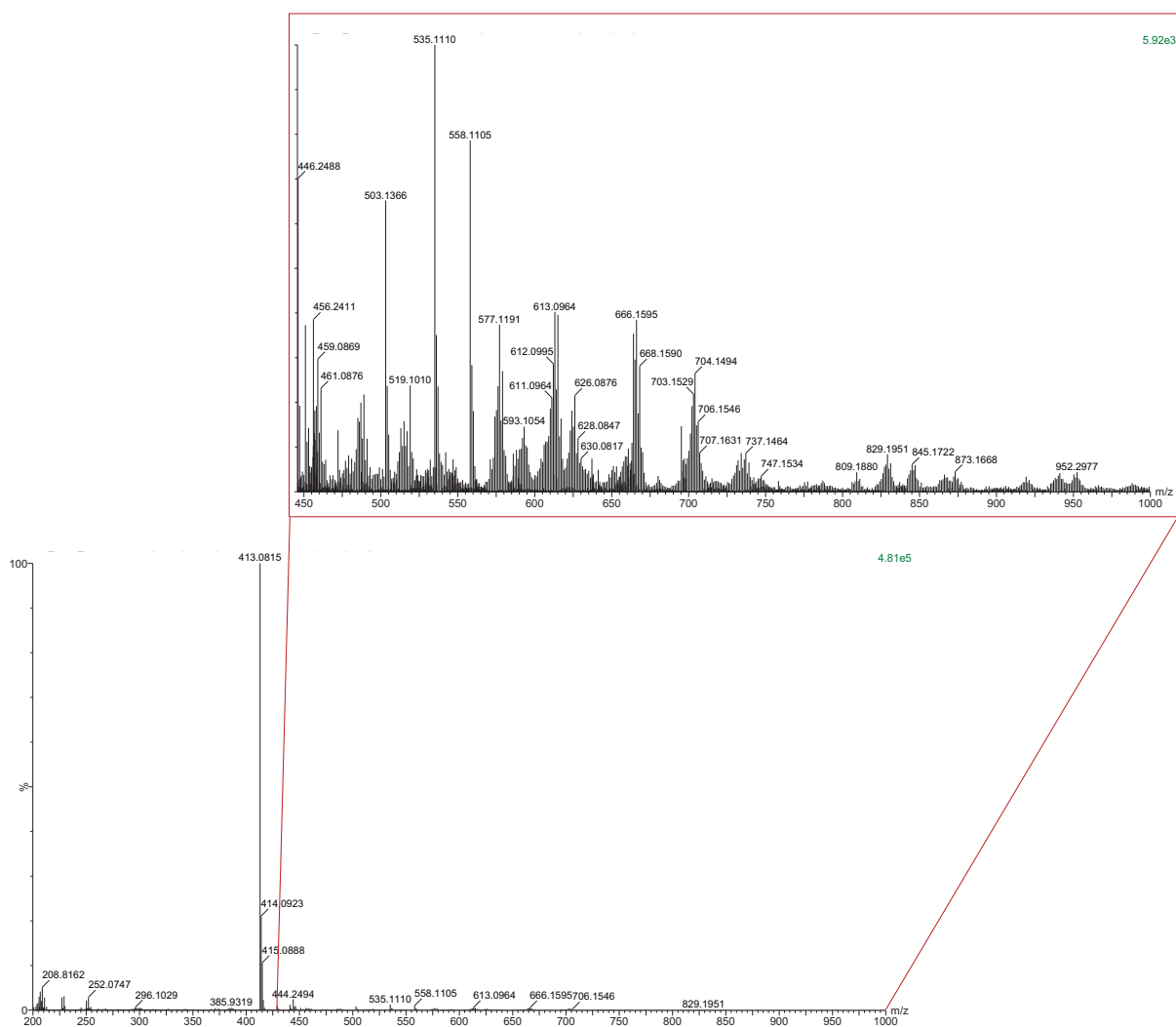


**Figure 26.** HRMS (+ve) of crude mixture after reacting **GI** with **18** / MeCN solution (1 eq., 20 mg/mL).

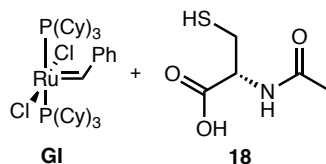
**Table 2.** Possible molecular ions for ligand exchanges in (+ve) mode



<b>[M]<sup>+</sup></b>	<b>+ none</b>	<b>+ 18</b>	<b>+ MeCN</b>	<b>+ 18 + MeCN</b>
- none	823.96	986.96	864.96	1027.96
- 1 Cl	788.51	951.51	829.51	992.51
- 2 Cl	753.06	916.06	794.06	957.06
- 1 P(Cy) <sub>3</sub>	543.73	706.73	584.73	747.73
- 2 P(Cy) <sub>3</sub>	263.5	426.5	304.5	467.5
- 1 Cl - 1 P(Cy) <sub>3</sub>	508.28	671.28	549.28	712.28
- 1 Cl - 2 P(Cy) <sub>3</sub>	228.05	391.05	269.05	432.05
- 2 Cl - 1 P(Cy) <sub>3</sub>	472.83	635.83	513.83	676.83
- 2 Cl - 2 P(Cy) <sub>3</sub>	192.6	355.6	233.6	396.6



**Figure 27.** HRMS (-ve) of crude mixture after reacting **GI** with **18** / MeCN solution (1 eq., 20 mg/mL).

**Table 3.** Possible molecular ions for ligand exchanges in (-ve) mode

[M]-	+ none	+ 18	+ MeCN	+ 18 + MeCN
- none	821.96	984.96	862.96	1025.96
- 1 Cl	786.51	949.51	827.51	990.51
- 2 Cl	751.06	914.06	792.06	955.06
- 1 P(Cy) <sub>3</sub>	541.73	704.73	582.73	745.73
- 2 P(Cy) <sub>3</sub>	261.5	424.5	302.5	465.5
- 1 Cl - 1 P(Cy) <sub>3</sub>	506.28	669.28	547.28	710.28
- 1 Cl - 2 P(Cy) <sub>3</sub>	226.05	389.05	267.05	430.05
- 2 Cl - 1 P(Cy) <sub>3</sub>	470.83	633.83	511.83	674.83
- 2 Cl - 2 P(Cy) <sub>3</sub>	190.6	353.6	231.6	394.6

It is thus established that **18** with MeCN as a co-solvent is a highly effective method for rapidly quenching a ruthenium catalysed metathesis reaction. MeCN itself was also found to hinder the **HGII** catalyst (Figure 28), and when combined with the **18**, the quenching is enhanced, as established for OM of several common catalysts, including **HGII**, the most active of the catalysts studied in this work (Figure 28). Furthermore, the chromatographic retention factor ( $R_F$ ) of the catalyst not bearing an NHC ligand were altered (Table 4). In this way, a readily available solution of **18** in MeCN can be used to aid in the chromatographic separation of ruthenium OM catalysts from target compounds.<sup>230, 231</sup>



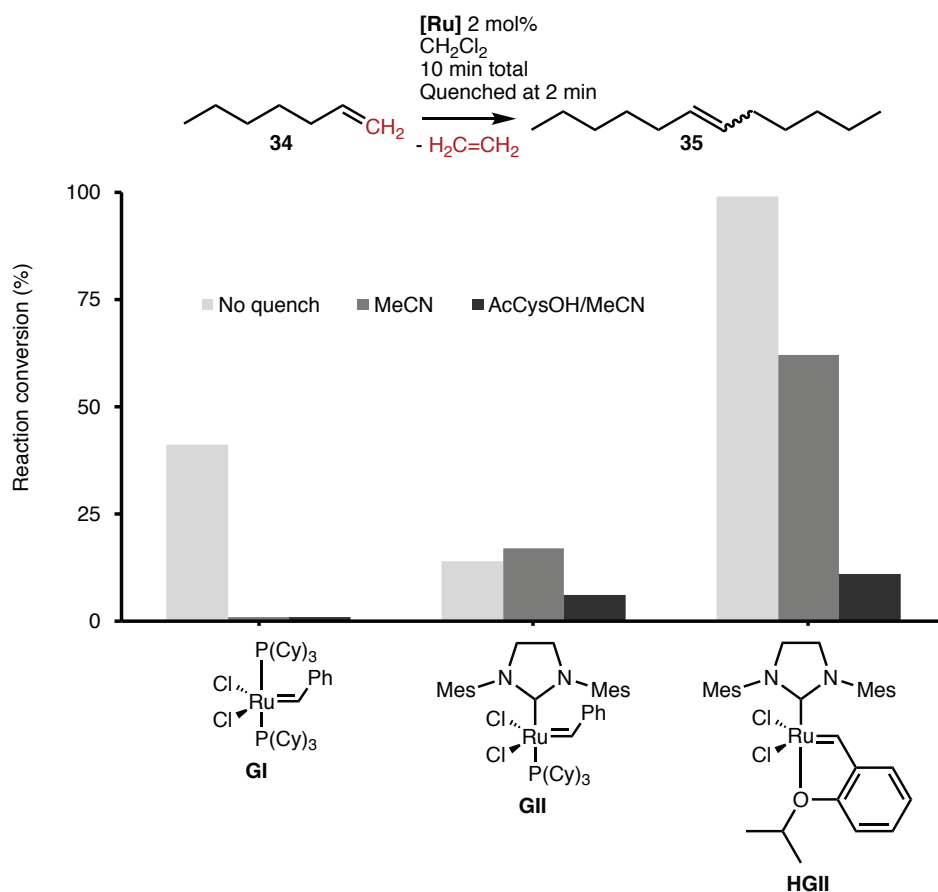


**Figure 28.** Quenching activity of both MeCN and a MeCN + **18** solution for three different Grubbs-type Ru-based OM catalysts.

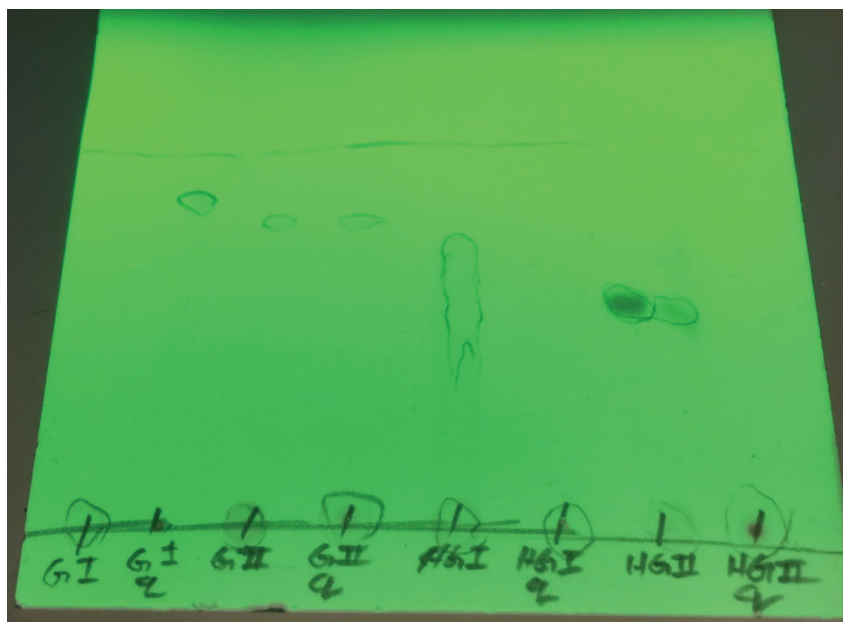


**Figure 29.** Chromatographic retention of the four different Ru-based OM catalysts, **GI**, **GII**, **HGI** and **HGII**. Mobile phase of 20% EtOAc in hexanes. Stationary phase of Silica coated aluminum plate. Visualized with UV light (256 nm).

**Table 4.** Chromatographic retention of the four different Ru-based OM catalysts, **G1**, **GII**, **HGI** and **HGII**. Mobile phase of 20% EtOAc in hexanes. Stationary phase of Silica coated aluminum plate. Visualized with UV light (256 nm). Table shows the retention factors ( $R_F$ ) of each catalyst, quenched and un-quenched.

$R_F$	<b>G1</b>	<b>GII</b>	<b>HGI</b>	<b>HGII</b>
<b><math>R_F</math> Free</b>	0.0	0.7	0.6	0.5
<b><math>R_F</math> Quenched</b>	0.9	0.7	0.0	0.5

In order to gain insight regarding the nature of the catalyst once quenched with the **18** in MeCN solution, the following UV-vis, NMR and mass spectra were recorded. Attempts to grow crystals of the resulting compounds were unsuccessful, likely due to the existence of multiple product compounds.

The colour of the complexes was clearly affected from the addition of the quenching agents. The UV-Vis spectra (Figure 30) for the catalyst **G1**, the catalyst **G1** with MeCN and the catalyst **G1** with the solution of **18** + MeCN (0.12 M) are likewise effected. This is also true for the colours observed in the reaction mixtures of **34**. This demonstrates the interaction with the active methyldene species (Figure 31).

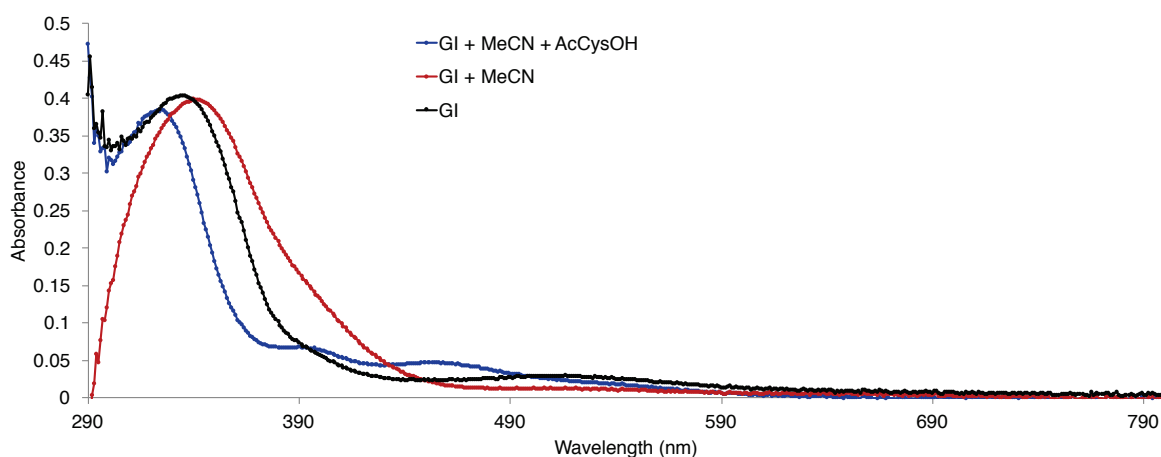


**Figure 30.** UV-Vis spectra in solutions of  $\text{CHCl}_3$ . Spectra for **G1**, **G1** with MeCN and finally the catalyst **G1** with the quenching solution of **18** in MeCN (0.12 M).

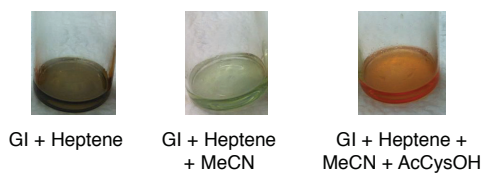
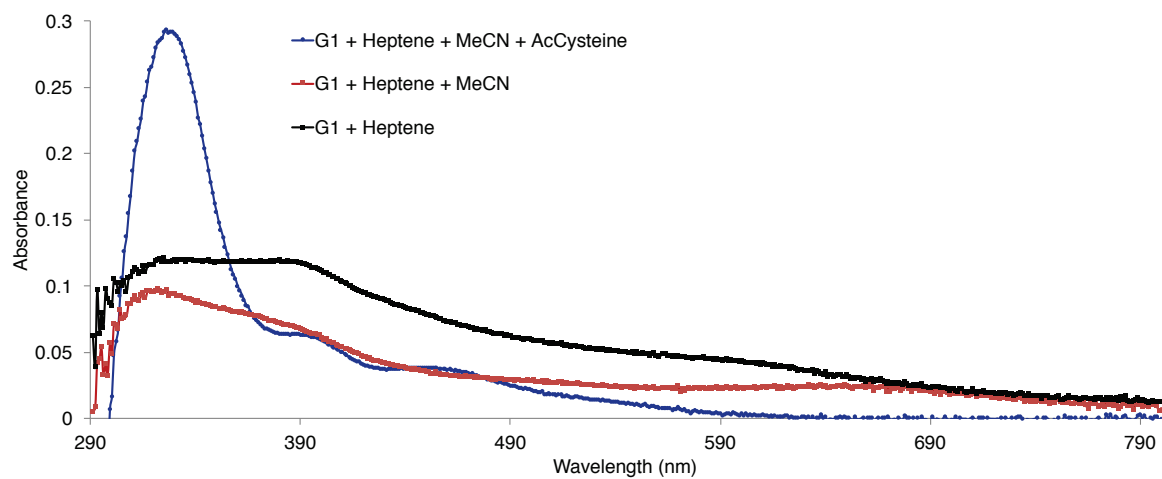


**Figure 31.** UV-Vis spectra and photographs of the **G1** catalyzed CM of **34** in solution ( $\text{CHCl}_3$ ), and also when quenched, both with MeCN and **18** + MeCN.

### 3.3 – In-Line Catalyst Separation

Homogenous catalyst systems inherently run the risk of requiring extravagant amounts of the catalyst when scaled up. This is also true for continuous flow catalytic applications. Flow systems that use a homogenous catalyst will require downstream purification to remove this catalyst. Heterogeneous catalysts are inherently a more promising option for continuous flow applications, due to the ability to immobilise or remove the catalyst in-line (filtration, magnetic retention ect.). With regard to OM, most catalysts are homogenous in nature, making flow applications difficult. Immobilised heterogeneous catalysts have found use in several OM applications.<sup>197, 232, 233</sup> However, care has to be taken to immobilise correctly.<sup>234</sup> If the tethering bond is placed on a labile ligand then the catalyst will detach and be washed away in flow. This not only decreases the lifetime of the catalyst, but also creates impurities in the solution that require downstream purification. Thus, when immobilising it is necessary to tether through a ligand that does not detach. When considering catalyst **HGII**, there are two sites for tethering – through the NHC ligand, or through the isopropoxyl-styrene ligand. If tethered through this isopropoxyl-styrene, the catalyst will detach from the support (see Figure 18B) and will be washed away in flow. In batch, this is not observed due to the resulting boomerang mechanism, which returns the ruthenium species back to the tethered ligand. This has led to tethering procedures being proposed when only studied in batch conditions. As such, many tethering options have been proposed, but are not viable in continuous flow. The alternative tethering site - the NHC ligand - will not depart from the active [Ru] species, and thus will be a viable tethering point for flow applications.

#### 3.3.1 – In-Line Catalyst Separation in the VFD

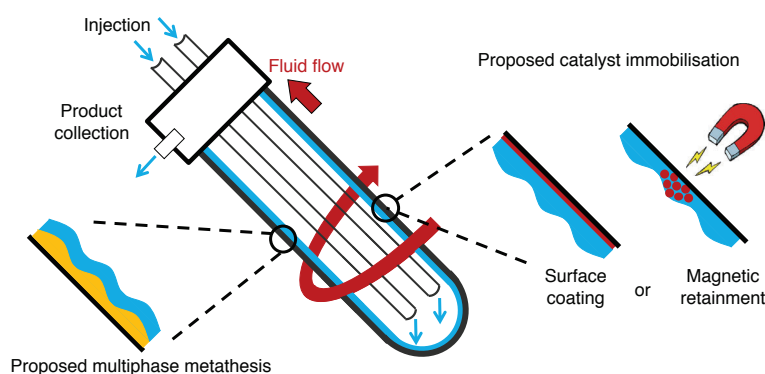


**Figure 32.** Diagram displaying the two different approaches to continuous flow catalyst separation in the VFD. On the left of the VFD is the proposed multiphase metathesis. On the right are the two methods for catalyst immobilisation.

A two-fold approach was proposed to utilise the unique benefits of the VFD (Figure 32). Firstly, reactions across phase boundaries in biphasic systems have been shown to be benefited in the VFD by the greater surface-area to volume ratio (SA:V). Thus, it was hypothesised that a two-phase system, with the catalyst in a separate phase from the olefins would efficiently react, and then separate upon after processing. Additionally, if the catalyst could then be recycled several times, the green-metrics of the process would be vastly improved. The biphasic system could be achieved with commercial catalysts in hydrophobic phase and a water-soluble olefin. The inverse of this was also proposed, with a water-soluble catalyst in a hydrophilic phase and a typical olefin in the hydrophobic phase. The second approach to achieve in-line catalyst separation was to immobilise the catalyst within the VFD, and then pass the reagent olefins over the catalyst. This immobilisation was proposed to be achieved either through direct tethering to the glass tube, or by tethering to magnetic

nanoparticles (MNPs) which could then be held in the rotating tube. If the catalyst could be withheld in the tube without leaching into the flowing solution, then no further downstream purification would be necessary for catalyst removal. This would be a promising and green process for scalable OM.

For the first approach – the multiphase metathesis – it was proposed that this would be achieved in a continuous manor by injecting both the catalyst solution and the olefin solution through separate jet feeds. Upon collection from the VFD these could be separated, such as an in-line phase separation membrane. Removing the catalyst solution in this way would allow for recycling of the catalyst, vastly improving the green metrics of this reaction. The first reaction to be trialed was the CM of allyl alcohol in confined mode VFD operation (Figure 33). This was performed with allyl alcohol in water, and catalyst HGII in toluene. As can be observed in Figure 33A, minimal conversion was achieved in both batch (0.81 %) and VFD (0.33 %). Also of note is the difficulty in monitoring the reaction progress using  $^1\text{H-NMR}$  analysis. This is due to peak overlap observed between the two products with the starting material peaks. The  $^{13}\text{C}$  satellite peaks are also intervening unless  $^{13}\text{C}$ -decoupling experiments are performed (Figure 33B). Furthermore, it was found that allyl alcohol was sparingly soluble in the toluene phase. This presented a problem, if the olefinic compounds are migrating into the organic phase, then product is being lost and the efficiency of the reaction is being deteriorated.

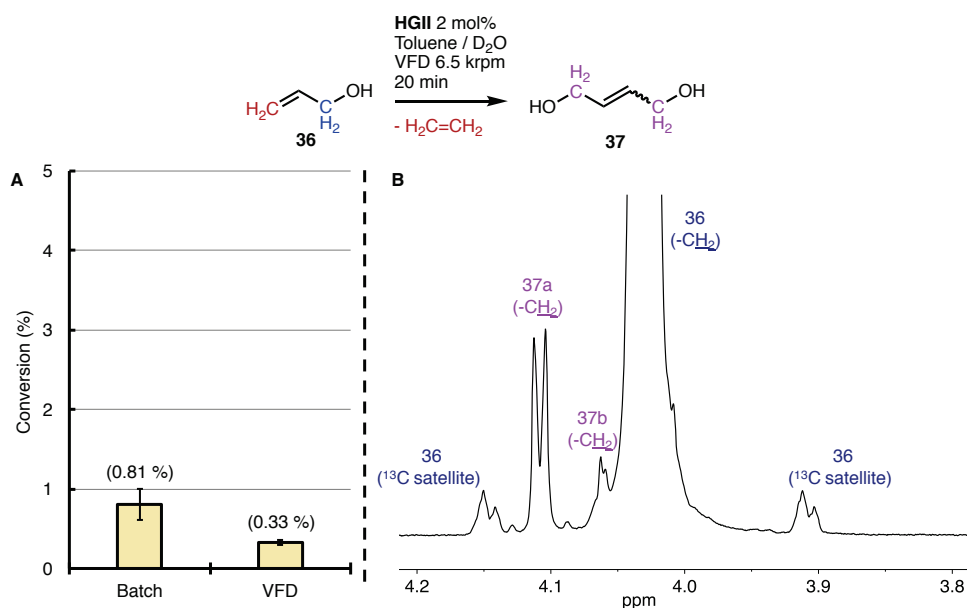


**Figure 33.** Multiphase CM of allyl alcohol. (A) Comparison between batch vs VFD processing, and (B) the  $^1\text{H-NMR}$  analysis, highlighting the overlap observed in the starting material and product peaks when using  $\text{D}_2\text{O}$  solvent.

Due to the low CM activity, difficulties with the  $^1\text{H-NMR}$  analysis and the degree of solubility in the toluene, a new olefin was sought after. It was proposed that the gluconyl-allyl sulphide (**45**) would be a suitable candidate for two main reasons. Firstly, the sugar-based structure would allow maximum solubility in water and reduced solubility in toluene. Secondly, the allyl sulphide moiety could allow for greater conversions, being a privileged substrate for OM.<sup>223</sup> Furthermore, being a sugar-based structure, this work was then hoped to be able to be translated in biochemical OM applications.

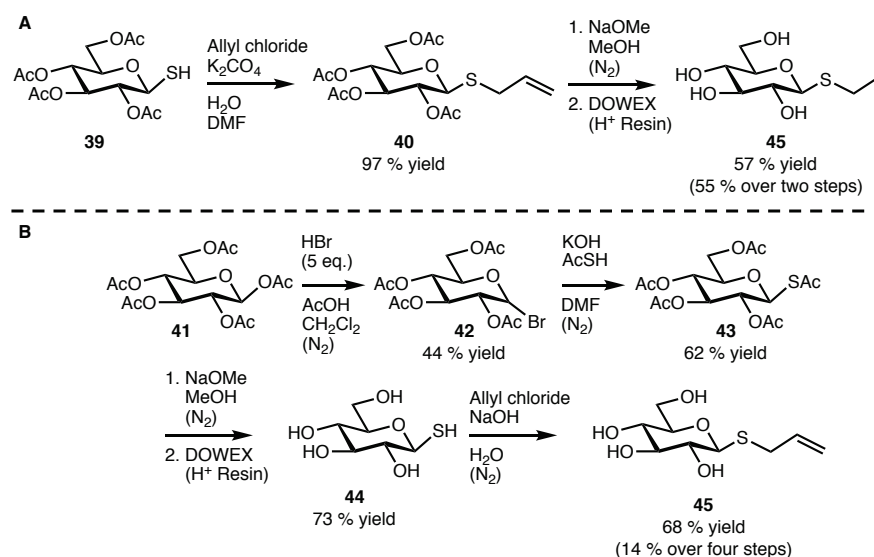


**Figure 34.** Two methods developed for the synthesis of **45**. (**A**) Synthesis in two steps (55 % yield) from 1-thio-β-D-glucose tetraacetate (**39**), and (**B**) Synthesis in four steps (14 % yield) from β-D-glucose pentaacetate (**41**).

The synthesis of this compound was originally proposed over two steps in 55 % yield (Figure 34A), starting from 1-thio-β-D-glucose tetraacetate (**39**). This synthesis gave moderate yield, however difficulties encountered in the purification of compound **46** consumed the limited amount of **39** available. Attempts to improve on the moderate yield of 55 % further consumed the **39**. Thus, a new synthesis from a more readily available source was desired.

Due to the lack of availability and high price of sourcing **39**, a new synthesis was proposed from β-D-glucose pentaacetate (**41**) (Figure 34B). This was achieved in four steps from **41** in a poor yield of 14 %. All of the compounds in both of these procedures were found to be unstable in ambient conditions, and must be stored in a freezer under inert atmosphere. Achieving a poor yield of 14 % is not desirable, and further optimisation of this synthesis is required, but beyond the scope of this Ph.D. For steps 1, 2 and 3,  $^1H$ -NMR analysis of the crude reaction mixture showed high conversions. Thus, the low yield indicates that the improvements can be made in the purification steps. This is made challenging by the fouling that occurs under ambient conditions.

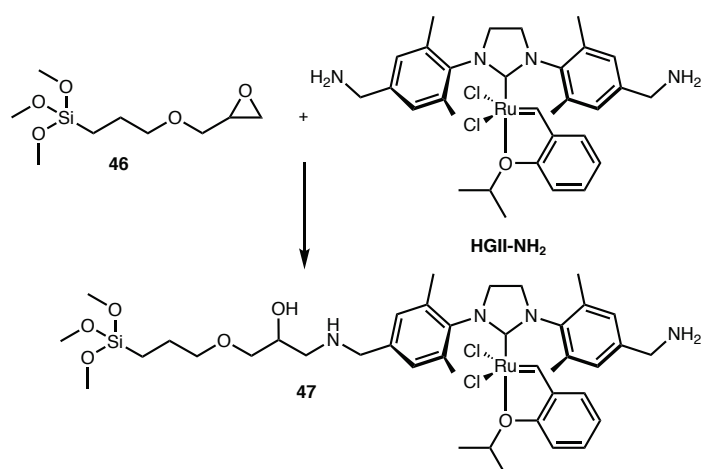


**Figure 35.** Proposed tethering method using catalyst  $HGII-NH_3^+$ . The Silane can be tethered to either the glass VFD tube or to  $SiO_2$  coated nanoparticles (Figure 32).

Catalyst **HGI**- $\text{NH}_3^+$  was identified as a key catalyst to be used in both the multiphase metathesis and the immobilisation (Figure 32). This is due to the primary amine functionality of this catalyst, providing both solubility in water and a target site for tethering. For tethering, the un-hindered primary amines were proposed to be linked through an epoxide, such as **46** (Figure 35). This linker molecule was proposed to form a silane anchoring to either the glass tube or  $\text{Fe}_3\text{O}_4@\text{SiO}_2$ . The pendant epoxide would then be a site for covalent attachment to the amine groups of the catalyst. The ability to tether through the non-labile NHC ligand gives maximum opportunity for the catalyst to be withheld in the tube, lowering the possibility for catalyst leaching. To obtain this catalyst, the synthesis reported by Robinson *et al.*<sup>235</sup> was attempted.

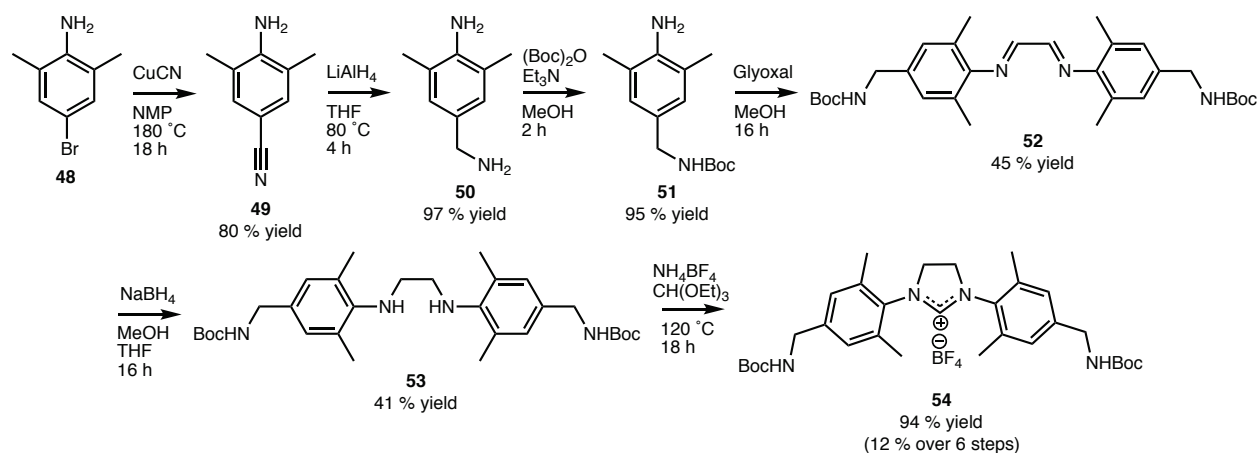
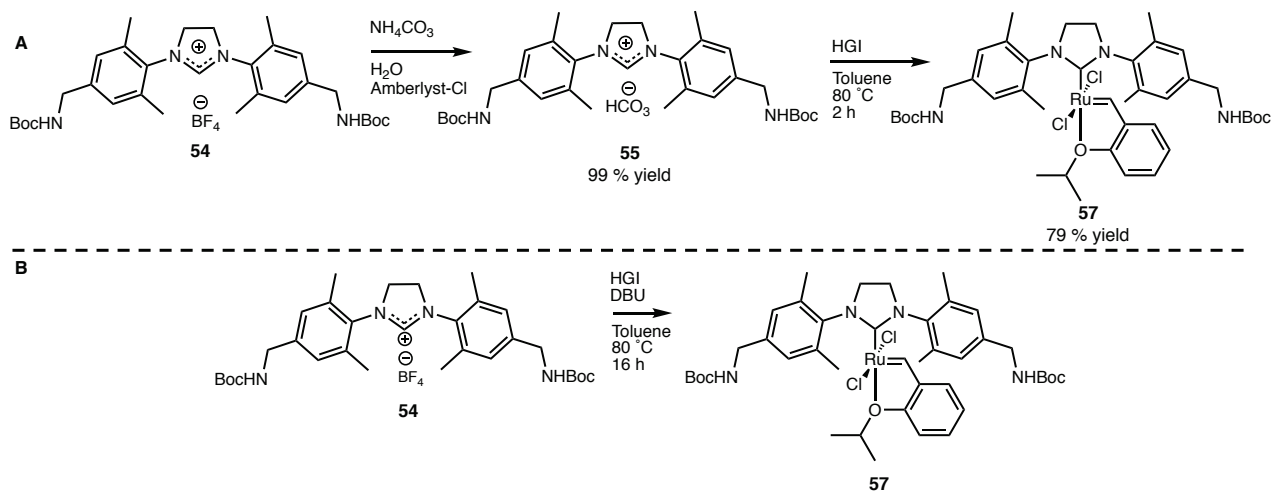


Figure 36. Pathway for the synthesis of the NHC ligand **54** as a tetrafluoroborate salt. This synthesis was adopted from Robinson *et al.*<sup>235</sup>

First, the imidazolium ligand was synthesised (Figure 36). This was achieved over six steps from 4-bromo-2,5-dimethyl aniline (**48**) in 12 % yield. This poor yield is a result of moderate yields in the reductive amination of glyoxal with **51** (45 % in amination & 41% in reduction). Clearly, further work optimising this is needed. Initially, each step gave moderate yields, but tweaking in the work-up from what was published managed to increase the yields on multiple steps in this case. Full optimisation of this synthesis proved to be beyond the scope of this Ph. D. However, over the course of optimising and carrying through each synthesis,  $\approx 4$  g of the imidazolium salt (**54**) was obtained. This was deemed enough to attempt the ligand exchange with catalyst **HGI** (Figure 37).



**Figure 37.** Ligand exchange of the imidazolium salt with the P(Cy)<sub>3</sub> ligand of the catalyst **HGI**. Shown is (A) the literature method from Robinson et.al.,<sup>235</sup> and (B) the exchange facilitated by DBU.

Troubles were also encountered with the ligand exchange. The method from Robinson et.al achieved this in two steps 78 % yield. The hindrance to this ligand exchange is the presence of the imidazolium hydrogen (-N-CH-N-). Ligand exchange with this hydrogen present does not occur. Thus, a base is required to extract this hydrogen. Robinson *et.al.* achieved this over two steps, first performing an ion exchange to replace the tetrafluoroborate anion (**54**) with carbonate (**55**). The carbonate salt is then reacted with **HGI** in toluene at 80 °C for 2 hours. This was reported to give 78 % yield over these two steps, however this was unable to be achieved despite attempts in this study. It was shown that the ion exchange was successful, but the ligand exchange was not found to occur with such conditions. The success of the ion exchange is shown in the <sup>1</sup>H-NMR spectrum, where full consumption the hydrogen of interest observed after the ion exchange. This suggests full consumption of the tetrafluoroborate salt (**54**) had occurred (Figure 38).

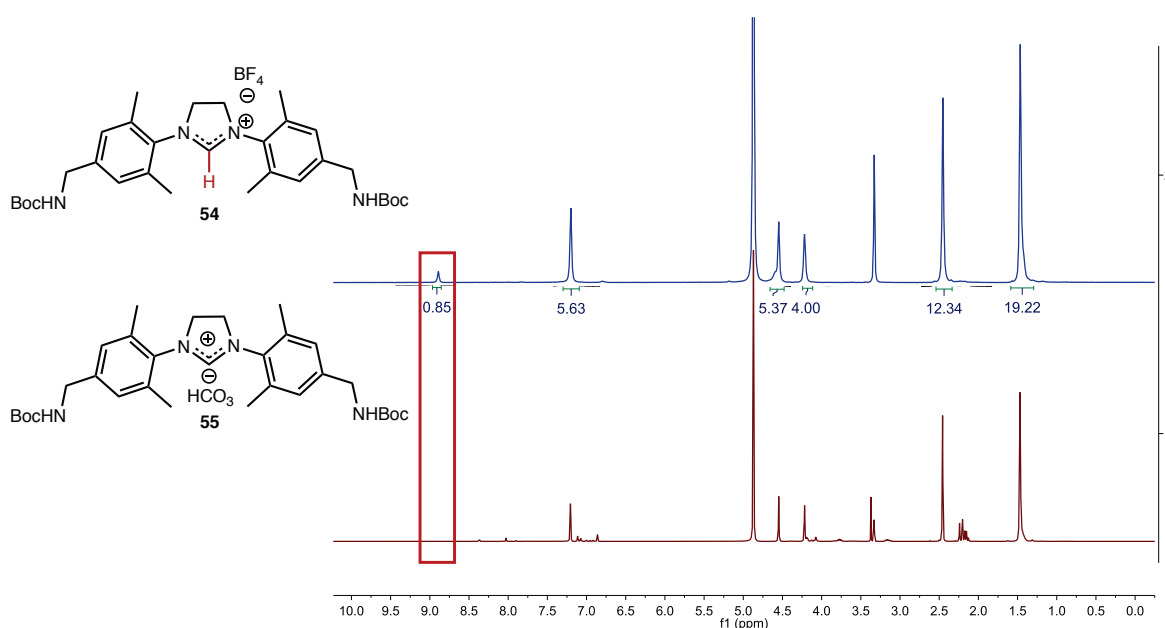


**Figure 38.** <sup>1</sup>H-NMR spectra of the imidazolium salt before and after ion exchange of the tetrafluoroborate (**54**) to the carbonate (**55**). This was performed in a column loaded with Amberlyst resin. Highlighted is the full consumption of the tetrafluoroborate salt proton peak.

Failing this ion exchange, other bases were sought after (Figure 39). Initially, additional carbonate, and also triethylamine were trialed, but to no avail. However, success was found using the base DBU, which successfully extracted this hydrogen and form a salt with the tetrafluoroborate. DBUH<sup>+</sup>/BF<sub>4</sub><sup>-</sup> is a known ionic liquid. Interestingly, it can be easily formed from the room temperature reaction with ammonium tetrafluoroborate. Simply mixing DBU with NH<sub>4</sub>BF<sub>4</sub> forms this ionic liquid, driven by the expulsion of ammonia gas.



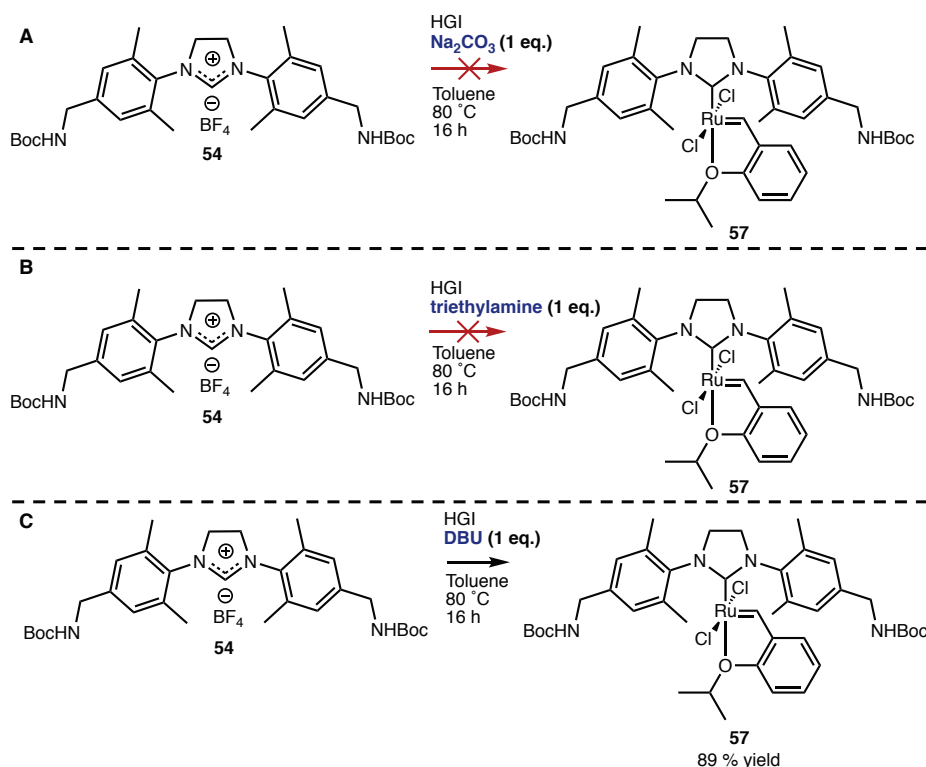


**Figure 39.** Attempts to achieve ligand exchange of the imidazolium to replace the -P(Cy)<sub>3</sub> of catalyst HGI. Various bases trialled were (A) sodium carbonate, (B) triethylamine and (C) DBU. DBU being the only successful base trialled.

The tethering of this catalysts was proposed to be done either directly to the glass surface of the tube, or to MNPs that could then be retained in the tube (Figure 32). Tethering to MNPs has the advantage of simply disposing the powder once the catalysts effective lifetime has been reached, rather than disposing of the entire tube. The MNP's chosen for synthesis were Fe<sub>3</sub>O<sub>4</sub>@SiO<sub>2</sub>. These are well known, robust MNP's with established synthesis and characterisation methods. The method used to synthesis the Fe<sub>3</sub>O<sub>4</sub>@SiO<sub>2</sub> is shown in Figure 40. Firstly, the Fe<sub>3</sub>O<sub>4</sub> magnetite was synthesised using a co-precipitation method using Fe(II)Cl<sub>2</sub> (1 eq.), Fe(III)Cl<sub>3</sub> (1 eq.) with ammonia (8 eq.) as the base. This produced spherical particles ≈ 20 nm in diameter, as determined by AFM. These particles were then isolated and coated in silica, using a reverse emulsion method. For this, micelles of IGEPAL CO-520 were formed in cyclohexane, effectively encapsulating the aqueous components, namely TEOS, base and the Fe<sub>3</sub>O<sub>4</sub>. The spherical encapsulating structures ensure a spherical package of the Fe<sub>3</sub>O<sub>4</sub> particles.

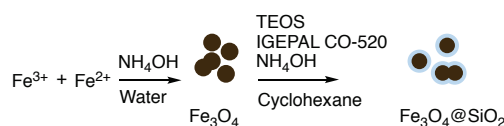


**Figure 40.** Method used for the preparation of Fe<sub>3</sub>O<sub>4</sub>@SiO<sub>2</sub>. This involves co-precipitation to form the Fe<sub>3</sub>O<sub>4</sub> and subsequent silane coating using a reverse-emulsion method.

### 3.3.2 – Summary and Outlook of In-Line Catalyst Separation in VFD Flow

In summary, although the proposed catalyst separation methods were beyond the scope of this Ph.D., the groundwork was placed as feasibility studies for future work. Several issues encountered in the synthesis of **45**, **HGII-N<sub>3</sub><sup>+</sup>** and **Fe<sub>3</sub>O<sub>4</sub>@SiO<sub>2</sub>** were addressed. These were mainly in the work-up procedures, where different volumes were used in the liquid/liquid extraction procedures in order to obtain higher yields. Also, some minor adjustments in the synthesis such as in some cases using longer reaction times to achieve higher yields. This work is vital for demonstrating scalable and sustainable methods for OM applications. It is suggested that the VFD may be able to overcome some of the obstacles prevalent in obtaining **45** and **HGII-NH<sub>3</sub><sup>+</sup>**. Since optimisation is clearly required, the VFD is potentially well suited to solve the issues with the synthesis of these compounds. Examples of this are with the problematic steps, such as the reductive amination of **51** with glyoxal to form the dimer product **52**. The VFD has proven to be beneficial to reactions where a small molecule by-product is driven from the reaction media, thus promoting the equilibrium to favour the reaction products.<sup>146</sup> This principle may well aid in this step as water is a by-product from this reductive amination. However, since methanol is employed as a solvent, which is more volatile than the water, the solvent may be driven off before the water. To account for this, another solvent may be employed, such as tertiary butanol. In such a way, performing this reaction in the VFD in this manor may aid in improving the yield of this problematic step, however optimisation will be required for solvent choice, rotational speed and reaction time. Alternatively, considering the same reaction, the solubility of compound **51** in methanol/glyoxal is somewhat limiting, with concentrations of just 0.73 M employed. The VFD may facilitate the use of a bi-phasic system for this reaction, such as toluene for **51** and water for the glyoxal. Since the VFD is well suited to promote reactions across phase boundaries,<sup>102</sup> it may facilitate this reaction at much higher concentrations compared to what are possible with conventional methods. Again, optimisation would be required, and this work would be directly aided by the development of surface-area-to-volume-ratio calculations proposed in chapter 6.2.

The proposed tethering method using compound **46** was not able to be attempted, and as such optimisation would need to be performed for the reaction conditions. Furthermore, it is possible that the length of the tethering molecule is crucial in ensuring strong attachment without compromising on the activity of the catalyst. Alternative tethering methods to be explored should expand on work by others in the Raston research group, such as Ms Jessica Phillips work tethering the catalyst to cellulose supports within the VFD.<sup>236</sup>

This work shows promise not just for OM, but for the immobilisation of any homogenous catalysts. It is hoped that this work offers alternative methods that can aid in overcoming the issues that plague industrial application of immobilised catalysts.<sup>237</sup> Such as allowing greener solvents that improve workable concentrations, made possible through bi-phasic reactions. Or the high reactive interfacial area for solid supported catalysts within the VFD for continuous flow applications.

### 3.4 – Exploring VFD Enhancement of OM

The following series of experiments initially set out to explore any enhancement of ruthenium-based Grubbs OM catalysts from VFD processing. This hypothesis arose from previous data that suggested for certain catalysts, there was a beneficial reaction conversion using the VFD (Figure 41). The catalyst receiving a boost to conversions from the VFD were **GII** and the o-toluene derivative **G793** (for structures see Figure 19).

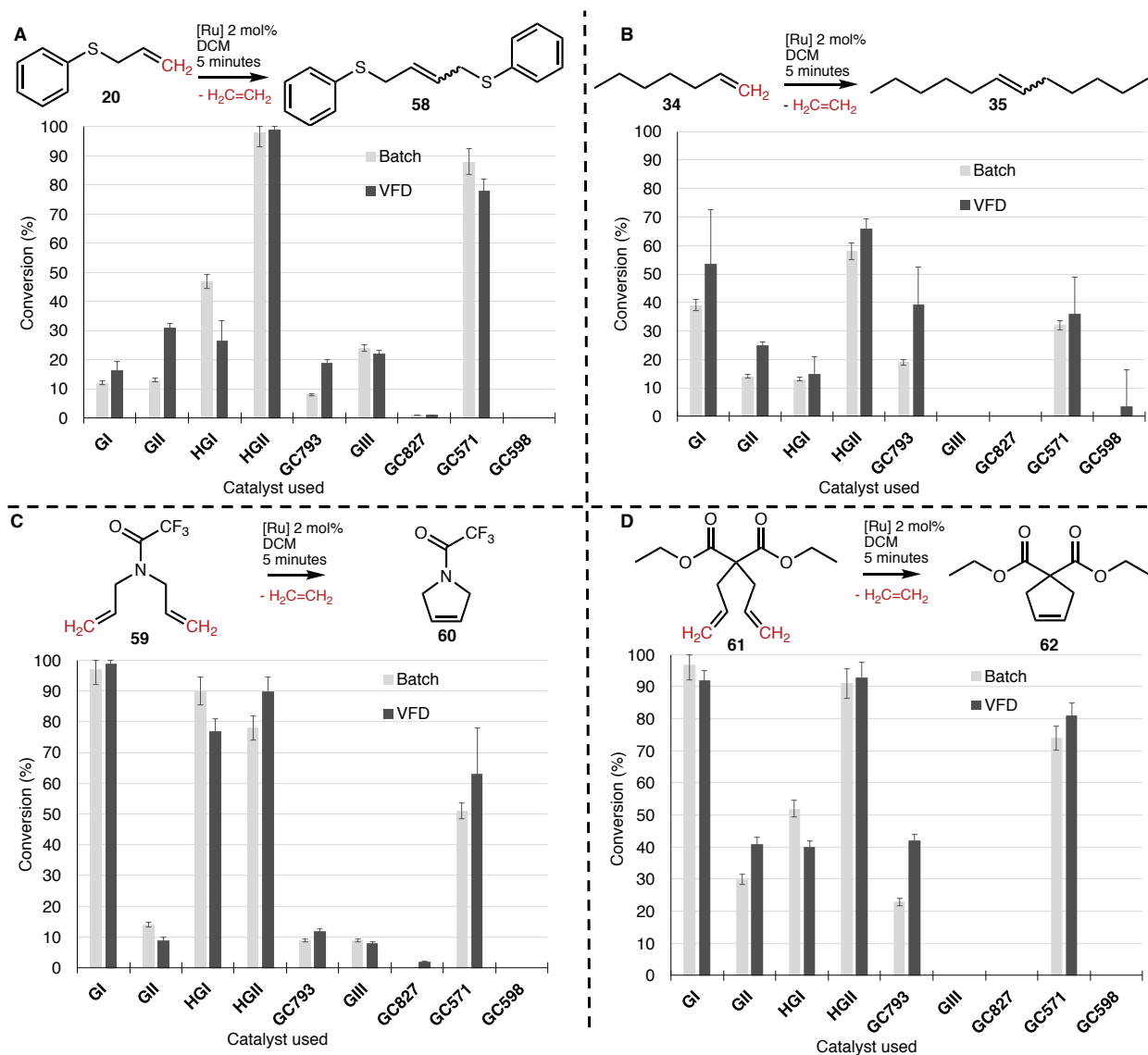


**Figure 41.** VFD and batch comparisons for 9 different catalysts, for the (A) CM of **20**, (B) CM of **34**, (C) RCM of **59** and (D) RCM of **61**. Conversions determined by <sup>1</sup>H-NMR. For catalyst structures, see pg. 50.

### 3.4.1 - Discussion on Exploring VFD Enhancement of OM

It was hypothesised that the VFD may be enhancing the mass transfer of O<sub>2</sub> into the reaction mixture, thus increasing the likelihood of the phosphine ligand to react with O<sub>2</sub> forming the phosphine oxide. This phosphine oxide would be less likely to re-coordinate to the ruthenium centre of the catalyst, thus increasing the amount of **GII**\* - the active catalyst. Figure 42A shows that the activity of **GII** can be increased in the presence of O<sub>2</sub> gas in the VFD over 5 minutes. This is observed when comparing the higher conversion within the VFD with an O<sub>2</sub> atmosphere (24 %) to a N<sub>2</sub> atmosphere within the VFD (5 %) and to an O<sub>2</sub> atmosphere in a stirred vial (6 %). To achieve higher, more workable conversions, the reaction was done over 1 hour (Figure 42B). It is noted that neither reaction went beyond 54 % conversion, and there is no discernible difference between atmospheric gasses of O<sub>2</sub> or N<sub>2</sub>.

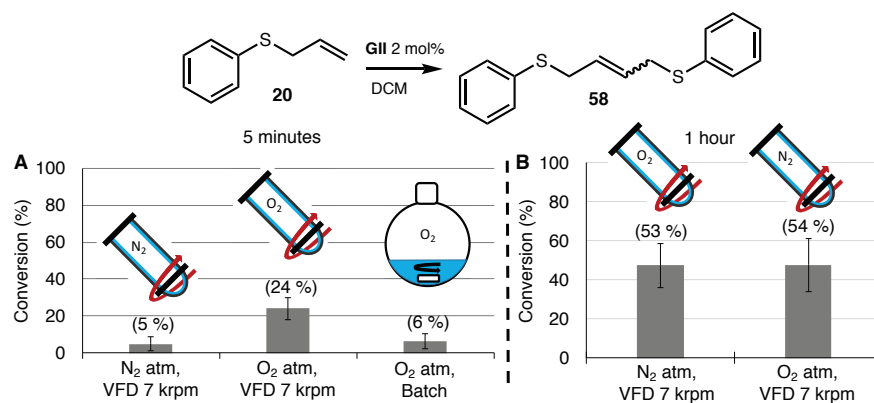


**Figure 42.** The CM reaction of 20, comparing both N<sub>2</sub> and O<sub>2</sub> atmospheres, in VFD at 7 krpm for (A) 5 minutes (also shown is batch control) and (B) for 1 hour.

To address the possibility of extended exposure to oxygen being detrimental to the catalytic activity, the reaction was performed with an oxygen atmosphere for the first 10 minutes only. After the 10 minutes, the O<sub>2</sub> atmosphere was removed by vacuum, and replaced with N<sub>2</sub>. As seen in Figure 43, this promoted a greater conversion (60 %, compared to the 50 % from Figure 42B). However, performing the reaction in a N<sub>2</sub> atmosphere for 10 minutes, and replacing it in the same manner with fresh N<sub>2</sub> showed an even greater increase in conversion (72 %). This set of experiments shows that the reaction may be reaching an equilibrium, where the produced ethene gas is building up within the sealed vessel and forcing the back reaction to consume the products. Removing the atmosphere in such a manner would also remove the ethene gas, thus departing from the equilibrated state, allowing for greater product formation.

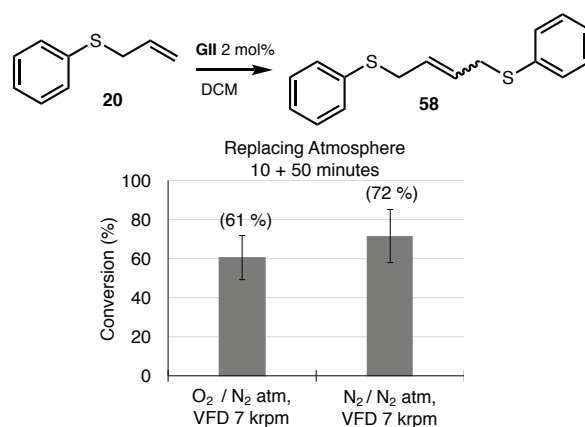


**Figure 43.** The CM reaction of **20**, in the VFD at 7 krpm. Atmosphere maintained for 10 minutes, before being replaced for the remaining 50 mins, for a total reaction time of 1 h.

The E/Z ratio of products **58a** and **58b** were also checked, and found to be unaffected throughout all CM reactions of **20**. As seen in Figure 44, the E/Z ratio was maintained at  $\approx 7.8$  (mean average across all four of the 1 h reactions.)

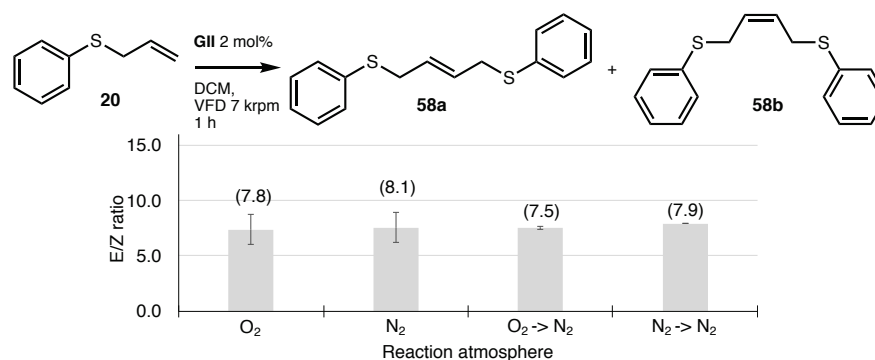


**Figure 44.** E/Z ratio of the CM reaction of **20** in VFD at 7 krpm, after 1 h. Comparisons between various atmospheric compositions are shown. Arrow (->) indicates that at 10 minutes, the atmosphere was evacuated and replaced with a new atmosphere.

With the possibility of CM behaving differently than RCM, being intermolecular and intermolecular respectively, the RCM reaction of malonate **61** was also carried out. As can be seen from Figure 45, the same trends can be observed as for the CM of **20**. That is, there is a slight reduction in conversion for reactions performed in O<sub>2</sub> (74 %) compared with N<sub>2</sub> (84 %). Furthermore, replacing the atmosphere 10 minutes into the reaction will increase the conversion observed after 1 hour.

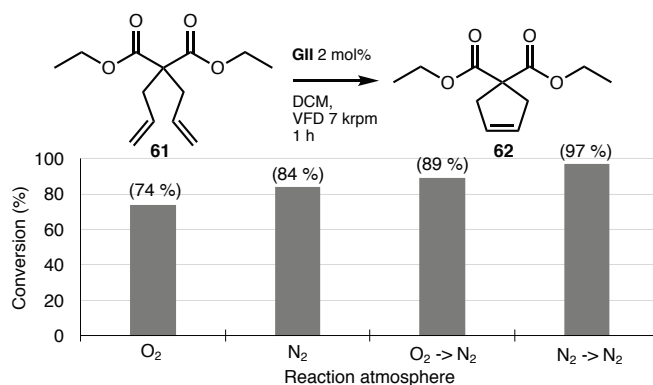


**Figure 45.** The RCM reaction of **61**. Plot showing the reaction conversions after an hour after maintaining atmospheric compositions of O<sub>2</sub> and N<sub>2</sub>, and reactions maintaining the initial atmosphere for 10 mins, then replacing the atmosphere with N<sub>2</sub> for the remaining 50 mins of reaction.

It is noted that throughout the longer experiments, no further evidence for aerobic enhancement of the catalysts can be observed. In account of this evidence, it was deemed necessary to demonstrate the enhanced aerobic-oxidative ability of the VFD, whilst decoupling from the effects of the ethene back-metathesis (ethenolysis) equilibrium. Ideally, a simpler reaction would be a better model to study any aerobic oxidation, and this work was further explored in Chapter - 2. However, attempts were made to decouple the equilibria effects from the enhanced oxidation, due to the importance of the olefin metathesis reaction.

It has been shown in this chapter that the benefits of the VFD are present after 5 minutes, but no longer present after 1 hour. Thus, it was hypothesized that monitoring the experiment over time would identify at what point the VFD is no longer providing any effect on activity. Figure 46 shows both the batch CM of **34** and the RCM of **59** monitored over 10 minutes with CH<sub>2</sub>Cl<sub>2</sub> as the solvent, and **GI** catalyst. Clearly, it can be seen from Figure 46B that the RCM of **59** is complete within 1 minute. Thus, to discern differences in processing this is not an ideal reaction to study. The reaction of **34** fares better for comparing VFD and batch processing (Figure 46A). However, when attempted in the VFD, due to the high volatility of CH<sub>2</sub>Cl<sub>2</sub> solvent, results may be affected by the changing in concentration as the enhanced evaporation of the solvent occurs. Thus, these reactions can't be used for a valid comparison between VFD and batch processing.

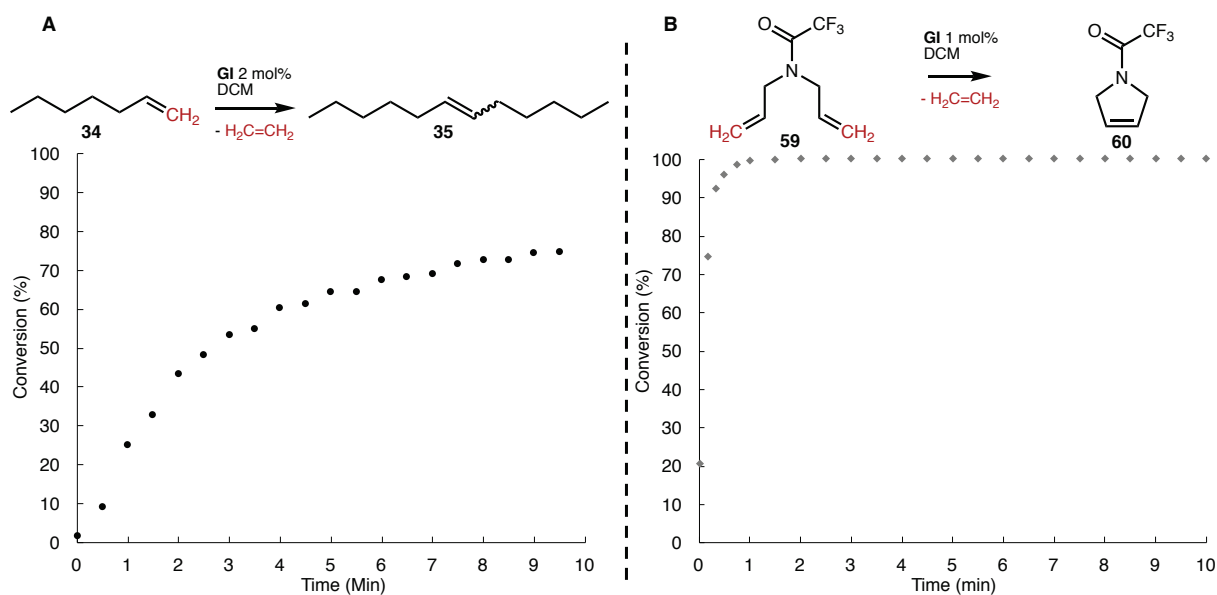


**Figure 46.** Monitoring the activity of catalyst GI in  $\text{CH}_2\text{Cl}_2$  for both the (A) CM of **34** and (B) RCM of **59**. Aliquots were taken at set time intervals and quenched in a solution of **18** in MeCN. Conversion determined by GCMS.

With evaporation of low boiling point  $\text{CH}_2\text{Cl}_2$  within 5 minutes in the VFD, a new solvent was required. Toluene was chosen, being a common solvent for OM applications and being significantly less volatile than  $\text{CH}_2\text{Cl}_2$ . However, Figure 47 shows that the activity of **GI** in toluene is low, as judged by low conversion in 10 minutes, in comparing VFD and batch. This was evident for both of the CM and both the RCM model compounds featuring in the study.

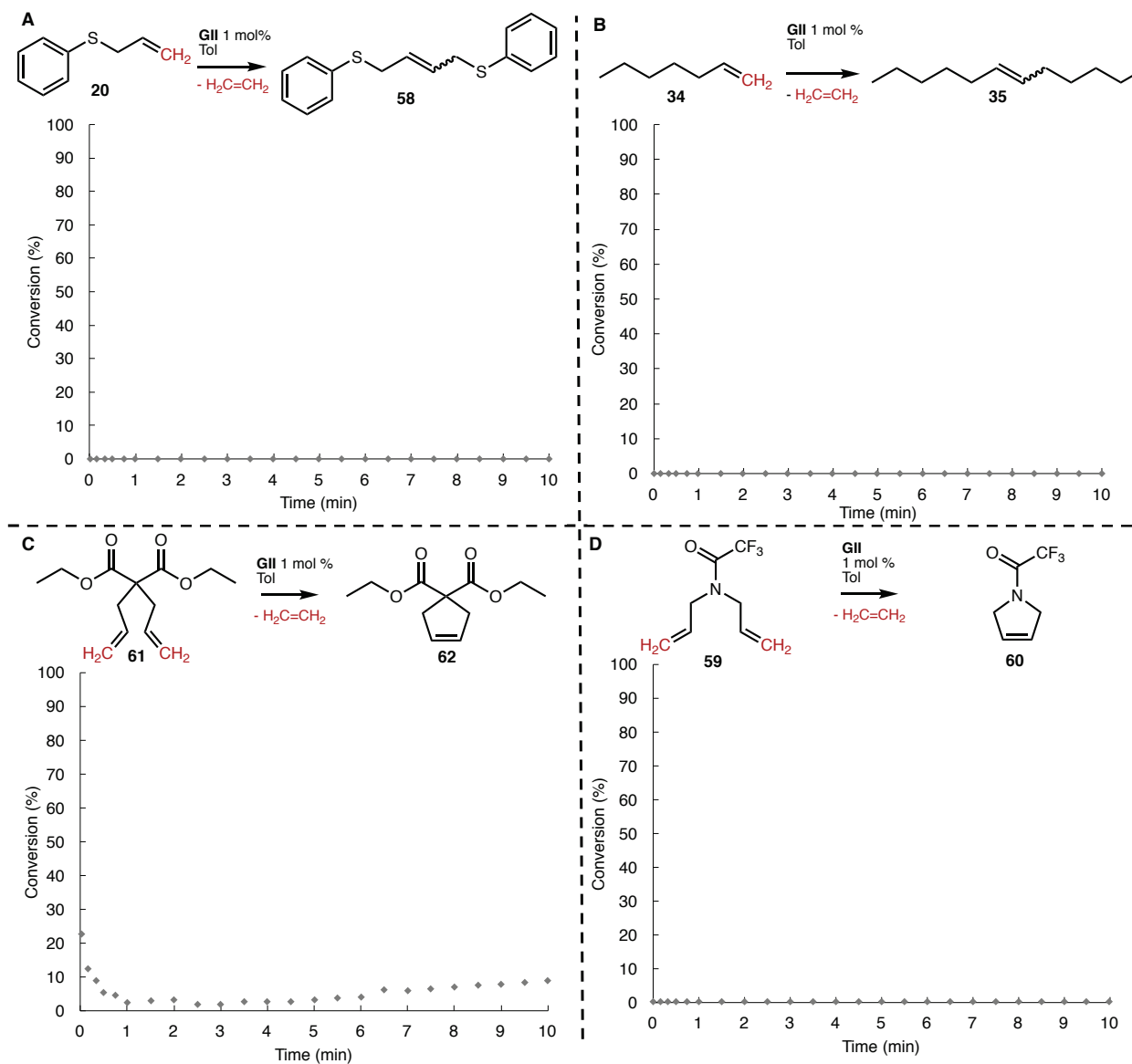


**Figure 47.** Monitoring the activity of catalyst **GII** in toluene for the (A) CM of **20**, (B) CM of **34**, (C) RCM of **61** and (D) RCM of **59**. Aliquots were taken at set time intervals and quenched in a solution of **18** in MeCN before GCMS analysis.

Clearly a new solvent was required, and inspiration was drawn from Skowerski *et al.*<sup>238</sup> Solvents chosen for trialling were two ester solvents, namely dimethyl carbonate (DMC) and ethyl acetate (EtOAc), an ether solvent, 2-methyl tetrahydrofuran (2MeTHF), and a formamide solvent, dimethyl formamide (DMF). The results from these trials can be seen in Figure 48. Note that the data for toluene from Figure 47 is also included. The best performing solvent/reagent system was the RCM reaction of **61** in DMF (82.4 %), and accordingly this was selected for further testing. It is also interesting to note that **20** is the only reagent to result in any significant conversion (22.8 %) after 10 minutes in 2MeTHF. THF in general is known to strongly coordinate to metals, and it is likely that this is why it shuts down the activity of the catalyst for all reactions, the exception being the CM of **20**. This is further evidence that allyl sulphides are privileged reagents for OM, as reported by Chalker *et al.*<sup>223</sup> for aqueous reaction medium. However, the present results suggest that this privilege extends to organic solvents.



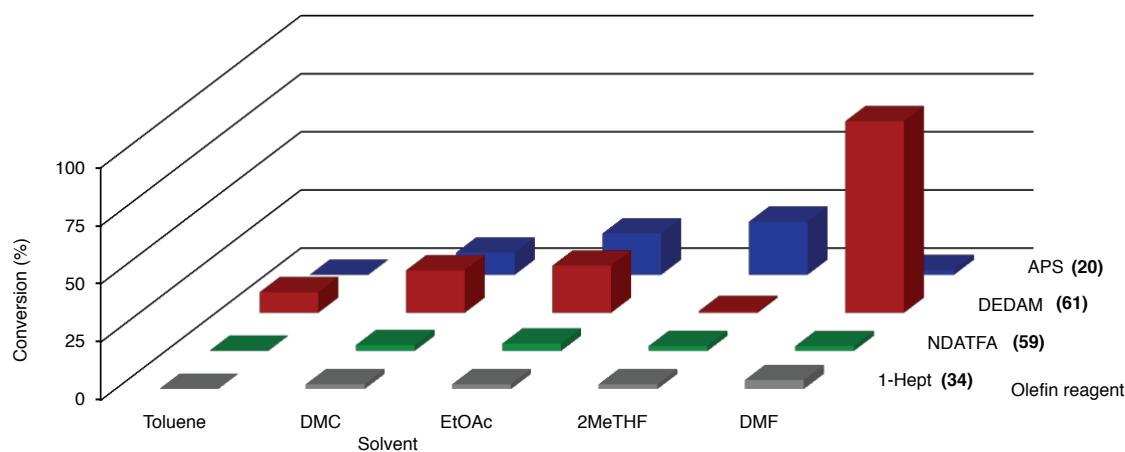


**Figure 48.** The activity of catalyst **GII** after 10 minutes in various solvents for two examples of CM (**20** and **34**) and two examples of RCM (**61** and **59**). Reactions were quenched with **18** in MeCN and conversions were determined by GCMS.

Despite the 82.4 % conversion noted after 10 minutes for the reaction of **61**, with catalyst **GII** in DMF, monitoring this reaction over time (Figure 49A) showed that there was no significant conversion. This is likely due to possible instability of **GII** in DMF, which is supported by a colour change over time (brown → green). With this reaction proving to be ineffective, the next solvent/reagent system chosen was **61** in DMC, as this showed a significant conversion over 10 minutes (18.2 %, Figure 48). Furthermore, DMC is also sufficiently non-volatile for VFD processing (*ie.* It will not evaporate rapidly). However, it can also be seen that this reaction failed to show any significant difference when monitored over time (Figure 49B). The reason why this no longer showed significant conversion is unclear, although it could be instability of catalyst **GII** in either DMC or DMF over time.

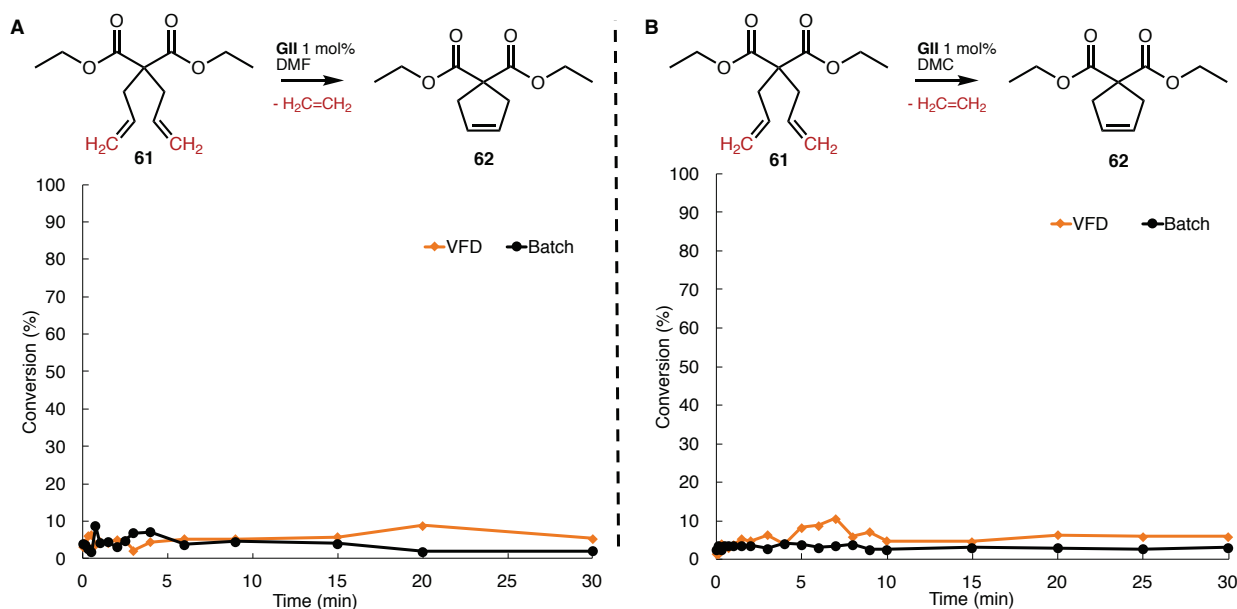


**Figure 49.** Monitoring the activity of **GII** in the catalysis of the RCM of **61**, in solvents of (A) dimethyl formamide (DMF) and (B) dimethyl carbonate (DMC). Comparisons were drawn between batch and VFD 7 krpm processing. Aliquots were taken at set time intervals and quenched in a solution of **18** in MeCN before GCMS analysis.

Regardless of enhanced aerobic oxidation of the phosphine ligand increasing the amount of active catalyst present, it was hypothesised that the shear forces in the VFD may aid in ligand removal, effectively reducing the induction period of the catalyst. This would result in a higher initial conversion in the VFD, and may account

for the results observed in Figure 42A. However, this was tested, with Figure 50 revealing that for catalyst **GI**, the reaction profile remains the same within the VFD as it does for batch.

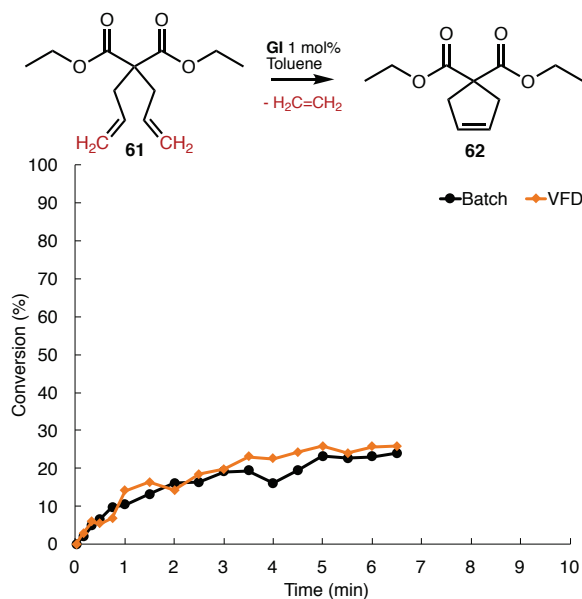


**Figure 50.** Activity of catalyst **GI** in the RCM of **61** in toluene, in VFD and batch. Comparisons were drawn between batch and VFD 7 krpm processing. Aliquots were taken at set time intervals and quenched in a solution of **18** in MeCN before GCMS analysis.

Another experiment that is worth noting was a replicate of the data seen in Figure 50. That is, monitoring the conversion of the RCM of **61** with catalyst **GI** in toluene in VFD versus batch. As can be seen in Figure 51 there is a significant drop in conversion between the 4 minute and 4.5 minute reactions. There was a 1 hour gap between these experiments, and an approximate drop of 1.8 °C in outside temperature (15.7 °C down to 13.9 °C) was recorded during this period. While the internal room temperature was not recorded, there would be some associated drop in the temperature indoors corresponding to the drop observed outdoors. This suggests that the reaction is highly sensitive to small changes in temperature and thus controlling the temperature is necessary. Unfortunately, this is not currently possible to achieve for the most recent version of the VFD. Future experiments should consider running the VFD submerged in a water bath with controlled temperature, to ascertain the effect of small changes of temperature in the liquid in the VFD. This aside, the result suggests that a true monitoring of the conversion over time has not been achieved, with uncontrolled change in room temperature during the different experiments. Thus the samples taken at 10 second reaction time and the 10 minute reaction time could have been performed at different temperatures, and are not truly representative of the reaction profile. Following this observation, it was deemed important to perform all batch and VFD comparisons simultaneously, to minimise any fluctuations in temperature, and also in humidity.

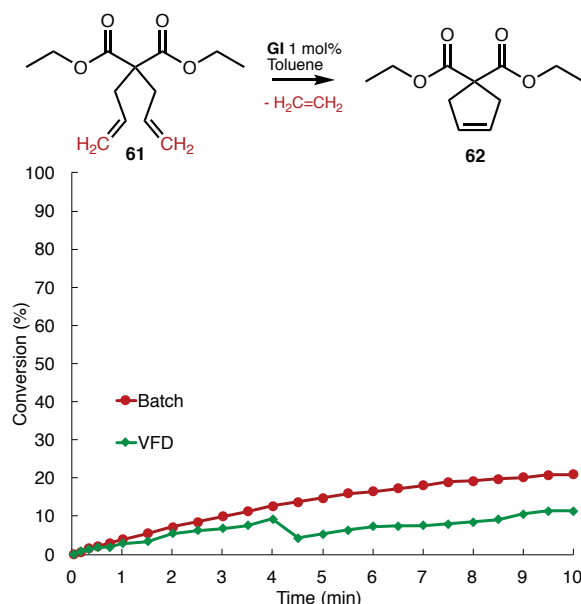


**Figure 51.** Activity of catalyst **GI** in the RCM of **61** in toluene, in VFD at 7 krpm compared to batch. Aliquots were taken at set time intervals and quenched in a solution of **18** in MeCN before GCMS analysis. Note that there was a 1 hour gap between collecting the data points for the 4-minute and 4.5-minute points for the VFD processed reaction. There was also a 1.8 °C drop in outside room temperature recorded in this time.

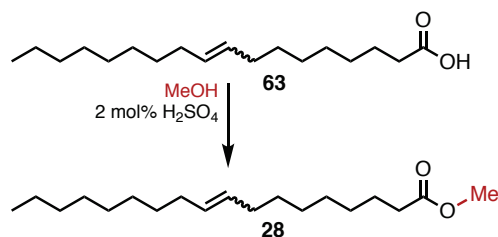
### 3.4.2 – Summary and Outlook of Exploring the VFD Enhancement

This section showed that the VFD enhancement is real for catalyst **GII** and related catalysts containing one phosphine and one isopropoxyl-styrene ligands. However, the extent of the effect of the aerobic oxidation facilitating phosphine ligand dissociation has not been established. Chapter - 2 details how aerobic oxidations are benefited by the VFD, and from these results it is likely that such aerobic oxidation is contributing to this enhancement to some degree. Given that other ill-defined factor(s) contribute to this enhancement, the results are inconclusive, and clearly further work is required to elucidate the origin of the enhancement. A recommended way forward would be to monitor the activity of **GII** over time, as proposed, but with a different substrate or solvent. Such a reaction would need to give enough conversion over a practical time frame for it to be readily quantified, but not too much such that both VFD and batch reactions give the same full conversion.

## 3.5 – Experimental Details and Spectra

### 3.5.1 – Esterification of Oleic Acid to Form Methyl Oleate

Ethenolysis was performed to demonstrate a scalable application, made possible through the unique techniques explored in this study. This was achieved by performing a continuous flow reaction, generating value added chemicals from renewable sources. The renewable source was oleic acid. Oleic acid is commonly found in cooking oils such as olive or canola oil. To allow for high throughput characterisation *via* GCMS, the oleic acid was first converted to methyl oleate through a simple esterification with methanol. Methyl oleate is more volatile, allowing for GCMS analysis.



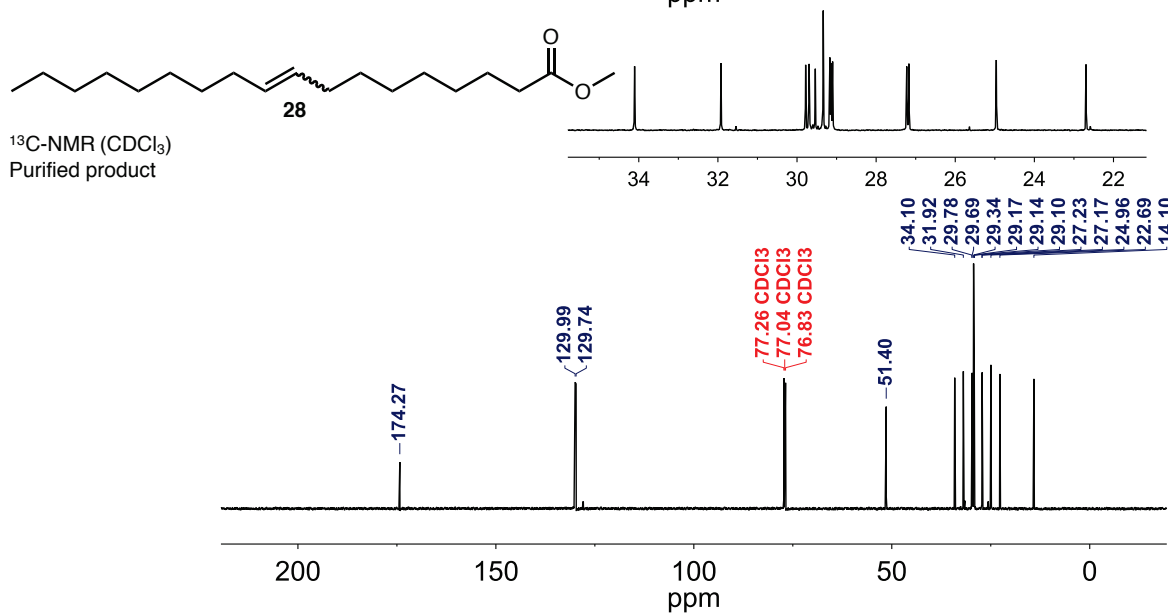
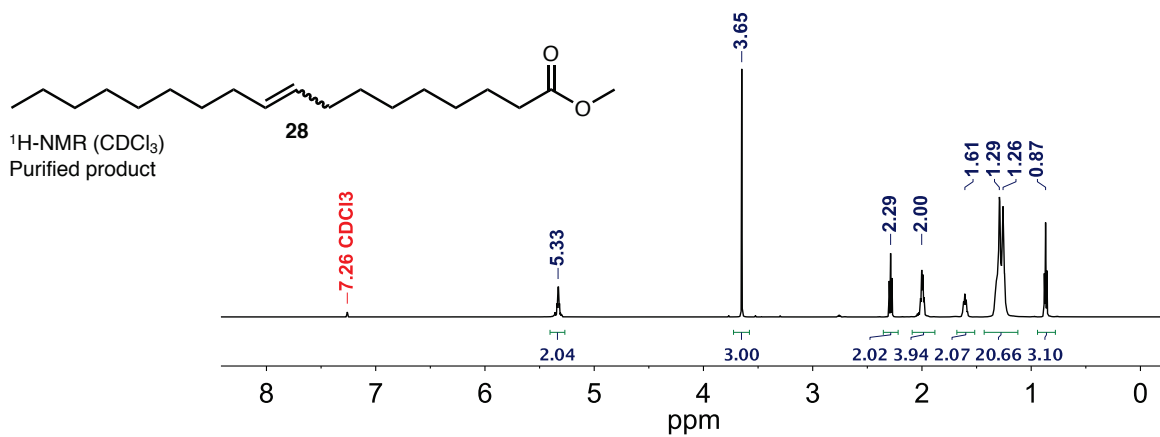
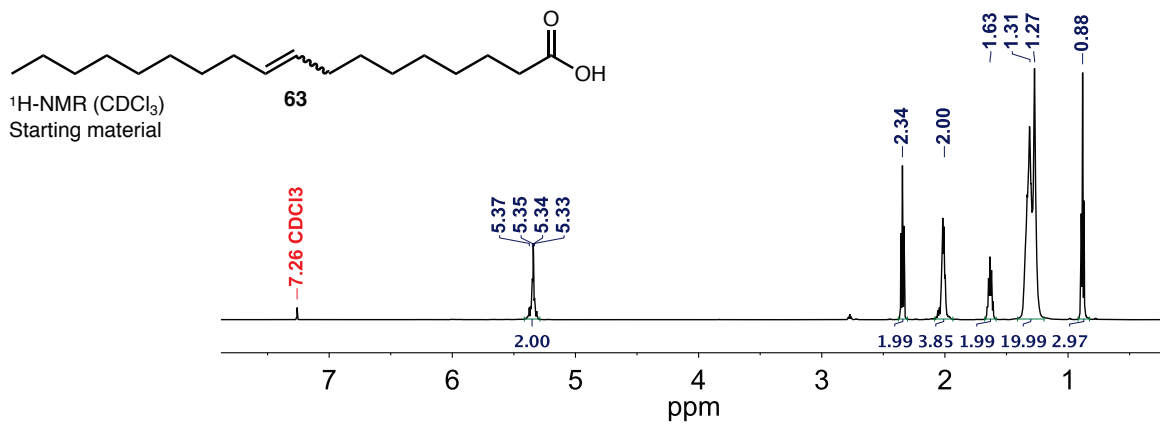
Oleic acid (9 mL, 28.5 mmol) was mixed with methanol (56 mL) and concentrated sulphuric acid (60 mg, 0.61 mmol) and stirred at 60 °C for 12 hours. Crude NMR at this point revealed a conversion from oleic acid to methyl oleate of 94%. The resulting solution was washed with a saturated aqueous solution of NaHCO<sub>3</sub> (2 x 15 mL), followed by washing with water (3 x 15 mL). The remaining solution was concentrated under reduced pressure affording a clear oil that freezes solid less than  $\approx$  20 °C. (8.41 mL, 87% yield). NMR, IR and MS data can be found below.

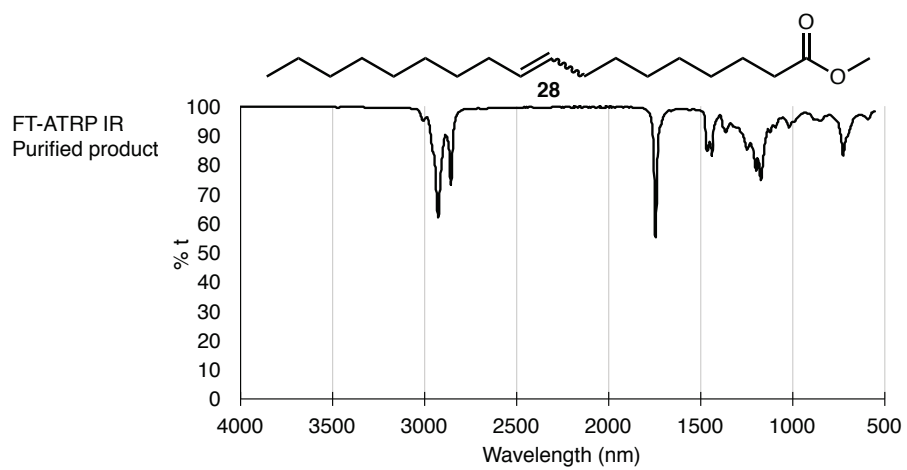
**<sup>1</sup>H NMR (600 MHz, CDCl<sub>3</sub>):**  $\delta_{\text{H}}$  = 5.33 (2H, m, -HC=CH-), 3.65 (3H, s, -COOCH<sub>3</sub>), 2.29 (2H, t, J=8 Hz, -CH<sub>2</sub>COOCH<sub>3</sub>), 2.00 (4H, m), 1.61 (2H, m), 1.26-12.9 (20H, m), 0.87 (3H, t, J = 7 Hz, -CH<sub>2</sub>CH<sub>3</sub>).

**<sup>13</sup>C NMR (600 MHz, CDCl<sub>3</sub>):**  $\delta_{\text{C}}$  = 174.2 (C=O), 129.9 (HC=C'H), 129.9 ((HC=C'H), 51.4, 34.1, 31.9, 29.8, 29.7, 29.5, 29.3, 29.2, 29.15, 29.1, 27.23, 27.17, 24.9, 22.7, 14.1

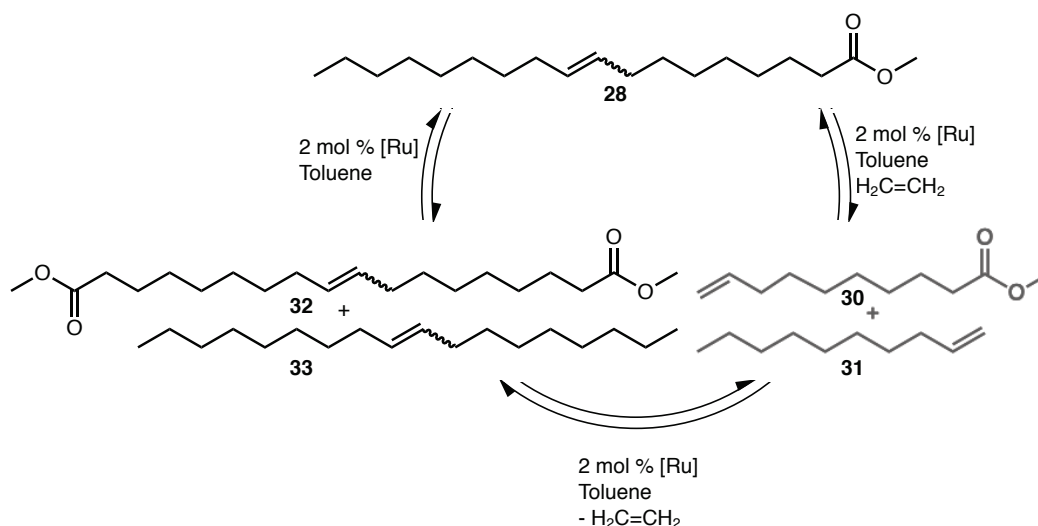
**IR ( $\nu_{\text{max}}$ , liquid ATR):** 3010, 2925, 2855, 2877, 1745, 1465, 1435, 1360, 1240, 1200, 1170, 1010, 880, 860, 725, 590

**LR-MS:** 297 m/v [M+H]<sup>+</sup>.



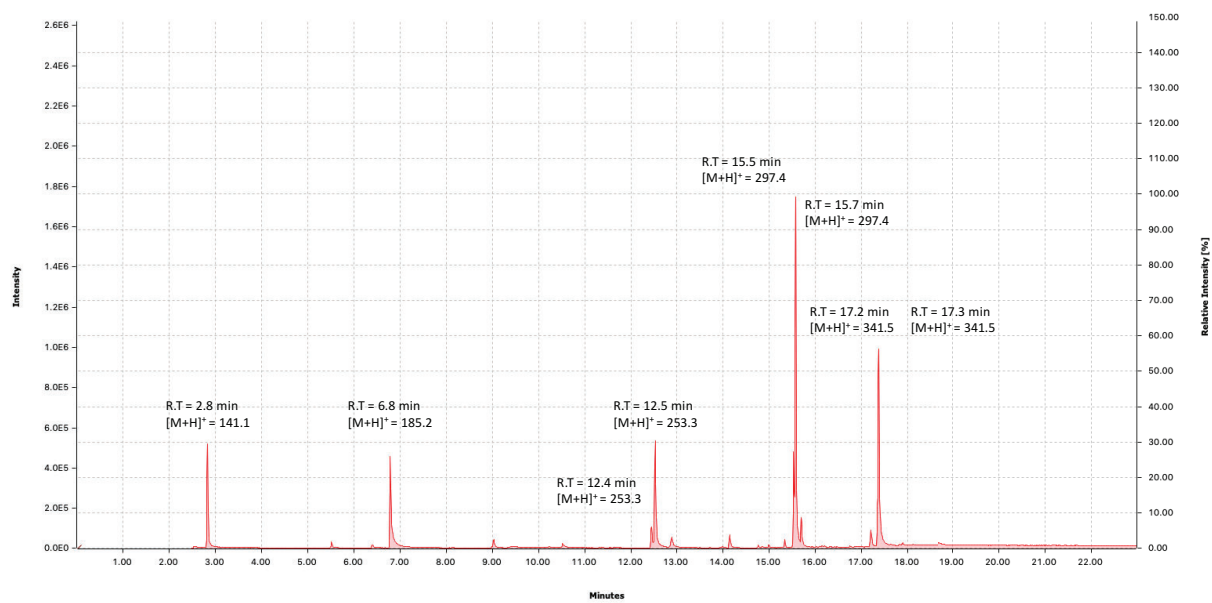


### 3.5.2 – Ethenolysis of Methyl Oleate



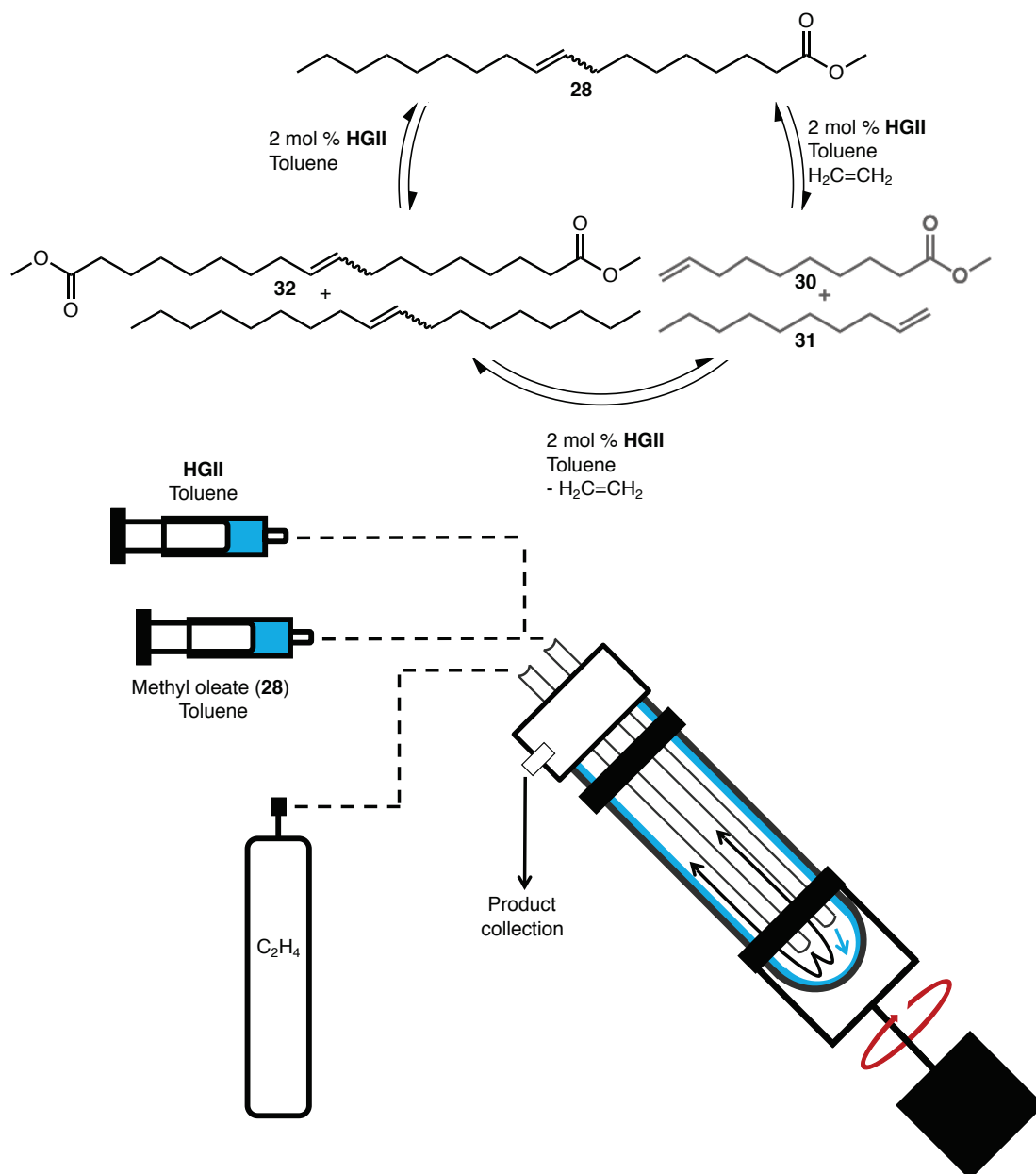
VFD experiments were performed first to establish optimal parameters before moving to continuous flow. The following procedure was employed. The atmosphere within two 20 mm (OD) VFD tubes was evacuated and then filled with ethene gas. The catalyst **GI** (4 mg,  $4.86 \times 10^{-3}$  mM) was weighed into a vial, and dissolved in toluene (2 mL). In a separate vial, methyl oleate (73 mg, 0.24 mM) was diluted in toluene (2 mL). Half of each solution (1 mL each) was added to each of the 2 VFD tubes, with the **28** solution added first followed by the catalyst solution. During which time an ethene atmosphere was maintained *via* balloons filled with ethene. One tube was magnetically stirred at  $\approx 300$  rpm, and the other tube was operated in the VFD at 7 krpm. After 30 minutes of reaction time, a solution of N-acetyl-L-cysteine in MeCN (1 mL, 0.12 M) was added to quench each reaction. Following this, each reaction mixture was diluted in CHCl<sub>3</sub> for GCMS analysis. In the GC trace, all 5 compounds could be accounted for, confirmed by the MS which showed the corresponding m/z of the molecular ions. The integrations of the peaks in the GC trace were used to calculate the % conversions. A representative GCMS spectrum can be found below.

The method for the GCMS was as follows. Injection port temperature was set to 250 °C. The column oven was held at 100 °C for 2 minutes, before ramping to 200 °C at 10 °C/min, then the temperature was ramped to 300 °C at 20 °C/min and held at 300 °C for 5 minutes. The MS operated with a mass detection range from 50 to 600 m/z.



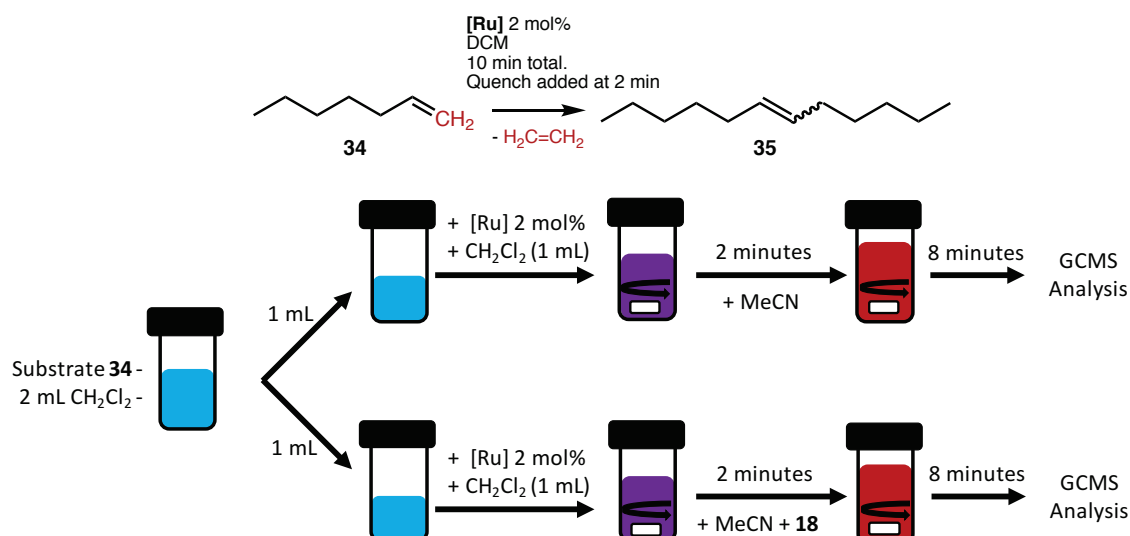


### 3.5.3 – Continuous Flow Ethenolysis



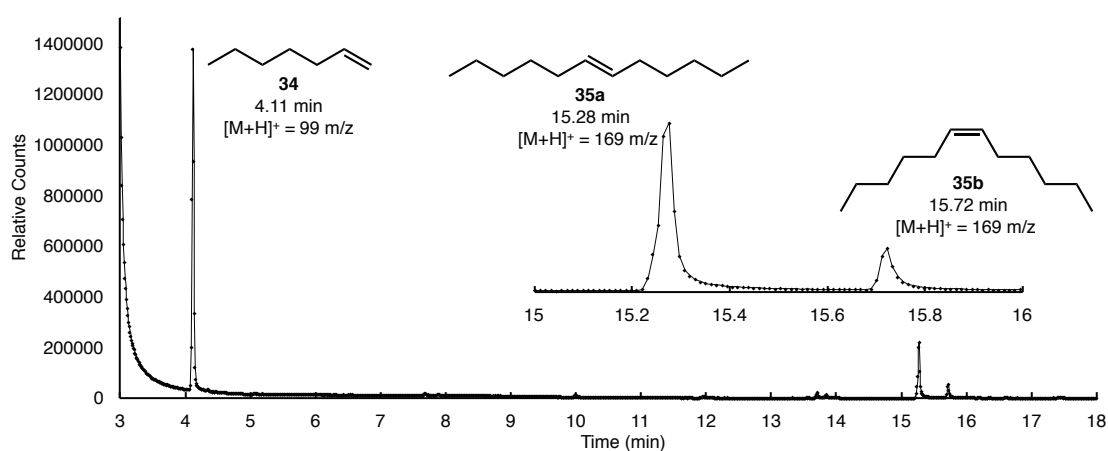
To demonstrate scalability, ethenolysis was performed in the continuous flow mode of operation of the VFD. The following method was employed. Two syringe pumps were set up to inject two separate solutions. In one syringe was a solution of catalyst **HGII** (9 mg,  $1.44 \times 10^{-5}$  mol, 1.59 mM) in toluene (9 mL), and in the other syringe was a solution of methyl oleate (212 mg,  $7.13 \times 10^{-4}$  mol, 79.2 mM) in toluene (9 mL). Each syringe was set to deliver their contents to the base of the rotating tube, each at a flow rate of 0.05 mL/min, giving a total flow of 0.1 mL/min. Simultaneously, ethene gas was flowed through a stainless-steel jet feed to base of the tube. This was delivered at  $\approx 0.5$  L/min for the duration of the experiment, maintaining an atmosphere of ethene at  $\approx 1$  atm. The product solution was collected into a pre-made quenching solution of 18 in MeCN (10 mL, 0.12 M). During the course of the reaction, the collection vial was replaced every 30 minutes, resulting in 6 fractions being collected. These 6 fractions were then analysed *via* GCMS. The first fraction (collected in the first 30 minutes) was omitted, because a steady state of flow had not been reached. From the final 5 fractions, the integrations in the GCMS trace were used to determine the conversions.

### 3.5.4 - CM of **34**, Establishing Quench of **18** + MeCN

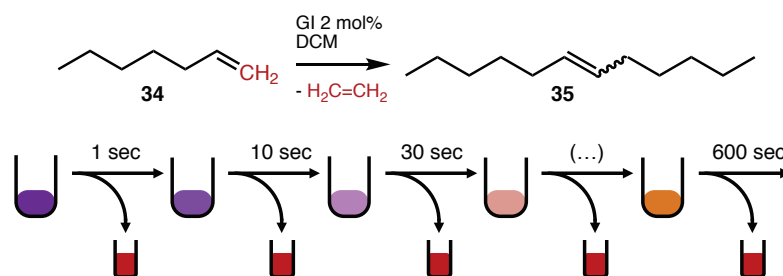


A solution of **34** (50 eq. relative to catalyst (depending on Mw of catalysts)) was dissolved in  $\text{CH}_2\text{Cl}_2$  (2 mL). Half (1 mL) of this solution was transferred into a new, separate vial, creating two separate *vials* with identical contents. To each of these vials, 1 mL of a  $\text{CH}_2\text{Cl}_2$  solution of catalyst (2 mg/mL) was added. Both solutions were stirred at room temperature. After 2 minutes of reaction time, a solution of **18** in MeCN (1 mg in 250  $\mu\text{L}$ ) was added to one vial, and MeCN (250  $\mu\text{L}$ ) was added to the other. Both solutions were stirred for a further 8 minutes. After this, small aliquots were taken and dissolved in chloroform for GCMS analysis. GCMS was then performed, and conversions were calculated from the ratios of the integrals of the starting material and the final product. Results, shown in figure below, show that MeCN has quenching properties, but when combined with **18** is a more efficient quenching solution for Grubbs-type OM catalysts. GCMS method is detailed below, along with a representative GC trace.

For GCMS, injection port temperature was set to 250 °C. The column oven was held at 100 °C for 2 minutes, before ramping to 200 °C at 10 °C/min, then the temperature was ramped to 300 °C at 20 °C/min and held at 300 °C for 5 minutes. The MS operated with a mass detection range from 50 to 600 m/z.

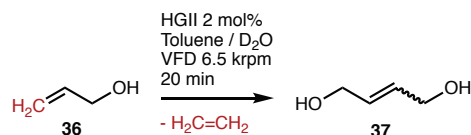


### 3.5.5 - Monitoring Conversion of **34** CM Over Time, Quench vs No-Quench

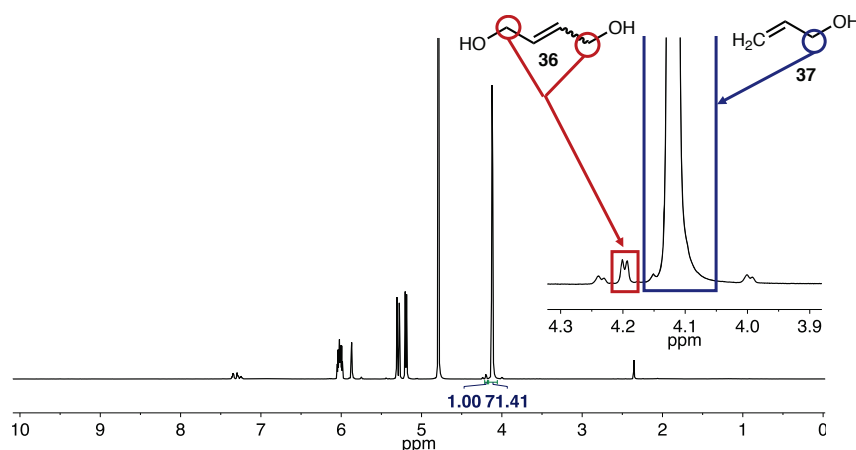


The following experiment was performed to monitor the reaction of **34** with the **GI** catalyst over time, and to monitor the quenching ability for the solution of **18** in MeCN. Firstly, a quenching solution was prepared by dissolving **18** (400 mg, 2.43 mmol) in MeCN (20 mL) creating a 20 mg/mL (0.122 M) solution. *NB* sonication was employed to aid in solvation. Secondly, a series of 24 GCMS vials were prepared with 1.25 mL of  $\text{CHCl}_3$  and 100  $\mu\text{L}$  of the quenching solution. For the reaction solution, the catalyst **GI** (10 mg,  $1.22 \times 10^{-5}$  mol, 2 mol %) was weighed in a glass vial and dissolved in 10 mL of  $\text{CH}_2\text{Cl}_2$ . To this solution, **34** (85  $\mu\text{L}$ , 0.6 mmol) was added. A 250  $\mu\text{L}$  aliquot of the reaction solution was taken and placed in one of the **24** pre-made quench solutions. At set time intervals of 1, 10, 20, 30, 45, 60, 90, 120 and then every 30 seconds until 600 seconds. GCMS was then performed on these samples, and conversions were calculated from comparing the integrations of the peaks corresponding to the two E & Z isomer products (**35a** & **35b**) with the starting **34**.

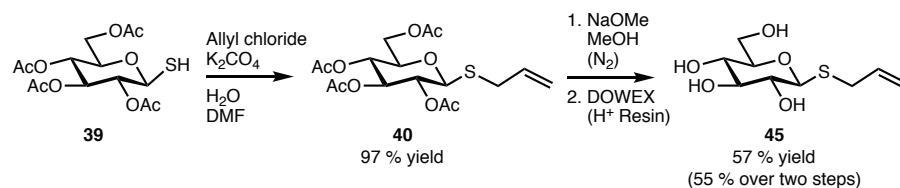
### 3.5.6 – Biphasic CM of Allyl Alcohol



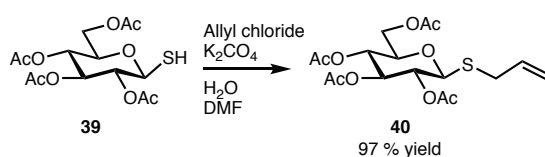
Batch vs confined mode VFD comparisons were performed using the following procedure. The catalyst **HGII** (4 mg,  $6.4 \times 10^{-6}$  mol) was dissolved in toluene (2 mL). To a separate vial, allyl alcohol (21  $\mu$ L,  $3.1 \times 10^{-4}$  mol) in D<sub>2</sub>O (2 mL). Half (1 mL) of each solution were then transferred into two separate 20 mm (OD) VFD tubes. A magnetic stirrer bar was used to stir one of these reaction mixtures for 20 minutes at room temperature. Simultaneously, the other tube was operated in the VFD at 6.5 krpm for 20 minutes at room temperature. Upon reaching the desired time, both reaction mixtures were halted, and the aqueous phase was removed by pipette for NMR analysis. Conversions were determined by comparing the integration of the peaks corresponding to the allylic  $-H_2COH$  hydrogen nuclei, noting that there are two contributing H nuclei for each molecule of starting material, compared to four in each of the products. Representative <sup>1</sup>H-NMR spectra can be found below. Note that monitoring the conversion of the CM of allyl alcohol in D<sub>2</sub>O is not ideal as there is overlap between the peaks of the starting material and the two products.



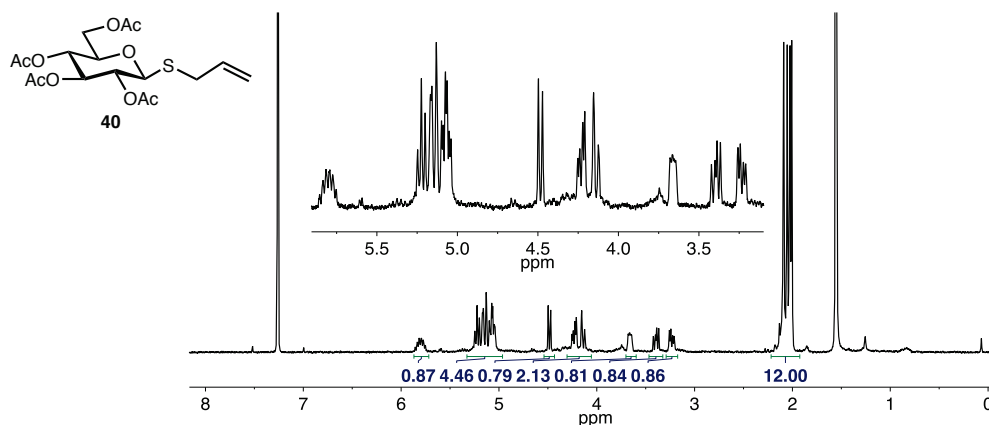
### 3.5.7 – Synthesis of Substrate 45 from 1-thio-β-D-glucose tetraacetate (39)

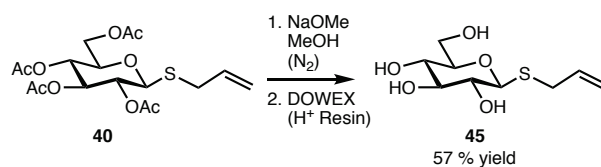


In order to obtain an olefin that is soluble in water, compound **45** was targeted for synthesis. This compound is not only soluble in water, it also bears an allyl sulphide moiety – a privileged substrate for OM. Furthermore, the glycosylic structure is desirable for site selective OM modifications in bio-chemistry. Using a procedure adapted from J. Chalker et al.<sup>222</sup> Compound **45** was prepared from 1-thio-β-D-glucose tetraacetate (**39**) in two steps in a total yield of 55%.



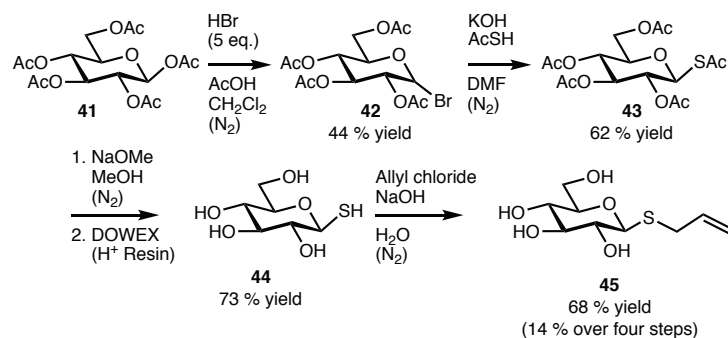
Alkylation of the thiol was performed using the following method. In a vial, 1-thio-β-D-glucose tetraacetate **39** (200 mg, 0.55 mmol) and K<sub>2</sub>CO<sub>3</sub> (76 mg, 0.55 mmol) were dissolved in DMF (2 mL). This was stirred at room temperature for 10 minutes before the addition of allyl chloride (134 μL, 1.65 mmol). This was then stirred for a further 24 hours. Removal of the solvent and remaining allyl chloride under reduced atmosphere resulting in an off-white solid. Re-crystallisation from CH<sub>2</sub>Cl<sub>2</sub>/hexane yielded **40** as a white solid (217 mg, 97 %).



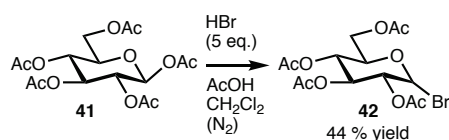


The de-acylation was performed in the following procedure. In a flame-dried vial, **40** (167 mg, 0.42 mmol) and NaOMe (24 mg, 0.44 mmol) was dissolved in MeOH (anhydrous, 2 mL). This was stirred at room temperature for 2 hours. Following this, the reaction was quenched by the addition of solid acid resin beads (DOWEX-50WX8 H<sup>+</sup>, added until neutral pH was achieved). The resin beads were then filtered off and washed with MeOH. This filtrate was then concentrated under reduced pressure yielding off-yellow oil. Recrystallizing from MeOH gave white crystals (55.61 mg, 57 %).

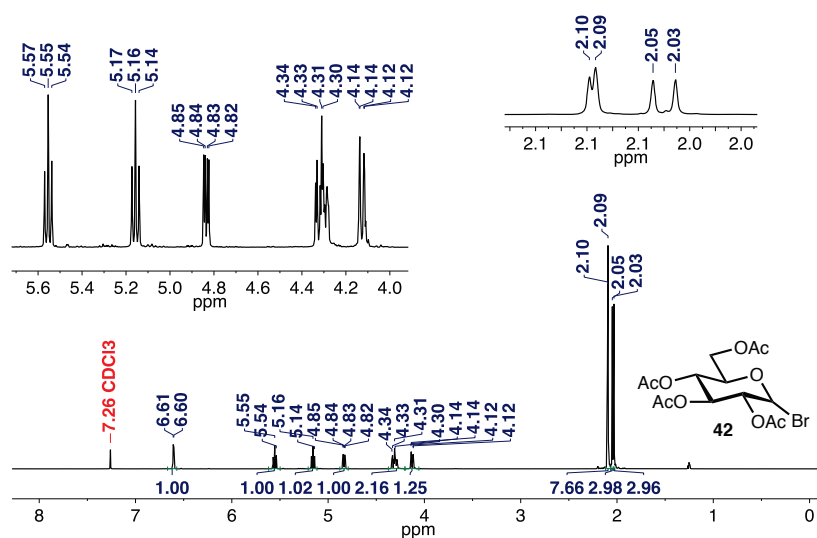
### 3.5.8 - Synthesis of Substrate 45 from $\beta$ -D-glucose pentaacetate (41)

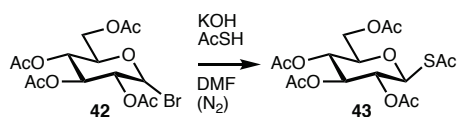


An alternate synthesis was required due to the difficulties sourcing 1-thio- $\beta$ -D-glucose tetraacetate (39). Using a procedure adapted from J. Chalker et al.<sup>222</sup> Compound 45 was prepared in 4 steps in a total yield of 14 %.



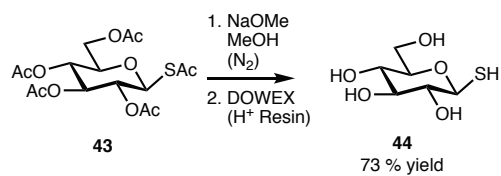
In a flame dried flask with an inert  $\text{N}_2$  gas atmosphere, compound 41 (20 g, 53.4 mmol) was dissolved in  $\text{CH}_2\text{Cl}_2$  (160 mL). To this, a solution of HBr (46 mL, 33 wt %, 254 mmol) was added and the reaction mixture was stirred under inert atmosphere for 2 hours. Upon reaching desired reaction time, the solution was poured into ice ( $\approx 100$  g). Once ice had melted at room temperature, the aqueous solution was washed with EtOAc (3x 100 mL). The combined organic layers were then combined and washed with a saturated aqueous  $\text{NaHCO}_3$  solution (2x 100 mL) followed by brine (2x 100 mL). The organic solution was then dried ( $\text{MgSO}_4$ ) and filtered, before solvent was removed under reduced pressure. The product was then recrystallized from EtOAc/hexane to yield a colorless crystalline solid. (9.69 g, 44 %). Note that this product is not stable in air and must be stored in a freezer under inert atmosphere ( $\text{N}_2$  gas).



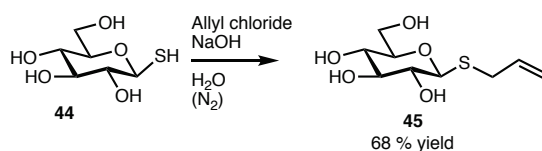


A solution of HSAc (2 mL, 29.1 mmol) and KOH (1.36 g, 24.3 mmol) in DMF (30 mL) was stirred over ice under an inert atmosphere (N<sub>2</sub> gas) for 15 minutes. Once KOH was in solution, compound **42** (2 g, 4.86 mmol) was added. Reaction mixture was stirred at room temperature under inert atmosphere for 16 h. Following this, the reaction mixture was diluted in EtOAc (≈ 100 mL) and washed with a saturated aqueous NaHCO<sub>3</sub> solution (2x 100 mL) followed by brine (2x 100 mL). The organic layer was then dried (MgSO<sub>4</sub>), filtered and solvents were removed under reduced pressure. The resulting product was recrystallized from CH<sub>2</sub>Cl<sub>2</sub>/hexane to produce a white crystalline solid (1.225 g, 62 %).



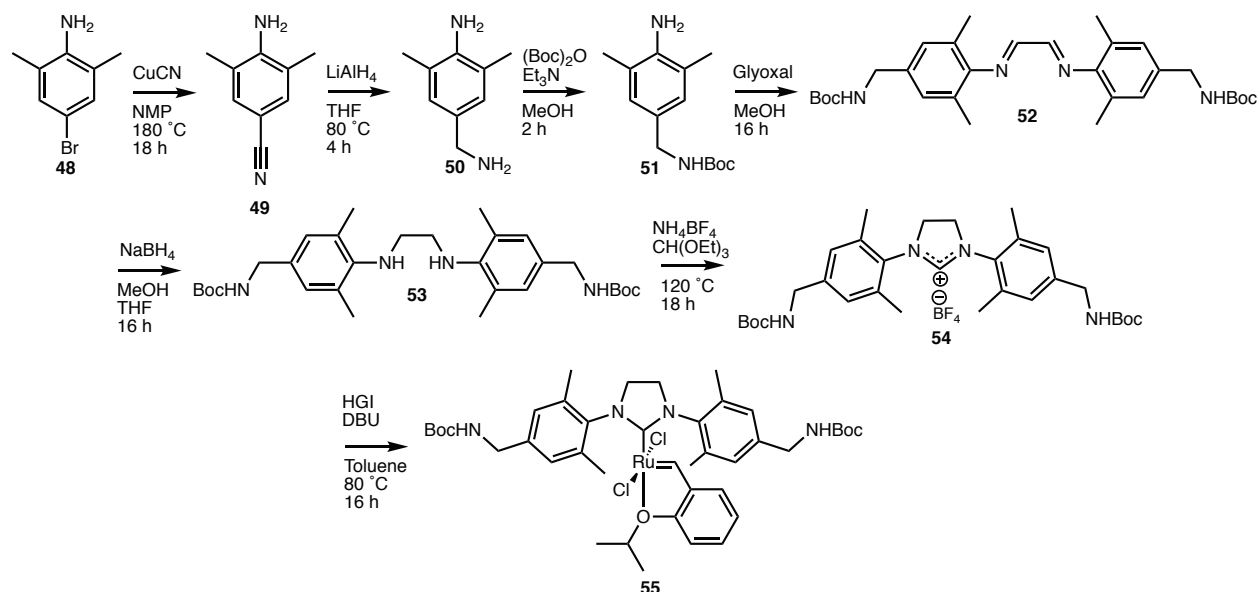


To a flame dried flask under an inert atmosphere (N<sub>2</sub>), compound **43** (1 g, 2.46 mmol) was dissolved in MeOH (anhydrous, 20 mL). Following this was the addition of NaOMe (560 mg, 10.4 mmol). This reaction mixture was stirred under inert atmosphere for 2 hours. This reaction was quenched by the addition of solid acid resin beads (DOWEX-50WX8 H<sup>+</sup>, added until neutral pH was achieved). The resin beads were then filtered and washed with MeOH. This filtrate was then concentrated under reduced pressure, yielding off-yellow oil. Recrystallizing from MeOH gave white crystals (381 mg, 73 %)

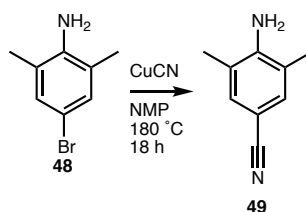


Alkylation of the thiol was performed using the following procedure. Under an inert atmosphere (N<sub>2</sub> gas), compound **44** (169 mg, 0.86 mmol) was dissolved in a de-gassed solution of NaOH (4 mL, 0.12 M Aq.). This was stirred for 20 minutes at room temperature. Following this, allyl chloride (350 μL, 4.3 mmol) was added and the solution was stirred vigorously for 6 hours at room temperature. The reaction mixture was concentrated under reduced pressure. Following this, column chromatography was performed with a mobile phase of 10 % MeOH in EtOAc. Removal of solvent under reduced pressure yielded white solid (118 mg, 68 %).

### 3.5.9 - Synthesis of Catalyst HGII-NH<sub>3</sub><sup>+</sup>



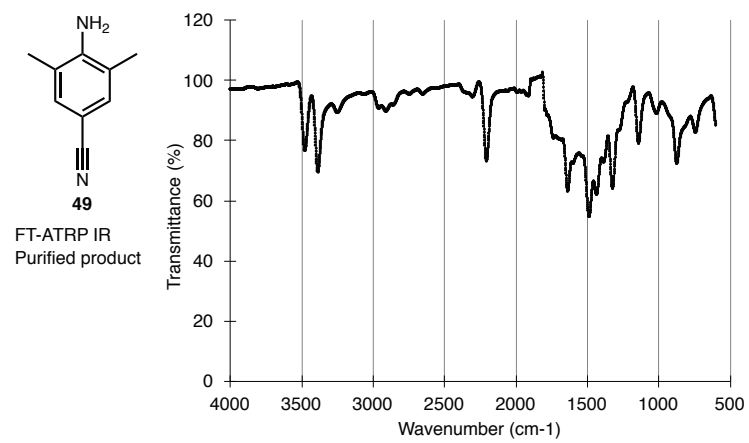
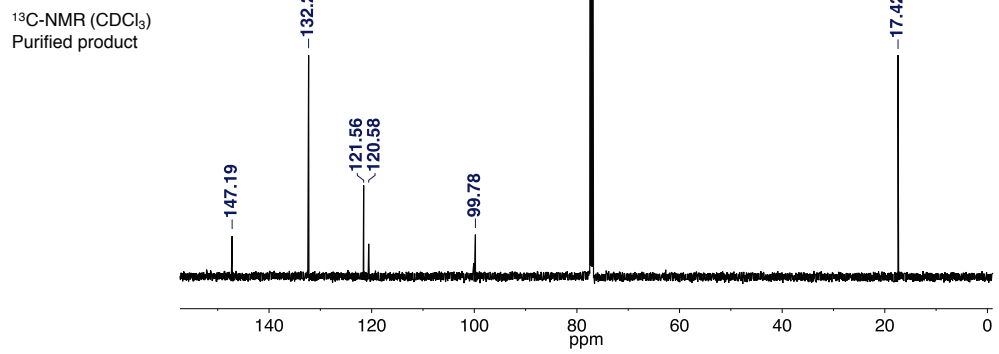
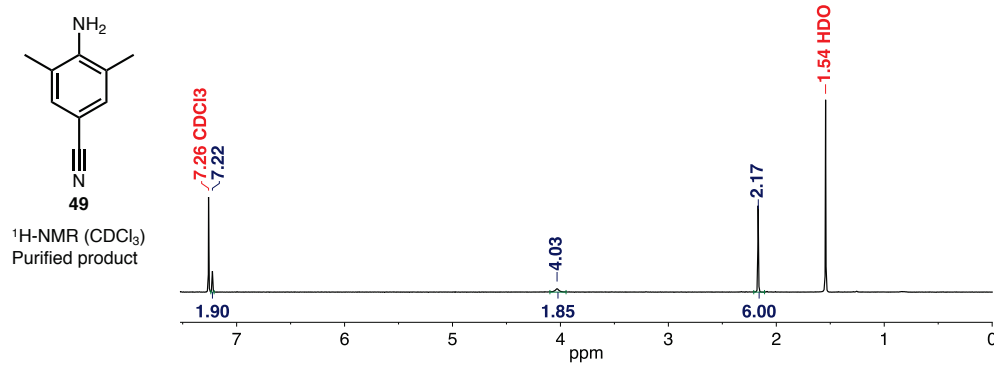
Synthesis of compound **55**, a pre-cursor to **HGII-NH<sub>3</sub><sup>+</sup>** was performed using a modified procedure reported by A. Robinson *et. al.*<sup>235</sup>

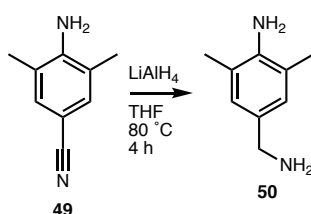


4-bromo-2,6-dimethylaniline (**48**) (10 g, 49.9 mmol) and CuCN (8.9 g, 99.4 mmol) were dissolved in NMP (130 mL) and heated under reflux at 160 °C for 16 hours. This solution was cooled to room temperature, followed by the addition of water (50 mL) and ammonium hydroxide (50 mL, 30 % NH<sub>3</sub>). The resulting precipitate was filtered and washed with EtOAc. The collected filtrate was extracted with EtOAc (3x 200 mL). The EtOAc extract was then washed with brine (2x 100 mL), then dried (MgSO<sub>4</sub>), filtered and concentrated under reduced pressure. This resulted in compound **49** as a brown solid (5.87 g, 80 %).

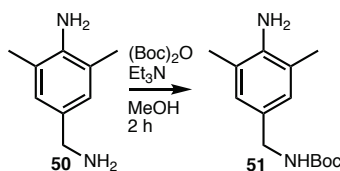
MP: 98-100 °C

HR-MS [M+H]<sup>+</sup>: 147.0921

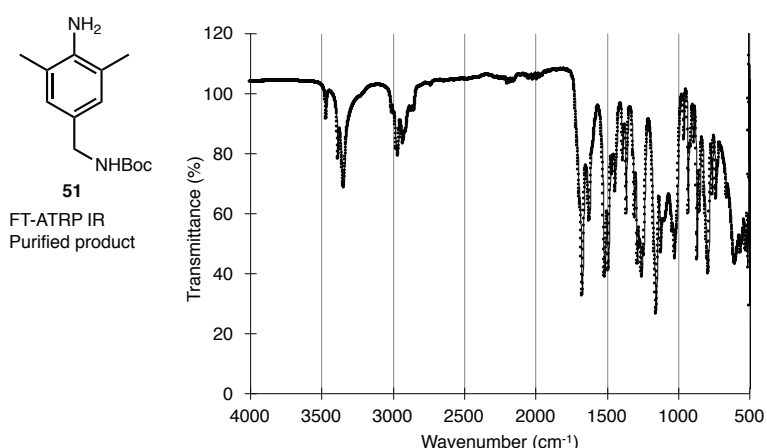


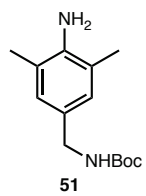


Under anhydrous conditions in a N<sub>2</sub> atmosphere, compound **49** (6.04 g, 41.3 mmol) in THF (20 mL) was added dropwise to a stirred THF solution of LiAlH<sub>4</sub> (35 mL, 2.4 M, 83 mmol). This was then heated under reflux at 80 °C for 4 hours. The solution was then cooled to room temperature and quenched with the careful addition of water (1 mL) and sodium hydroxide (1 M Aq., 1 mL). Solution was then extracted with EtOAc (3 x 100 mL) and washed with brine (2 x 100 mL), dried (MgSO<sub>4</sub>), filtered and concentrated under reduced pressure to afford compound **50** (6.02 g, 97 %) as a brown oil. This was then used immediately in the next step to avoid degradation.

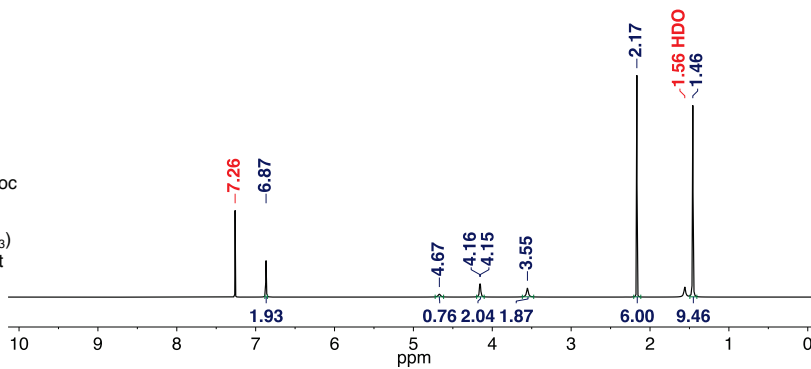


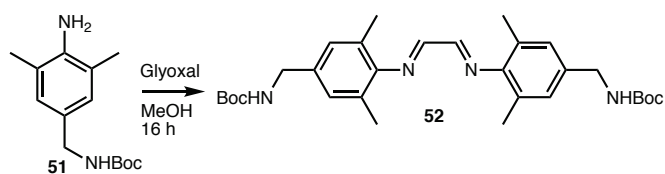
Compound **50** (6.02 g, 0.0402 mol) was dissolved in MeOH (80 mL) and mixed with Et<sub>3</sub>N (9 mL). This solution was then cooled to 0 °C over ice and a solution of (Boc)<sub>2</sub>O (8.76 g, 0.04 mol) in MeOH (20 mL) was added dropwise over 5 minutes. The solution was removed from ice and stirred at room temperature for 2 hours. Once required reaction time was reached, solution was diluted in Et<sub>2</sub>O (50 mL) and washed with water (2x 100 mL) and then brine (2x 100 mL). Organic layer was then dried (MgSO<sub>4</sub>), filtered and concentrated under reduced pressure, resulting in compound **51** (9.506 g, 95 %) as a brown solid.





<sup>1</sup>H-NMR (CDCl<sub>3</sub>)  
Purified product

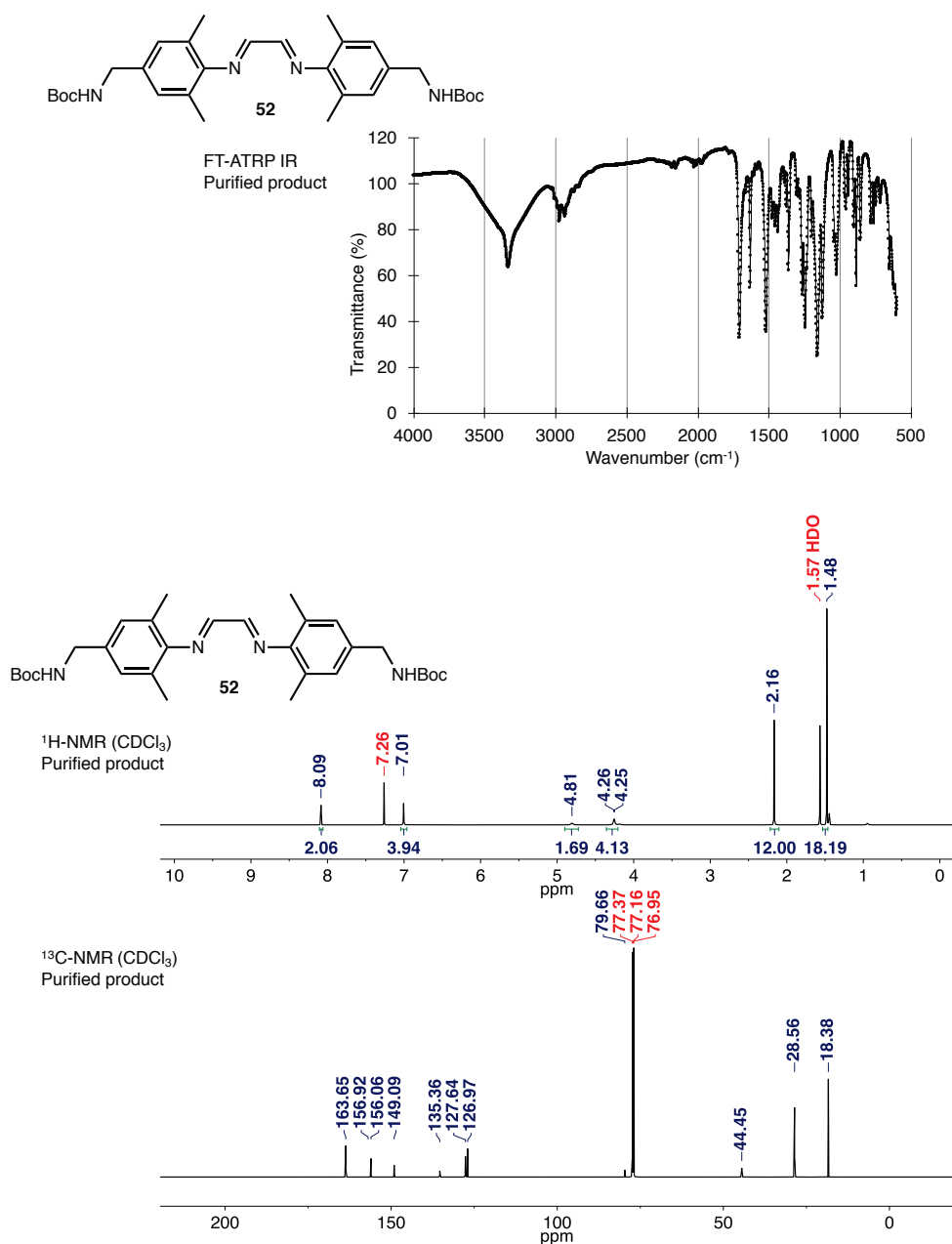


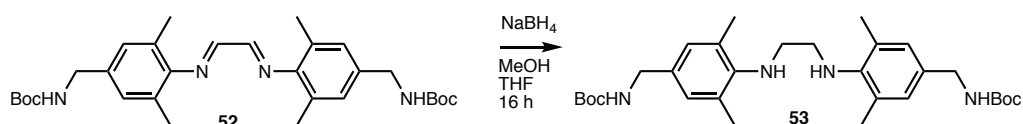


Compound **51** (9.5 g, 37.9 mmol) was dissolved in MeOH (50 mL) at 50 °C with stirring. To this, glyoxal (2.2 mL, 40 wt.% in water, 15.2 mmol) and acetic acid (0.1 mL) were added. Solution was removed from heat and stirred for 16 hours at room temperature. A yellow precipitate formed and was filtered from solution and washed with MeOH (2x 50 mL). Filtrate was collected and recrystallized from MeOH. Yellow solid was combined and dried under reduced pressure, resulting in compound **52** (8.99 g, 45 %).

MP: 188-191 °C

HR-MS  $[M+H]^+$ : 523.329

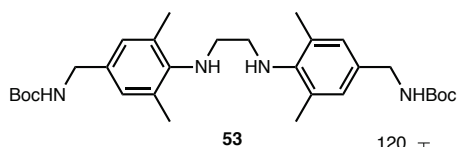




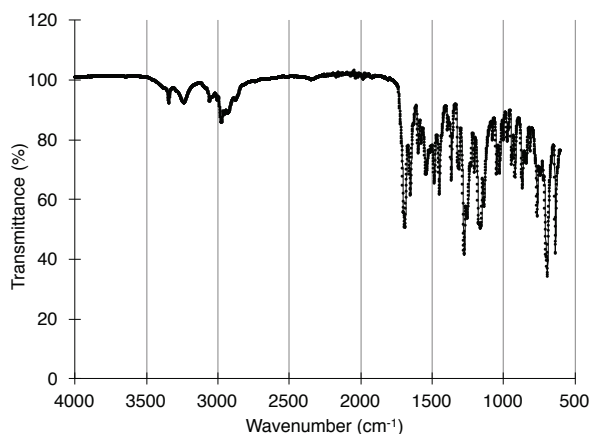
Compound **52** (9.5 g, 1.8 mmol) was dissolved in THF (50 mL) and MeOH (25 mL) and cooled to 0 °C over ice. To this, NaBH<sub>4</sub> (3.85 g, 0.102 mmol) was added in small portions and the mixture was stirred at room temperature for 16 h. Reaction was then quenched by the addition of saturated ammonium chloride (10 mL). Extraction was performed with Et<sub>2</sub>O (3x 100 mL), and combined extracts were washed with brine (2x 50 mL). Solution was then dried (MgSO<sub>4</sub>), filtered and concentrated under reduced pressure. Column chromatography (mobile phase of 1:1 EtOAc: hexane) was then performed, resulting in compound **53** as a colourless solid (3.92 g, 41%).

MP: 106-108 °C

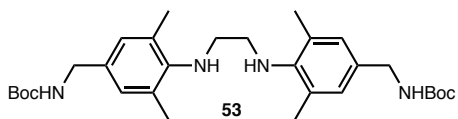
HR-MS [M+H]<sup>+</sup>: 527.3584



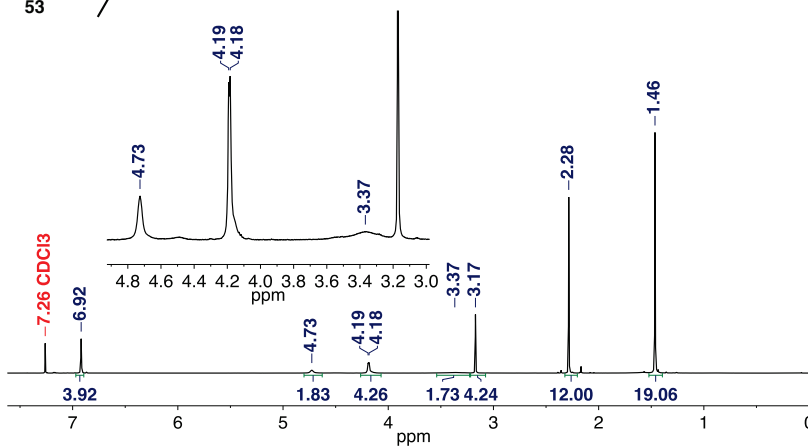
53  
FT-ATR IR  
Purified product



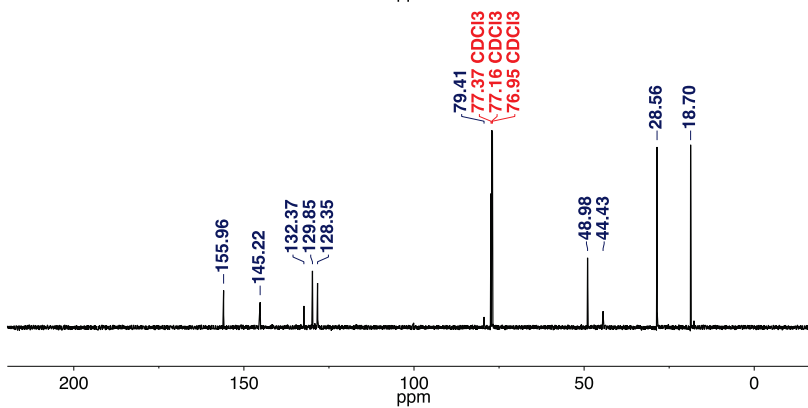


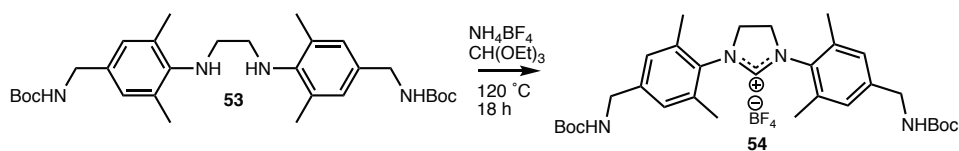


<sup>1</sup>H-NMR (CDCl<sub>3</sub>)  
Purified product



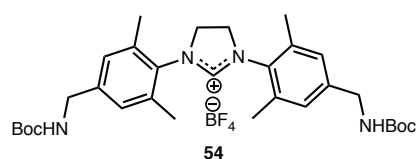
<sup>13</sup>C-NMR (CDCl<sub>3</sub>)  
Purified product



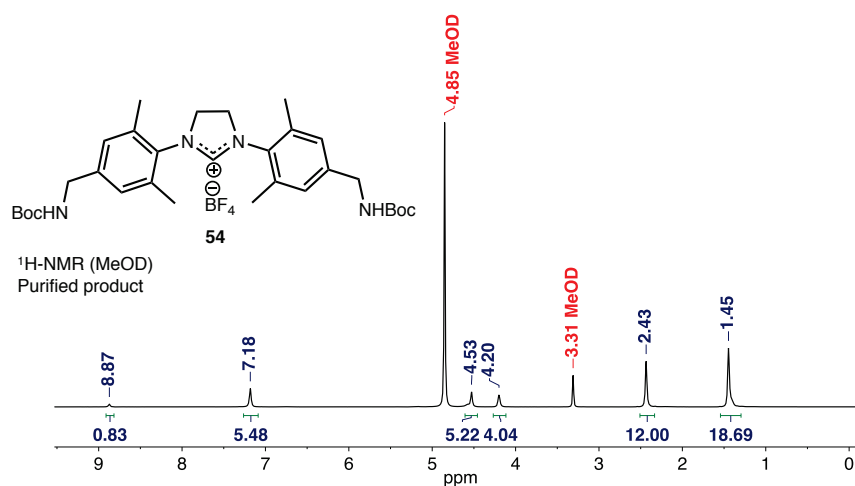
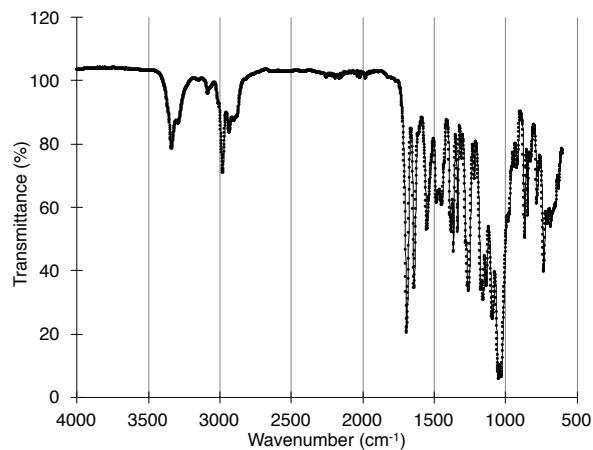


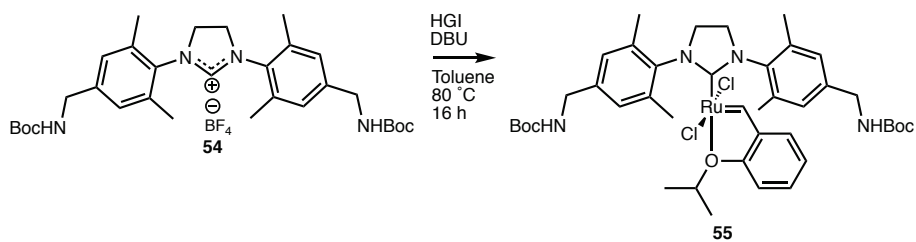
$\text{NH}_4\text{BF}_4$  (780 mg, 7.44 mmol) was added to a solution of compound **53** (3.9 g, 7.44 mmol) in  $\text{EtO}_3\text{CH}$  (35 mL). The mixture was stirred under reflux at 150 °C for 16 hours. Once cooled to room temperature, the resulting white precipitate was filtered and washed with  $\text{CH}_2\text{Cl}_2$  (2 x 50 mL) and  $\text{Et}_2\text{O}$  (2 x 50 mL). Solid was dried under reduced pressure, resulting in compound **54** (4.32 g, 94%).

MP 228 °C (decomposes)



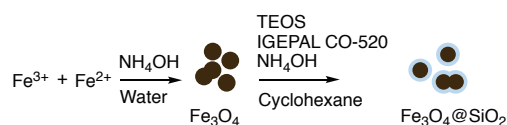
FT-ATR IR  
Purified product



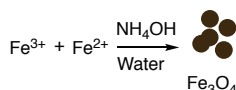


The tetrafluoroborate salt **54** (8 mg, 0.013 mmol) was dissolved in toluene (2 mL). To this, DBU (20  $\mu$ L, 0.13 mol) and HGI (8 mg, 0.013 mmol) were added. This solution was stirred at 80 °C for 2 hours. The reaction mixture was then diluted in extra toluene (20 mL) and washed with water (3x 20 mL). The organic layer was then dried ( $\text{MgSO}_4$ ) and filtered. Following this, the excess solvent was removed under reduced pressure, and the reaction mixture was purified by column chromatography. Resulting product was a green solid (5.8 mg, 53 %).

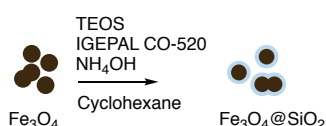
### 3.5.10 - Synthesis of Fe<sub>3</sub>O<sub>4</sub>@SiO<sub>2</sub>



The magnetic nanoparticles chosen were magnetite (Fe<sub>3</sub>O<sub>4</sub>). These would then be coated in silica so that the same method could be applied to tether the catalyst directly to the tube or to the silica coated nanoparticles.

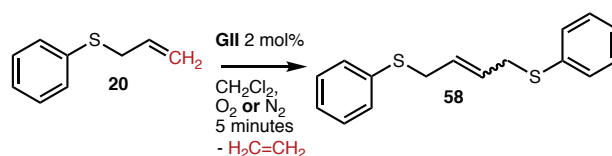


A co-precipitation method for the formation of Fe<sub>3</sub>O<sub>4</sub> nanoparticles was employed. For this, Fe(III)Cl<sub>3</sub>•6H<sub>2</sub>O (1g, 3.7 mmol) and Fe(II)Cl<sub>2</sub>•4H<sub>2</sub>O (0.735 g, 3.7 mmol) were dissolved in water (30 mL). To this stirred solution, a solution of ammonium hydroxide (30 wt%, 260 μL, 29.6 mmol) was slowly added. This was then stirred overnight at room temperature. The solution was then centrifuged down to a pellet, discarding the supernatant and re-suspending in ethanol (≈40 mL). This was wash performed 6 times. Following this, the dark brown solid was dried under reduced pressure resulting in a fine dark brown and magnetic powder. AFM revealed spherical particles between 10-30 nm in diameter.

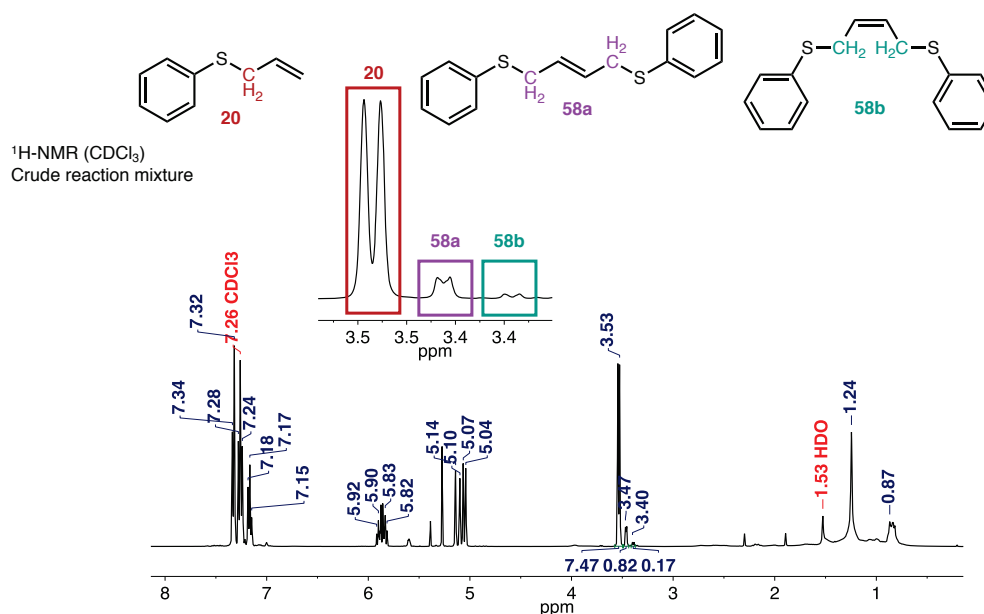


A reverse emulsion method was employed for coating these particles with silica. A solution of IGEPAL CO-520 (234 μL) in cyclohexane (10 mL) was prepared and sonicated for 10 minutes. To this, the Fe<sub>3</sub>O<sub>4</sub> (20 mg) was added and sonicated for a further 10 minutes. A solution of ammonium hydroxide (30 wt%, 40 μL, 0.308 mmol) followed by the addition of TEOS (30 μL, 0.13 mmol). This was sonicated for a further 10 mins and then stirred for 2 days at room temperature. The resulting solution was centrifuged down into a pellet, discarding the supernatant. This was dispersed and in EtOH and centrifuged a further 3 times. Following the washes, the powder was dried under reduced pressure. The silica particles were then separated from the MNP's by the use of a magnet.

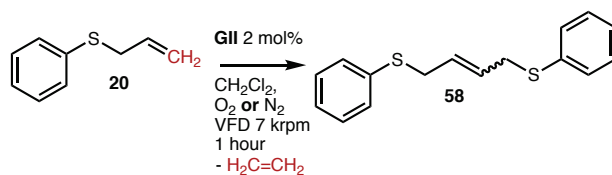
### 3.5.11 – 5 minute CM of **20** in Batch vs VFD Under O<sub>2</sub>, With N<sub>2</sub> Control



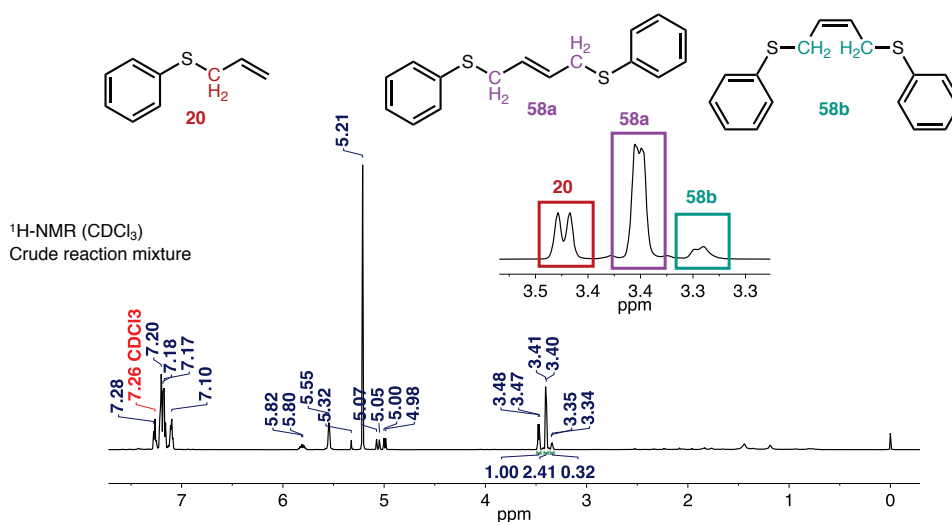
A VFD tube was sealed with a rubber septum and purged with the desired gas ( $\text{N}_2$  or  $\text{O}_2$ ). Meanwhile, the catalyst (2 mg, 0.0024 mmol, 2 mol%) was weighed and dissolved in  $\text{CH}_2\text{Cl}_2$  (1 mL). Separately, **20** (17  $\mu\text{L}$ , 0.11 mmol) was dissolved in  $\text{CH}_2\text{Cl}_2$  (1 mL). These two separate solutions were then added to the sealed tube via a needle. All input needles were removed from the tube and rotation of the tube was begun at 7 krpm. Once the time had passed, the seal was removed and the solvent was evaporated under a stream of  $\text{N}_2$ . Samples were then stored in freezer ( $-20^\circ\text{C}$ ) until NMR analysis (for no longer than 2 hours). In addition, batch experiments were performed for the CM of **20** under  $\text{O}_2$ . These experiments were identical to the experiments described above, excepting that the VFD tube was not rotated, and instead a magnetic stirrer bar was used to stir the reaction mixture.



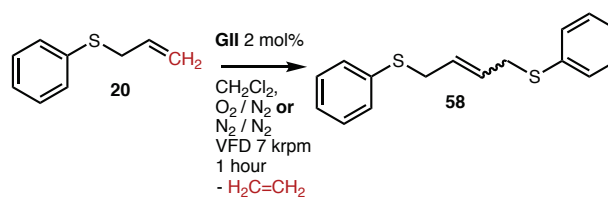
### 3.5.12 – 1 hour CM of **20** in VFD, comparing O<sub>2</sub> vs N<sub>2</sub> Atmospheres



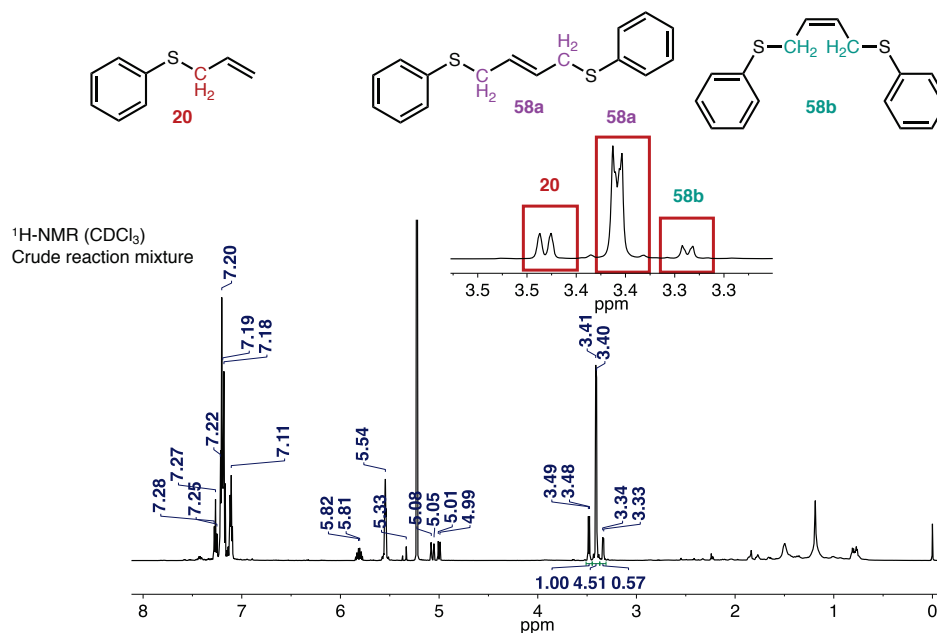
Comparisons of the CM of **20** under atmospheres of N<sub>2</sub> and O<sub>2</sub> in the VFD were performed in the following manner. To a dried 20 mm (OD) VFD tube, under inert (N<sub>2</sub> gas) atmosphere, the catalyst **GII** (4 mg, 4.7 x10<sup>-6</sup> mol) was dissolved in CH<sub>2</sub>Cl<sub>2</sub>. Following this was the addition of **20** (36 μL, 0.24 mmol). Half of this solution was then transferred to a tube pre-filled under an O<sub>2</sub> atmosphere. Immediately following this, both tubes were operated at 7 krpm in separate VFD's for 1 hour. Upon completion of desired reaction time, once the time had passed, the seal was removed and the solvent was evaporated under a stream of N<sub>2</sub>. Samples were then stored in freezer (-20 °C) until NMR analysis (for no longer than 2 hours). The conversion of **20** to the product **58** was made by comparing the integrals of the SCH<sub>2</sub>- protons, noting that there are 2 contributing hydrogens from the starting material, and 4 from each of the product E & Z isomers. A representative NMR can be found below, highlighting the peaks of interest.

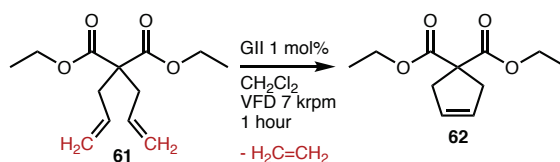


### 3.5.13 - 1 Hour CM of 20, Replacing Atmosphere N<sub>2</sub> After 10 Minutes

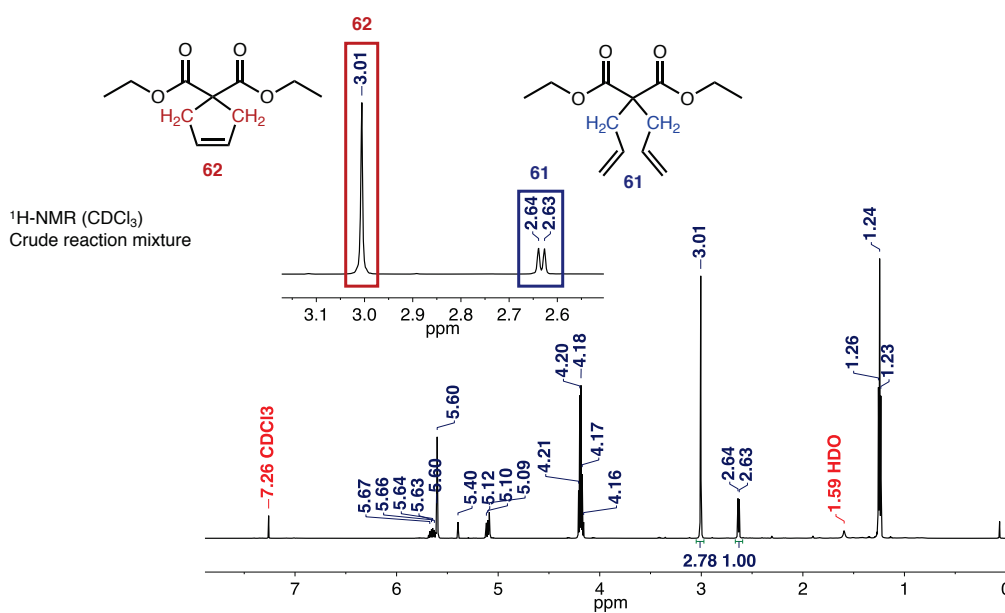


Replacing the atmosphere after 10 minutes with inert gas was hypothesized to give the benefits of oxidative phosphine scavenging, with lower amounts of oxidative catalyst degradation. In order to observe the effect of replacing the atmosphere, including any build-up of ethane, this was performed alongside the control experiment which replaced an inert N<sub>2</sub> atmosphere with fresh N<sub>2</sub> after 10 minutes. Comparisons of the CM of **20** in VFD whilst replacing the atmosphere) were performed in the following manner. To a dried 20 mm (OD) VFD tube, under inert (N<sub>2</sub> gas) atmosphere, the catalyst **GII** (4 mg, 4.7 x10<sup>-6</sup> mol) was dissolved in CH<sub>2</sub>Cl<sub>2</sub>. Following this was the addition of **20** (36 μL, 0.24 mmol). Half of this solution was then transferred to a tube pre-filled under an O<sub>2</sub> atmosphere. Immediately following this, both tubes were operated at 7 krpm in separate VFD's for 10 minutes. After 20 min., the VFD rotation was halted and the atmosphere in both tubes was evacuated and filled with N<sub>2</sub> gas. Both tubes were then operated in the separate VFDs for a further 50 minutes (1 hour total reaction time). Upon completion of desired reaction time, the seal was removed and the solvent was evaporated under a stream of N<sub>2</sub>. Samples were then stored in freezer (-20° C) until <sup>1</sup>H-NMR analysis (for no longer than 2 hours. The conversion of **20** to the product **58** was done by comparing the integrals of the SCH<sub>2</sub>- protons, noting that there are 2 contributing hydrogens from the starting material, and 4 from each of the product E & Z isomers. A representative NMR spectrum can be found below, highlighting the peaks of interest.



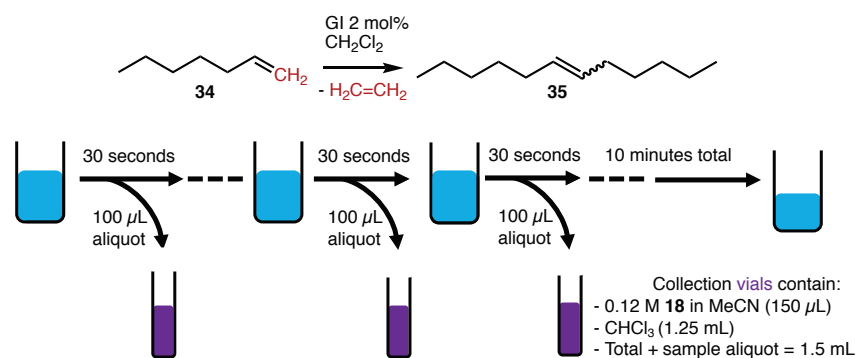


The comparisons of N<sub>2</sub> and O<sub>2</sub> atmosphere and the replacing of the atmospheres with N<sub>2</sub> after 10 minutes for the RCM of diallyl diethylmalonate (**61**) (58 μL, 0.24 mmol) were repeated as above for allylphenylsulfide (**20**). NMR analysis was then performed to determine the conversion of **61** to the product **62**. This done by comparing the integrals of the CH<sub>2</sub>-C=C protons. A representative NMR can be found below, highlighting the peaks of interest.



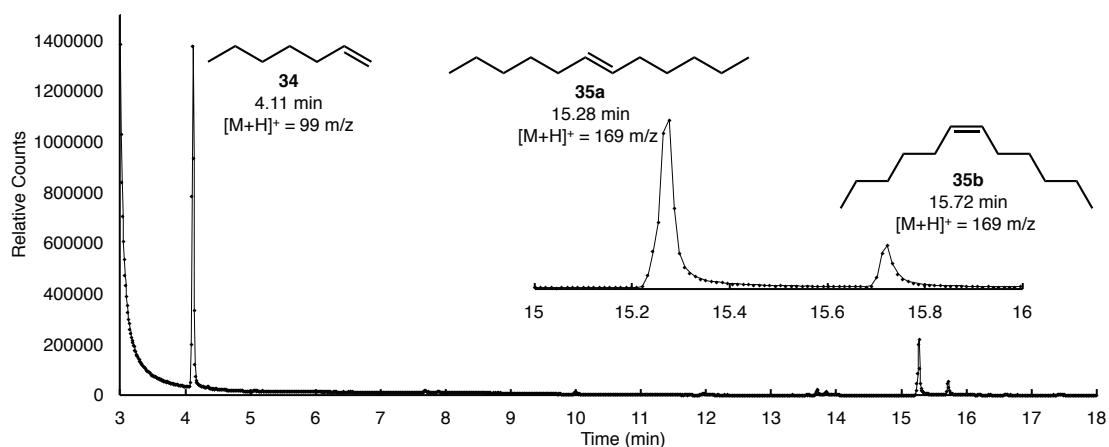


### 3.5.14 – Monitoring the GI Catalysed CM of **34** over 10 Minutes in Batch

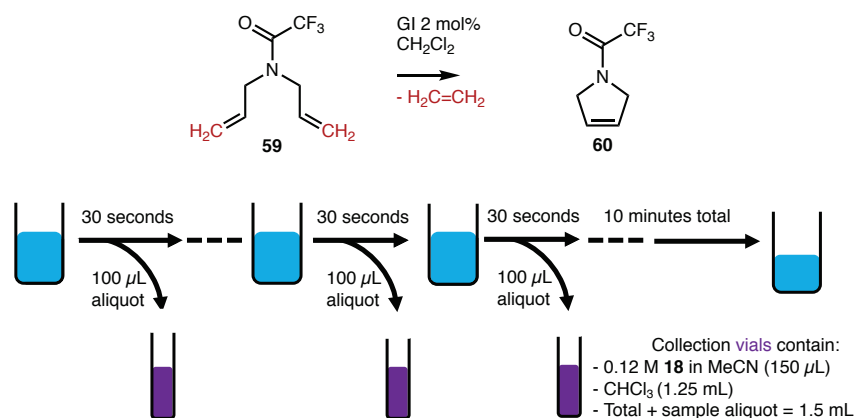


The CM of **34** with **GI** in  $\text{CH}_2\text{Cl}_2$  was monitored over 10 minutes in a magnetically stirred batch reaction in the following manner. A series of 24 GCMS vials were prepared by mixing  $\text{CHCl}_3$  (1.25 mL) with a saturated solution of **18** in MeCN (150  $\mu\text{L}$ , 0.12 M,  $1.8 \times 10^{-5}$  mol). The reaction mixture was prepared by dissolving catalyst **GI** (10 mg, 0.012 mmol) in  $\text{CH}_2\text{Cl}_2$  (10 mL), followed by the addition of **34** (170  $\mu\text{L}$ , 1.2 mmol). Aliquots of the reaction mixture (100  $\mu\text{L}$ ) were then transferred into the pre-made quenching solutions. These aliquots were taken at times of 1, 15, 30, 45, 60, 90 seconds and then every 30 seconds until 600 seconds. GCMS was then performed on these samples. The conversion of **34** to the products **35a** and **35b** were then determined from the integrals of the GC trace. Sample GC trace with corresponding MS  $[\text{M}+\text{H}]^+$  can be found below.

The GCMS was performed to the following method. Injection port temperature of 250  $^\circ\text{C}$ . Column Initial column oven temperature of 30  $^\circ\text{C}$ , ramping up to 200  $^\circ\text{C}$  over 15 minutes, then holding for 5 minutes. MS was operated over a mass detection range between 50 – 600  $m/z$ .

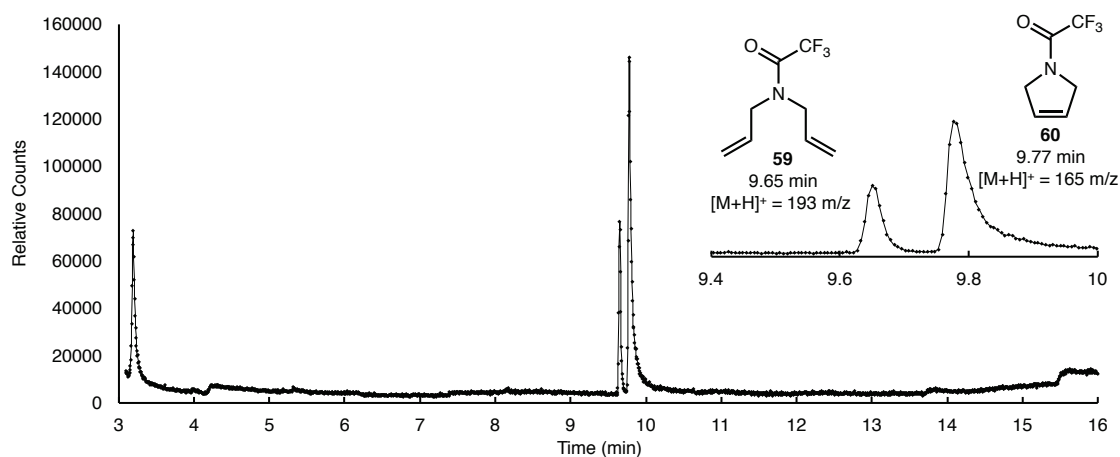


### 3.5.15 - Monitoring the GI catalysed RCM of **59** Over 10 Minutes

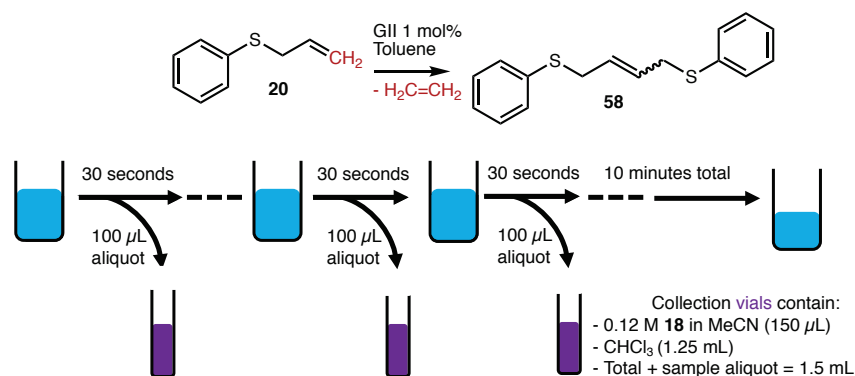


The RCM of **59** with **GI** in CH<sub>2</sub>Cl<sub>2</sub> (Fig 9B) was monitored over 10 minutes in a magnetically stirred batch reaction in the following manner. A series of 24 GCMS vials were prepared by mixing CHCl<sub>3</sub> (1.25 mL) with a solution of **18** in MeCN (150 µL, 0.12 M, 1.8 x 10<sup>-5</sup> mol). The reaction mixture was prepared by dissolving catalyst **GI** (10 mg, 0.012 mmol) in CH<sub>2</sub>Cl<sub>2</sub> (10 mL), followed by the addition of **59** (206 µL, 1.2 mmol). Aliquots of the reaction mixture (100 µL) were then transferred into the pre-made quenching solutions. These aliquots were taken at times of 1, 15, 30, 45, 60, 90 seconds and then every 30 seconds until 600 seconds. GCMS was then performed on these samples. The conversion of **59** to the product **60** was then determined from the integrals of the GC trace. Sample GC trace with corresponding MS [M+H]<sup>+</sup> can be found below.

The GCMS was performed to the following method. Injection port temperature of 250 °C. Column Initial column oven temperature of 30 °C, ramping up to 200 °C over 15 minutes, then holding for 5 minutes. MS was operated over a mass detection range between 50 – 600 m/z.

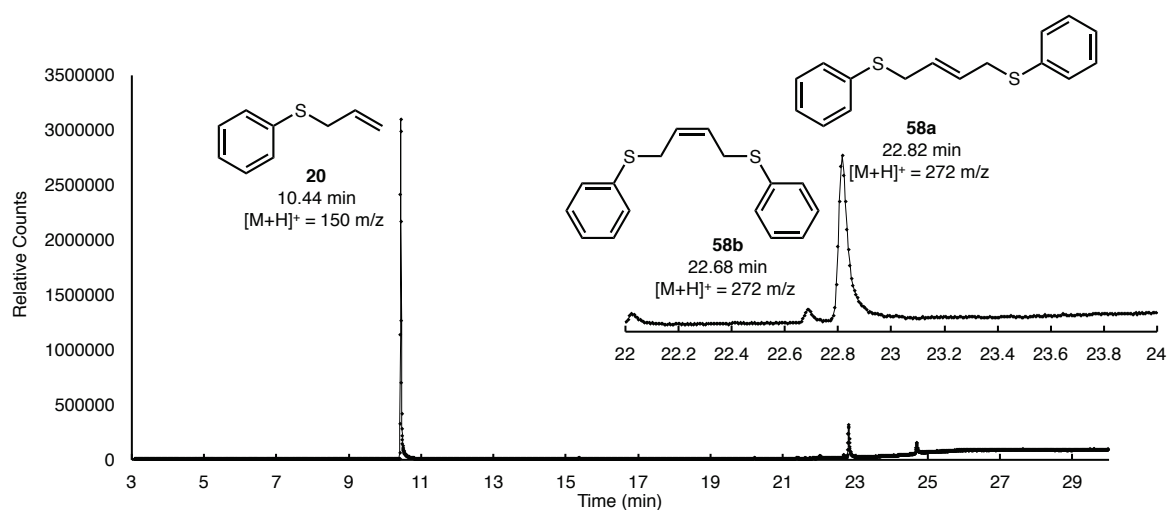


### 3.5.16 - Monitoring the GII Catalysed CM of **20** Over 10 Minutes

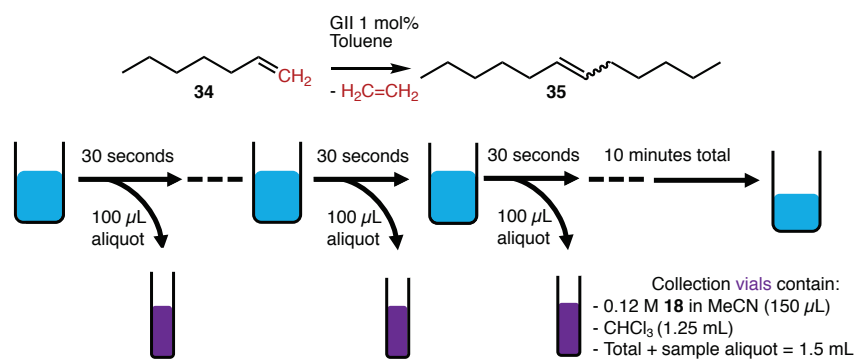


The CM of **20** with **GII** in toluene was monitored over 10 minutes in a magnetically stirred batch reaction in the following manner. A series of 24 GCMS vials were prepared by mixing  $\text{CHCl}_3$  (1.25 mL) with a solution of **18** in MeCN (150  $\mu\text{L}$ , 0.12 M,  $1.8 \times 10^{-5}$  mol). The reaction mixture was prepared by dissolving catalyst **GII** (13 mg, 0.015 mmol) in  $\text{CH}_2\text{Cl}_2$  (10 mL), followed by the addition of **20** (220  $\mu\text{L}$ , 1.5 mmol). Aliquots of the reaction mixture (100  $\mu\text{L}$ ) were then transferred into the pre-made quenching solutions. These aliquots were taken at times of 1, 15, 30, 45, 60, 90 seconds and then every 30 seconds until 600 seconds. GCMS was then performed on these samples. The conversion of **20** to the products **58a** and **58b** were then determined from the integrals of the GC trace. Sample GC trace with corresponding MS  $[\text{M}+\text{H}]^+$  can be found below.

The GCMS was performed to the following method. Injection port temperature of 250  $^\circ\text{C}$ . Column Initial column oven temperature of 30  $^\circ\text{C}$ , ramping up to 200  $^\circ\text{C}$  over 15 minutes, then holding for 5 minutes. MS was operated over a mass detection range between 50 – 600  $m/z$ .

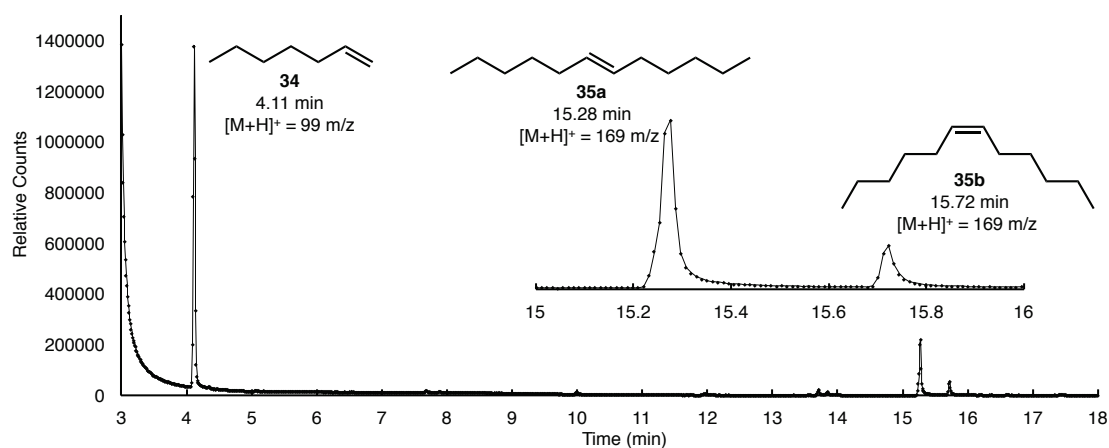


### 3.5.17 – Monitoring the GII Catalysed CM of **34** Over 10 Minutes

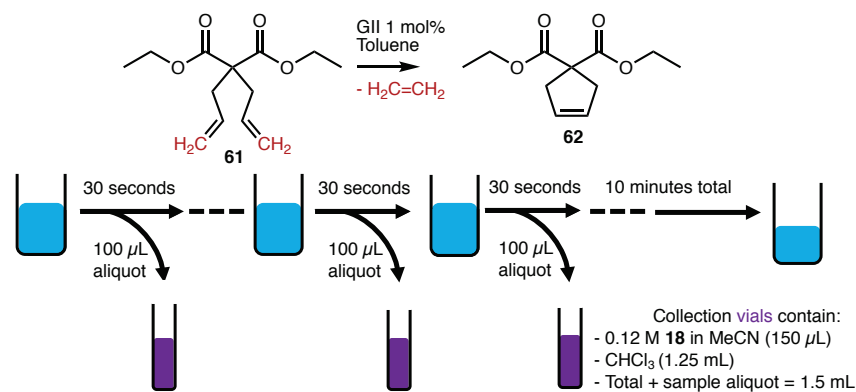


The CM of **34** with **GII** in toluene was monitored over 10 minutes in a magnetically stirred batch reaction in the following manner. A series of 24 GCMS vials were prepared by mixing CHCl<sub>3</sub> (1.25 mL) with a solution of **18** in MeCN (150 µL, 0.12 M, 1.8 × 10<sup>-5</sup> mol). The reaction mixture was prepared by dissolving catalyst **GII** (13 mg, 0.015 mmol) in toluene (10 mL), followed by the addition of **34** (210 µL, 1.5 mmol). Aliquots of the reaction mixture (100 µL) were then transferred into the pre-made quenching solutions. These aliquots were taken at times of 1, 15, 30, 45, 60, 90 seconds and then every 30 seconds until 600 seconds. GCMS was then performed on these samples. The conversion of **34** to the products **35a** and **35b** were then determined from the integrals of the GC trace. Sample GC trace with corresponding MS [M+H]<sup>+</sup> can be found below.

The GCMS was performed to the following method. Injection port temperature of 250 °C. Column Initial column oven temperature of 30 °C, ramping up to 200 °C over 15 minutes, then holding for 5 minutes. MS was operated over a mass detection range between 50 – 600 m/z.

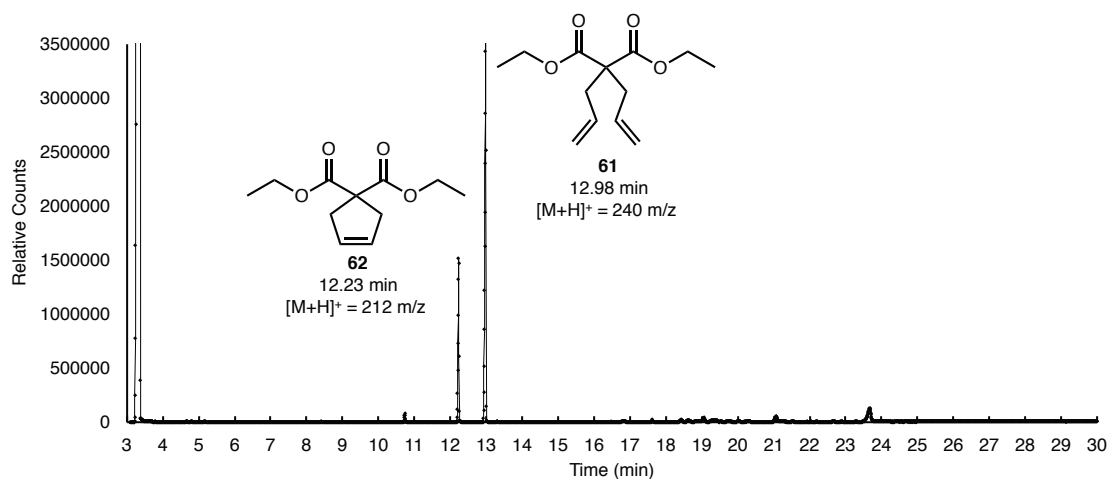


### 3.5.18 - Monitoring the GII Catalysed RCM of **61** in Toluene Over 10 Minutes

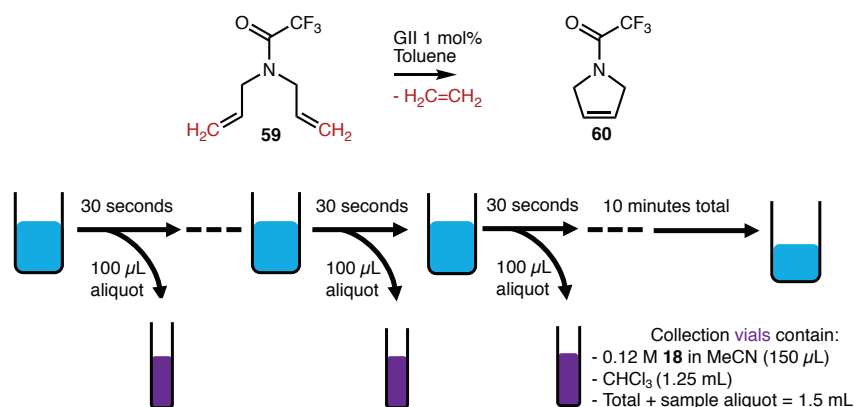


The RCM of **61** with **GII** in toluene was monitored over 10 minutes in a magnetically stirred batch reaction in the following manner. A series of 24 GCMS vials were prepared by mixing  $\text{CHCl}_3$  (1.25 mL) with a solution of **18** in MeCN (150  $\mu\text{L}$ , 0.12 M,  $1.8 \times 10^{-5}$  mol). The reaction mixture was prepared by dissolving catalyst **GII** (13 mg, 0.015 mmol) in toluene (10 mL), followed by the addition of **61** (363  $\mu\text{L}$ , 1.5 mmol). Aliquots of the reaction mixture (100  $\mu\text{L}$ ) were then transferred into the pre-made quenching solutions. These aliquots were taken at times of 1, 15, 30, 45, 60, 90 seconds and then every 30 seconds until 600 seconds. GCMS was then performed on these samples. The conversion of **61** to the product **62** was then determined from the integrals of the GC trace. Sample GC trace with corresponding MS  $[\text{M}+\text{H}]^+$  can be found below.

The GCMS was performed to the following method. Injection port temperature of 180  $^\circ\text{C}$ . Column Initial column oven temperature of 30  $^\circ\text{C}$ , ramping up to 200  $^\circ\text{C}$  over 15 minutes, then holding for 5 minutes. MS was operated over a mass detection range between 50 – 600 m/z.

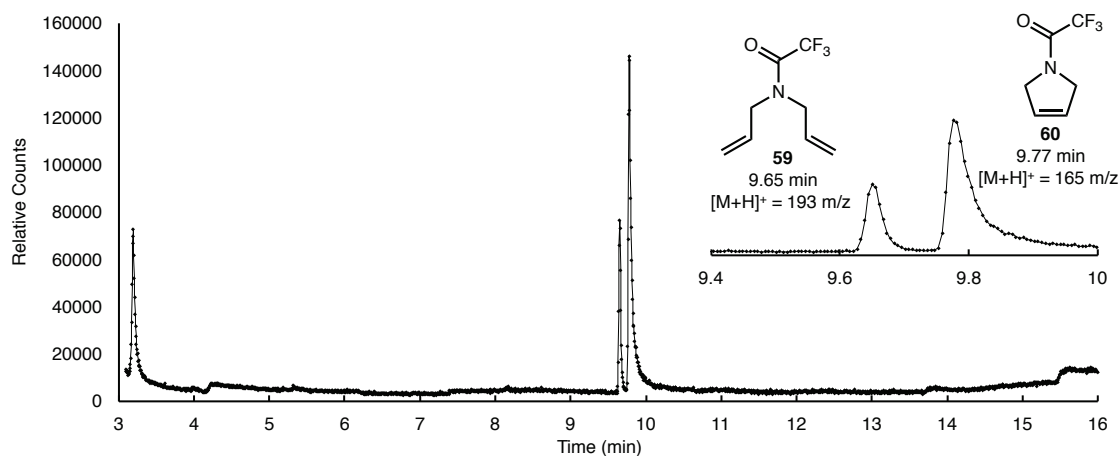


### 3.5.19 - Monitoring the GII Catalysed RCM of **59** in Toluene Over 10 Minutes

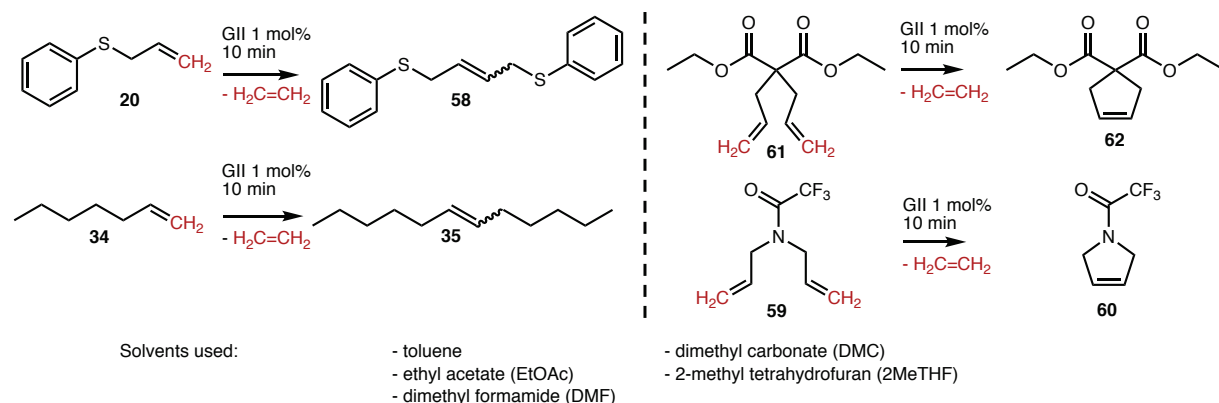


The RCM of **59** with **GII** in toluene was monitored over 10 minutes in a magnetically stirred batch reaction in the following manner. A series of 24 GCMS vials were prepared by mixing  $\text{CHCl}_3$  (1.25 mL) with a solution of **18** in MeCN (150  $\mu\text{L}$ , 0.12 M,  $1.8 \times 10^{-5}$  mol). The reaction mixture was prepared by dissolving catalyst **GII** (13 mg, 0.015 mmol) in toluene (10 mL), followed by the addition of **59** (256  $\mu\text{L}$ , 1.5 mmol). Aliquots of the reaction mixture (100  $\mu\text{L}$ ) were then transferred into the pre-made quenching solutions. These aliquots were taken at times of 1, 15, 30, 45, 60, 90 seconds and then every 30 seconds until 600 seconds. GCMS was then performed on these samples. The conversion of **59** to the product **61** was then determined from the integrals of the GC trace. Sample GC trace with corresponding MS  $[\text{M}+\text{H}]^+$  is provided below.

The GCMS was performed to the following method. Injection port temperature of 250  $^\circ\text{C}$ . Column Initial column oven temperature of 30  $^\circ\text{C}$ , ramping up to 200  $^\circ\text{C}$  over 15 minutes, then holding for 5 minutes. MS was operated over a mass detection range between 50 – 600  $m/z$ .

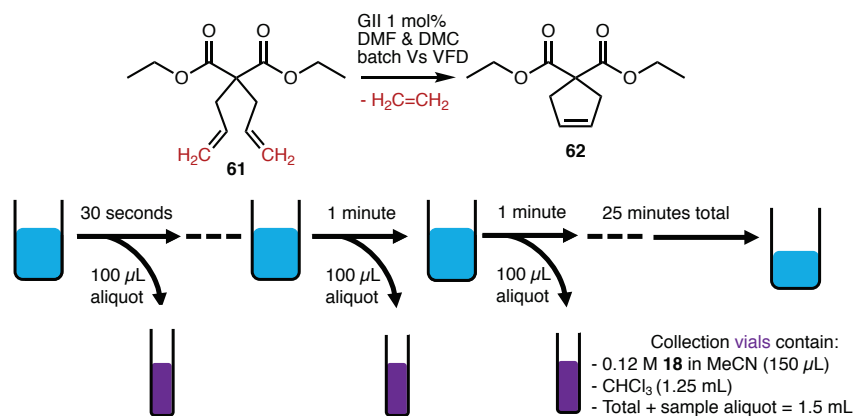


### 3.5.20 - Monitoring the GII Catalysed Metathesis in Various Solvents



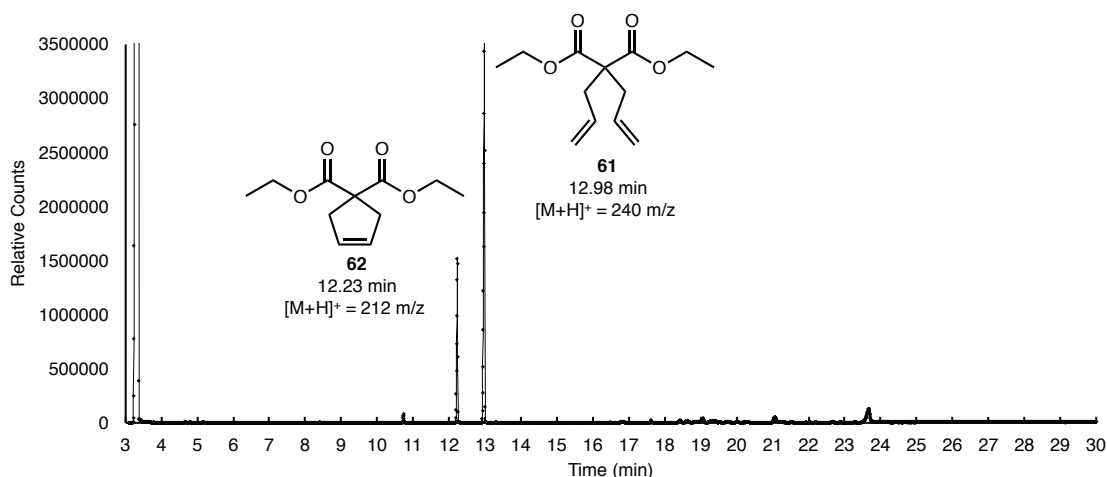
This processing was instigated to determine the activity of catalyst **GII** over 10 minutes for two CM (**20** & **34**) and two RCM (**61** & **59**) in the solvents toluene, dimethyl carbonate (DMC), EtOAc, 2-methyl tetrahydrofuran (2MeTHF) and DMF. Firstly, 20 quench vials were prepared by mixing  $\text{CHCl}_3$  (1.05 mL) with a solution of **18** in MeCN (200  $\mu\text{L}$ , 0.12 M,  $2.5 \times 10^{-5}$  mol). Next, stock solutions of the catalyst **GII** (3 mL, 2 mM, 5.09 mg,  $6.0 \times 10^{-6}$  mol) were prepared in each of the five solvents. For the reactions in toluene, 250  $\mu\text{L}$  ( $4.0 \times 10^{-7}$  mol) of the **GII** in toluene stock solution was added to four separate vials. To one of these, the **20** (5.8  $\mu\text{L}$ ,  $4.0 \times 10^{-5}$  mol) was added to each vial and the reaction mixture was diluted to 0.5 mL (244.2  $\mu\text{L}$ ) with toluene. To the second vial, **34** (5.6  $\mu\text{L}$ ,  $4.0 \times 10^{-5}$  mol) and toluene (244.4  $\mu\text{L}$ ) were added. To the third vial, **61** (9.7  $\mu\text{L}$ ,  $4.0 \times 10^{-5}$  mol) and toluene (240.3  $\mu\text{L}$ ) were added. Finally, to the fourth vial, **59** (6.8  $\mu\text{L}$ ,  $4.0 \times 10^{-5}$  mol) and toluene (243.2  $\mu\text{L}$ ) were added. After each vial had been reacting for 10 minutes, a 250  $\mu\text{L}$  aliquot was transferred to one of the pre-made quench vials. This was then repeated for each of the four other solvents. This resulted in 20 quenched reaction mixtures. GCMS was then performed on these quenched reaction mixtures. Conversions were determined by comparing the integration of the peaks corresponding to the starting material and product(s) in the GC trace. See above for GCMS procedures and sample traces for each respective reaction.

### 3.5.21 – Monitoring the GII Catalysed RCM of **61** in DMF vs DMC over 25 Minutes



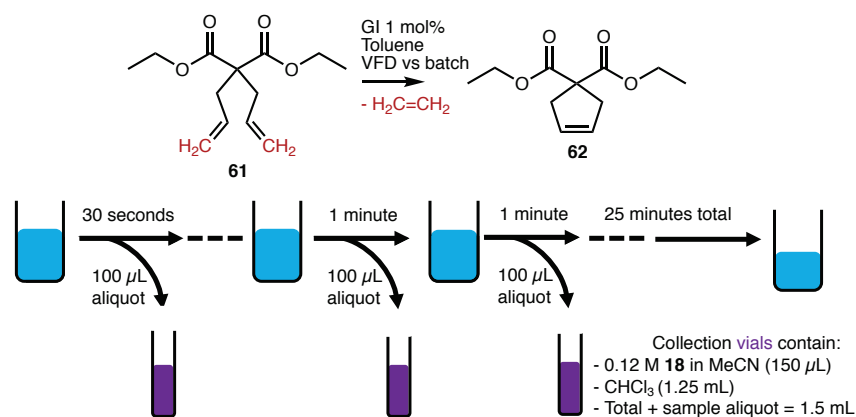
The RCM of **61** was compared between batch vs VFD over 25 minutes. This was first performed with DMF as a solvent, and the repeated with dimethyl carbonate (DMC). For these, the following procedure was used. Firstly, a series of 20 quenching vials were prepared by mixing CHCl<sub>3</sub> (1.25 mL) with a solution of **18** in MeCN (150 µL, 0.12 M, 1.8 x 10<sup>-5</sup> mol). Note: It is important that the VFD and batch comparisons are performed simultaneously as variations in room temperature over different days was shown to alter the observed conversions. The reaction mixtures were prepared in two separate 20 mm OD VFD tubes. Firstly, the catalyst **GII** (13 mg, 0.015 mmol) was dissolved in DMF (10 mL), followed by the addition of **61** (363 µL, 1.5 mmol). Aliquots of each reaction mixture (100 µL) were then transferred into the pre-made quenching solutions. These aliquots were taken at times of 1, 15, 30, 45, 60, 120, 180, 240, 300, 360, 420, 480, 540, 600, 900, 1200 and 1500 seconds. The VFD run was staggered by +2 minutes to allow time to transfer the aliquots from both reactions. GCMS was then performed on these 40 samples. The conversion of **61** to the product **62** was then determined from the integrals of the GC trace.

The GCMS was performed to the following method. Injection port temperature of 250 °C. Column Initial column oven temperature of 30 °C, ramping up to 200 °C over 15 minutes, then holding for 5 minutes. MS was operated over a mass detection range between 50 – 600 m/z.



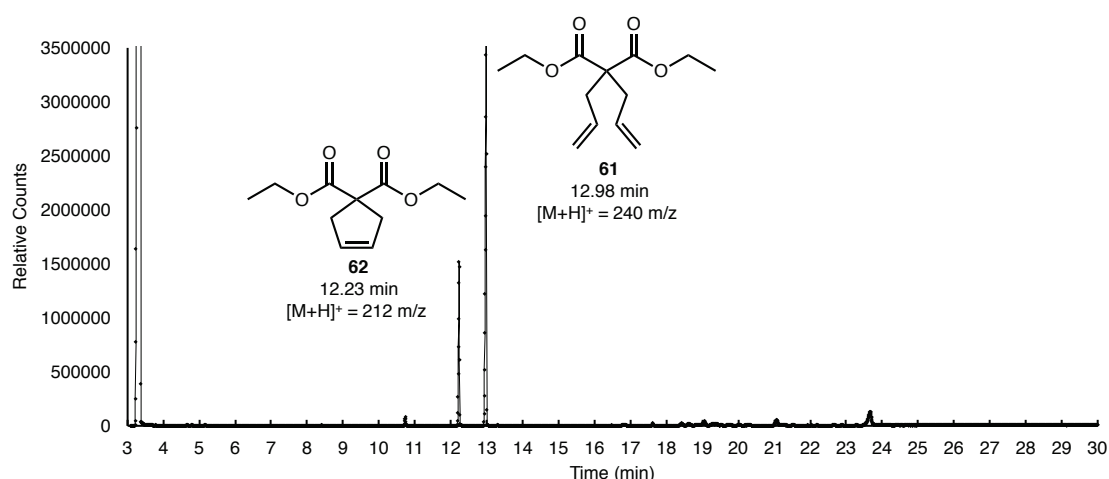


### 3.5.22 – Monitoring the GI Catalysed RCM of **61** Over 25 Minutes in Batch vs VFD



Firstly, a series of 20 quenching vials were prepared by mixing  $\text{CHCl}_3$  (1.25 mL) with a solution of **18** in MeCN (150  $\mu\text{L}$ , 0.12 M,  $1.8 \times 10^{-5}$  mol). Note it is important that the VFD and batch comparisons are performed simultaneously as variations in room temperature over different days was shown to alter the observed conversions. The reaction mixtures were prepared in two separate 20 mm OD VFD tubes. Firstly, the catalyst **GI** (12 mg, 0.015 mmol) was dissolved in toluene (10 mL), followed by the addition of **61** (363  $\mu\text{L}$ , 1.5 mmol). Aliquots of each reaction mixture (100  $\mu\text{L}$ ) were then transferred into the pre-made quenching solutions. These aliquots were taken at times of 1, 15, 30, 45, 60, 120, 180, 240, 300, 360, 420, 480, 540, 600, 900, 1200 and 1500 seconds. The VFD run was staggered by +2 minutes to allow time to transfer the aliquots from both reactions. GCMS was then performed on these 40 samples. The conversion of **61** to the product **62** was then determined from the integrals of the GC trace.

The GCMS was performed to the following method. Injection port temperature of 250  $^\circ\text{C}$ . Column Initial column oven temperature of 30  $^\circ\text{C}$ , ramping up to 200  $^\circ\text{C}$  over 15 minutes, then holding for 5 minutes. MS was operated over a mass detection range between 50 – 600 m/z.



## Chapter 4 – Polymer Synthesis in the VFD

The VFD has shown many unique applications for both small molecule synthesis and materials processing. Different aspects of the VFD have shown to have an effect on various size scales.<sup>82</sup> Firstly, for small-molecule transformations, the VFD has been demonstrated to effect the reaction outcome with benefits relative to batch processing. This includes examples of cross-coupling,<sup>100, 236</sup> Diels-alder reactions,<sup>96, 239</sup> amide synthesis,<sup>94</sup> esterification<sup>98, 240</sup> and more.<sup>102, 241, 242</sup> The benefits of the VFD arise from the complex environment and fluid flows found within the thin film, and whilst it is not fully understood, certain themes arise. These include enhanced mass transfer from the massive surface-area-to-volume-ratio (SA:V). This enables efficient mass transfer, allowing volatile small molecule by-products to be driven from the reaction media. It is also speculated that vibrational induced waves create pressure fluctuations within the liquid, which can alter the stability of reaction intermediates. For these reasons, it was hypothesised that the synthesis of polymers could be effected by the VFD, and that the vortex fluidics could be harnessed to aid the reaction efficiencies of one of the biggest chemical industries. Secondly, regarding relatively larger size-scale material processing, multiple vortex processing effects have been demonstrated. This includes the slicing of carbon nano tubes (single and multi-walled),<sup>89</sup> and the exfoliation of 2D materials.<sup>243, 244</sup> In both of these cases, the shear forces in the VFD is clearly responsible for the effects. Furthermore, the unexpected crystal growth of C<sub>60</sub> to form conical structures appears to also be related to shear stress.<sup>101</sup> Thus there are certain fluid flows within vortex that are having effects on these size scales. It was therefore further hypothesised that the synthesis of polymers would present opportunities to simultaneously combine the benefits of both small and larger scale aspects of the VFD, ie. effect the bond forming reactions and also the rheology of the macromolecule. Furthermore, the VFD benefits in the synthesis of exothermic compounds by efficiently dissipating heat, thereby preventing run-away exotherms.<sup>102</sup> Such exotherms in batch processing have resulted in catastrophic damage in polymer plants, with recent tragic examples in the United States, Japan and China.<sup>245</sup> The explosions from such accidents have caused destruction of the chemical-plant and surrounding areas, commodity shortages (such as a world-wide diaper shortage in 2012,<sup>246</sup>), and tragically with the loss of many lives<sup>77</sup>. It was hypothesised that the VFD could assist in improving the efficiency, safety and green metrics of one of the largest polluting industries. Additionally, manipulating the macro structure gives rise to the prospect of accessing novel forms of polymers. Furthermore, the continuous flow processing in the VFD lends itself to developing scalable processing.

## 4.1 - Polyurethane and Polythiourethane Synthesis

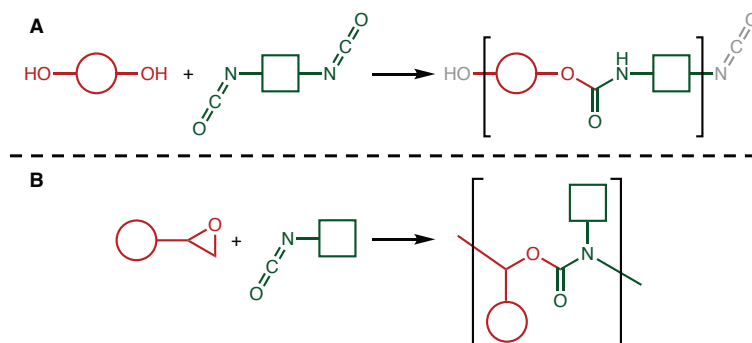


**Figure 52.** General schematics showing the formation of polyurethane from (A) conventional method using di-alcohols and di-isocyanate, and (B) from an epoxide and an isocyanate.

The conventional synthesis of polyurethanes is from a di-isocyanate and a di-alcohol (Figure 52A). Alternatively, promising work from the L. Adriaenssens group have developed a catalyst that produced a polyurethane from isocyanate and an epoxide (Figure 52B). Preparing polyurethane in this way increases the number of potential starting materials, giving access to cheaper, greener and safer starting materials. It also gives greater potential for adding functionality to the polymer, which is desirable for fine tuning the physical properties of the resulting material. This method requires a catalyst, such as the salen based **64-Mg** (Figure 53A). An example of forming a polyurethane in this way is from cyclohexene oxide and phenyl isocyanate (Figure 53B). However, the issue of selectivity arises. This is due to the possibilities of forming the polyurethane versus forming either the polyallophinate or the isocyanurate (**67**). These impurities can be avoided by performing this reaction with the isothiocyanate, such as phenyl isothiocyanate (**68**, Figure 53C). The polymer produced from this reaction involves a rapid Newman-Kwart rearrangement of the position of the sulphur, such that only the thiolester (-S-C=O) exists, and none of the thionoester (-O-C=S) is observed.

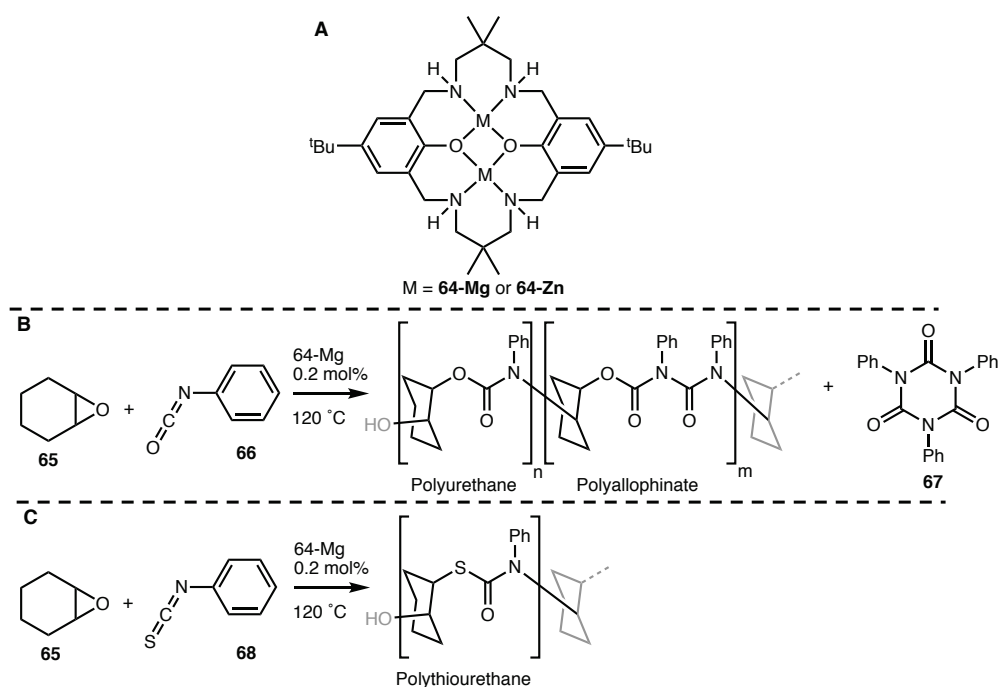


**Figure 53.** (A) The salen based catalyst, either the Mg or the Zn variant. (B) The **64-Mg** catalysed reaction of phenyl isocyanate (**66**) with cyclohexene oxide (**65**), producing the polyurethane, polyallophinate and the isocyanurate (**67**).

(C) the **64-Mg** catalysed reaction of cyclohexene oxide with phenyl isothiocyanate (**68**), which does not form the allophanate or the cyanurate. Note that a Newman-Kwart re-arrangement of the thiol is taking place.

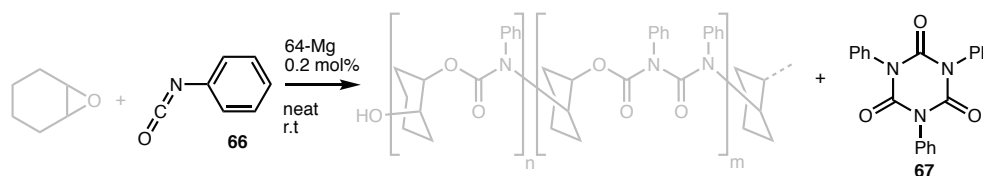
The VFD is a promising processing thin film micro-processing platform, and was hypothesised to effect the selectivity outcomes associated with using **66**. Thus, studies were performed in the VFD, monitoring the outcome of the chemical reactions and the physical properties that may be altered. Further to altering the reaction outcome, it was also hypothesised that the unique conditions in the VFD could have an effect on the macro-structure of polymers produced in the VFD. This claim is supported by a myriad of examples of macro materials experiencing unique processing in the VFD. Examples include the exfoliation of graphene, slicing of carbon nanotubes and unique crystallisation of C<sub>60</sub> & C<sub>70</sub>, and the formation of a polymer comprised of BSA and gluteraldehyde,<sup>247</sup> protein folding,<sup>86</sup> and more. Testing the utility of the VFD in the synthesis of polymers is important in advancing VFD-mediated processing in general as well establishing the ground rules for making polymers under high shear in the device, for then commercial considerations. There may be potential niche applications using the VFD, but more detailed fundamental studies are required.

#### 4.1.1 – Discussion on Polyurethane and Polythiourethane Synthesis in VFD

Direct comparisons were made between VFD and batch processing. Initial results were promising in that they showed clear differences between VFD and batch processing, with the VFD procedures resulting in higher conversion and selectivity. However, these results were plagued by small changes in reaction temperature. These temperature fluctuations were shown to dramatically affect the outcome of the polymerisation reactions independent of VFD processing. This promoted the engineering of methods that give greater confidence in the heating in the rapidly rotating tube in the VFD. Once the temperature issues were dealt with, as detailed below, all experiments showed that VFD processing does not provide any benefit in either the conversion or the M<sub>w</sub> of the polymers produced. This is detailed below.

Firstly, experiments were performed to observe the effect of the VFD on the formation of the isocyanurate (**67**) from the phenyl isocyanate (**66**). The results are summarised in Table 5, which show that for confined mode VFD and batch processing, both only produce trace amounts of **67** at room temperature. Note that this requires the presence of the catalyst. Also, there is no difference between VFD and batch processing.

**Table 5.** Pre-liminary experiments for observing the effect of the VFD on the formation of isocyanurate (**66**). Comparisons between VFD @ 7 krpm vs batch are shown, entries 1 & 2 are 12 hour runs without catalyst (**64-Mg**), 3 & 4 are 0.5 hour runs with 2 mol % catalyst (**64-Mg**), followed by entries 5 & 6 which extend to 2 hours with the catalyst. Conversions were determined by <sup>1</sup>H-NMR analysis.



Entry	66 (eq.)	64-Mg (mol %)	Vessel	Time (min)	Temp. (°C)	Atmosphere	67
1	1	0	VFD 7 krpm	12	Room	N <sub>2</sub>	n.r
2	1	0	Batch	12	Room	N <sub>2</sub>	n.r
3	1	0.2	VFD 7 krpm	0.5	Room	N <sub>2</sub>	Trace
4	1	0.2	Batch	0.5	Room	N <sub>2</sub>	Trace
5	1	0.2	VFD 4 krpm	2	Room	N <sub>2</sub>	Trace
6	1	0.2	Batch	2	Room	N <sub>2</sub>	Trace

The experiments in Table 5 produced an un-expected result for runs in the VFD, with the formation of a bi-product, identified as diphenyl urea (Figure 54A). This was found from the investigation of small crystals which formed on the VFD tube during processing (Figure 54B). These were found to be a urea by-product (**69**), the formation of which requires water (Figure 54C). This urea product was not present in the batch processes. A suggested rationale is that there is extra water relative to the amount of **66** in the VFD compared to that encountered batch processing. This would result in additional formation of urea **69**. The extra water is a result of the glass being coated in a layer of water under ambient conditions (as all surfaces are), and that there is more contact between the liquid reaction medium and the glass in the VFD compared to batch. This was then supported from experiments performed in flame-dried glassware under an inert atmosphere of N<sub>2</sub> gas (Figure 54D), which showed no formation of the unwanted by-product **69**. Thus, it was concluded that an inert atmosphere must be maintained in order to avoid the production of **69**.

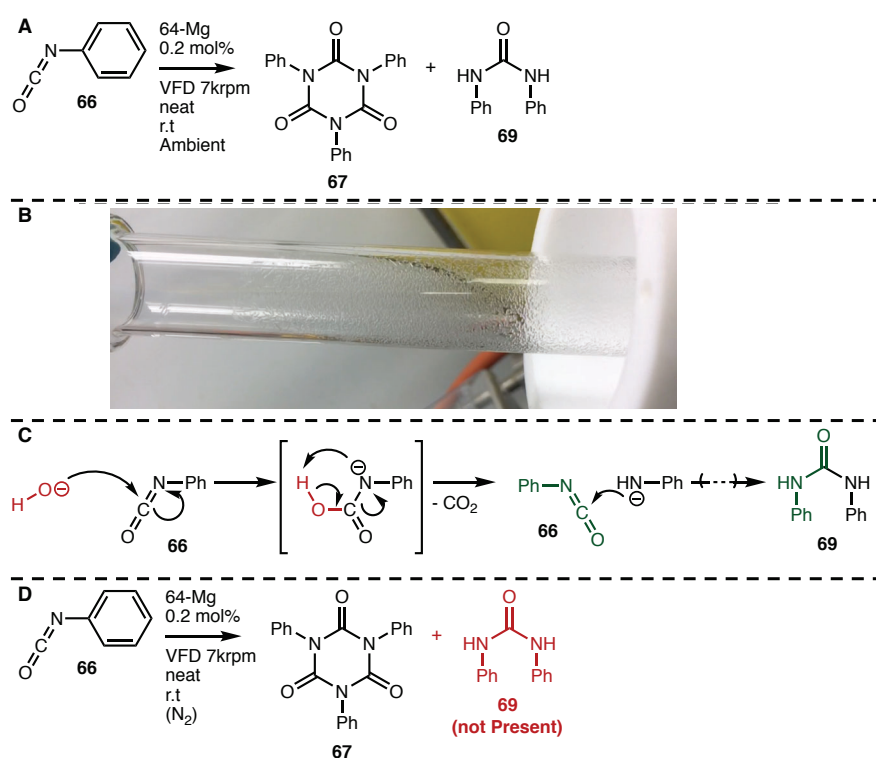


**Figure 54.** (A) Formation of di-phenyl urea (**69**) in the VFD, (B) evident from the small crystals that form on the VFD tube. (C) the speculative mechanism for the production of **69** from **66** and water. (D) none of the urea **69** is formed when performed under inert atmosphere with flame-dried glassware.

Another preliminary experiment was performed before undertaking the synthesis in the VFD. Here, pre-made polymer samples were subject to VFD processing. This was done in order to understand the stability of the polymers in the VFD. It was thought possible that the shear forces in the VFD may result in bond rupture and reduce the length of the polymer strands. Samples of polyurethane and polyallophanate dissolved in dioxane were run for 12 hours in the VFD at 7 krpm in the confined mode of operation of the device. The VFD was at 45° tilt with 1 mL of solution. The resulting solution was then studied using <sup>1</sup>H-NMR. This established that there was no degradation of the polymers (Figure 55), and with this in mind, the synthesis of the polymer in the VFD was explored.

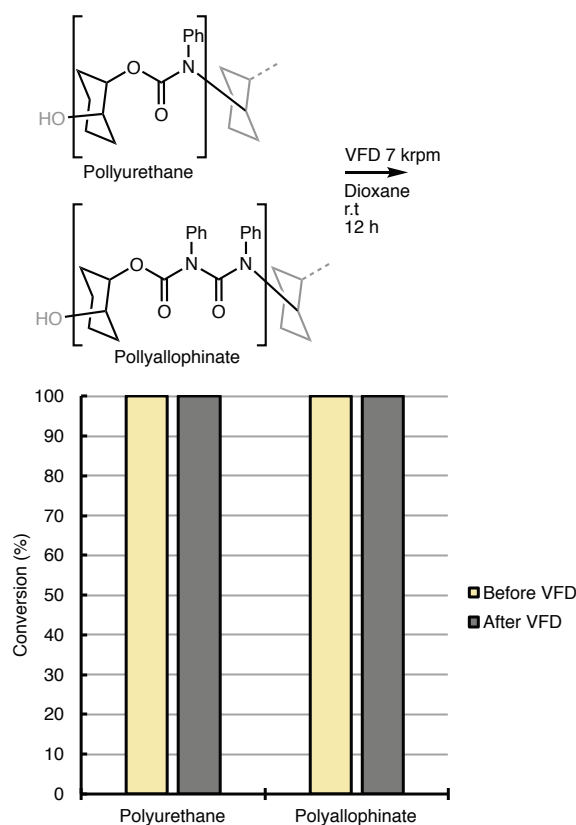
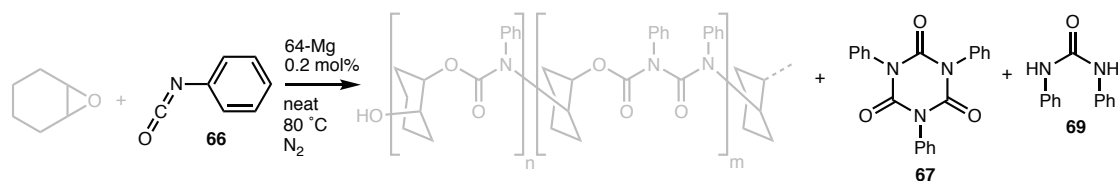


**Figure 55.** Stability of both the polyurethane and the polyallophinate was established in the VFD before undertaking further any synthesis of polyurethanes or polyallophinates. This shows that after 12 h processing in the VFD at 7 krpm, dissolved in dioxane, there is no degradation of the polymers.

Next, lone isocyanate **66** was then reacted with catalyst **64-Mg** without the presence of an epoxide. This was performed to establish if the VFD directly effects the formation of the un-wanted isocyanurate product **67**. Identical VFD and batch procedures were then compared, with 0.2 mol % catalyst loading in 1 mL of neat isocyanide at 80°C. In the VFD, the rotational speed was set to 7 krpm and a tilt angle of 45°. Heating in the VFD was achieved by using a custom made aluminium block spaced  $\approx 2$  mm along the length of the rotating tube. The temperature is controlled by a separate command module. The separate batch procedure was performed in a VFD tube, with a magnetically stirred stir bar. This batch sample was heated in an oil bath. These results are summarised in Table 6. From this, it can be observed that there is more of the unwanted isocyanurate (**67**) in batch (74 % conversion) compared to VFD processing (44 % conversion). However, the heating method for the VFD procedure was later shown to be unreliable, in that an accurate measure of the temperature in the VFD could not be obtained. This flawed temperature reading came from referencing the heating block using an IR thermal imaging camera. Although the temperature was set to 80 °C, the real temperature produced by the heating unit was unknown (estimated to be off by up to  $\pm 20$  °C). This wild variation is due to reflections in the curved glass surface giving wild variation in the IR thermal imaging. This problem needed to be resolved, however further experiments were performed before being made aware of these issues. None the less, they produce results of interest and so are described here.

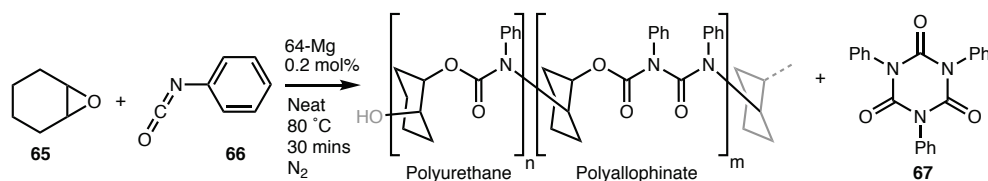
**Table 6.** Reaction of phenyl isocyanate (**66**) in VFD at 7 krpm, vs batch. However, the temperature of VFD reaction was later proven un-reliable.



Entry	65 (eq.)	66 (eq.)	64-Mg (mol %)	Vessel	Time (hours)	Temp. (°C)	Atmosphere	67	69
1	0	1	0.2	VFD 7 krpm	12	≈ 80 ?	N <sub>2</sub>	44 %	0 %
2	0	1	0.2	Batch	12	80	N <sub>2</sub>	74 %	0 %

Whilst un-aware of this flaw in the method for setting the temperature in the VFD, further experiments were performed (Table 7). Averaging the duplicates of VFD (entries 1 & 3) and batch (entries 2 & 4) showed that similar isolated yields of the polymer were being obtained the VFD @ 7 krpm (413 mg) and in batch (472.5 mg). Entries 6 & 7 highlight the importance of subtle changes in temperature, where a 15 °C difference in temperature resulted in 547 mg (95 °C) compared to 401 mg (80 °C) for batch processes.

**Table 7.** Comparisons of the 64-Mg catalysed reaction of epoxide (**65**) with isocyanate (**66**) in batch vs VFD. Entries 1 & 2 and 3 & 4 are duplicates of the same conditions, entry 5 is a lone experiment in the VFD at 4 krpm. Entries 6 & 7 are both in batch, comparing different temperatures (80 & 95 °C).



Entry	Solvent	65 (eq.)	66 (eq.)	64-Mg (mol %)	Vessel	Time (min)	Temp. (°C)	Atmosphere	Recovered Polymer (mg)
1	neat	1	1	0.2	VFD 7 krpm	30	≈ 80 ?	N <sub>2</sub>	436
2	neat	1	1	0.2	Batch	30	80	N <sub>2</sub>	383
3	neat	1	1	0.2	VFD 7 krpm	30	≈ 80 ?	N <sub>2</sub>	390
4	neat	1	1	0.2	Batch	30	80	N <sub>2</sub>	562
5	neat	1	1	0.2	VFD 4 krpm	30	≈ 80 ?	N <sub>2</sub>	499
6	neat	1	1	0.2	Batch	30	95	N <sub>2</sub>	547
7	neat	1	1	0.2	Batch	30	80	N <sub>2</sub>	401

The flawed VFD heating procedure was then identified and controlled for. The new method for calibrating the heating block used the melting point of vanillin (81 – 83 °C) and phenylenediamine (100 – 102 °C), rather than using an IR thermal imaging camera. Work by another lab member (Mr. Daniel Dein) showed that using an IR-camera to calibrate the heating unit created issues due to reflections in the cylindrical tube causing higher temperature readings compared to the actual temperature. Thus, the above experiments are *not accurate* comparisons. They are included here though, for multiple reasons. Firstly, these results show that if any difference between VFD and batch processing is subtle, if it exists. Secondly, these experiments highlight this sensitivity of the reactions for changes in temperature.

Knowing that the formation of the urea can be avoided under inert atmospheres (Figure 54), and that any polymer formed would not be instantly degraded (Figure 55), and with a reliable heating method established, the synthesis was then attempted. Batch vs VFD comparisons of the 64-Mg catalysed reaction of epoxide (**65**)

with isocyanate (**66**) was performed (Figure 56). Both VFD and batch methods used 1 equivalent each of the epoxide (**65**) and the isocyanate (**66**) as neat mixtures, and the catalyst loading was 0.2 mol%. From this it was found that neither the conversion after 30 minutes ( $\approx$  410 mg yield), nor the resulting selectivity of polyurethane versus polyallophinate ( $\approx$  80:20, polyurethane:polyallophinate) were affected by the VFD processing. This suggests that the all of the above apparent benefits of the VFD were indeed a result of the differences in temperature. For details on the  $^1\text{H-NMR}$  method for determining polyurethane and polyallophinate selectivity, see pg. 139.

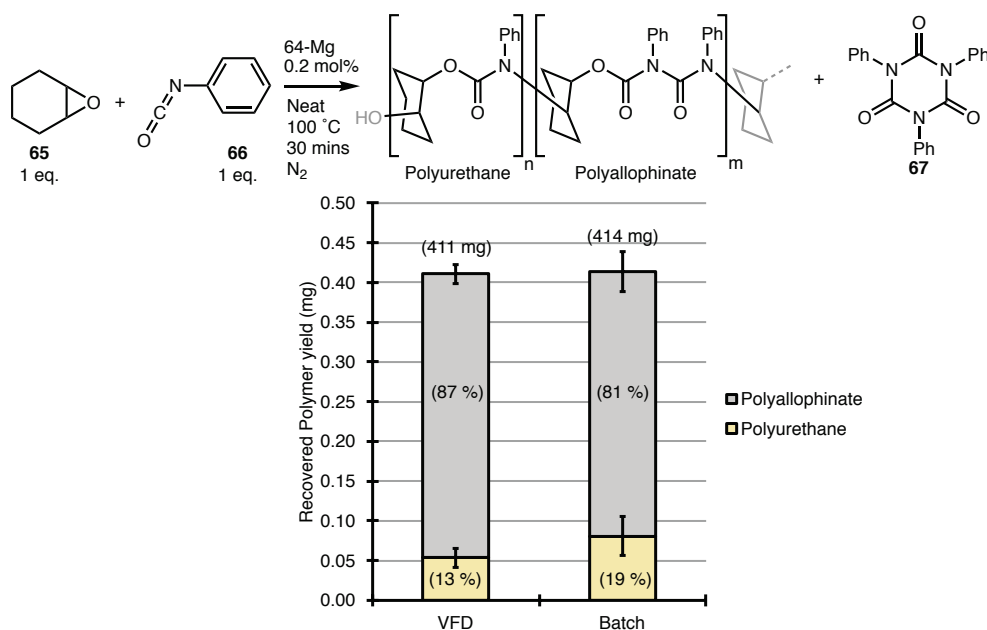


**Figure 56.** Comparisons of batch vs VFD processing for the **64-Mg** (7 mg, 0.2 mol %) catalysed polymerisation of **65** (0.5 mL, 4.9 mmol) and **66** (0.54 mL, 4.9 mmol). The recovered yields are reported as the weight (mg) due to the  $M_w$  not being possible to determine. Composition of the polymers were determined by  $^1\text{H-NMR}$  analysis (80 °C,  $\text{D}_6\text{-DMSO}$  - see pg. 139).

A variant of this reaction was also performed with the isothiocyanate (**68**) in place of the isocyanate (Figure 53C). This reaction completely avoids the formation of the allophinate, isocyanurate and urea by-products, thus avoiding the selectivity issues. This is promising for studying continuous flow applications of the VFD as performing continuous flow under inert atmosphere. Whilst excluding atmospheric water is possible, current VFD units are not air tight around the bearings and inert atmospheres can't be easily maintained. Another benefit for using the isothiocyanate is that the room temperature analysis by  $^1\text{H-NMR}$  becomes possible, due to better defined polymer peaks and also increased separations of the peaks of interest. This allows conversions to be determined from the crude reaction mixture. Next, the batch process was compared with the VFD process, for the **64-Mg** catalysed reaction of epoxide (**65**) with isothiocyanate (**68**, Figure 57). Again, 1 equivalent of each reagent were used neat, with 0.2 mol% catalyst loading. These comparisons show that there is no difference in the reactivity in batch vs VFD at either room temperature or at 100 °C.



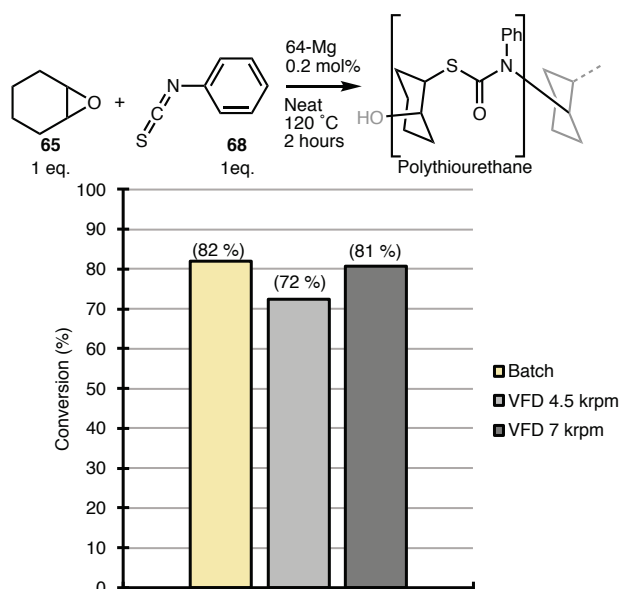


**Figure 57.** Comparisons of the conversions to the polythiourethane in batch vs VFD processing for the **64-Mg** (7 mg, 0.2 mol %) catalysed polymerisation of **65** (0.5 mL, 4.9 mmol) and **68** (0.59 mL, 4.9 mmol). Conversions determined by  $^1\text{H-NMR}$  analysis ( $\text{CDCl}_3$ ).

This work shows that the VFD does not have a major effect on the outcome of this reaction. Nevertheless, what has been shown is that these reactions are sensitive to temperature changes and care must be taken for direct comparisons to be achieved. The use of GPC for determination of the  $M_w$  is only possible for a sample containing single polymer product. This is not possible for the reactions of isocyanate **66**, due to the ratio of polyurethane to polyallophanate not being identical between each sample. It is possible for the polymer formed from the isothiocyanate (**68**). As such, further to the reactivity, the  $M_w$  as determined by GPC was compared between batch and VFD processing (Figure 58). This also shows that there is no major difference for these polymers in using batch processing or VFD processing. Although no direct benefit to the reaction outcome or to the rheology is found for VFD processing, these results are promising for the adaptation of existing polymerisation procedures as continuous flow VFD processes. The benefits of the VFD being scalability and enhanced safety from efficient heat transfer.<sup>102</sup> Although further work would be required to demonstrate a scaled-up application.

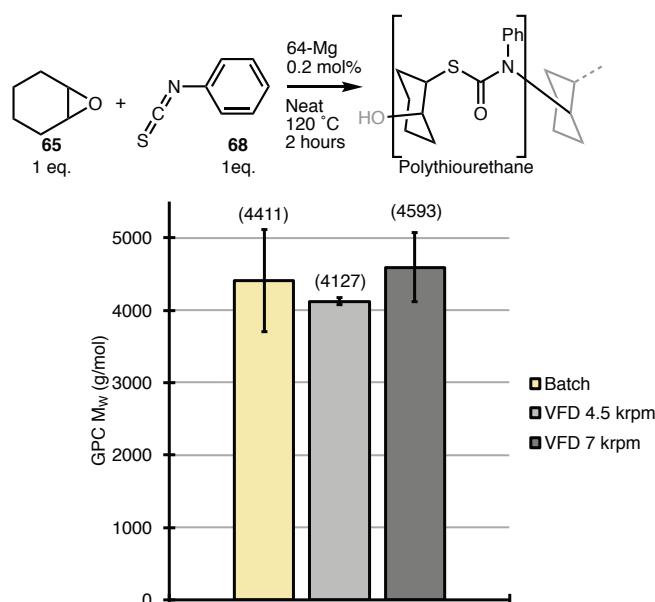


**Figure 58.** Comparisons of the  $M_w$  of polymers produced in batch vs VFD processing for the **64-Mg** (7 mg, 0.2 mol %) catalysed polymerisation of **65** (0.5 mL, 4.9 mmol) and **68** (0.59 mL, 4.9 mmol).  $M_w$  determined by GPC.

The **64-Mg** catalysed polymerisation of the epoxide (**65**) with a different isothiocyanate, hexyl-isothiocyanate (**70**) was attempted. However, there was no evidence for the reaction taking place (Figure 59). This reaction was attempted in order to increase the scope of this reaction. Linear hydrocarbons moieties on the polymer can drastically effect the rheology of the resulting polymer. As such this was attempted to be studied in the VFD, to no avail.

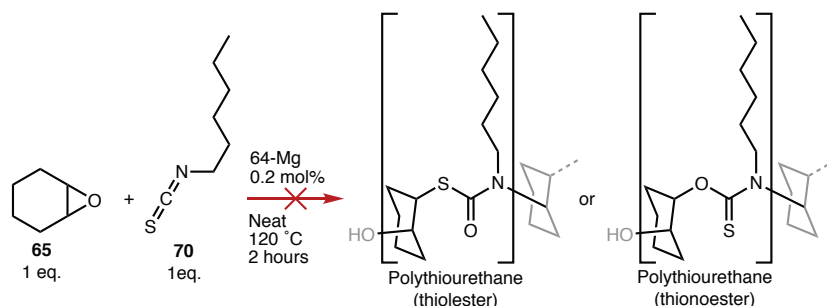


**Figure 59.** Attempted **64-Mg** catalysed polymerisation of epoxide **65** with isothiocyanate (**70**). This was not found to occur with the stated conditions. Only recovered starting material was identified by  $^1\text{H-NMR}$  analysis.

#### 4.1.2 – Conclusion for Synthesis of Polyurethane & Polythiourethane in VFD

The above results suggest that the VFD does not alter the outcome of the reaction. This is important to know if considering implementing any such reaction into a scalable VFD process. Knowing that conventional method will be able to be scaled up in flow without effecting the outcome is vital. Such processes could benefit from the inherent scalability of the continuous flow process. Furthermore, exothermic reactions may be able to be performed safely to the previously established heat transfer properties of the VFD.<sup>102</sup> However, no direct benefits were found here for VFD processing on small scales. Noting that although it is possible to have inert atmospheres in the confined modes of operation, it is currently difficult to achieve continuous flow whilst maintaining an inert reaction atmosphere. The synthesis of polythiourethane – the synthesis of which is tolerant to air – is more promising for scalable applications. Further work into engineering solutions for continuous flow

under inert atmospheres may be necessary. These include acquiring air tight bearings, and housing that only allows for reagent input, and no atmosphere to leak through. Only then would the VFD be able to facilitate continuous flow applications of the polyurethane reactions.

## 4.2 – Polycarbonate Synthesis in the VFD

Reacting CO<sub>2</sub> with epoxides to form carbonates or polycarbonates is a promising way to utilise CO<sub>2</sub> from industrial waste, reducing worldwide greenhouse gas concentrations.<sup>248-250</sup> As such, there has been a vast amount of research in this field.<sup>249, 251-253</sup> A major issue faced when scaling up such procedures is the mass transfer of the gaseous CO<sub>2</sub> into the liquid phase. This is avoided in some cases by using a gaseous epoxide, such as ethene oxide or propene oxide, resulting in a completely gaseous reaction. However, this limits the possible reagents that can be used – an issue when optimising for physical properties in the resulting polymer.<sup>254</sup> Continuous flow processing is promising for the scale up.<sup>255, 256</sup> Here, the VFD was employed as a method for the formation of polycarbonates from epoxides and CO<sub>2</sub> gas. Utilising the ability for the VFD to deliver gas reagents, it was hypothesised that the VFD could allow for the uptake of CO<sub>2</sub> gas in a highly efficient manner, thereby promoting reactions of the small molecule.

### 4.2.1 – Discussion on Polycarbonate Synthesis in the VFD

Initially, the model reaction studied was the **64-Mg** catalysed reaction of cyclohexene oxide (**65**) with CO<sub>2</sub>. Comparisons between batch vs VFD neat, at 100 °C were performed (Table 8). Averaging the result of these replicates shows that there is no major difference between the formation of the polycarbonate in batch (entries 2 & 4, 22 %) versus VFD (entries 1 & 3, 18 %). The small differences are in the error margin associated with analysis using <sup>1</sup>H-NMR.

**Table 8.** Comparisons of the conversion to the polycarbonate and cyclic carbonate (**71**) in batch vs VFD for the **64-Mg** catalysed reaction of the epoxide (**65**) with CO<sub>2</sub>. Conversions were determined by <sup>1</sup>H-NMR analysis.

Entry	<b>65</b> (eq.)	<b>64-Mg</b> (mol %)	Vessel	Time (hours)	Temp. (°C)	Atmosphere	Polycarbonate (conv. %)	<b>71</b> (conv. %)
<b>1</b>	1	0.2	VFD 7 krpm	2	100	CO <sub>2</sub>	19	0.6
<b>2</b>	1	0.2	Batch	2	100	CO <sub>2</sub>	20	0.5
<b>3</b>	1	0.2	VFD 7 krpm	2	100	CO <sub>2</sub>	17	0.3
<b>4</b>	1	0.2	Batch	2	100	CO <sub>2</sub>	23	0.8

The reaction of CO<sub>2</sub> with a different epoxide (**72**) was performed (Table 9). This again showed that there was no discernible difference in the formation of the polycarbonate between batch (entry 2, 5 %) versus VFD (entry 1, 10 %) processing. Following this, the reaction was then performed at 115 °C, in order to observe the effect of raising the temperature. This result shows a slightly higher conversion in VFD (entry 3, 27 %) compared to batch (entry 4, 15 %) processing. However, it was hypothesised that this may be due to increased evaporation of the epoxide in the VFD compared to the batch process. Even though the vessel was sealed with a rubber septum, the septum may be permeable to the epoxide at these temperatures.

**Table 9.** Comparisons of the conversion to the polycarbonate and cyclic carbonate (**73**) in batch versus VFD for the **64-Mg** catalysed reaction of the epoxide (**72**) with CO<sub>2</sub>. Entries 1 and 2 were performed at 100 °C, whilst entries 3 & 4 were at 115 °C. The conversion were determined by <sup>1</sup>H-NMR analysis.

Entry	<b>72</b> (eq.)	<b>64-Mg</b> (mol %)	Vessel	Time (hours)	Temp. (°C)	Atmosphere	Polycarbonate (conv. %)	<b>73</b> (conv. %)
1	1	0.2	VFD 7 krpm	2	100	CO <sub>2</sub>	0	10
2	1	0.2	Batch	2	100	CO <sub>2</sub>	0	4
3	1	0.2	VFD 7 krpm	2	115	CO <sub>2</sub>	0	27
4	1	0.2	Batch	2	115	CO <sub>2</sub>	0	15

To control for any evaporation of **72** in the VFD, an internal standard with very low volatility was employed. For this, trimethoxy benzene was chosen (boiling point is 255 °C). This standard was added with the reagents at the beginning of the reaction, and the reaction outcome was then monitored by <sup>1</sup>H-NMR (Figure 60). Indeed, this showed that there was less **72** present in the VFD after operating at 7 krpm for 12 hours at 100 °C, with only 16% remaining, when compared to a magnetically stirred batch sample for 12 hours at 100 °C which has 91% remaining. This suggests that 84% of the **72** had escaped from the reaction solution after 12 hours in the VFD, whilst only 9 % escaped in the batch method. This is consistent with visibly reduced amount of liquid remaining in the tube after the processing. Thus, the method used did not successfully seal the reaction mixture within the tube. This finding accounts for the slightly increased amount of polycarbonate relative to the **72** that was observed over 2 hours (Table 9, entries 3 & 4). As such, no benefit for using the VFD can be observed in this case.

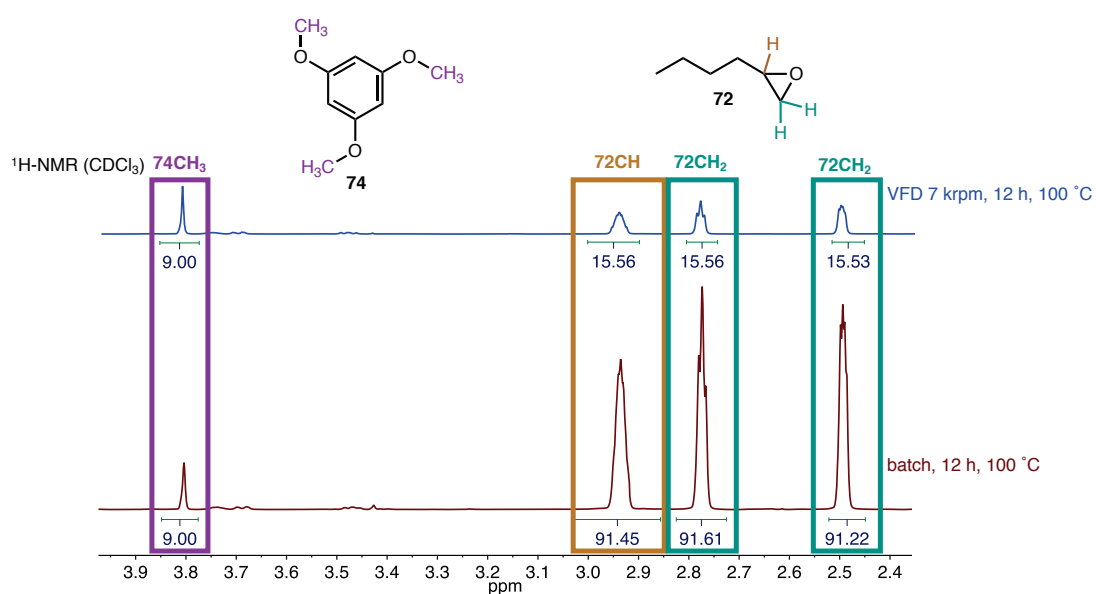


**Figure 60.** Stacked <sup>1</sup>H-NMR spectra of **72** operated in the both batch and the VFD@7 krpm for 12 hours at 100 °C. Also present is 0.01 equivalents of trimethoxy benzene (**74**). These were both performed in VFD tubes sealed with a rubber septum. This shows that the **72** permeates the rubber seal, and that more is lost in VFD processing compared to batch.

#### 4.2.2 – Conclusions and outlook for Polycarbonate Synthesis in VFD

The VFD remains a promising processing vessel for utilising CO<sub>2</sub> in the synthesis of carbonates or polycarbonates. However, the reactions here show that the scope is limited to reactions that occur at a fast-enough rate to be scaled into continuous flow. Ideally this is where the residence time is less than 3 minutes, allowing for a high throughput production of polymer per VFD unit. Since none of the reactions explored here give reasonable product yields in the required 3 minute processing time, none are suitable for direct implementation into continuous flow processes. Comparisons between VFD and batch processing were compared for the **64-Mg** catalysed polymerisation of epoxides with CO<sub>2</sub>. This work showed that using the salen derived Mg-ligated catalyst, low conversions at high temperatures were evident in both batch and VFD, and thus there is no advantage of using the VFD. Future work to find a reaction, with either a different catalyst or different epoxide-reagents could see the potential of the VFD to be realised for the utilisation of CO<sub>2</sub>. Examples of salen catalysts with various metal centres and have shown good utilisation of CO<sub>2</sub> for polycarbonates and also for producing cyclic carbonate. Examples of such salen catalysts exist with metal centres of zinc, aluminium, chromium, cobalt ruthenium (both Ru(II) and Ru(III)), manganese, tin and even metal-free organocatalysis.<sup>257</sup> Clearly there is much to explore within salen variants, and many such catalysts are promising for achieving the required reaction rates for continuous flow processing. Here, only the simple Mg-salen catalyst was trialled, as successful utilisation of this cheap and readily available catalyst would have benefits over some of the more expensive and difficult to obtain catalyst variants. This being unsuccessful, future work could start by exploring the myriad of salen variants, especially those shown to be more active. Beyond salen catalysts, there is a vast array of catalysts to choose from. Another suggested starting point are certain ionic liquids, which are promising catalysts for this process.<sup>257</sup> Especially when combined with an applied electrochemical potential.<sup>258</sup> Specific examples are that reported by F. Shi *et.al.* such as 1-*n*-butyl-3-methylimidazolium (BMIM) cations with tetrafluoroborate (BF<sub>4</sub>) anions.<sup>259</sup> Similar such work with applying external electric fields to this ionic liquid for Deils-Alder reactions are being developed in the Raston research group, spearheaded by Mr Matt Jellicoe Dr Daryl Jones. Applying expertise learned here may be directly applicable to using CO<sub>2</sub> in a continuous flow VFD process.

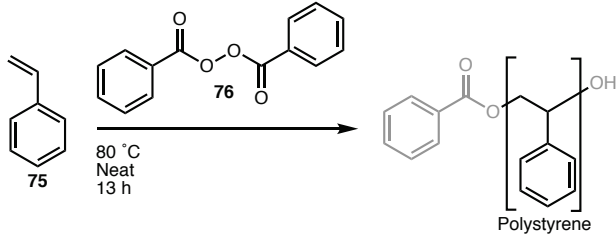
### 4.3 – Polystyrene Synthesis

Polystyrene is common model system for free-radical polymerisations. The chemistry of which is studied extensively, and the world-wide production is at massive proportions. Radical initiation is either achieved thermally, or photochemically. Continuous flow has much to offer to all radical initiated polymerisations,<sup>260</sup> and has been applied to the production of polystyrene.<sup>261, 262</sup> The synthesis of polystyrene in the VFD followed up on previous un-published work done in the group, involving spinning disk processing. This indicated that spinning-disk processing was able decrease the polydispersity of the resulting polystyrene compared to batch procedures. These findings were attempted to be studied in the VFD, and extrapolated for phot-initiation methods. Photochemical reactions have been previously demonstrated to benefit from VFD processing.<sup>241</sup>

#### 4.3.1 – Discussion on Polystyrene Synthesis in VFD

Firstly, thermal initiation was performed for the polymerisation of styrene (**75**). For this, benzoyl peroxide (**76**) was employed as the radical initiator and reactions were performed at 80 °C. Continuing from un-published work in the group performed in a spinning disk processor, a ratio of 240 equivalents of styrene was used with respect to the initiator (**76**). Comparisons were then made between batch and VFD processing (Table 10, entries 1 & 2). As can be observed, the yields are identical after 13 h in either the VFD and batch. It was shown that there is a difference of  $\approx 32,000 M_w$  of the product styrene from batch (entry 2) vs VFD (entry 1) processing. This result suggests that VFD processing may have an effect on the  $M_w$  of the polystyrene. However, some factors still need to be addressed. Firstly, this difference corresponds to a difference in the GPC retention time of only 14 seconds between the batch (8.868 min) vs VFD (9.105 min) processed polymers. This is within the run by run variance of the GPC instrument used. Secondly, since different heating instruments are used, it is not impossible that there is a slight difference in actual temperature, which would affect the  $M_w$ . Thus, more work is required to elucidate the effect of the VFD on this reaction. Another reaction was also performed with double the amount of initiator relative to **75** (entry 3). This showed that full yield was achieved, and the  $M_w$  was reduced by  $\approx 52,000 \text{ g/mol}$  ( $60,421 M_w$  for 140 equivalents compared to  $112,164 M_w$  for 240 equivalents). This simply highlights the importance of maintaining precise stoichiometry.

Table 10. Thermally initiated free radical polymerisation of styrene (**75**) with benzoyl peroxide (**76**).

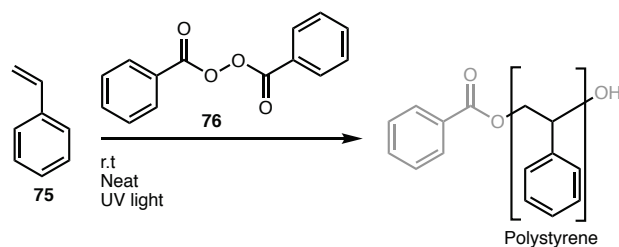


Entry	75 (eq.)	76 (eq.)	Vessel	Time (hours)	Temp. (°C)	Atmosphere	Yield (%)	GPC ( $M_w$ )
1	280	1	VFD 7 krpm	13	80	N <sub>2</sub>	99	80,576
2	280	1	Batch	13	80	N <sub>2</sub>	99	112,164
3	140	1	Batch	13	80	N <sub>2</sub>	99	60,421

Photo-initiated polystyrene synthesis was then explored. Initially, benzoyl peroxides (**76**) ability to act as a photo-initiator was studied in the VFD (Table 11). A series of control experiments established that **76** will not be able to initiate the reaction at room temperature either in the dark or with exposure to room lighting (entries

1 & 2). Further controls also showed that styrene alone will not react when exposed to light of either 254 nm or 364 nm wavelength (entries 3 & 4). Finally, the ability of **76** to photo-initiate the reaction is poor (entry 5).

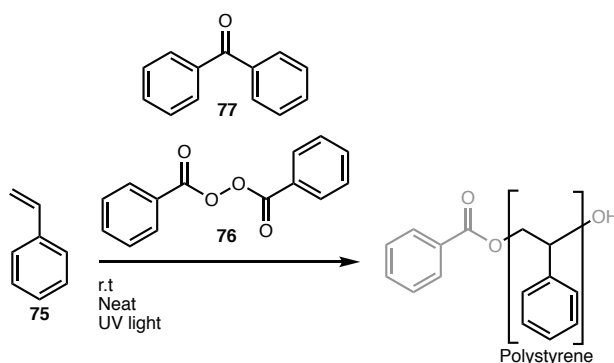
**Table 11.** Ability for benzoyl peroxide (**76**) to initiate the polymerisation of styrene (**75**) at room temperature. (n.r = no reaction).



Entry	<b>75</b> (eq.)	<b>76</b> (eq.)	Vessel	Time (hours)	Temp. (°C)	Atmosphere	Light	Yield (%)	GPC ( $M_w$ )
1	140	1	VFD 7 krpm	13	r.t	N <sub>2</sub>	Dark	n.r	-
2	140	1	VFD 7 krpm	13	r.t	N <sub>2</sub>	Room	n.r	-
3	1	0	VFD 7 krpm	24	r.t	N <sub>2</sub>	254 nm	n.r	-
4	1	0	VFD 7 krpm	24	r.t	N <sub>2</sub>	364 nm	n.r	-
5	140	1	VFD 7 krpm	13	r.t	N <sub>2</sub>	254 nm	30	5,497

The radical initiator **76** was then paired with a photosensitiser, benzophenone (**77**, Table 12). Controls were performed to see if the VFD could aid in the initiation, but this was not shown to occur in either room lighting (entry 1), or with a wavelength not suitable for **77** (254 nm, entry 2). The initiation was shown to take place at 364 nm – a wavelength suitable for **77**. However, this reaction was shown to give poor yield over 13 hours. This means that scaling up in a continuous flow procedure would be very slow. The low yield was thought to be due to the process relying on the reactive collision of the two initiators, both of which are at low concentrations.

**Table 12.** Benzophenone (**77**) as a photosensitiser for **76** to be a radical initiator of the polymerisation of **75**. (n.r = no reaction).

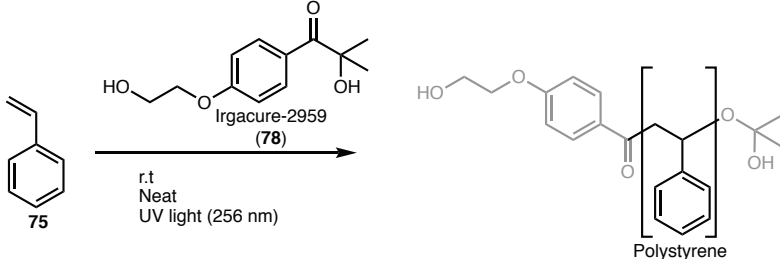


Entry	<b>75</b> (eq.)	<b>76</b> (eq.)	<b>77</b> (eq.)	Vessel	Time (hours)	Temp. (°C)	Atmosphere	Light	Yield (%)	GPC ( $M_w$ )
1	140	1	1.3	VFD 7 krpm	13	r.t	N <sub>2</sub>	Room	n.r	-
2	140	1	1.3	VFD 7 krpm	13	r.t	N <sub>2</sub>	254 nm	n.r	-
3	140	1	1.3	VFD 7 krpm	13	r.t	N <sub>2</sub>	364 nm	45	46,783

To remove the problem of a two-component initiator system, a single component photosensitiser & initiator was employed. For this, irgacure-2959 (**78**) was studied for the room temperature, photo-initiated polystyrene synthesis (Table 13). This was shown to give full conversion after 13 hours, and that there was no major difference in the  $M_w$  of the resulting polystyrene. However, no polymer was formed after 1 hour of processing

(No isolated powder, and no presence in the  $^1\text{H-NMR}$  spectrum of crude reaction mixture). Unfortunately, this rules out continuous flow with the current set up. Furthermore, in order to achieve good yields, the residence times required are beyond that of what available pumps can deliver. This would be accentuated by the fact that continuous flow would require a solvent to ensure a flow state.

**Table 13.** The polymerisation of styrene initiated by Irgacure-2959 (78).



Entry	75 (eq.)	78 (eq.)	Vessel	Time (hours)	Temp. (°C)	Atmosphere	Yield (%)	GPC ( $M_w$ )
1	280	1	VFD 7 krpm	13	r.t	N <sub>2</sub>	99	80,576
2	280	1	Batch	13	r.t	N <sub>2</sub>	99	90,456
3	280	1	VFD 7 krpm	1	r.t	N <sub>2</sub>	0	-

#### 4.3.2 – Summary and outlook for Polystyrene Synthesis in VFD

The above results show that the rate of the reactions for the experiments are too slow for effective scaling up under continuous flow in the VFD. These results also establish that the VFD does not dramatically affect the  $M_w$  of the produced polymers. This is surprising given that the VFD has previously been shown to alter the outcome of several reactions, including increasing the rate of organic reactions, along with the formation of polymers of BSA and glutaraldehyde.<sup>247</sup> There is still work to be done in achieving polymerisation under 1 hour, so that the scalability of the VFD can be demonstrated (as with the previously discussed polyurethane and polycarbonate synthesis). Suggested ways to achieve this are to use initiation methods that are far more active than the ones used here, such as high temperature methods and/or more exotic initiators. These were attempted to be avoided here in the first stage, focussing on green and low energy consumption methods. However, more energy- and resource intense processing may be necessary moving forward.



#### 4.4 - Conclusions and Outlook on Polymer Synthesis in the VFD

The findings discussed thus far in this chapter show that the synthesis of polymers in the VFD is possible. These methods are inherently scalable due to the continuous flow nature of the device. However, they do not alter the reaction outcomes, or the properties of the polymers produced. Previous work demonstrates that photochemical or biphasic systems are benefited from VFD processing.<sup>82, 102, 241</sup> VFD processing often proves offer a highly consistent, safe, scalable and efficient method for synthesis.<sup>82</sup> Here, these were attempted to be applied directly to the synthesis of a variety of polymers, however no immediate benefits were discovered for VFD processing. Specifically, the VFD was applied to overcome several issues identified in the synthesis of polyurethanes from di-isocyanates with epoxides, using Mg-salen based catalysts. It was hypothesised that the VFD may influence the reaction outcome, such as by enhancing the rates of the competing reactions and altering the selectivity for polyurethane compared to polyallophanate. However, this was not found to be the case. Failing this, the work was redirected to where a more-obvious rational for VFD enhancement would occur, that of utilising the large surface-area-to-volume-ratio (SA:V) for aiding reactions across gas/liquid reactions.<sup>102</sup> This was hypothesised to aid in the production of polycarbonate using epoxides and CO<sub>2</sub> gas. However, no benefit was found for the **Mg-64** catalysed reaction of CO<sub>2</sub> with either cyclohexene oxide or *n*-hexene oxide. It should be noted that these were attempted at ambient pressures, a feat rarely achieved with even the most state-of-the-art methods.<sup>263</sup> Despite establishing here that that reactivity is not benefited in the VFD compared to small scale batch processes, there may be benefits for large scale processes where mass transfer becomes an issue.<sup>207</sup> On the scales used here (1-2 mL), mass transfer of CO<sub>2</sub> into the reaction mixture is not a limiting factor in either VFD or batch methods. However, as scale increases, only the batch processes would be negatively affected, due to mass transfer problems.<sup>29</sup> Further work is required to achieve reactions rates that are fast enough to produce respectable yields in the  $\approx$  3 minute timescales required for continuous flow. Only then may the power of the VFD for scaling up gas/liquid reactions be demonstrated. Finally, a third system was studied, that of the radically initiated polystyrene synthesis from styrene. Both thermal- and photo-initiation was attempted, and no benefit of the VFD was found.

Despite no direct benefits to reaction outcomes or rheology, the VFD may still find use in the polymer industry, especially regarding overcoming safety issues, especially those associated with polyethylene plants, which have encountered recent tragedy regarding run-away exotherms.<sup>77</sup> In at least two cases, run-away exotherms and resulting explosions have claimed the lives of workers in polymer plants. Combining the above results with the high heat-transfer in the VFD, as seen in the epoxidation of alkenes,<sup>102</sup> where exotherms are completely avoided, are promising methods provide a safer working environment.

Further future work to be explored in the VFD, for the synthesis of polymers, is to take advantage of the increased mixing across phase boundaries in multiphase liquid/liquid reactions.<sup>102</sup> For this, the classic synthesis of the polyamide nylon-6,6 is worthy of a detailed study using the VFD. Nylon-6,6 can be formed from the reaction of adipoyl chloride (**79**) and hexamethylene diamine (**80**) (Figure 61). This is typically done in a biphasic water/hydrophobic solvent (typically chlorinated solvents) system.<sup>264</sup> This is known as the nylon rope trick – a classically known science demonstration. The polymer film forms at the interface of the two liquid phases, and a nylon string is created by simply drawing up the resulting polymer film with a spatula or pencil. The string can be coiled up and the polymer will be instantly replenished at the interface of the two liquids.

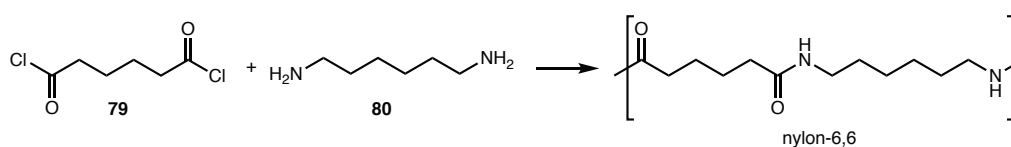
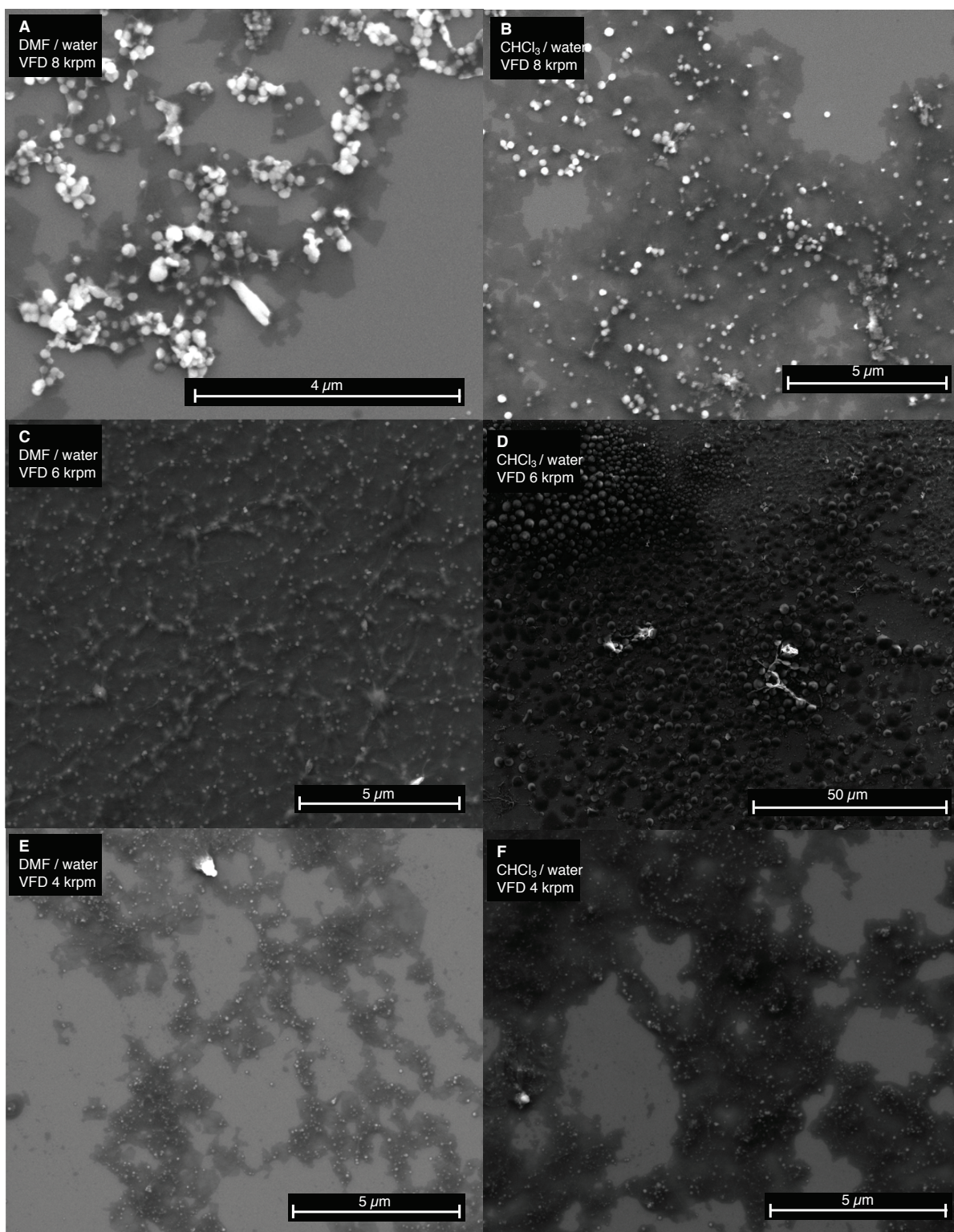


Figure 61. Synthesis of nylon-6,6 – The famous nylon rope trick.<sup>264</sup>

The VFDs generates a large surface-area-to-volume ratio (SA:V) between immiscible liquids, and can promote such reactions.<sup>102</sup> Progress in the Raston laboratory is advancing to being able to fully understand the fluid flow in the device, whereupon there will be a high level of predictability of the processing capabilities of the VFD, especially in the synthesis of polymers. These factors combined hold promise for aiding the synthesis of Nylon-6,6, especially by increasing the scalability. Furthermore, since the reaction would now be occurring at the interface of two liquid films of high shear stress, it may be the case that the VFD will affect the resulting properties – such as molecular weight. This is hypothesised to occur due to the fluid flows experienced in the microfluidic thin film. Complex eddies, liquid movements (such as Stewartson and Eckman layers) and other factors may be able to affect the rheology of the produced polymer. A foreseeable problem is that it may be difficult to obtain a solvent system so as to fully dissolve the produced polymer. If the product is not soluble in the solvents, then clogging of the VFD exit channels will occur and continuous flow will not be possible. However, if this is the case, this could also reveal some crucial information. For if the polymer formed is able to effectively create a mould of the interface of the two liquids, this could reveal information on the complexities of the interaction of the two layers. Information gained on the nature of the interaction of the highly stressed layers in the VFD would be highly beneficial, as only theories and speculations exist for the true nature of this aspect of biphasic systems in the VFD.

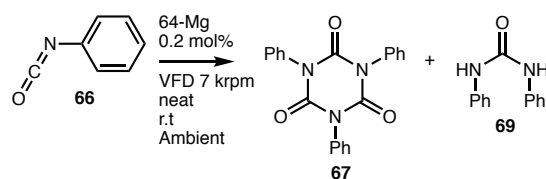
Further to this, preliminary results were obtained with the polymers studied here, which were found to produce novel composite compounds when mixed with graphene oxide in the VFD. This work was performed alongside Dr. Louis Adriaenssens and Mr Thaar Alharbi. As can be observed in Figure 62, the isolated and purified polyurethane appears to form spheres and coat the outside of the graphene oxide sheets when operated in the VFD. This was observed when the polyurethane is dissolved in DMF and mixed with graphene oxide in water resulting in a monophasic reaction solution. This is also found to be the case when the polyurethane is dissolved in chloroform, resulting in a biphasic reaction mixture when graphene oxide is in water. These results highlight the variance observed when changing the operational rotational speed of the VFD. Also, these indicate that the VFD's ability to facilitate reactions across phase boundaries holds true for materials processing. Furthermore, the spherical structures of the polyurethane formed at 8 krpm are highly uniform. These spheres are uniform and may have several real-world applications. Such as in the field of creating bacterial resistant coatings, such as for medical devices. Rough surfaces have shown to prevent the formation of biofilms. However, care must be taken as polymer micro-plastic beads pollute waterways.<sup>265</sup> This work is being explored further in a collaborative effort between the Raston and Adriaenssens research groups. Different polymers along with different carbon material, such as nanodiamonds are being combined to form novel composite materials. Following this, the physical properties such as conductivity and microbial resistance are to be recorded for performance in a variety of applications.



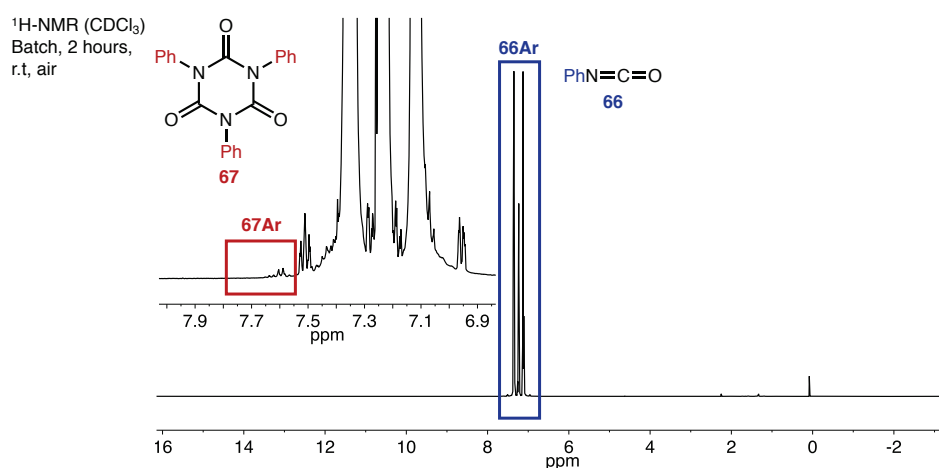
**Figure 62.** SEM images of polyurethane / graphene oxide composites formed after continuous flow processing in VFD at 45° tilt angle. Two feeds were employed, one of polyurethane solution the other of the graphene oxide solution. The graphene oxide was dissolved in water, the polyurethane was dissolved in either DMF (A, C & E) or CHCl<sub>3</sub> (B, D & F)) as indicated in image annotation. Each feed was delivered by syringe pump to the base of the rotating tube at a rate of 0.5 mL/min for a total flow rate of 1 mL/min (≈ 20 minute residence). Rotational speeds used were 8 krpm (A & B), 6 krpm (C & D) and 4 krpm (E & F), as specified in image annotation.

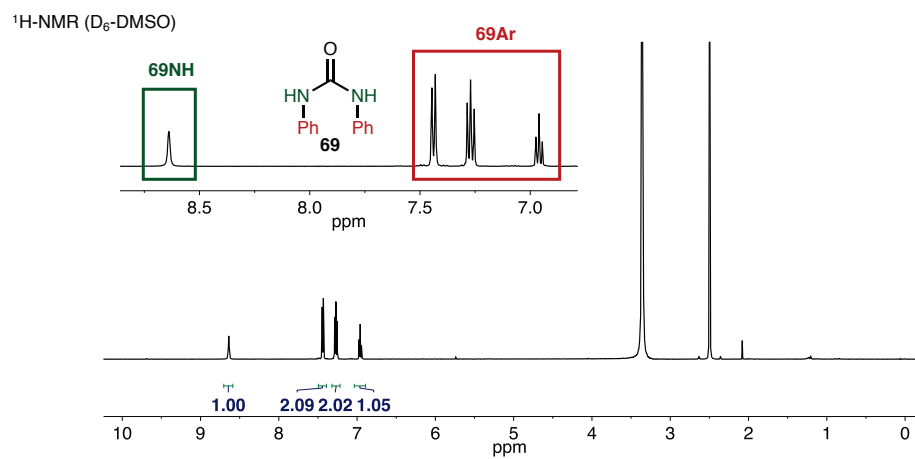
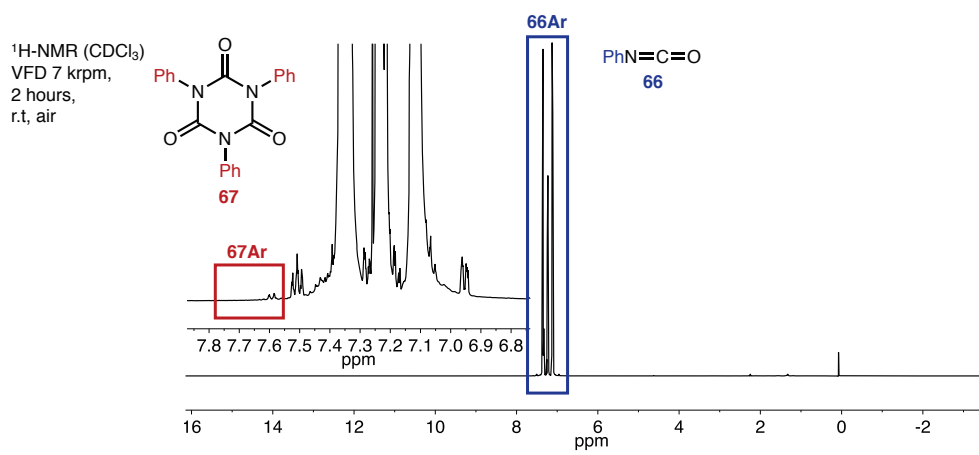
## 4.5 - Experimental Details and Spectra

### 4.5.1 - Controls for the Formation of Urea 69

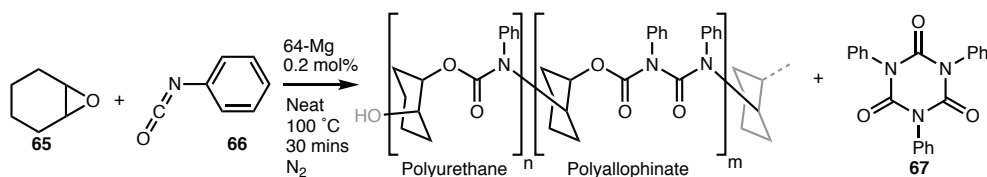


These experiments established that the reactions with catalysts **64-Mg** and **66** require the exclusion of water. To a VFD tube, the catalyst **64-Mg** (13.1 mg, 0.02 mmol) was dissolved in **66** (1 mL, 9.15 mmol). Half of this solution (0.5 mL) was transferred to a separate VFD tube with a magnetic stirrer bar. The tube with the stirrer bar was stirred for 2 hours at room temperature, whilst the other tube was operated at 7 krpm at room temperature for 2 h. After 2 hours, stirring of both tubes was ceased and a small aliquot ( $\approx 250 \mu\text{L}$ ) was taken and diluted in  $\text{CDCl}_3$  for  $^1\text{H-NMR}$  analysis. This showed trace amounts of **67** had formed in both VFD and Batch. However, for the tube operated in the VFD, small crystals were observed on the surface of the tube. These crystals were insoluble in  $\text{CDCl}_3$ , so  $^1\text{H-NMR}$  analysis was performed in  $\text{D}_6\text{-DMSO}$  - revealing diphenyl urea (**69**). When these experiments were repeated in oven-dried tubes and performed under an inert atmosphere, no **69** was found to form.

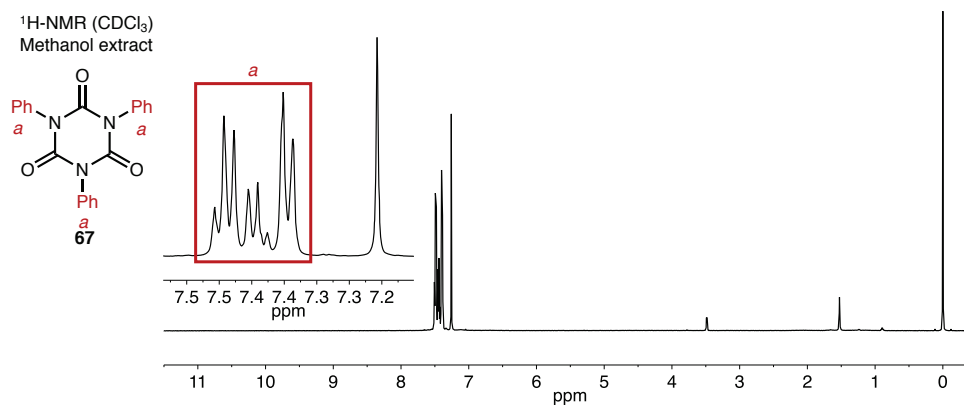
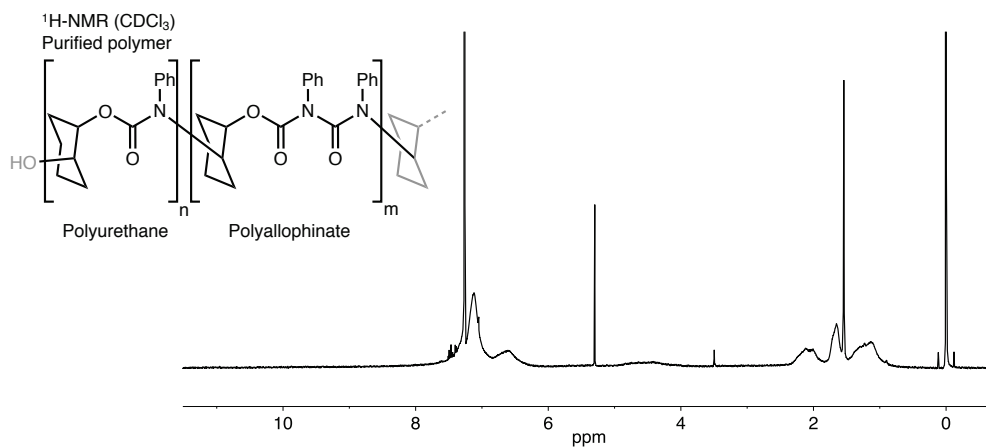
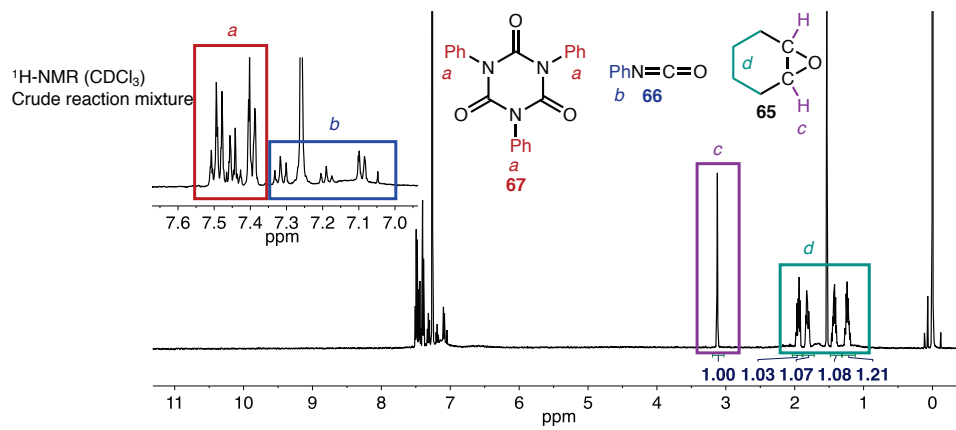




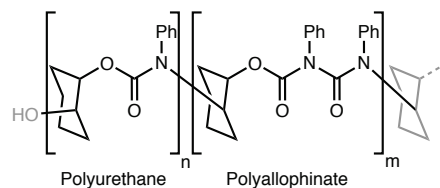
#### 4.5.2 – Polyurethane and Polyallophinate Formation in Batch vs VFD



Two 20 mm (OD) VFD tubes were dried in an oven at 160 °C. To one of these tubes, the catalyst **64-Mg** (14 mg,  $1.98 \times 10^{-4}$  mol), followed by cyclohexene oxide (**65**) (1 mL, 9.88 mmol) and phenyl isocyanate (**66**) (1.08 mL, 9.88 mmol) were added and homogenised by gently mixing. Half of this reaction solution was then transferred into the other dried VFD tube. Care was taken to maintain dry conditions through this transfer. One of these reaction mixtures was magnetically stirred whilst the other was rotated in a VFD at 7 krpm for 1 hour at 100 °C. After the allocated reaction time, both reaction mixtures were allowed to cool to room temperature. At this stage, a sample of this crude reaction mixture was taken for <sup>1</sup>H-NMR analysis (see below). Once cooled the reaction mixture was taken up into CH<sub>2</sub>Cl<sub>2</sub> and the reaction products were precipitated by dropping into a stirred vial of hexane (150 mL). The white solid was isolated by filtration and washed with MeOH (3 x 10 mL). This resulted in a white solid, confirmed to be the polymer by NMR, GPC, TGA, IR and MS analysis, spectra found below. Note that the MeOH extract is shown to be the **67** (see below).



### 4.5.3 - Polyurethane and Polyallophinate Selectivity by $^1\text{H-NMR}$



The **64-Mg** catalysed reactions of **66** and **65** results in a block co-polymer chain containing  $n$  amount of polyurethane and  $m$  amount of polyallophinate.  $^1\text{H-NMR}$  was used to determine the ratio between these two. Room temperature spectra are not able to give this ratio, as the polymer peaks are too broad. Spectra at  $90^\circ\text{C}$  are suitable. This method uses the integrals of the peaks for the phenyl compared to either the methyne or the methyl peaks. Each repeating unit of polyurethane will contribute phenyl:methyne:methyl in the ratio of 5:2:8, whereas each polyallophinate will contribute a ratio of 10:2:8. Thus, taking the ratio of phenyl:methyl group nuclei, a pure sample of the polyallophinate would be 10:8, so any increasing amount of polyurethane would decrease the phenyl contribution whilst maintaining the methyl contribution. The following equations show the workings for determining the fraction of polyurethane ( $U$ ) in the polymer produced in the VFD at 7 krpm at  $100^\circ\text{C}$  for 30 minutes.

$$1 - A = U$$

$\therefore$

$$10A + 5(1 - A) = 9.35$$

$$10A + 5 - 5A = 9.35$$

$$5A + 5 = 9.35$$

$$5A = 4.35$$

$$A = 0.87$$

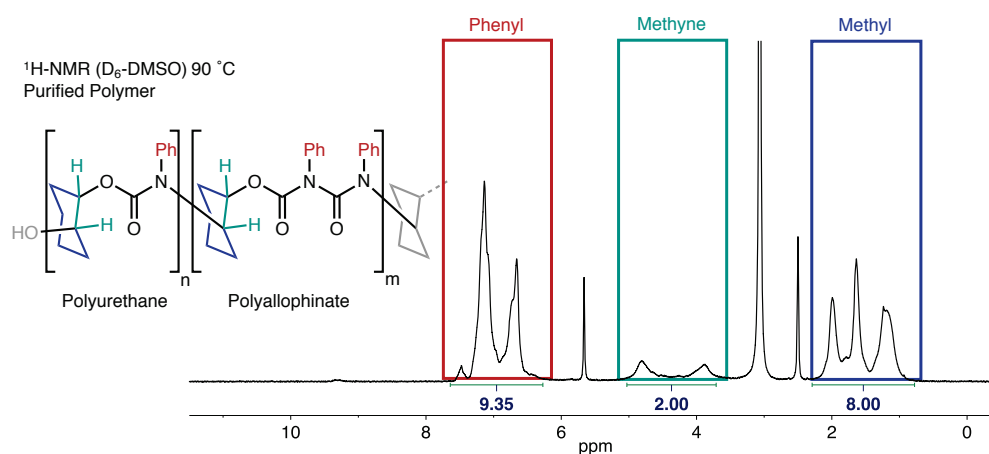
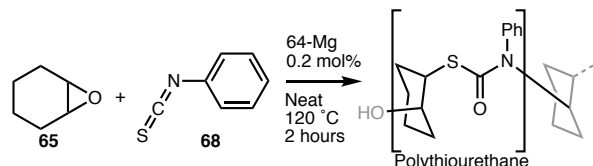


**Figure 63.**  $^1\text{H-NMR}$  ( $\text{D}_6\text{-DMSO}$ ,  $90^\circ\text{C}$ ) spectrum of the polymer produced from **65** and **66** in the VFD at 7 krpm, at  $100^\circ\text{C}$  for 30 minutes (Figure 56). Highlighted are the Phenyl, methyne and methyl contributions from each of the polyurethane and polyallophinate fractions.

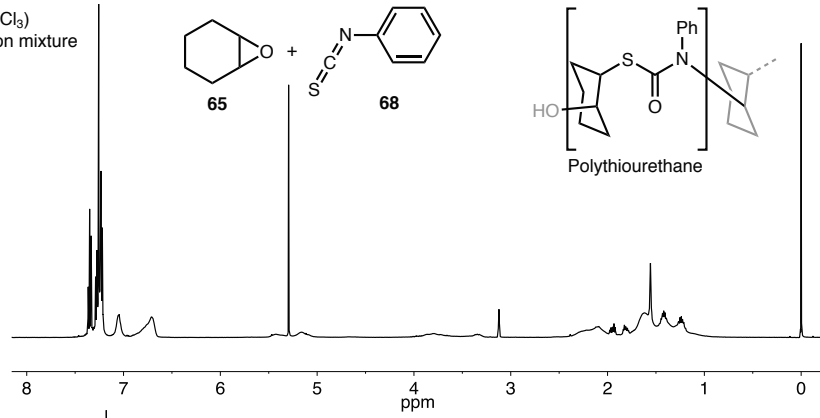


#### 4.5.4 - Polythiourethane Procedure for Batch vs VFD

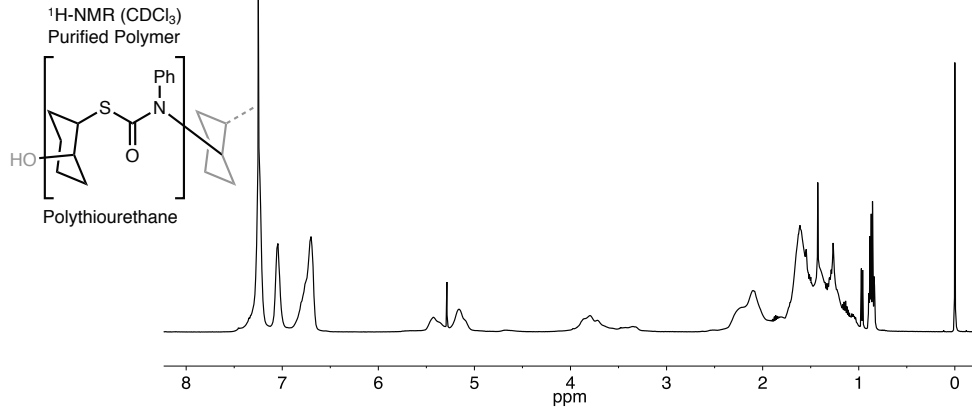


Two 20 mm (OD) VFD tubes were dried in an oven at 160 °C. To one of these tubes, the catalyst **64-Mg** (14 mg,  $1.98 \times 10^{-4}$  mol), followed by cyclohexene oxide (**65**) (1 mL, 9.88 mmol) and phenyl isothiocyanate (**68**) (1.18 mL, 9.88 mmol) were added and homogenised by gently mixing. Half of this reaction solution was then transferred into the other dried VFD tube. Care was taken to maintain dry conditions through this transfer. One of these reaction mixtures was magnetically stirred whilst the other was rotated in a VFD at 7 krpm for 1 hour at 100 °C. After the allocated reaction time, both reaction mixtures were allowed to cool to room temperature. At this stage, a sample of this crude reaction mixture was taken for  $^1\text{H-NMR}$  analysis. Once cooled the reaction mixture was taken up into  $\text{CH}_2\text{Cl}_2$  and the reaction products were precipitated by *slowly* dripping into a stirred vial of hexane (150 mL). The white solid was isolated by filtration and washed with MeOH (3 x 10 mL). This resulted in a white solid, confirmed to be the polymer by NMR, spectra found on the following page. GPC was performed on the purified polymer using the following method.

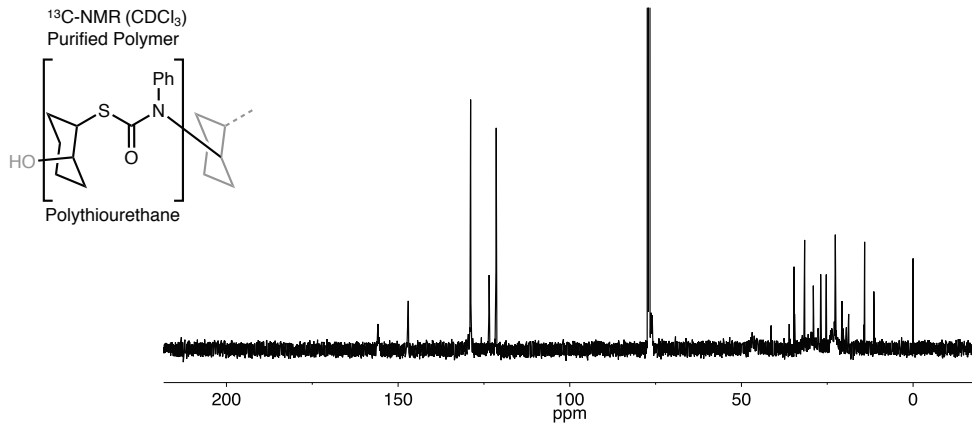
<sup>1</sup>H-NMR (CDCl<sub>3</sub>)  
Crude reaction mixture



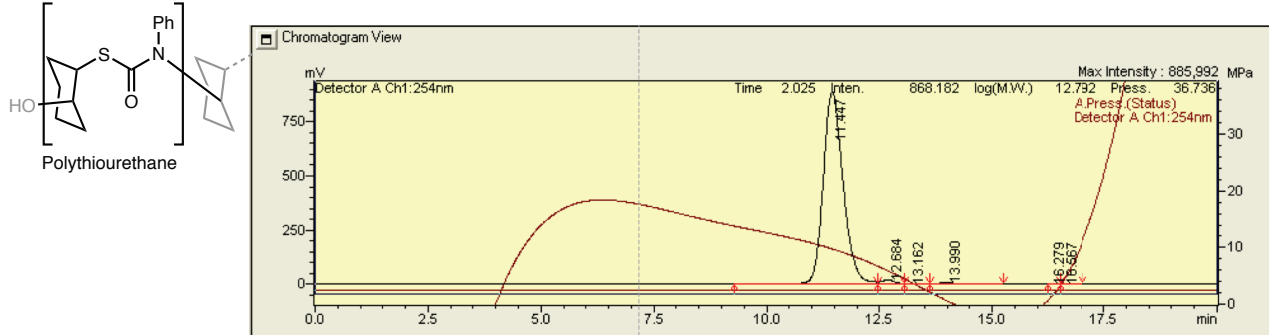
<sup>1</sup>H-NMR (CDCl<sub>3</sub>)  
Purified Polymer



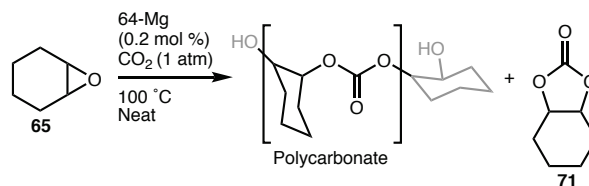
<sup>13</sup>C-NMR (CDCl<sub>3</sub>)  
Purified Polymer



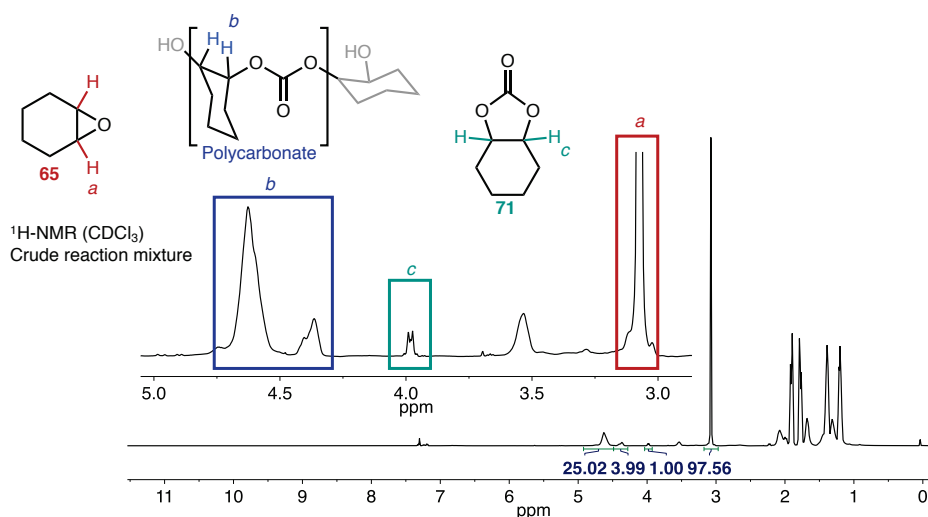
GPC (THF)  
Purified Polymer



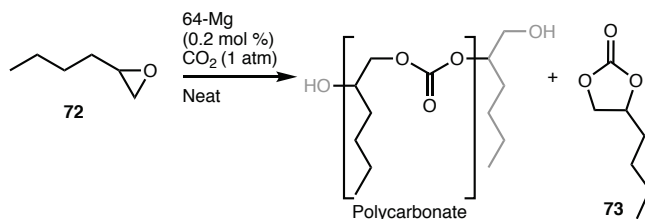
#### 4.5.5 – Polycarbonate Synthesis From **65** and CO<sub>2</sub> in Batch vs VFD



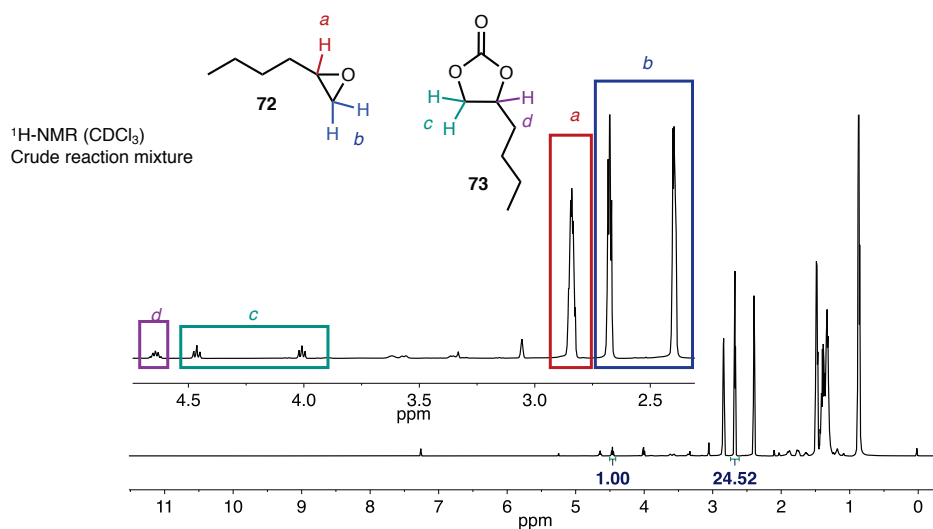
Two 20 mm (OD) VFD tubes were dried in an oven and then, after purging atmosphere under reduced pressure, were placed under atmosphere of CO<sub>2</sub> gas. To one of these tubes, a stirrer bar and catalyst **64-Mg** (14 mg,  $1.98 \times 10^{-4}$  mol) were added. To the same tube, still under CO<sub>2</sub>, the cyclohexene-oxide (**65**) was added (2 mL, 1.98 mol). Half (1 mL) of this solution was then transferred to the other tube. The tube with a stirrer bar was mixed at 100 °C for the desired time, whilst the other was operated in the VFD at 7 krpm for the same period of time at 100 °C. Upon completion of the desired time, both tubes were cooled to room temperature. A small sample was dissolved in CDCl<sub>3</sub> for NMR analysis at this point. The remaining the product was dissolved in CH<sub>2</sub>Cl<sub>2</sub> ( $\approx$  5 mL) and then *slowly* dripped into a stirred solution of hexane ( $\approx$  50 mL). The product crashed out as a white precipitate and was collected by filtration. This solid was then washed with MeOH (3 x 15 mL). Removal of trace solvent under reduced pressure resulted in a white powder.



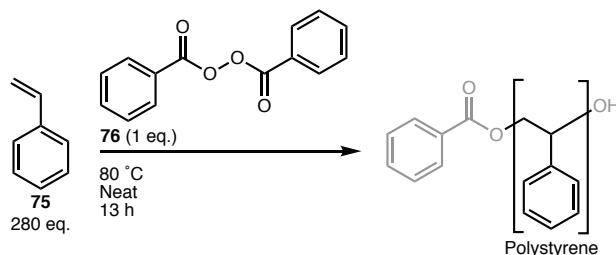
#### 4.5.6 – Polycarbonate Formation from 72 and CO<sub>2</sub> in Batch vs VFD



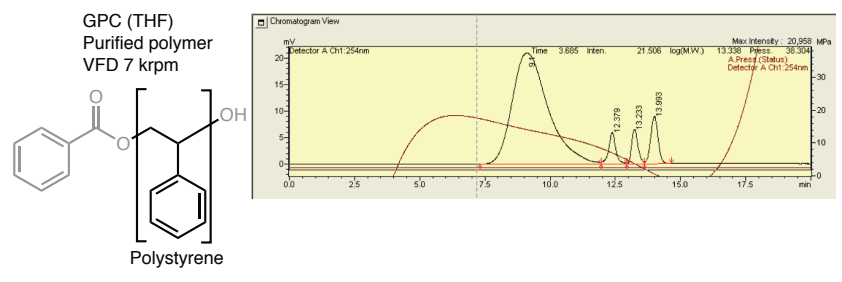
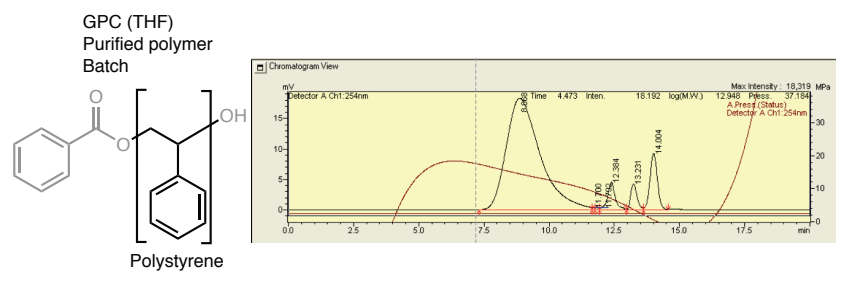
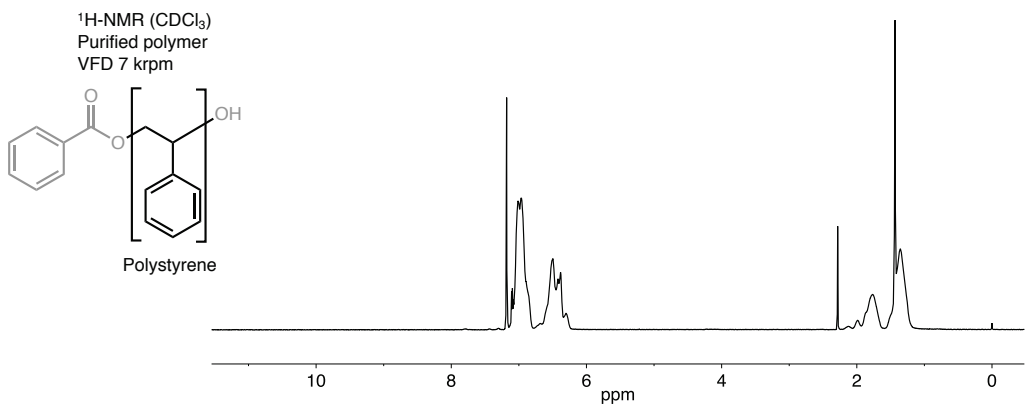
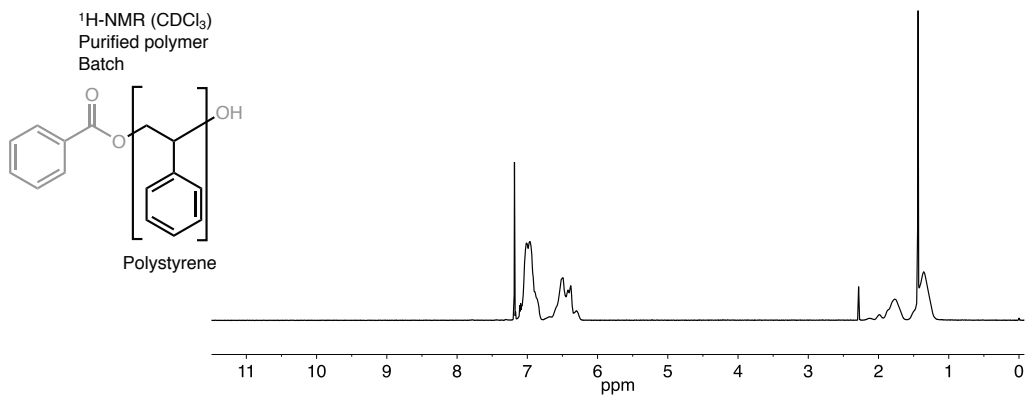
Two 20 mm (OD) VFD tubes were dried in an oven and then after purging atmosphere under reduced pressure were placed under atmosphere of CO<sub>2</sub> gas. To one of these tubes, a stirrer bar and catalyst **64-Mg** (24.4 mg, 3.4 x 10<sup>-5</sup> mol) were added. To the same tube, still under CO<sub>2</sub>, the hexene-oxide (**72**) was added (2 mL, 17 mmol). Half (1 mL) of this solution was then transferred to the other tube. The tube with a stirrer bar was mixed at 120 °C for the desired time, whilst the other was operated in the VFD at 7 krpm for the same period of time at 120 °C. Upon completion of the desired time, both tubes were cooled to room temperature. A small sample was dissolved in CDCl<sub>3</sub> for NMR analysis at this point. The remaining the product was dissolved in CH<sub>2</sub>Cl<sub>2</sub> (≈ 5 mL) and then slowly dropped into a stirred solution of hexane (≈ 50 mL). The product crashed out as a white precipitate and was collected by filtration. This solid was then washed with MeOH (3 x 15 mL). Removal of trace solvent under reduced pressure resulted in a white powder.



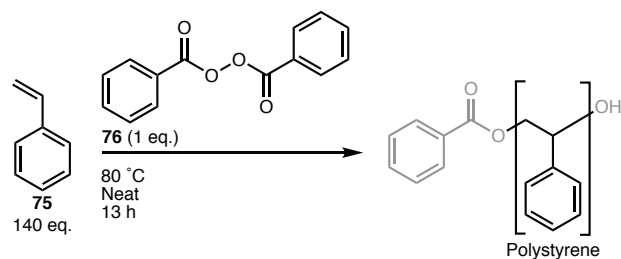
#### 4.5.7 - Thermally Initiated Polystyrene Synthesis, at 280 Equivalents of BPO



Two 20 mm (OD) VFD tubes were dried in an oven and then, after purging atmosphere under reduced pressure, were placed under inert atmosphere of  $N_2$  gas. To one of these tubes, a stirrer bar and benzoyl peroxide (22.5 mg, 0.09 mmol) were added. To the same tube, still under  $N_2$ , styrene (**75**) was added (3 mL, 26.2 mmol). Half (1.5 mL) of this solution was then transferred to the other tube. The tube with a stirrer bar was stirred at 80 °C for 13 h, whilst the other was operated in the VFD at 7 krpm for the same period of time at 80 °C. Upon completion of the desired time, both tubes were cooled to room temperature. After 13 hours, reaction mixture had turned solid. A small sample was dissolved in  $CDCl_3$  for NMR analysis at this point. Purification of the remaining the product was performed dissolving in toluene (25 mL) and then *slowly* dripping into a stirred solution of cold methanol ( $\approx$  50 mL). The product crashed out as a white precipitate and was collected by filtration. Removal of trace solvent under reduced pressure resulted in a white amorphous powder.  $^1H$ -NMR and GPC analysis was then performed, see spectra below.

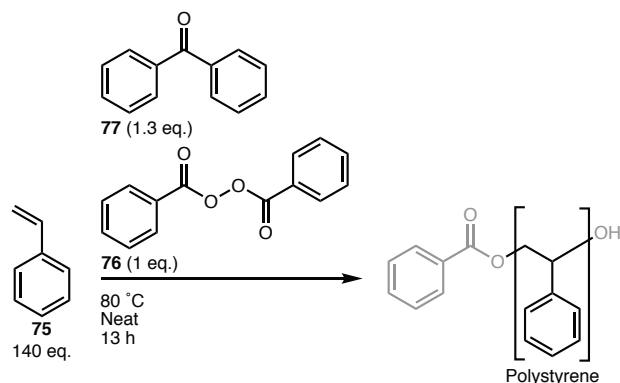


#### 4.5.8 - Thermally Initiated Polystyrene Synthesis, at 140 Equivalents of BPO



Two 20 mm (OD) VFD tubes were dried in an oven and then, after purging atmosphere under reduced pressure, were placed under inert atmosphere of  $N_2$  gas. A solution of benzoyl peroxide (75.5 mg, 0.31 mmol) and styrene (5 mL, 43.7 mmol) was prepared and kept over ice. Aliquots (1 mL) of this solution were then transferred to each of the dry VFD tubes, one of which contained a magnetic stirrer bar. The tube with a stirrer bar was stirred at 80 °C for 13 h, whilst the other was operated in the VFD at 7 krpm for the same period of time at 80 °C. Upon completion of the desired time, both tubes were cooled to room temperature. After 13 hours, reaction mixture had turned solid. A small sample was dissolved in  $CDCl_3$  for NMR analysis at this point. Purification of the remaining the product was performed dissolving in toluene (25 mL) and then *slowly* dripping into a stirred solution of cold methanol ( $\approx$  50 mL). The product crashed out as a white precipitate and was collected by filtration. Removal of trace solvent under reduced pressure resulted in a white amorphous powder.

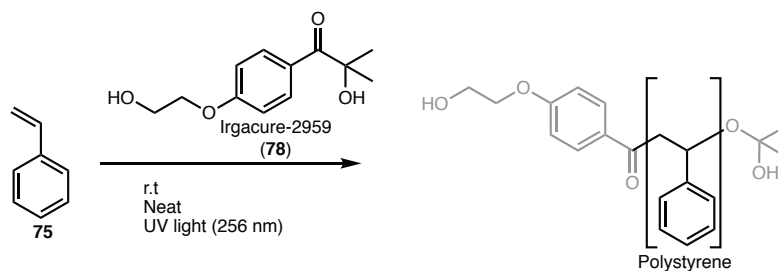
#### 4.5.9 – Photo-initiated Polystyrene Synthesis with Benzophenone and Benzoyl Peroxide



Two 20 mm (OD) VFD tubes were dried in an oven and then, after purging atmosphere under reduced pressure, were placed under inert atmosphere of N<sub>2</sub> gas. A solution of benzoyl peroxide (**76**) (75.5 mg, 0.31 mmol), benzophenone (**77**) (75.5 mg, 0.41 mmol) and styrene (**75**) (5 mL, 43.7 mmol) was prepared and kept over ice. Aliquots (1 mL) of this solution were then transferred to each of the dry VFD tubes, one of which contained a magnetic stirrer bar. The tube with a stirrer bar was stirred at 80 °C for 13 h, whilst the other was operated in the VFD at 7 krpm for the same period of time at 80 °C. Upon completion of the desired time, both tubes were cooled to room temperature. After 13 hours, reaction mixture had turned solid. A small sample was dissolved in CDCl<sub>3</sub> for NMR analysis at this point. Purification of the remaining the product was performed dissolving in toluene (25 mL) and then *slowly* dripping into a stirred solution of cold methanol (≈ 50 mL). The product crashed out as a white precipitate and was collected by filtration. Removal of trace solvent under reduced pressure resulted in a white amorphous powder.



#### 4.5.10 - Photo-initiated Polystyrene Synthesis with Irgacure-2959



Two 20 mm (OD) VFD tubes were dried in an oven and then after purging atmosphere under reduced pressure were placed under inert atmosphere of N<sub>2</sub> gas. To one of these tubes, a stirrer bar and irgacure-2959 (**78**) (13.9 mg, 6.12 x10<sup>-5</sup> mol) were added. To the same tube, still under N<sub>2</sub>, styrene (**75**) was added (2 mL, 17.5 mmol). Half (1 mL) of this solution was then transferred to the other tube. The tube with a stirrer bar was mixed at room temperature with exposure to a UV lamp (256 nm) for the desired time, whilst the other was operated in the VFD at 7 krpm for the same period of time at 80 °C. Upon completion of the desired time, both tubes were removed from the UV light source. A small sample was dissolved in CDCl<sub>3</sub> for NMR analysis at this point. The remaining the product was dissolved in toluene (25 mL) and then *slowly* dripped into a stirred solution of cold methanol (≈ 50 mL). The product crashed out as a white precipitate and was collected by filtration. Removal of trace solvent under reduced pressure resulted in a white powder.

## Chapter 5 – Oxidative Sulphitolysis (OS)

*This work was done jointly with Ms. Emily M. Crawley*

Oxidative sulphitolysis (OS) is the cleavage of a sulphur-sulphur bond, whilst increasing the oxidation state of both sulphurs.<sup>266</sup> This is typically achieved by reaction of a disulphide with tetrathionate and sulphite ions (Figure 64). This holds particular promise for the purification of proteins containing disulphide bridging, such as insulin.<sup>267, 268</sup> When insulin is produced, it typically contains misfolded insulin as a by-product. OS can be used to cleave all cysteine linkages, and simultaneously protect the resulting thiols with sulphite groups. This protection allows for greater tolerance in the purification steps, and can be then be easily reduced back to give the disulphides of correctly folded insulin.

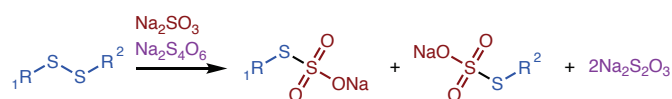


**Figure 64.** General scheme for the oxidative sulphitolysis (OS) reaction, cleaving a disulphide with sulphite and tetrathionate. This process results in sulphite protected thiols.

Despite OS holding promise for protein purifications, there is limited reported work on this procedure, and it has fallen out of favour in recent times. Furthermore, there is little known about the reaction mechanism, and the exact role of each reagent is not known, and therefore can't be optimised for. It was hoped here that utilising VFD methods could re-ignite interest into this reaction and provide a green, effective method for protein purification. In the first instance, the effect of the VFD was studied on small molecule systems (cysteine), and moved up in complexity to study insulin. This approach was taken to identify if the VFD can give control to the reactivity of breaking the disulphide bridge, and to decouple any such effect from macromolecular effects that the VFD may be imparting.

### 5.1 - Oxidative Sulphitolysis in the VFD

The VFD was hypothesised to aid in the OS of insulin. The chief reason amongst this was thought to be the mechanical shear in the VFD physically aiding in the separation of the 2 peptide chains of insulin. The VFD has also extensively shown to be beneficial in achieving the correct folding of proteins.<sup>86</sup> It was demonstrated that the VFD aided in folding four proteins back to their natural state – including the “unboiling” of hen egg white lysozyme. This was successful with much lower dilutions compared to batch methods, achieving refolding times up to 100 times faster. The methodology as to how the VFD aids in this refolding is unknown, although it is a major research effort in the Raston laboratory, in establishing a detailed understanding of the fluid flow in the first instance. Although the underlying mechanism is unknown, several theories have been proposed. Firstly, the shear forces and flow vectors experienced within the stressed microfluidic liquid films may twist, and bend the protein in ways that facilitate re-arranging of the quaternary structure of proteins. Applying this to the OS of insulin, imparting mechanical energy could essentially aid in overcoming the energy barrier to bond cleavage, if the structure is altered in such a way as that the disulphide linkages experience extra strain. This may allow for less harsh conditions, and also may lower processing times for the disulphide cleavage. Achieving this would make OS a more promising choice for purifying proteins with disulphide

linkages. Once the two strands of insulin come apart (Figure 65), and are capped with  $-\text{SO}_3^-$  groups, they are then protected for any purification steps. Upon obtaining the purified A- and B-chains, they then would need to be re-combined. This reduction is typically achieved with dithiothreitol (DTT) or similar reducing agent. The VFD may also be able to assist this reduction step, rationalised in the same manner as how the VFD was able to facilitate the correct folding of hen egg white lysozyme.<sup>86</sup> Here, the culmination of the unique conditions experienced in the VFD processing (shear, vibrational effects, fluid flow vectors ect.) aided the protein to return to its correctly folded state. This same rationale may also facilitate the correct refolding and orientation of the two insulin chains, aiding in the reduction step. It is hypothesised here that the VFD may assist in the breaking down of insulin, or in the re-formation of insulin in the reductive step. If the VFD can assist in one or both of these steps, it could be highly beneficial for insulin production applications.

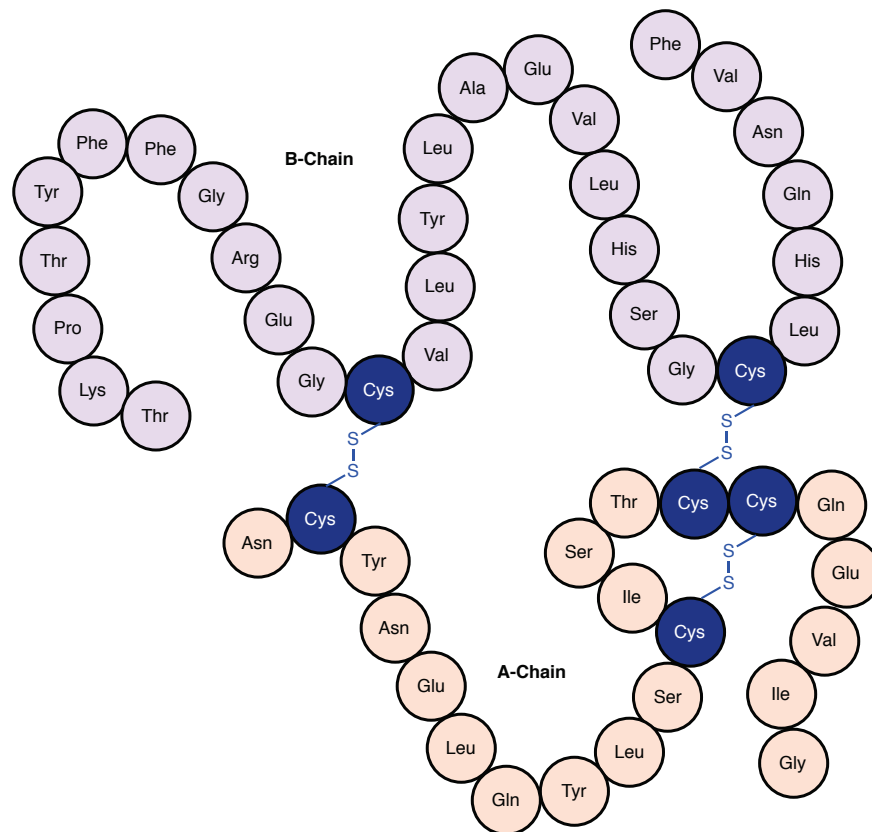


**Figure 65.** Representation of insulin, highlighting the two chains that are linked through two disulphide bridges. These are the A-chain and the B-chain. There is also a disulphide bridge in the A-chain

### 5.1.1 – Discussion on the OS of L-Cystine

Due to previous unexpected and remarkable results in small molecule transformations in the VFD,<sup>82</sup> the chemical nature of the OS in the VFD was first studied using the simplest peptide system possible, *L*-cystine (**82**). The sulphitolysis of **82** to produce sulphinated-cysteine (**83**) was performed in the VFD and compared to batch processing. Due to the inability to achieve HPLC separation in the available columns, the analysis of this reaction was performed by <sup>1</sup>H-NMR spectroscopy. For this, larger concentrations were required compared to published procedures. As a starting point, rotational speeds of 4, 6, 7.5 and 9 krpm were chosen. These speeds were selected to give a range of shear regimes. Also, performing such reactions at multiple speeds is crucial for finding any dependence on rotational speed, which is a re-occurring theme in VFD processing.<sup>96</sup> The tilt angle was maintained at 45° as this has proven optimal in several studies of small scale synthesis.<sup>82</sup>

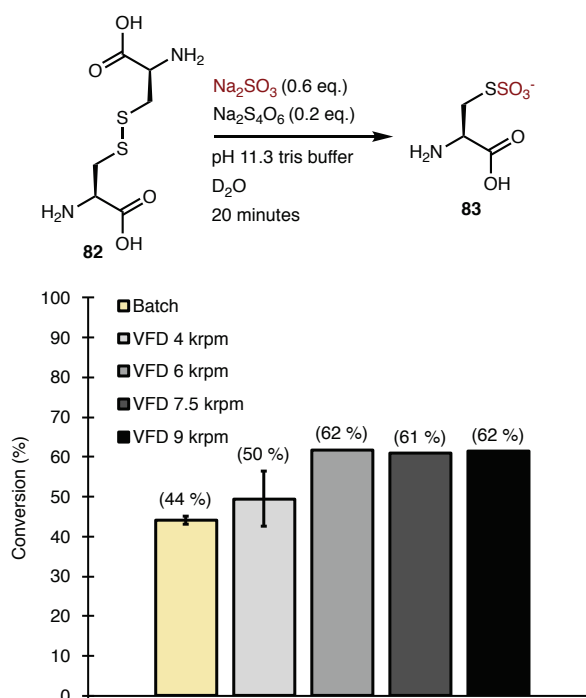


**Figure 66.** OS of L-cystine (**82**) in a tris buffered D<sub>2</sub>O solution (pH 11.3). Conversions determined by <sup>1</sup>H-NMR analysis. Comparisons between batch and four VFD rotational speeds (4, 6, 7.5 and 9 krpm).

Initially, literature conditions were attempted for the OS of insulin.<sup>269</sup> This involved a basic TRIS buffered solution with 0.6 molar equivalents of the Na<sub>2</sub>SO<sub>3</sub> and 0.2 molar equivalents of Na<sub>2</sub>S<sub>4</sub>O<sub>6</sub>. These reactions were reportedly left overnight at room temperature. These conditions were adapted here for the OS of cystine. As can be seen in Figure 66, having 0.6 equivalents of Na<sub>2</sub>SO<sub>3</sub> appears to be the limiting factor, as evident from a maximum conversion of 60 % being observed. The tetrathionate must not be rate limiting since the 0.2 equivalents of the Na<sub>2</sub>S<sub>4</sub>O<sub>6</sub> would limit the maximum conversion to 20 %. Therefore, it is likely that the tetrathionate is being re-generated. There is no current mechanistic understanding for the OS, and this result may be a vital clue for the fundamental underpinnings of this reaction, and thus deserves to be explored further.

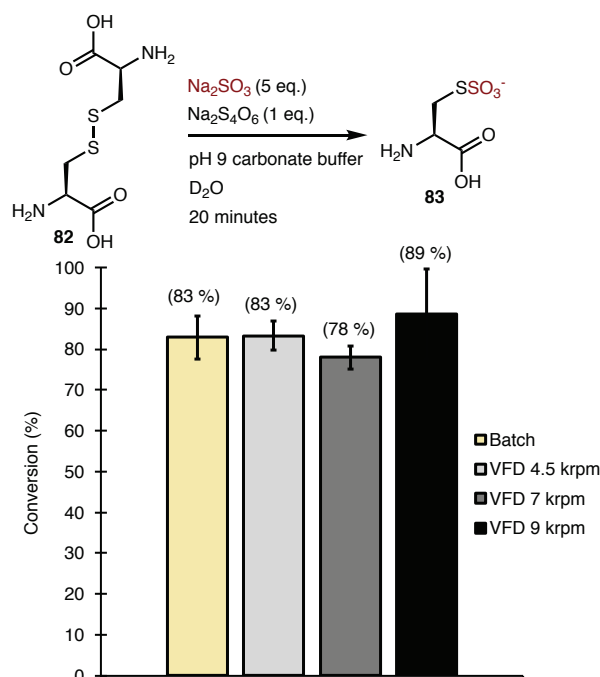


**Figure 67.** OS of L-cystine in a carbonate buffered  $\text{D}_2\text{O}$  solution (pH 9). Conversions determined by  $^1\text{H-NMR}$  analysis. Comparisons between batch and three VFD rotational speeds (4.5, 7 & 9 krpm).

Next, 1 equivalent of the sodium tetrathionate was used with 5 equivalents of the sodium sulphate. The results in Figure 67 suggest that near-full consumption of the cystine had occurred in all processing methods. However, it should be pointed out that there would be a large error margin in the conversions as determined by  $^1\text{H-NMR}$  analysis. This is due to the low amounts of remaining **82**, pushing on the lower limit of detection. This would increase the background noise on the peak integrals. The concentration could not be increased to account for this as **82** was at saturation in the pH 9 carbonate buffered  $\text{D}_2\text{O}$  ( $\approx 10$  mM). It appeared though, that the OS of **82** reached near-full conversion regardless of the processing method, thus no meaningful comparisons between batch and VFD could be made from this set of experiments.

The OS of **82** (Figure 66 & Figure 67) suggested that the conversions were similar in the VFD versus batch. However, there is an enhanced conversion in the VFD for the tris buffered  $\text{D}_2\text{O}$  solutions at pH 11.3 (Figure 66). This was especially evident at speeds of 6 krpm and above. The cause of this enhanced activity is unknown. Regardless, both conditions trialed suggested that 20 minutes at room temperature is enough time with the  $\text{Na}_2\text{SO}_3$  and  $\text{Na}_2\text{S}_4\text{O}_6$  at 5 and 1 equivalents respectively. Thus, using these conditions, the OS of more complex peptides (Oxytocin and Insulin) were explored further detail in following chapter.

### 5.1.2 – Discussion on the OS of Oxytocin

To observe the effect of the VFD on another biologically relevant compound with a disulphide bridge, the OS of oxytocin (**84**) was carried out. This was able to be successfully analysed by HPLC, which has a lower limit of detection than the <sup>1</sup>H-NMR method used for cystine above. For this reaction, 2 equivalents of sodium tetrathionate was used with an excess of sodium sulphide (80 equivalents). Comparing the reaction progress in the VFD and batch processing across the buffering range of basic carbonate buffer. From this, a considerable difference was evident (Figure 68). The data shows that the OS of **84** in a carbonate buffer is dependent on pH. Under typical batch conditions, the reaction doesn't go to completion in 20 minutes for the lower pH buffered solutions (12 %, 9 % and 2 % conversions at pH values of 9, 9.5 and 10 respectively). At pH 10.5, full conversion was observed in the batch conditions after 20 minutes. This suggest that this reaction is highly dependent on pH, and that pH of 10.5 is minimum to have this reaction progress to a respectable yield in 20 minutes. However, when processed in the VFD, full conversion can be achieved throughout the entire buffer range of carbonate (pH 9 to 10.5), although the upper limit of rotational speed in the VFD, 9 krpm, was required to reach full conversion at the lowest pH trialled (pH 9).

This result is unexpected and it is not obvious as to why the VFD is enhancing this reaction. As such, further work is required to achieve understanding of this phenomenon. There are many possible explanations, and de-coupling these possible effects would be difficult. Possible explanations lie in the complex fluid flows experience within microfluidic thin films. Firstly, shear is known to increase proportionally to rotational speed. Perhaps the shear is directly influencing the destruction of the annular compound oxytocin. This result is promising for the VFD being able to benefit the OS of large molecules, and is promising for insulin applications. However, it would be necessary to expand upon this result and find the underlying cause for the VFD to benefit this reaction. This would rely on current work being undertaken in the Raston group, in order to understand and predict the fluid flow in the VFD.

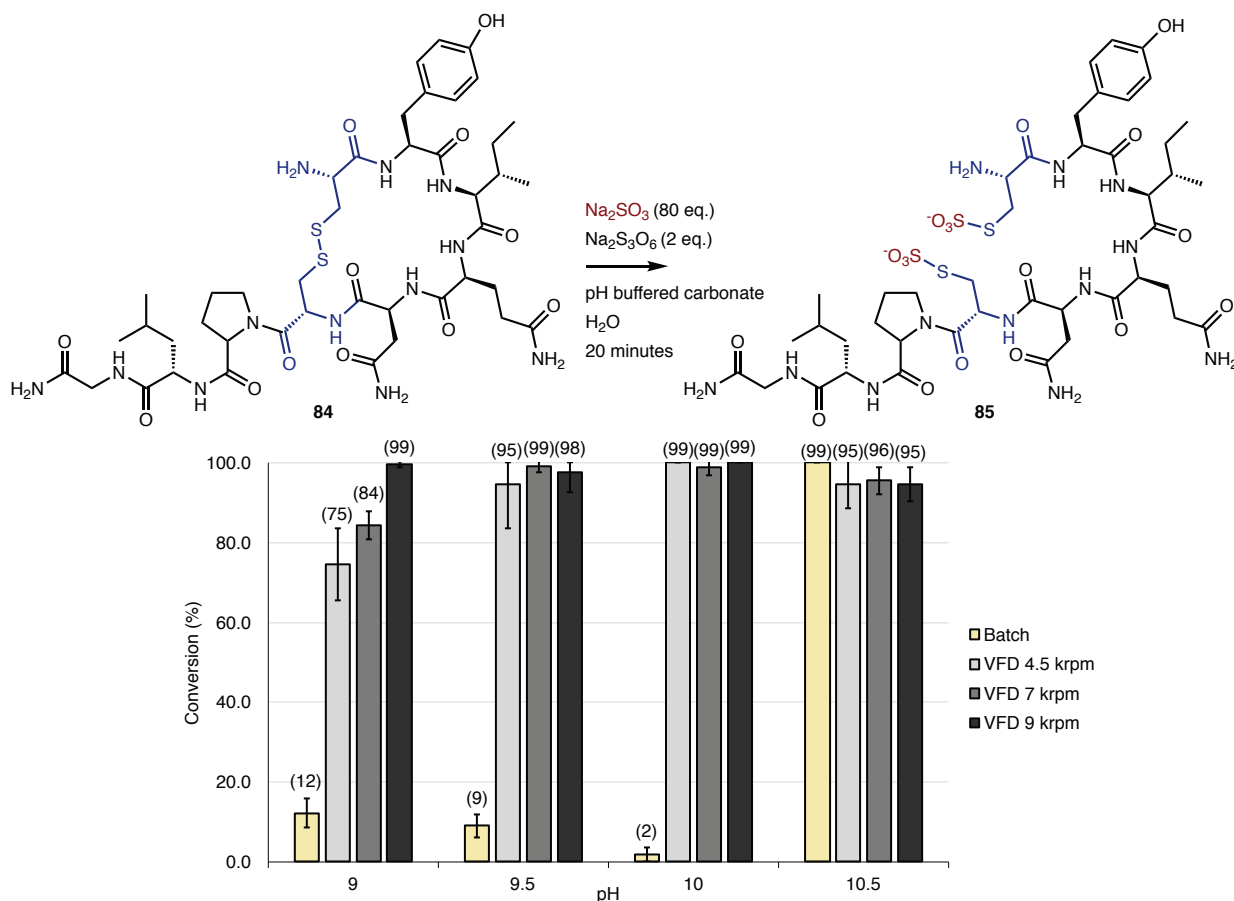


**Figure 68.** OS of oxytocin (**84**) in carbonate buffer. Comparisons between batch vs three VFD operational speeds (4.5, 7 and 9 krpm) were performed in carbonate buffered to pH's of 9, 9.5, 10 and 10.5. The conversions were determined using HPLC.

The results from the VFD processed reaction in a pH 9 buffered solution also reveal a result of interest (Figure 68). These are that the reaction reaches 75% conversion at 4.5 krpm, 84 % at 7 krpm and 99% conversion is obtained at 9 krpm. These indicate that the conversion of the formation of **85** correlates to increasing rotational speed (linear  $R^2 = 0.96$ ). This correlation indicates an enhancement in the VFD to being proportional to increasing rotational speeds. However, this relationship was not evident from the OS of cystine (**82**, Figure 66). Another interesting note is that for the batch results, a massive increase occurs from pH 10 (2%) to pH 10.5 (99 %). This suggests that this reaction spikes rapidly above a pH threshold between pH 10 and pH 10.5. This is an interesting observation that may require further investigation. Further study may seek to answer what is the exact pH threshold for allowing such rapid conversion, and why does this reaction depend so heavily on pH.

Further work should be performed to observe this phenomenon in another system. If this is robust and holds true, this result may be crucial in explaining the benefit observed. Shear is thought to be one such factor that increases proportionally with increasing rotational speed, thus this result may be a result of shear stress. This could be verified by decoupling shear from other forces in the VFD, such as film thickness, Eddie currents, helical flow regimes or vibrational interferences. To decouple these factors would be difficult, but it may be possible using other devices, such as a Couette cell, or other devices to apply shear forces to a liquid.<sup>270</sup> If this reaction is found to be directly proportional to increasing shear stress then the VFD would stand as a highly promising continuous flow device for facilitating this reaction.

### 5.1.3 – Discussion on the OS of Insulin

Attempts to monitor the OS of insulin (**86**) in VFD versus batch proved troublesome. Figure 69 shows that the insulin was not stable in the tris buffered solution of 8 M urea, which is typical for previously reported procedures. It was also found that the insulin was not stable either with or without the presence of EDTA. The degradation products and pathway remains unknown, with the analysis of the HPLC-MS spectra not matching that of any known degradation products. It is likely that an unknown reaction is taking place involving the insulin with the solution components, or possibly an unknown contaminant.

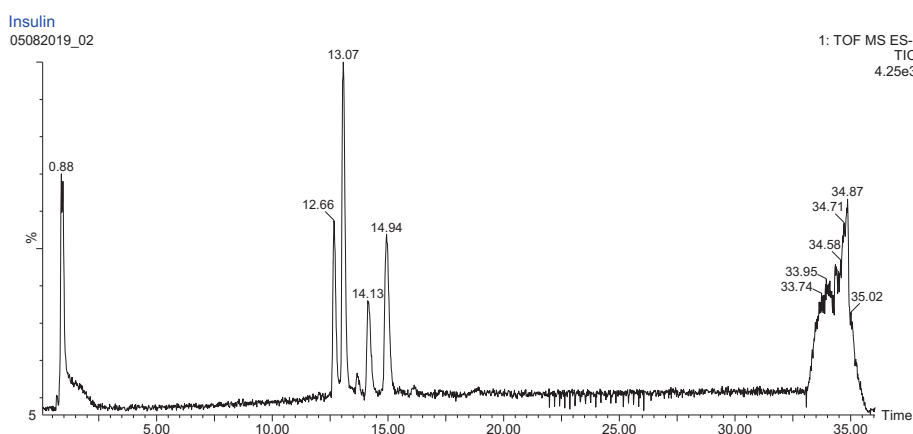


**Figure 69.** HPLC-MS TIC trace for the insulin in a tris buffered (pH 9) urea solution (8 M aq.) with EDTA. Shown are (A) the freshly prepared solution and (B) the same solution after 24 hours. Peaks of interest are the five observed peaks between 12 – 15 minutes.

Despite the apparent degradation, the OS reaction was attempted on this. It was hypothesised that since the tris buffered urea solution with EDTA is a typical solution in which insulin is stable, these by-products may be encountered in insulin production. Thus, a successful OS of the complex solution may help produce the pure A-chain and B-chain of insulin. As can be seen from Figure 70, this reaction indeed resulted in two products. One of which was confirmed to be the B-chain of insulin with both thiol sites capped with the  $-\text{SO}_3^-$  (Table 15). However, the other observed product proved difficult to identify, and was also unstable. The observed masses of this compound of 1815.33 & 1209.91 m/z do not correspond to any of the expected A-chain masses, with or without  $-\text{SO}_3^-$  capping of the four possible cysteine thiol residues (Table 14). If a modification of either chain is responsible for this peak, it would have to correspond to an increase in the mass of the A-chain ( $4\text{SO}_3^-$ ) by 930.9 m/z, or an increase of the B-chain ( $2\text{SO}_3^-$ ) by 45.1 m/z. The observed presence of the B-chain, along with the absence of any A-chain could hint that the peak at 19.07 minutes (Figure 70), along with the impurities shown in Figure 69 are likely a result of modification on the A-chain of insulin. However, it is still unclear what products are forming in this process.



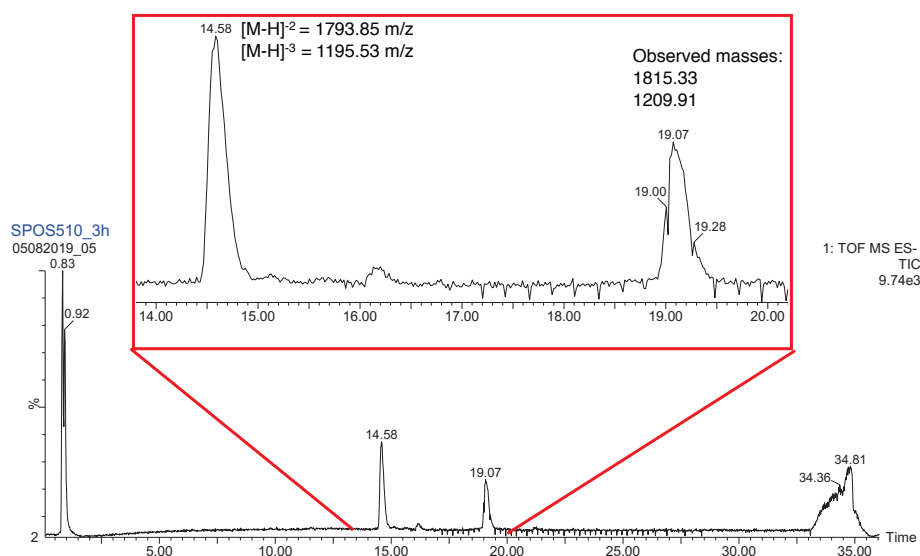


**Figure 70.** HPLC-MS TIC trace of the reaction mixture following OS of the complex degraded insulin seen in Figure 69. The peak at 14.58 min retention can be identified as the B chain of insulin with both thiols capped with  $\text{SO}_3^-$ . The peak at 19.07 mins does not match expected masses for A chain with any possible combination of  $-\text{SO}_3^-$  capping on the possible four cysteine residues (Table 14).

**Table 14.** Insulin A-chain expected (-) ve mode masses. Shown are the expected masses with increasing amount of charge in the columns, and the increasing amount of possible  $-\text{SO}_3^-$  groups, capping the four possible cysteine thiol residues. Numbers calculated from native A-chain chemical formula of  $\text{C}_{99}\text{H}_{155}\text{N}_{25}\text{O}_{35}\text{S}_4$ .

Charge	Native A-chain	1 $\text{SO}_3$	2 $\text{SO}_3$	3 $\text{SO}_3$	4 $\text{SO}_3$
-6	395.9922	409.3183	422.6445	435.9706	449.2967
-5	475.3922	491.3835	507.3749	523.3663	539.3576
-4	594.4922	614.4814	634.4706	654.4598	674.449
-3	792.9922	819.6445	846.2967	872.949	899.6013
-2	1189.9922	1229.9706	1269.949	1309.9274	1349.9058
-1	2380.9922	2460.949	2540.9058	2620.8627	2700.8195

**Table 15.** Insulin B-chain expected (-) ve mode masses. Shown are the expected masses with increasing amount of charge in the columns, and the increasing amount of possible  $-\text{SO}_3^-$  groups, capping the two possible cysteine thiol residues. Numbers calculated from native B-chain chemical formula of  $\text{C}_{158}\text{H}_{234}\text{N}_{40}\text{O}_{42}\text{S}_2$ .

Charge	Native B-chain	1 $\text{SO}_3$	2 $\text{SO}_3$
-6	570.2729	583.5991	596.9252
-5	684.5291	700.5205	716.5118
-4	855.9133	875.9025	895.8917
-3	1141.5537	1168.206	1194.8582
-2	1712.8345	1752.8129	1792.7913
-1	3426.6768	3506.6336	3586.5904

## 5.2 – Summary and Outlook of Oxidative Sulphitolysis in the VFD

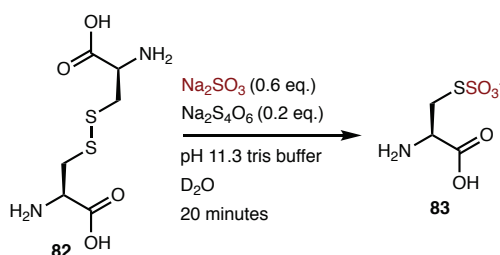
Although the differences between OS of insulin in the VFD versus batch were unable to be ascertained, an interesting result was uncovered in studying oxytocin. This showed a major benefit for VFD processing, where full conversion of oxytocin to the sulphite capped product was achieved. This occurred even at pH levels where minimal conversion is achieved in batch. This is highlighted at pH 10, where 2 % conversion is achieved in a stirred vial, whereas with identical conditions at any of the rotational speeds trialled in the VFD give full conversion (99 %). The results at pH 9 are also interesting. Here, the conversion after 20 minutes was found to correlate in a linear fashion to increasing rotational speed (linear  $R^2 = 0.96$ ), and full conversion was achieved at 9 krpm, the highest speed trialled. These experiments also established that the reaction is highly dependent on the pH, where with batch processes, full conversion in 20 minutes can only be achieved at pH 10.5. This is the upper limit to the buffer chosen for this study (carbonate buffer). This result is extremely promising for reactions limited by pH. In many cases, the workable pH of a process may be limited by the buffer used, or if the process requires a physiological pH level. It appears from these early results that the VFD may be able to enable methods at lower than normal pH levels, which has applications in many processes beyond OS. This result requires further study and is a focus within the Raston research group moving forward. If a process exists requires harsh processing, (ie. More expensive, toxic and energy intensive), it may be possible that the VFD enables less harsh methods to achieve the same outcome. OS is an example of this, where the work here is promising for achieving a process with shorter times, potentially lower stoichiometric amounts and lower temperatures for the purification of insulin. This however requires further work in optimising for parameters such as rotational speed, flow rates and stoichiometry. Unfortunately, the work required is beyond the scope of this Ph.D, but it is hoped that a platform has been laid for future studies.

The exact nature of this increased activity across a larger pH range is unknown, and further work is required to understand this. Suggested for future work would require understand the nature of pH under the unique conditions found in the thin vortexed liquid film. It may be possible that the dissociation of water in the VFD is not comparable to that experienced in round bottom flask chemistry. If the shear, and/or other features of the VFD are able to effect the disassociation equilibrium of water, it may be possible that different concentrations of  $\text{OH}^-$  ions are experienced at the same pH. This is theoretical and needs to be proven. Although directly probing the pH of a rotating liquid is not trivial. Any probe would need to work in a film of liquid between 200 – 500 nm in thickness, depending on rotational speed and volume.<sup>271</sup> Any probe physically submerged in this film then runs the risk of disturbing the fluid flows, and may alter the flow regime experienced. This would mean that the probed environment is not comparable to the “native” flow experienced in typical VFD processing. Spectroscopic methods are promising for the probing the pH of water. The Raman spectrum of water is well understood from extensive studies. As such, a real-time Raman spectroscopy instrument is being developed in the Raston research group, and this may be vital for understanding the disassociation of water experienced in the VFD.

Also discovered in this research is that the limiting reagent appears to be the sodium sulphate, and not the sodium tetrathionate. This is an interesting result and future study should be performed to confirm this result. This may prove vital for understanding the mechanism of the OS reaction.

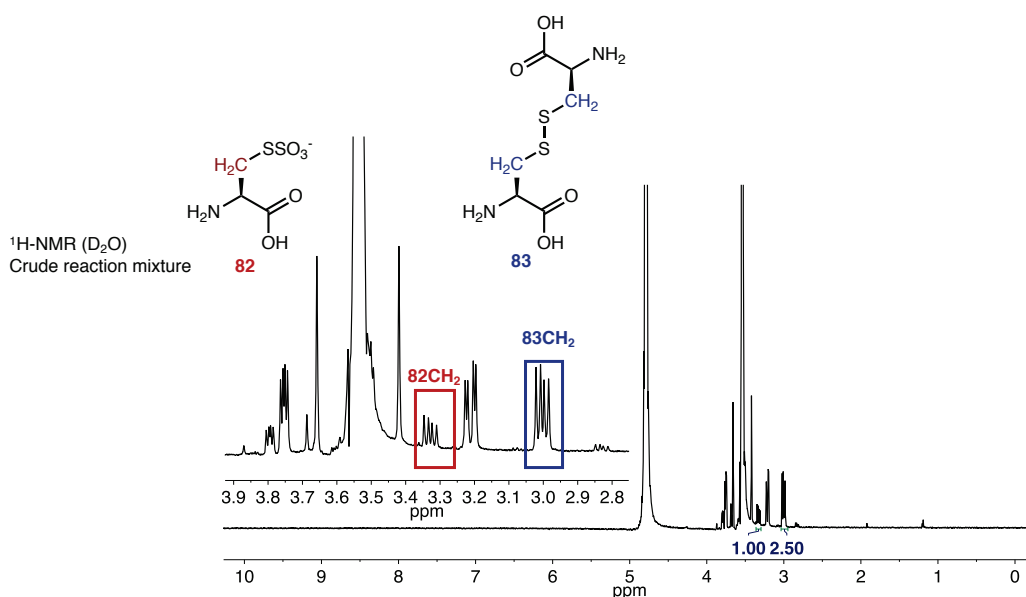
## 5.3 – Experimental Details and Spectra

### 5.3.1 – Cystine OS at pH 11.3, Batch versus VFD

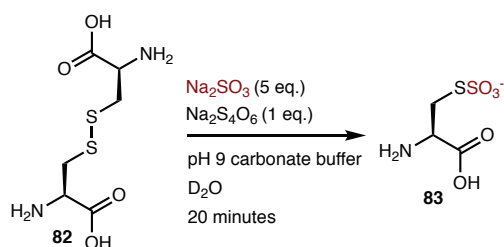


Adapting an OS method for insulin,<sup>269</sup> here for the OS of cystine resulted in the following procedure. Firstly, a tris buffered  $\text{D}_2\text{O}$  solution was preparing TRIS buffered  $\text{D}_2\text{O}$  solution. The pH of this solution was then found to be pH 11.3. Next, a stock solution of the cystine was prepared by dissolving the cystine (**82**) (5 mg,  $2.08 \times 10^{-5}$  mol, 5.2 mM) in the tris buffered  $\text{D}_2\text{O}$  solution (4 mL). A stock solution containing both  $\text{Na}_2\text{SO}_3$  and  $\text{Na}_2\text{S}_4\text{O}_6$  was then prepared by dissolving  $\text{Na}_2\text{SO}_3$  (3.5 mg,  $2.77 \times 10^{-5}$  mol, 27.7 mM) and  $\text{Na}_2\text{S}_4\text{O}_6$  (2.5 mg,  $9.26 \times 10^{-6}$  mol, 9.26 mM) in the tris buffered  $\text{D}_2\text{O}$  solution (1 mL).

The reactions were then performed in either a magnetically stirred vial or operated in the VFD at either 4, 6, 7.5 or 9 krpm. For these, the cystine stock (1.8 mL) and the  $\text{Na}_2\text{SO}_3/\text{Na}_2\text{S}_4\text{O}_6$  stock (0.2 mL) were combined and mixed for a total of 20 minutes at room temperature. The resulting reaction mixture contained cystine (4.68 mM),  $\text{Na}_2\text{SO}_3$  (2.77 mM) and  $\text{Na}_2\text{S}_4\text{O}_6$  (0.93 mM). Upon completion of the desired time, the reaction was quenched by the addition of trifluoro-acetic acid (20  $\mu\text{L}$ ).  $^1\text{H-NMR}$  was then performed directly on the crude reaction mixtures. Conversions were then made by comparing the integrals of the peaks corresponding to the  $-\text{CH}_2$  nuclei. Note that there are four H nuclei for each molecule of the cystine and only two for each molecule of the sulphinated-cysteine product (**83**). This was repeated in triplicate, with results shown in Figure 66. Representative NMR spectra can be found below.

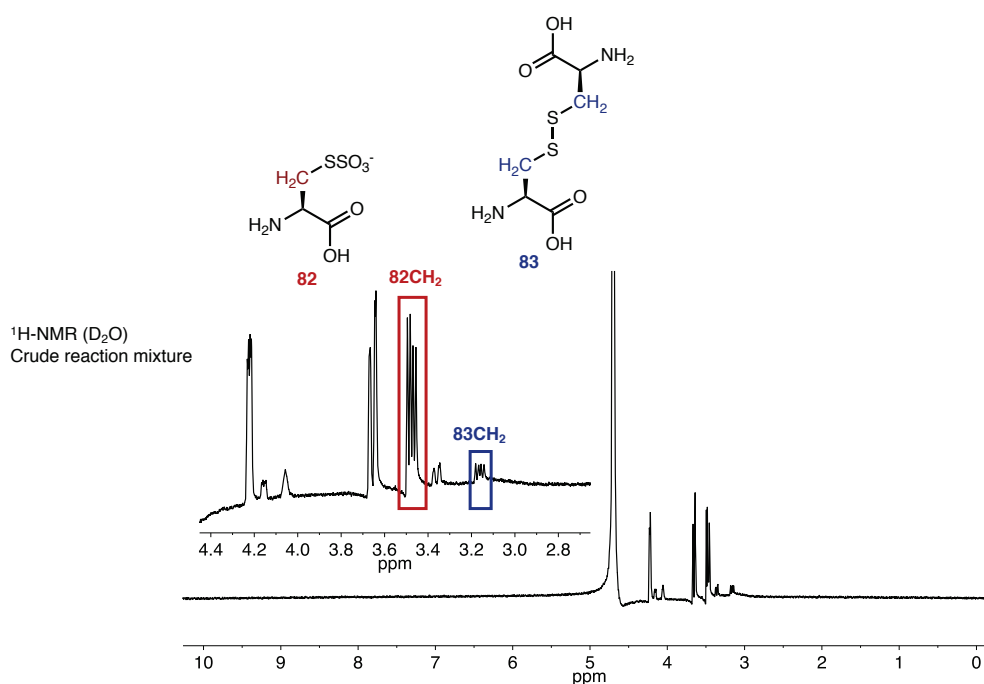


### 5.3.2 - Cystine OS at pH 9, Batch vs VFD

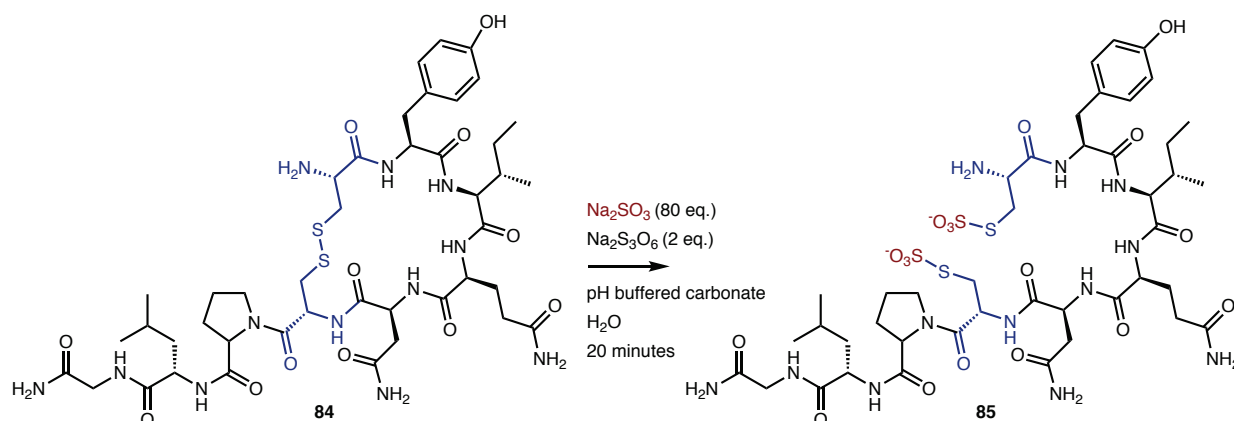


Oxidative sulphitolysis was performed on L-cystine (**82**) using the following procedure. First, a carbonate buffered  $\text{D}_2\text{O}$  solution was prepared by the dissolution of  $\text{NaHCO}_3$  (168 mg, 2 mmol) and  $\text{Na}_2\text{CO}_3$  (21.2 mg, 0.2 mmol) in  $\text{D}_2\text{O}$  (20 mL). The pH of this solution was found to be pH 9. Next, the stock solution of cystine was prepared by dissolving cystine (40.0 mg, 0.166 mmol, 11.1 mM) in the carbonate buffered  $\text{D}_2\text{O}$  (15 mL). A stock solution containing both  $\text{Na}_2\text{SO}_3$  and  $\text{Na}_2\text{S}_4\text{O}_6$  was then prepared by dissolving  $\text{Na}_2\text{SO}_3$  (189 mg, 1.5 mmol, 500 mM) and  $\text{Na}_2\text{S}_4\text{O}_6$  (81 mg, 0.3 mmol, 100 mM) in the carbonate buffered  $\text{D}_2\text{O}$  (3 mL).

The reactions were then performed in either a magnetically stirred vial or operated in the VFD at either 4.5, 7 or 9 krpm. For these, the cystine stock (0.9 mL) and the  $\text{Na}_2\text{SO}_3/\text{Na}_2\text{S}_4\text{O}_6$  stock (0.1 mL) were combined and mixed for a total of 20 minutes at room temperature. The resulting reaction mixture contained cystine (10 mM),  $\text{Na}_2\text{SO}_3$  (50 mM) and  $\text{Na}_2\text{S}_4\text{O}_6$  (10 mM). Upon completion of the desired time, the reaction was quenched by the addition of trifluoro-acetic acid (20  $\mu\text{L}$ ).  $^1\text{H-NMR}$  was then performed directly on the crude reaction mixtures. Conversions were then made by comparing the integrals of the peaks corresponding to the  $-\text{CH}_2-$  nuclei. Note that there are four H nuclei for each molecule of the cystine and only two for each molecule of the sulphinated-cysteine product (**83**). This was repeated in triplicate, with results shown in Figure 67. Representative NMR spectra can be found below.



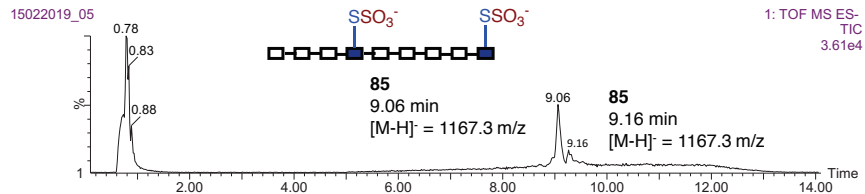
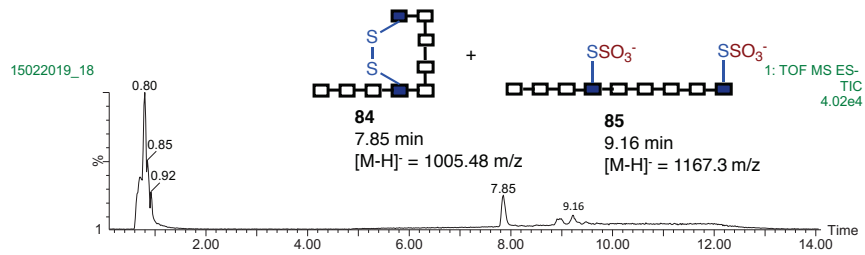
### 5.3.3 – Oxytocin OS Batch versus VFD



Oxidative sulfitolysis was performed on oxytocin (**84**) using the following procedure. First, a series of carbonate buffered solutions were prepared by the dissolution of  $\text{NaHCO}_3$  (168 mg, 2 mmol) and  $\text{Na}_2\text{CO}_3$  (21.2 mg, 0.2 mmol) in water (20 mL). The pH of each of these solutions was raised with  $\text{NaHCO}_3$  or lowered with  $\text{Na}_2\text{CO}_3$  to produce a series of pH solutions of 9, 9.5, 10 & 10.5. Next, the stock solution of oxytocin was prepared by dissolving oxytocin (1 mg,  $9.93 \times 10^{-7}$  mol, 0.1 mM) in each of the carbonate buffered solutions (10 mL). A stock solution containing both  $\text{Na}_2\text{SO}_3$  and  $\text{Na}_2\text{S}_4\text{O}_6$  was then prepared by dissolving  $\text{Na}_2\text{SO}_3$  (100 mg, 0.8 mmol, 80 mM) and  $\text{Na}_2\text{S}_4\text{O}_6$  (5.4 mg, 0.02 mmol, 20 mM) in each of the carbonate buffered solutions (10 mL).

The reactions were then performed in either a magnetically stirred vial or operated in the VFD at either 4.5, 7 or 9 krpm. For these, the oxytocin stock (800  $\mu\text{L}$ ) and the  $\text{Na}_2\text{SO}_3/\text{Na}_2\text{S}_4\text{O}_6$  stock (80  $\mu\text{L}$ ) were combined and diluted in the pH buffered carbonate solution (3120  $\mu\text{L}$ ), and reacted for a total of 20 minutes at room temperature. The resulting reaction mixture contained oxytocin (0.02 mM),  $\text{Na}_2\text{SO}_3$  (1.6 mM) and  $\text{Na}_2\text{S}_4\text{O}_6$  (0.04 mM). Upon completion of the desired time, the reaction was quenched by the addition of trifluoro-acetic acid (20  $\mu\text{L}$ ). Aliquots (50  $\mu\text{L}$ ) were then diluted in water (1.5 mL) for HPLC analysis. HPLC-MS analysis was performed to identify the peaks in the HPLC trace, whilst a UV detector at 252 nm was used for determining peak integrals for the conversions. This was repeated in triplicate, with results shown in Figure 68. Representative HPLC-MS spectra can be found below.

HPLC-MS was performed with the following conditions. A C18 column was used with flow rates of 0.2 mL/min. A binary solvent system was used, the solvents being a formic acid solution (0.1 % V/V aq.) and acetonitrile. Initial flow consisted of 90 : 10 formic acid : acetonitrile, before ramping to 70 : 30 over 10 minutes. This ratio was held for 4 minutes giving a total time of 14 minutes. Mass detection was 300 – 2000 m/z. A photodetector at 252 nm was also used.



## Chapter 6 – Vortex Fluid Behaviour

Understanding the behaviour of the dynamic fluids within the VFD is of utmost importance in understanding the anomalous and remarkable phenomena established using VFD processing. There has been a large amount of progress towards this goal since the start of this Ph.D., but there is still much work to be done. This chapter goes towards further understanding of the fluid flow in the device.

### 6.1 – Vortexed Liquid Film Shape

An important starting point in understanding the holistic dynamic-fluid behaviour is the total shape and space that the liquid will occupy. Because the liquid will coat the inside of the glass tube, it is frequently referred to as a film. This is despite the “film” in this case being a dynamic liquid. This differs from typical films in that the shape will dynamically change based on various factors, such as rotational speed, volume of the liquid in the tube, and tilt angle. It is shown here that film thickness will change as it makes a single rotation, shown by a thicker film observed at the bottom than when at the top of its rotation (arising from the effect of gravity). The dynamic nature of the film is especially evident in continuous droplet flow, where droplets generate perturbations and waves when they contact the vortex film. This work was spearheaded by Dr. Jenny Leveidrou, a Ph.D. candidate in Prof. Stuart Dalziels’ fluid dynamic group, Department of Applied Mathematics and Theoretical Physics, The University of Cambridge University, U.K., and I refer to her Ph.D. thesis. This contains detailed analysis of the shape of the vortex, the fingering instabilities that occur upon spin-up, the impact and disruption caused by droplets landing upon the rotating liquid, diffusion of liquids within the film and more.

Along with the film shape in continuous flow, is the shape of the film in confined mode. This is also a key area of study. Confined mode of operation is when a finite amount of liquid is held within the tube. This is achieved either by using a rotational speed and volume such that the apex of the vortex does not reach the exit of the tube. Alternatively, a cap can be used to contain the liquid. Confined mode also differs as there are no liquid feeds to disturb the liquid film. The main focus of the work in this field has been in understanding the effect of liquid volume and rotational speed on the height and thickness of the liquid film. To experimentally find these dimensions, VFD parameters were varied and the film height and film thickness were monitored using neutron imaging. This was made possible by securing beam time at ANSTO, in collaboration with Dr Filomena SALVEMINI. The data produced from these experiments was then used to experimentally verify a theoretical model developed by fellow group member, Dr Timothy Solheim.

### 6.1.1 – Confined Mode Liquid Film Shape

Using neutron imaging, images of H<sub>2</sub>O (1 mL) at rotational speeds of 50 rpm increments between 2-8 krpm were obtained (Figure 71). These images were taken on the “DINGO” neutron imaging camera, located at the Australian Nuclear Science and Technology Organisation (ANSTO), located in Lucas Heights, Sydney NSW. The instrument features a thermal neutron beam gathered through in-pile collimators positioned upstream of the beam line. In the case of real-time imaging of dynamic process, the inlet aperture of 20 mm in diameter (D) is configured to provide high flux and high spatial resolution (L/D of 500) at the length path (L) from the collimator to the sample position. The detector system was equipped with the CMOS camera (Andor NEO 5.5 sCMOS, 16 bit, 2560(w) × 2160(h) pixels sensor) coupled with 100 μm thick ZnS/6LiF scintillation screens. The field of view was adjusted to a nominal pixel size ≈ 67 μm by using a Carl Zeiss lens with a fixed focal length of 50 mm.<sup>272</sup> Exposure time for the camera was 1 s, with an additional 0.02 s of read out time required to transmit the data, resulting in a sampling frequency of 0.98 Hz. The image of the liquid film was isolated from the tubes and VFD frame by obtaining the rotating VFD (Figure 71A) and subtracting an image of the VFD with an empty tube. This results in an image of the liquid film (Figure 71B). Image processing software (ImageJ) was then able to measure the thickness of these films along the height of the tube. This work was utilised to experimentally verify a theoretical model developed by Dr. Timothy Solheim in the Raston laboratory group member (Figure 72).<sup>271</sup>

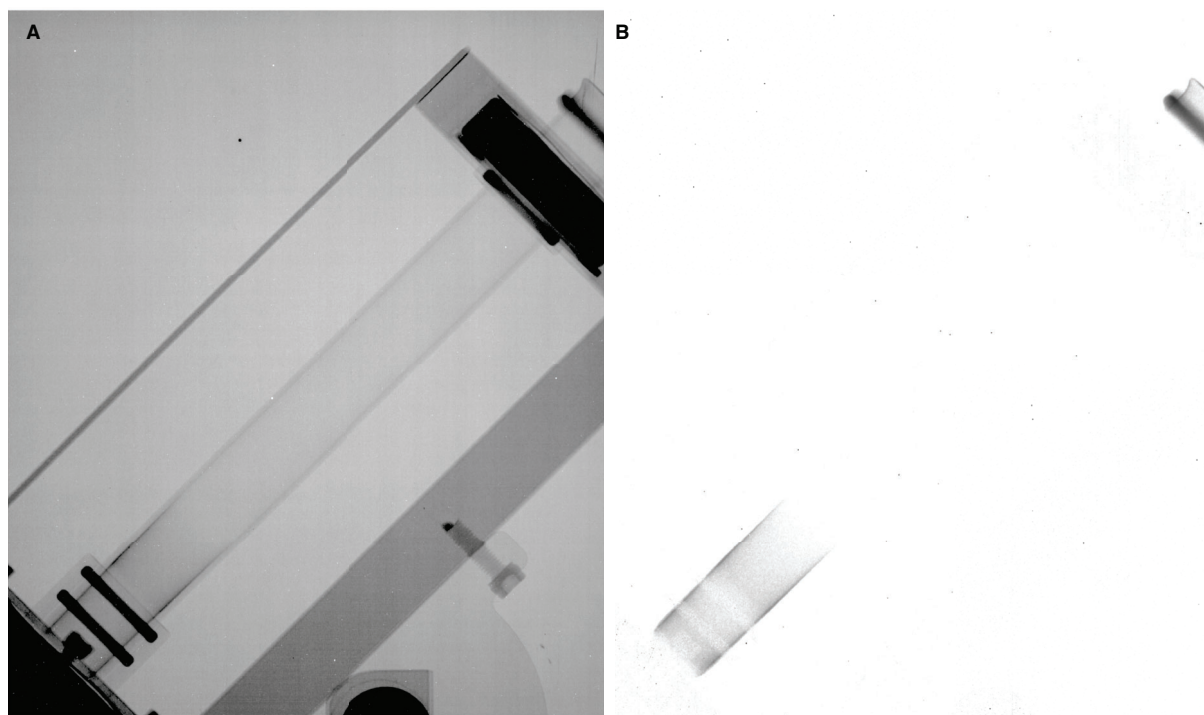


**Figure 71.** Representative neutron images of the VFD with 1 mL H<sub>2</sub>O. (A) shows the raw image, and (B) shows the result of subtracting an image of the VFD with an empty tube. VFD was operated at 45° tilt angle. Images were taken at 50 rpm increments from 2-8 krpm.



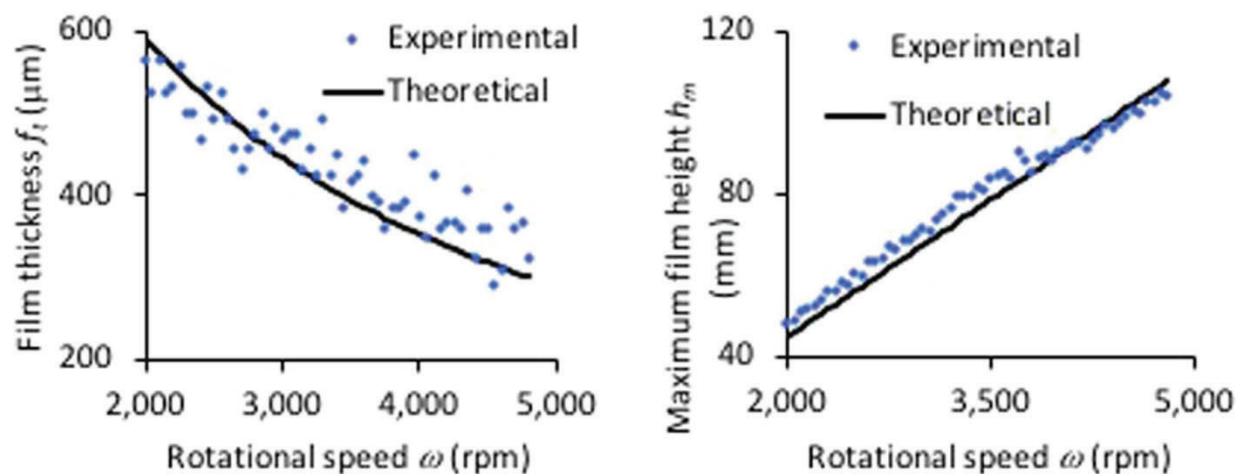
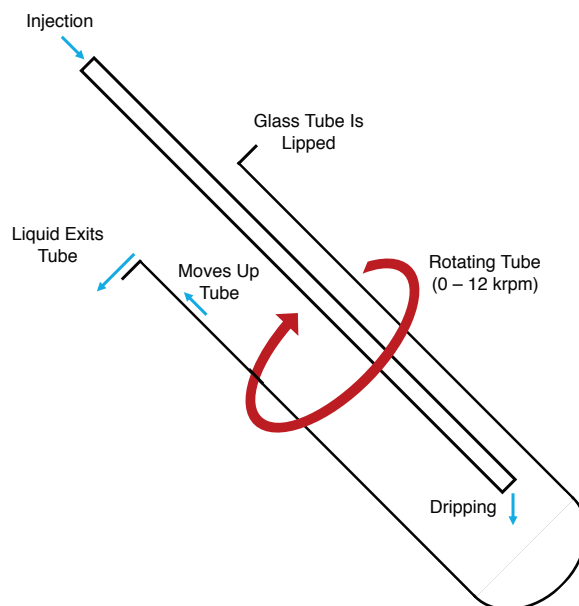


Figure 72. Experimentally validating a theoretical model for predicting film thickness and maximum film height of water within the VFD.<sup>271</sup>

Using neutron imaging to measure the dimensionality of the liquid film was successful. From this, a theoretical model for predicting the thickness, and film height of liquid within a rotating tube was developed by Dr Tim Solheim and good predictability was achieved.<sup>271</sup> This allows predicting key properties of the liquid film. Film thickness is vital for performing real time analysis within the VFD. Techniques such as UV-vis, Small Angle Neutron Scattering (SANS), Ultra Small Angle Neutron Scattering (uSANS) and Raman require precise knowledge of the path length of liquid sample. This model provides access to this. This has allowed for in situ SANS directly monitoring rotating samples in the VFD. This also will aid in real-time monitoring with UV-vis spectroscopy and Raman spectroscopy. Both of which techniques are utilised within the Raston group for real-time VFD analysis. Real time monitoring provides vital information on samples such as reaction progress. Additionally, it can be used to verify changes in a sample whilst rotating, and decouple this from samples when rotation has ceased.

## 6.1.2 – Continuous Flow by Dripping Liquid Delivery



**Figure 73.** A) Cross sectional diagram and B) photograph of a typical single feed continuous flow VFD process. Shown is the lipped glass tube which is rotating independently of a stainless-steel jet feed. Liquid is injected into the steel jet feed, forms droplets and travels to the hemispherical base of the rotating tube. It then forms a vortex and moves up and out of the tube. The liquid then exits perpendicular to the rotating tube due to centrifugal forces.

Continuous flow is typically achieved in the VFD by delivering liquid reagents to the base of the rotating tube (Figure 73). The liquid then moves up the tube, eventually reaching the open lip of the tube. The time taken for this, (*ie.* the retention time) can be controlled by altering the rate of liquid delivery and rotational speed. The delivery of the liquid is typically achieved by the use of syringe pumps, which can be set to deliver liquid reagents at a defined rate. The liquid is pumped from the syringe pump through a jet feed, typically made from stainless steel. As such, this process is typically obscured from view, however neutron imaging was able to show this. An image was taken every 3 seconds over a 20-minute period, and these images were culminated into a video clip. Key frames of this process are displayed in Figure 74. These images show that once the liquid leaves the syringe and enters the jet feed, it will first form a droplet (Figure 74B) before moving from the jet feed into the rotating tube (Figure 74C). The formation of droplets will control the actual flow rate delivered to the VFD tube. Rotational speed was set to 7 krpm and a tilt angle of  $45^\circ$  was used. These are standard operating conditions for the VFD. Without the use of neutron imaging, the formation of droplets within the jet feed is not immediately obvious. This result suggests that the actual flow rate experienced may not be what is set on the syringe pump. This may be important to keep in mind, especially for cases where a slow injection rate is utilised. In such cases, the difference between set flow rate and actual flow rate would be more pronounced.

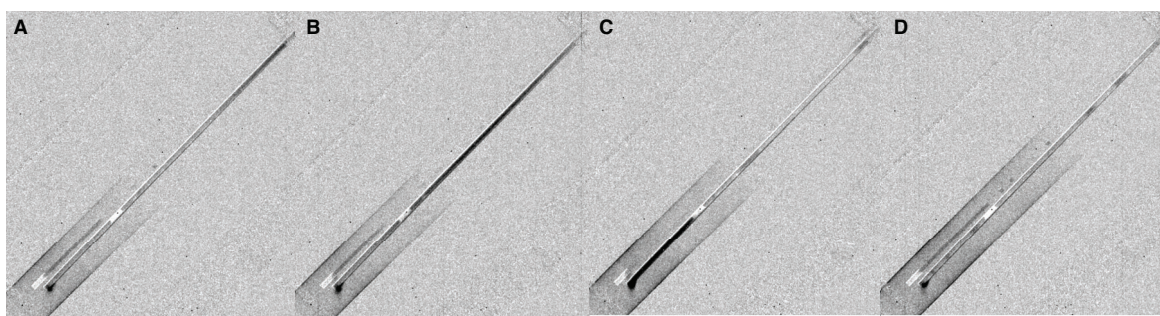


**Figure 74.** Neutron images of a continuous flow process in the VFD, at 45° tilt. H<sub>2</sub>O is being delivered via stainless steel jet-feed to the base of the tube, rotating at 6.5 krpm. Shown are frames progressing as (A) the droplet of liquid forms within the jet-feed, (B) moves down the jet-feed and (C) enters the rotating tube. (D) After the droplet has been delivered, the increased volume within the tube is evident by the film reaching a higher point of the tube.

Once the liquid exits the tube, it is flung out perpendicular to the tube as small droplets, as indicated by the spatter pattern of liquid leaving the tube (Figure 75). These measurements were obtained simply by securing a piece of paper 10 cm from the open end of a VFD unit. Water dyed red with food dye (1 mL) was added to the tube and then rotation was begun. During spin-up, a piece of paper towel was used to block any spray from reaching the paper until the desired speed was reached. This was used to prevent droplets making contact with the paper sheet, being flung from unknown speeds as the machine reaches the desired speed.

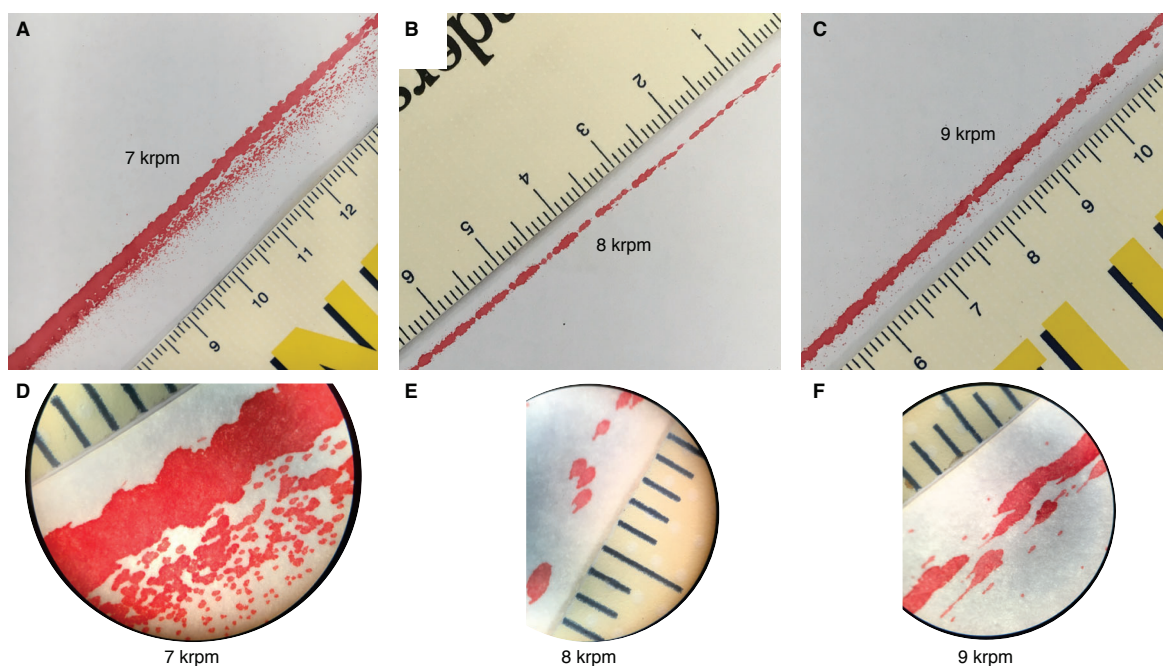


**Figure 75.** Photographs of the spatter patterns of red dye exiting the rotating VFD tube at rotational speeds of (A) 7 krpm, (B) 8 krpm and (C) 9 krpm.

Using image processing software (ImageJ), the sizes of these droplets were measured (Figure 76). As can be observed, 7 krpm and 9 krpm have a much tighter size distribution compared to 8 krpm. It is unknown why this is observed. Most importantly, the size range of the droplets observed is between 50 – 1000  $\mu\text{m}$ . For reference, typical medical nebulisers produce a liquid mist, with droplets in the size range of approximately 1 – 50  $\mu\text{m}$ .<sup>273</sup> It should be noted that typical methods for measuring droplet sizes is achieved through dynamic light scattering (DLS) method of the droplet whilst in flight (*ie.* After leaving the device and before making contact with a surface). As such, the results shown here only provide a rough estimate for the size of droplets

produced upon exiting the VFD. This suggests that the liquid upon exiting the rotating tube is of higher size, and a broader size range than typical nebulisers. This is an interesting aspect of the VFD to keep in mind, as chemistry in nebulised liquid is a developing field of research.<sup>274, 275</sup> The benefits of which are mostly attributed to the large surface-area : volume ratio (SA:V) of the liquid micro-droplet. This has been demonstrated to be very beneficial for many organic transformations, especially for aerobic oxidations.<sup>276</sup> As such this part of the continuous flow VFD process could actually be having some effect on the outcome of certain reactions. This is important to keep in mind when altering VFD methods. For example, a method for achieving continuous flow in the VFD alternatively to the method discussed above has been proposed. This involves operating a fixed amount of liquid in a tube, and upon reaching desired reaction time, to rotate the tube so as to tip out the liquid. This could be achieved with a robotic arm for example. Replenishing the liquid and repeating this process would result in a continuous flow process, but would not involve the formation of micro-droplets. This is mentioned here simply as it may affect the outcome of chemical transformation.

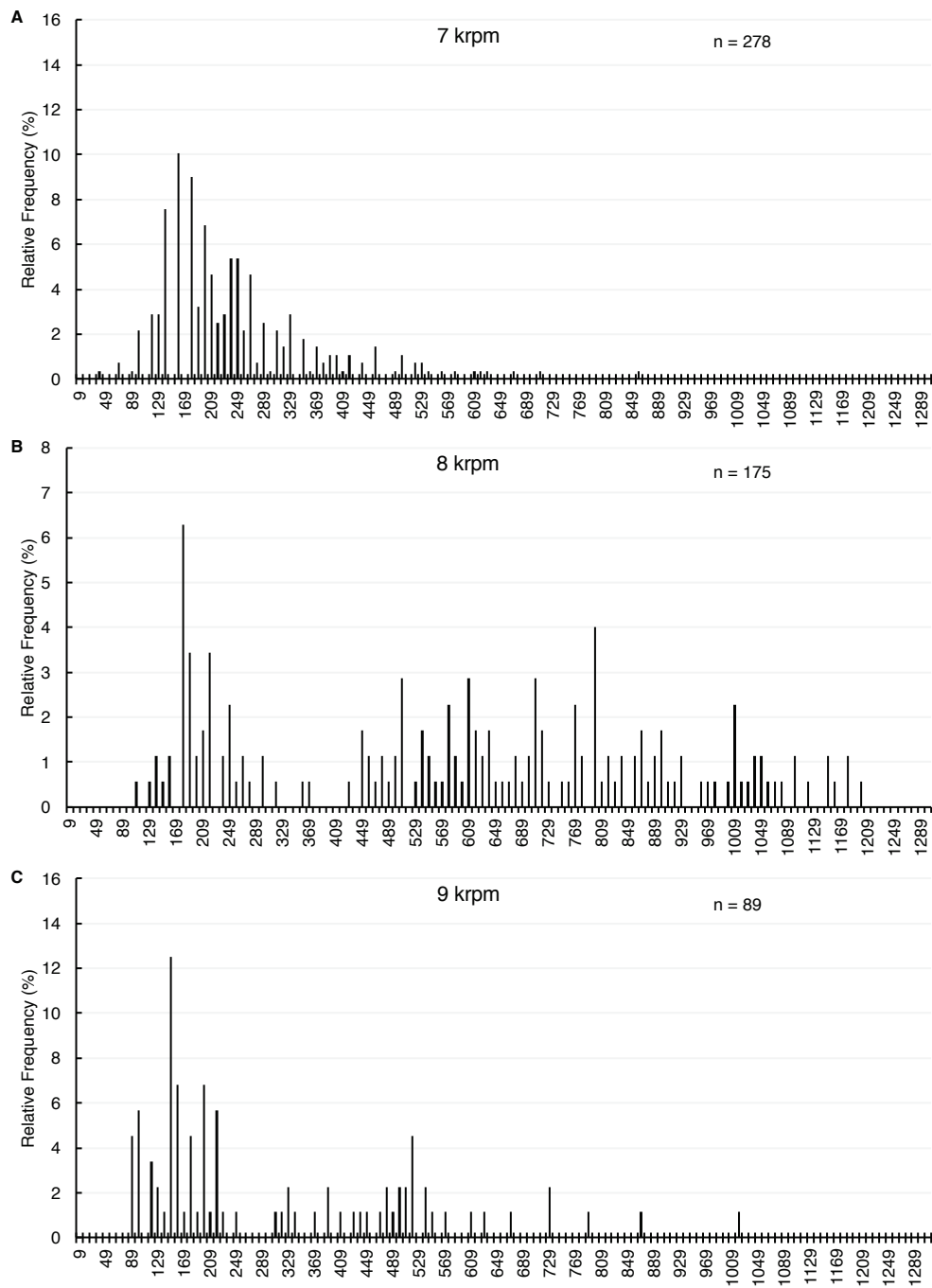


**Figure 76.** Frequency distribution plots of the size (width,  $\mu\text{m}$ ) of the droplets after exiting the rapidly rotating VFD tube. Droplets are shown in Figure 75. The size of the droplets in  $\mu\text{m}$  are graphed, for speeds of (A) 7 krpm, (B) 8 krpm and (C) 9 krpm. “n” indicates sample size of droplet spatters.

### 6.1.3 – Summary and Outlook on the Vortexed Liquid Film Shape

The shape of the liquid film in the VFD was explored here for both confined mode and continuous flow modes of operation. Neutron imaging was utilised for confined mode, where a finite amount of liquid is retained within the rotating tube. Neutron imaging of H<sub>2</sub>O within the tube was used to obtain images of the liquid film in the VFD, without obscuration from the visually opaque components of the VFD. These images were used to experimentally verify a theoretic model developed by another group member, Dr. Timothy Solheim.<sup>271</sup> This model describes the film height and thickness for a film of water at rotational speeds between 0 – 9 krpm. This is fundamentally important for many uses of the VFD, especially for utilising real-time monitoring. For such techniques, an understanding of the path-length of the sample is crucial, and only this model is able to provide this.

Monitoring the behaviour of the liquid film whilst continuously delivering reagents *via* syringe pump was also performed. This revealed that the exact delivery rate of liquids is controlled by the formation of droplets within the jet-feed. These then move down the jet feed and form a drop at the exit of the steel jet feed. This indicates that the real rate of delivery is controlled by the droplet formation and not by what is set on the syringe pump device. This is especially relevant for slower injection rates where the droplet will take longer to form. This has implications in continuous flow chemical processes where control of the stoichiometry is important. Further work into understanding the effect of viscosity of liquids at various temperatures are being investigated in the Raston research group.

## 6.2 – Biphasic Systems

One aspect of VFD processing that was previously unknown is investigated in this work – that is how two immiscible liquids behave. Chemical reactions across phase boundaries are greatly improved in the VFD, allowing reactions of immiscible reagents that are not traditionally accessible.<sup>102</sup> This obviates the need for auxiliary phase transfer agents, which are typically employed.<sup>33</sup> Removing the need for phase transfer agents inherently improves the green metrics of a reaction, in regards to atom economy and safety. This also enables reagents that were previously excluded from consideration for solubility reasons. An example is the use of hydrogen peroxide for the oxidation of hydrophobic compounds, which is typically overlooked in favour of organic oxidants.<sup>102</sup> This work progresses towards experimentally describing the surface-area-to-volume-ratio (SA:V) observed for toluene and water within the vortex. The SA:V is a vital component when engineering a multiphase chemical process, and thus is necessary for any industrial application of the VFD, or similar vortex processing. The behaviour of liquids in immiscible systems within the VFD were unknown. Two main speculations arose: (i) The immiscible liquids will sit upon each other, where the centrifugal forces separate them based on density differences, and (ii) the forces present in the liquid associated with the induced mechanical energy are effective in micro-mixing the two liquids. It was also thought that these two factors would not be mutually exclusive, *i.e* there could exist two distinct phases separated based on density, and that micro-mixing is occurring to some unknown degree at the interface.

### 6.2.1 – Discussion on Biphasic Systems

Neutron imaging work using D<sub>2</sub>O and toluene shows two distinct liquid phases. This is due to the ability of neutron imaging to differentiate deuterated compounds from normal hydrogen containing compounds. In this work, D<sub>2</sub>O is transparent to neutrons, and is thus not observed in neutron imaging. However, the hydrogen present toluene interacts with the neutrons, with scattering and absorption obscuring the neutrons before reaching the camera. Thus, toluene is opaque, whilst D<sub>2</sub>O is transparent in a neutron image. The interplay of D<sub>2</sub>O and toluene in an operating VFD was studied using neutron imaging. Typical operating parameters of the VFD were trialled, with a tilt angle of 45°. Initially, the studies were attempted at 1 mL scales (0.5 mL toluene and 0.5 mL D<sub>2</sub>O, Figure 77). This volume was chosen as typical confined mode operations in the VFD utilise 0.5 – 2 mL, with 1 mL volumes being common. However, at these volumes the two phases were unable to be clearly resolved at speeds above 3 krpm (Figure 78C). This issue was addressed by increasing the volume to 4 mL (Figure 78), which clearly shows good resolution between the two phases, even at the higher speeds trialled. The images were processed in the following manner. Firstly, three background control images were taken. These were I) a “raw” image of a VFD with an empty tube, dubbed the “empty tube” image. II) An image of the blank space with the VFD removed, dubbed the “empty beam”, and III) an image of the background with all neutrons blocked at the source, dubbed the “closed beam”. Secondly, an image of the operating VFD with liquid was taken. The three background controls were then subtracted from the sample image. This removes the background and the structure of the VFD from the final processed image, this “subtracted” image leaves only the liquid visible. A higher resolution set-up of the neutron imaging camera was used here compared to the previous work, resulting in a much smaller area of the VFD being imaged. Due to this, a series of images were taken, with the VFD being moved on its hydraulic platform so as to take a series of overlapping images up the length of the 45° tilted tube. These images were then stitched together using image processing software

to generate the images observed in Figure 77. This series of experiments shows that 4 mL scales are necessary to study the behaviour of toluene and water in the VFD at all speeds.

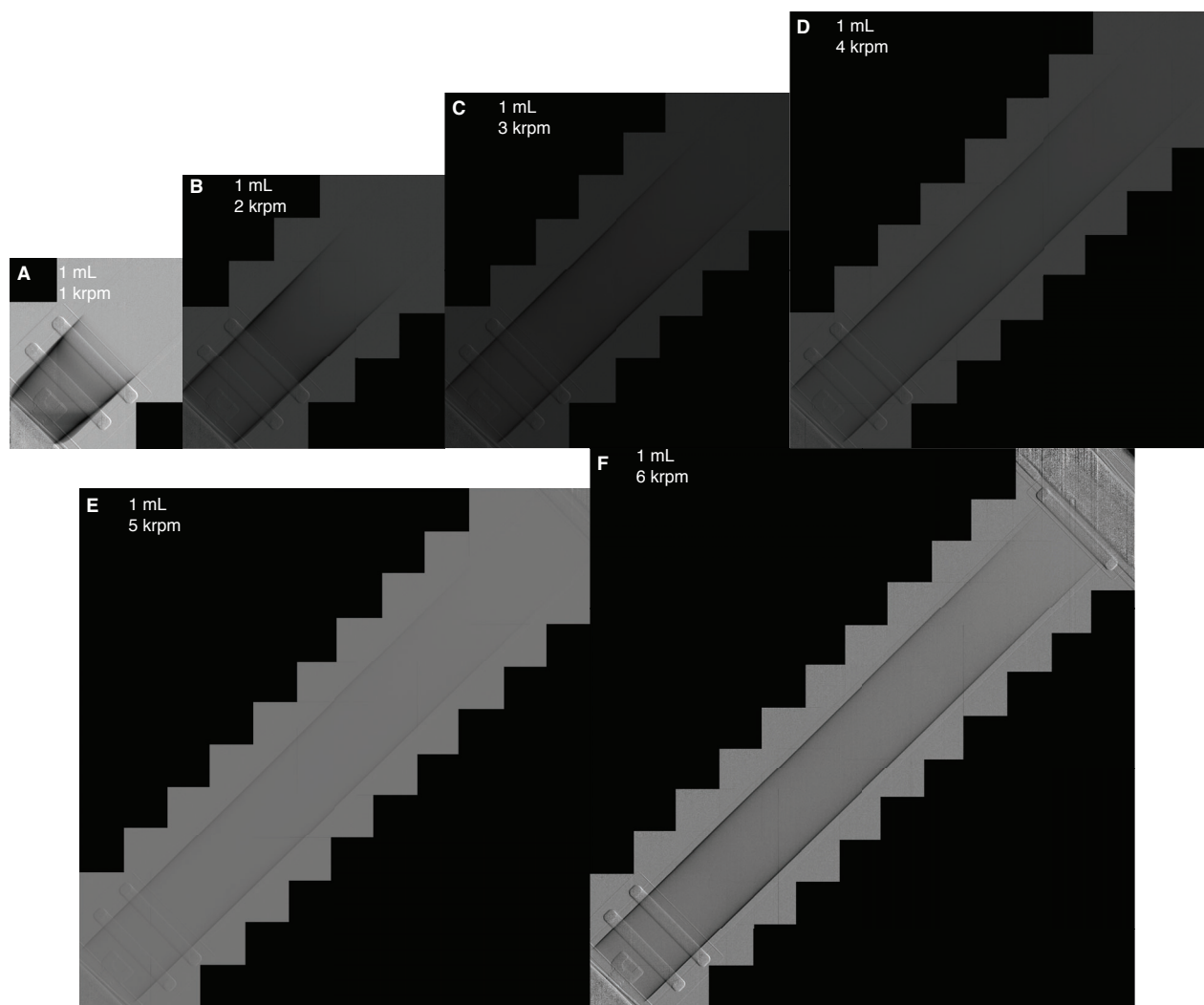


**Figure 77.** Stitched neutron images showing toluene (0.5 mL) and D<sub>2</sub>O (0.5 mL) in the VFD at various speeds. These speeds are (A) 1 krpm, (B) 2 krpm, (C) 3 krpm, (D), 4 krpm, (E) 5 krpm and (F) 6 krpm.



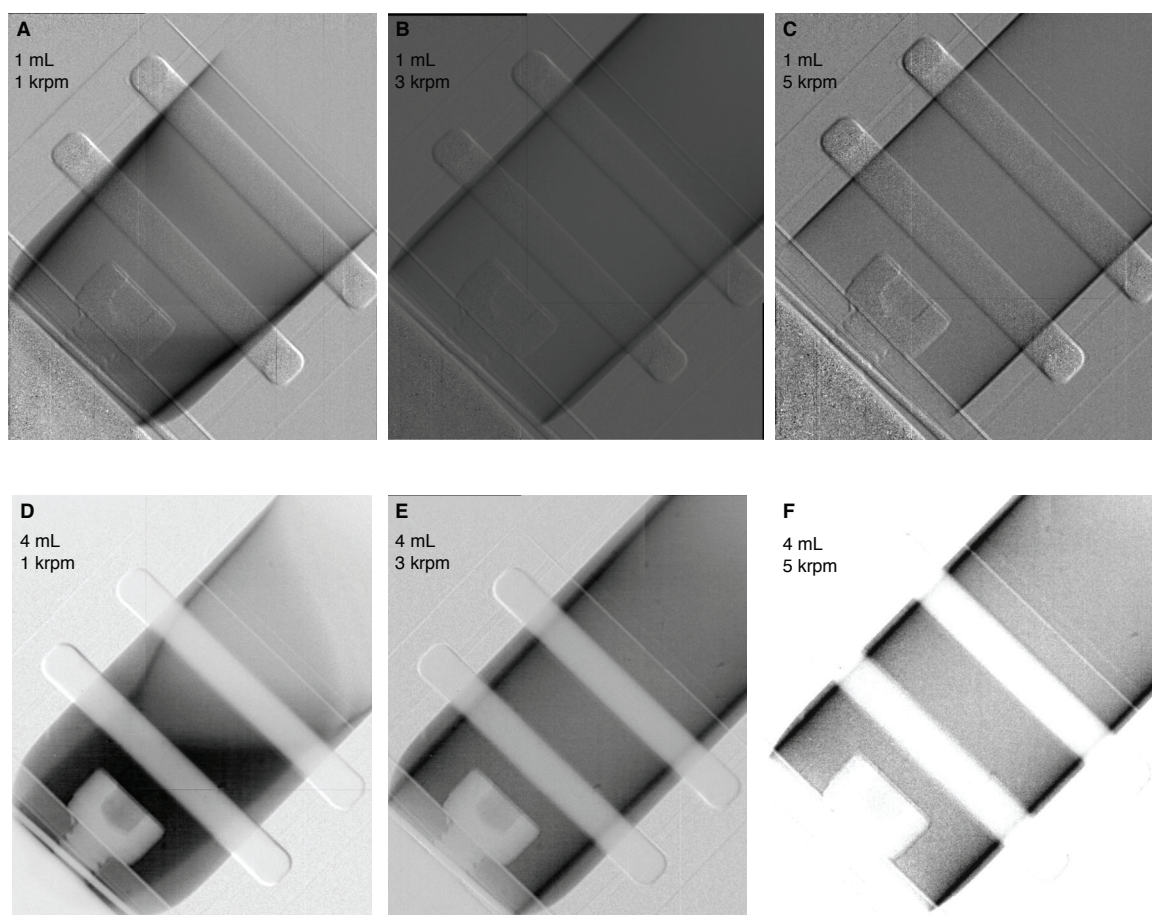


**Figure 78.** Neutron images of the base of rotating tube with 1:1 toluene to  $D_2O$ . The top row (A-C) contains 1 mL total (0.5 mL of each liquid) and the bottom row (D-F) contain 4 mL total (2 mL of each). The resolution between layers, especially at high speeds is vastly improved with larger volumes. Image contrasts are adjusted to clearly show two phases where possible.

In order to study further the behaviour of toluene and water, a rotational speed landscape was performed at 4 mL scales (2 mL  $D_2O$ , 2 mL toluene). For this, images were taken at each 50 rpm increment between 1 – 9 krpm. Instead of a series of images, only one image at the base of the tube was produced. This results in 180 total images. This was then repeated at various ratios (1:3, 1:9 and 3:1  $D_2O$ :toluene). A video was then produced, with each from being an image at +50 rpm from the previous image. By eye, it can be quantitatively observed that two distinct phases remain, and that the thickness of each phase reduces steadily as rotational speed increases. To quantify the thickness of each layer in this massive amount of data, an automated image processing tool is necessary. Work is on-going within the research group to develop code in order to automate the process of finding the thickness of each layer at each speed imaged. Only then can this be used to determine the SA:V - vital for engineering biphasic applications of the VFD. Details of this method can be found below in the experimental details at the end of this chapter.

Additionally, the VFD has been shown to aid in the separation of emulsified liquids.<sup>277</sup> This has many applications, especially in the purification of proteins. To study this, the emulsion of toluene and water was used as a model system. Toluene and water form an emulsion upon the sonication of the two liquids, without the presence of any surfactant or emulsification agent. This emulsion is unstable and will phase separate, but this process is slow – taking several days. Previous work in the VFD showed that phase separations are facilitated in the VFD, reducing the separation time by up to 9.3-fold for a two-phase system.<sup>278</sup> This was further

studied here in the phase separation of the water / toluene emulsion. To monitor this separation by neutron imaging, a pre-sonicated emulsion of toluene/D<sub>2</sub>O in the VFD was operated at 45° tilt, and monitored for 15 minutes. Over this period, 300 images, each with a 3 second exposure were taken for a total of 15 minutes. Rotational speeds of 0, 4, 6 and 8 krpm were performed separately. It is hoped that the work being developed in the group for automating the film thickness measurements from these neutron images can be applied here to quantify the separation over time. In the meantime, a rough comparison can be made by comparing the thicknesses of each phase from the culmination of the initial 30 seconds to the final 30 seconds of the 15-minute process. This is found in Table 16, with a representative image found in Figure 79. Because the total thickness appears to increase from 6 to 8 krpm, it is likely that the measuring method is not accurate. Thus, it is vital that a more accurate method is developed, as mentioned this is currently being worked on by other members within the group. However, this work does suggest an enhanced phase separation at 6 krpm, but not at either 4 or 8 krpm. The reason for this is unclear, but it may hint at the underlying fluid dynamics. This result is consistent with many other results found in the VFD, in that a particular speed is vastly different from other speeds. This is most notably observed in the VFD enhanced activity of enzymes.<sup>87</sup>

**Table 16.** Measurements of the thickness of the toluene and D<sub>2</sub>O phases in a pre-sonicated emulsion after operating in the VFD at various rotational speeds. Measurements are taken from images from the initial 30 seconds, and the final 30 seconds of a 15 minute spin time. Ratios of each layer are shown, and the change in the ratio is calculated. From this, positive values indicate increased mixing and negative values indicate phase separation.

Rotation	First 30 second exposure				Final 30 second exposure				Change in ratio
	Toluene film (μm)	D2O film (μm)	Total (μm)	Ratio	Toluene film (μm)	D2O film (μm)	Total (μm)	Ratio	
0 krpm	8085.12	12203.41	20288.53	0.662	8220.8	12698.5	20919.3	0.647	-0.0151
4 krpm	271.524	685.908	957.432	0.395	305.472	610.944	916.416	0.5	0.1041
6 krpm	237.588	322.44	560.028	0.736	214.956	367.74	582.696	0.584	-0.1523
8 krpm	305.6	452.5	758.1	0.675	362	351	713	1.031	0.3559

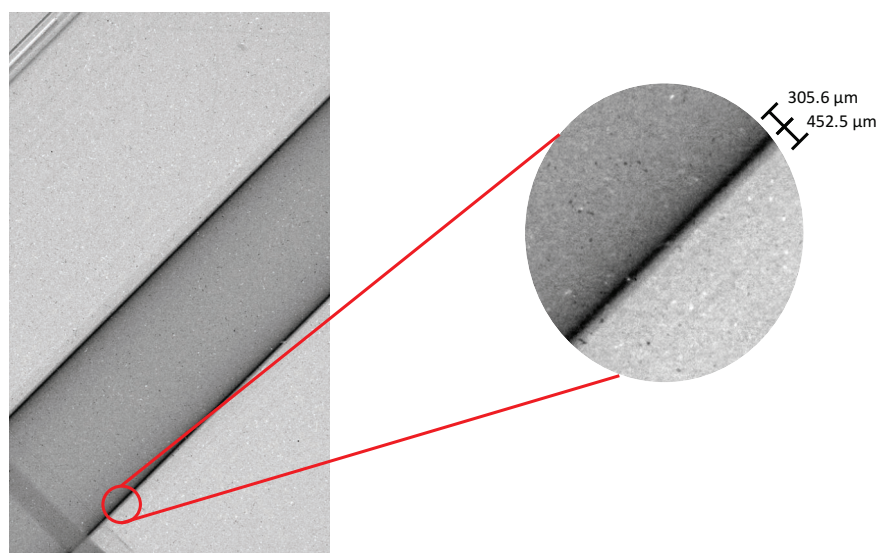


**Figure 79.** Representative neutron image from monitoring the phase separation of a pre-sonicated emulsion of toluene and D<sub>2</sub>O. Image from the combined exposure over the initial 30 seconds of rotating the emulsion at 8 krpm.

To gain further insight into the behaviour biphasic systems in the VFD, small angle neutron imaging (SANS) was also performed on toluene/water mixtures (Figure 80). If any micro-mixing resulted in regular structure in

the size range of SANS ( $\approx 1 - 200 \text{ nm}$ ), then this could be observed in SANS. This was thought to possibly occur as bubbles of one phase within the other phase for example. However, Figure 80 shows that there is no difference in the scattering patterns of a biphasic system compared to a single  $\text{D}_2\text{O}$  phase, other than the higher intensities from having a thicker film at the lower rotational speeds. Any structure - such as an emulsion - would give the decay some sort of shape that could then be modelled. This is not observed and it is concluded that no regular shape within the size range of SANS can be observed when mixing  $\text{D}_2\text{O}$  and toluene.

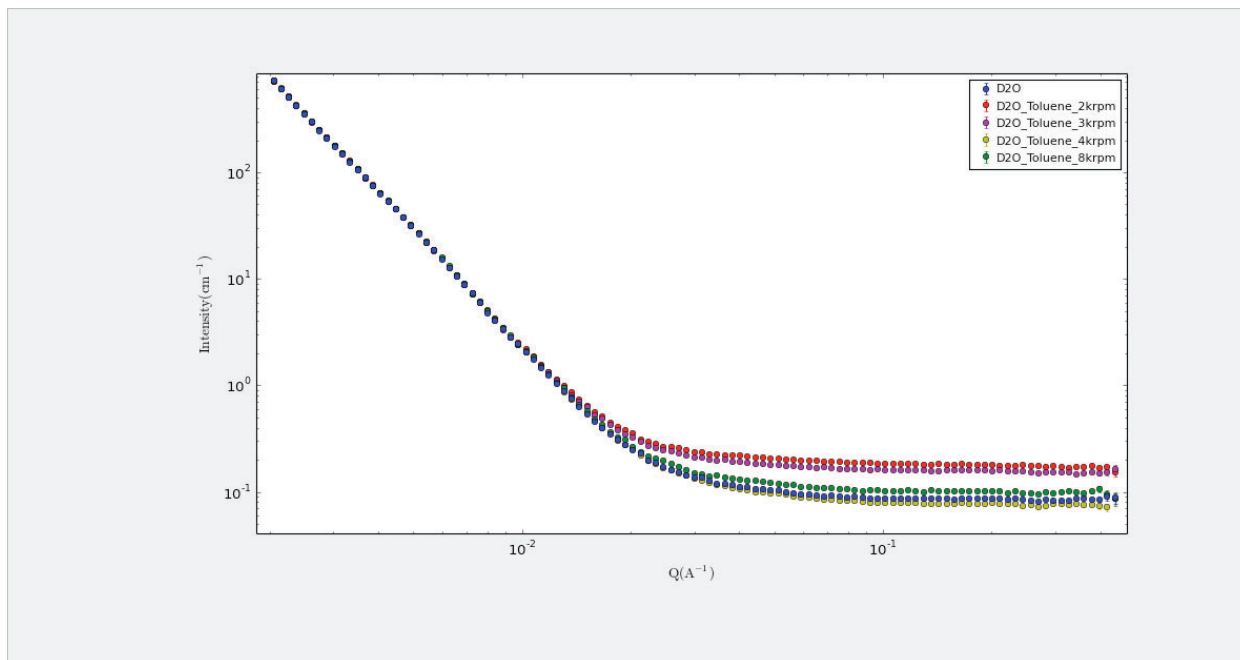


**Figure 80.** In-situ SANS pattern of  $\text{D}_2\text{O}$ , and mixtures of  $\text{D}_2\text{O}$ /toluene at various speeds in the VFD. This pattern is baseline – no structure can be elucidated.

Performing SANS on the operating VFD is a novel process, and the honing of techniques for performing this ground-breaking work has led to many applications of in-situ SANS on the VFD. Note that this should not be called a real-time process, due to the nature of SANS monitoring. SANS accumulates a scattering pattern of a sample over time, and can take several hours to accumulate enough data for a statistically significant result. The time required for a successful scattering pattern depends on the path length of sample, as well as the samples concentration, and the samples ability to scatter neutrons. A typical path-length of sample obtained in SANS is 2 mm. However, the VFD produces a film with a thickness between 250 – 600  $\mu\text{m}$ . With the neutron beam passing through both walls of the rotating tube, a path length between 500 – 1200  $\mu\text{m}$  can be achieved. The processing time required to accumulate good statistics in the data increases by a squared function with decreasing path length, thus much longer accumulation times are required for in situ SANS VFD monitoring. With a typical accumulation time of 3 hours being employed, the monitoring cannot be called real-time.

### 6.2.2 – Summary and Outlook on Biphasic Systems in the VFD

This work shed important insight into how immiscible liquids behave in the VFD, something unknown at the start of this Ph.D. This work showed that the immiscible liquids form distinct layers, separated based on density. At this stage, only qualitative results could be obtained from the data. Work is currently ongoing in the group into obtaining quantitative results for this data. This involves the formulation of an automated way of finding the thickness of the liquid films from the images. The results of which it will be possible to determine the effect of rotational speed directly on the SA:V. This is a vital piece of information when formulating a biphasic VFD process. For now, it appears that the liquid phases separate purely on differences in density, and there is no evidence for micro-mixing between the liquid phases. This is backed up by both neutron imaging, and SANS data. Preliminary work here also shows that the phase separation of emulsions is enhanced at 6 krpm, when compared to 0, 4 and 8 krpm. This has implications for in-line phase separations, and may shed insight into the nature of the complex fluid flows occurring within the VFD. This may aid the explanations of previously demonstrated work in the VFD, which produces unexpected, and often beneficial results for VFD processing that is highly rotational speed dependant.<sup>82, 87</sup> Developing an understanding of the complex fluid flows experienced in the VFD is a major focus of the Raston research group. This work may be vital for progressing towards the development of a predictive model for outcomes in the VFD.

## Chapter 7 – Future Works

Throughout this work many questions were answered, however several more questions were prompted. Specific to each chapter above are the recommended further directions. However, several projects are separate to those mentioned above. These projects did not immediately reveal any novel phenomena. However, some interesting concepts were found that warrant further studies. The work in this chapter is reported in hopes of aiding any future work in these areas. Regardless of this, reporting work that has not led to publication is an important practice. This is becoming increasingly relevant as more and more algorithms are reported, for the purpose of sorting and searching through large databases of chemical data.<sup>279-282</sup> Examples of this are software for performing retrosynthetic analysis.<sup>279, 282</sup> These methods are greatly benefited from being able to reference work that has not produced a desirable outcome.<sup>283</sup> throughout this Ph. D candidature, several projects of this nature were explored. This involved multiple aspects of ferrocene – the VFD mediated synthesis of, and the subsequent oxidation to form ferrocenium. Another attempted project was that of studying oscillation reactions, and the last project discussed here is the attempt to use the VFD as a platform for the “degumming” of biodiesels. These are all discussed below.

### 7.1 – Ferrocene Processing in the VFD

Ferrocene was identified as a synthesis target that could benefit from VFD processing. A common undergraduate lab involves cracking dicyclopentadiene (**87**) into cyclopentadiene (**88**).<sup>284-286</sup> This is then used as the starting point to first form the aromatic conjugate base (**89**) followed by ligand exchange with Fe(II)Cl<sub>2</sub> to form ferrocene (Figure 81). It is the initial step – the cracking of **87** – that is time consuming and is often fickle in producing the **88**. It was hypothesised that the shear forces in the VFD may facilitate the room temperature cracking of **87**. Several preliminary experiments were performed to test this hypothesis.

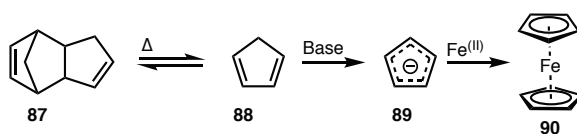
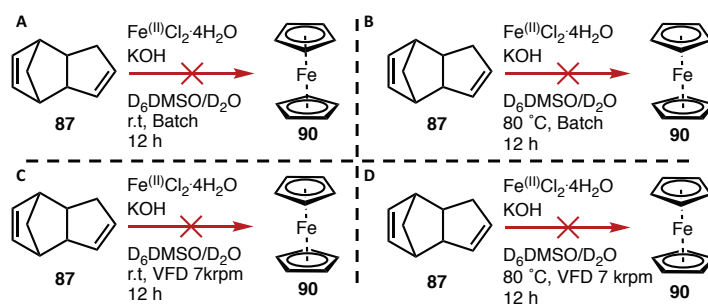


Figure 81. Common procedure for the synthesis of ferrocene.

Initially, the synthesis of ferrocene was attempted in a one-pot, VFD process. For this, dicyclopentadiene (**87**), Fe(II)Cl<sub>2</sub>·4H<sub>2</sub>O and the base KOH were dissolved in a D<sub>6</sub>-DMSO/D<sub>2</sub>O mixture and operated in the VFD at 7 krpm. Deuterated solvents were used so as that <sup>1</sup>H-NMR analysis could be performed directly on the crude reaction mixture. However, no reaction was found to occur in the VFD or batch at either room temperature or at 80 °C (Figure 82). Analysis revealed that only starting materials remained, no reaction had occurred.



**Figure 82.** Attempts to achieve one-pot synthesis of ferrocene in the VFD. This involved room temperature in batch (**A**) and VFD @ 7 krpm (**B**), and also at 80 °C in batch (**C**) and VFD @ 7 Krpm (**D**). Reactions were performed in deuterated solvents and  $^1\text{H-NMR}$  analysis was performed directly on crude reaction mixtures after 1 h. No ferrocene was detected in any case.

Due to the fact that only starting materials being found in both the VFD and batch processing, it was deemed that no cracking of the dicyclopentadiene (**87**) via the retro-Deils Alder had occurred after 1 hour. This was thought to be limiting to this reaction. It has been reported that IR light can achieving small scale room temperature cracking of **87**. Success in the group in using IR laser beams to achieve C-C bond cleavage, such as that in the slicing of carbon nanotubes.<sup>287</sup> Thus it was hypothesised that treating the **87** with an IR laser beam would help achieve this retro-Deils Alder. To study this, the reaction was performed at room temperature, whilst exposed to a pulsed laser beam (1000 nm). This was performed at laser energies of 650 mJ, and 460 mJ. However, the analysis of the crude reaction mixture by  $^1\text{H-NMR}$  revealed that a small no reaction had taken place.

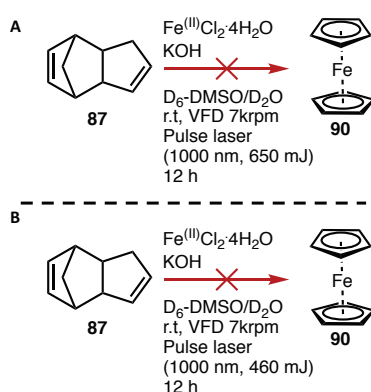


**Figure 83.** Attempted on-pot synthesis of ferrocene in the VFD with laser (1000 nm), with laser power at (**A**) 650 mJ and (**B**) 460 mJ.  $^1\text{H-NMR}$  analysis revealed only starting materials remained.

The observation that only starting material was obtained after both room temp, heating and pulsed laser treatment suggested that none of these methods were able to achieve the retro-Deils Alder product (**88**) after 1 hour. Thus, further studies were performed on pure (**87**) to ascertain what conditions are required to achieve the retro-Deils Alder. Initially, it was hypothesised that the large surface area of liquid in the VFD would facilitate the evaporation of the resulting **88**, thus driving the Deils Alder equilibrium to consume more of the **87**. In order to test for this, **87** (1 g) was placed in the VFD tube and operated at 7 krpm. During processing, a gentle stream of  $\text{N}_2$  gas was flowed over the liquid film (Figure 84B). This was intended to be a carrier gas to remove the more volatile **88**, whilst leaving the solid **87** in the tube. This **88** would then be collected in a cold trap (-180 °C) downstream of the VFD. After 3 hours of operation in the VFD, there was no residual material in the VFD tube, barring trace amounts of **87**. This rapid removal hinted that the **87** had successfully transformed into the more

volatile form (**88**). However, no material was present in the cold trap. Thus, it was deemed that the material had exited through leaks in the sealing. Despite attempts to plug these leaks, it was deemed that leakage was occurring through the rubber o-rings that connect the VFD tube to the spin-guide bearings (Figure 84B), and that a true seal could not be achieved without re-designing a new VFD. This does not confirm the formation of **88**, since it is possible that the increased surface area and carrier gass combination in the VFD is sufficient to effectively sublime all **87** in the tube.

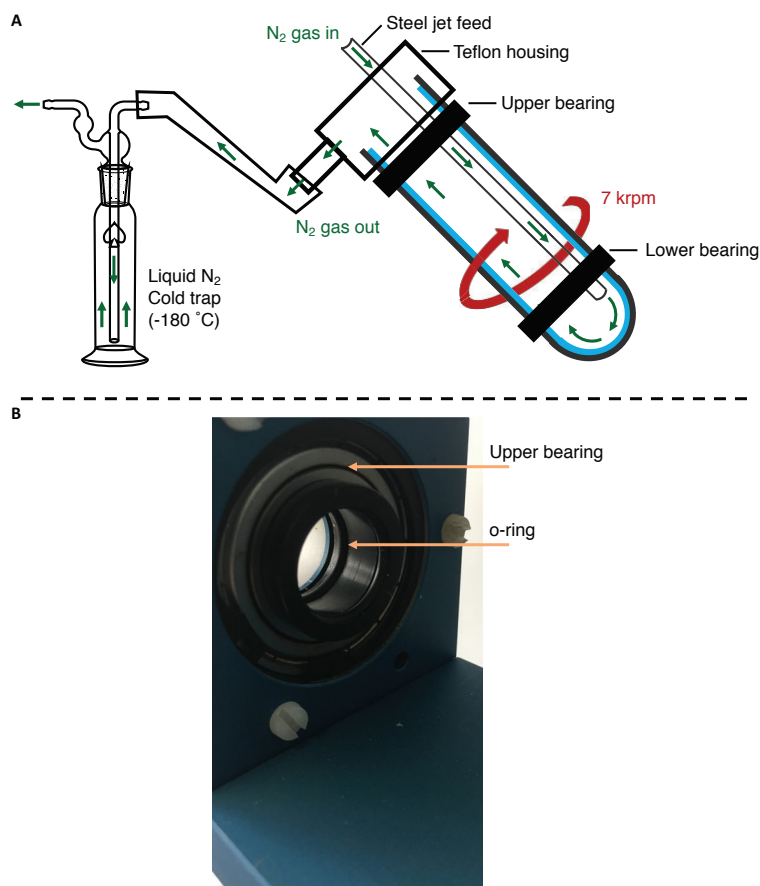


**Figure 84.** (A) cross sectional schematic of the experimental set-up. A steady stream of N<sub>2</sub> gas is gently flowed over the vortex film (**87**), exits the VFD at passes through a cold trap (-180 °C). (B) photograph of the o-ring in the “upper bearing”, where leaks are occurring.

Due to the likelihood of leaks with this set-up, this reaction was performed in a sealed tube. Also, a small amount of toluene ( $\approx 250 \mu\text{L}$ ) was added to ensure that the **87** remained a liquid and did not solidify.\* The results of which revealed that no retro-Deils Alder was found to take place after 15 minutes, at any of the rotational speeds trialled (3, 4, 5, 6, 7, 8 & 9 krpm).

\* This work was carried out by 3rd year students India Shackleford and Ally Krenn.

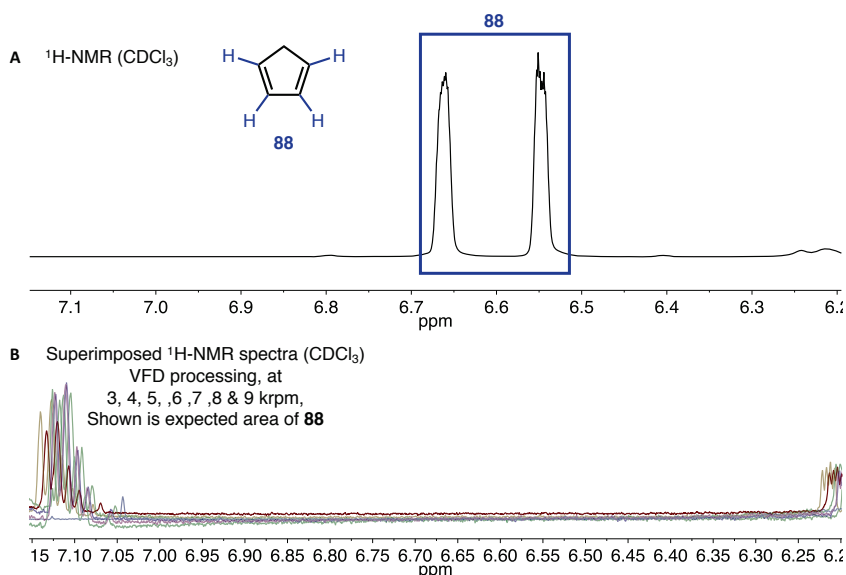


**Figure 85.** (A)  $^1\text{H-NMR}$  spectra of **88**, and (B) superimposed  $^1\text{H-NMR}$  spectra of attempts to crack **87** in the VFD at rotational speeds of 3, 4, 5, 6, 7, 8, & 9 krpm. Showing area of the spectrum where **88** is expected.

These experiments reveal that the VFD is unable facilitate the cracking of dicyclopentadiene (**87**) to form cyclopentadiene (**88**) in under 1 hour. This was found to be the case at room temperature, at  $80^\circ\text{C}$  and also at room temperature with a pulse laser (1000 nm, 650 mJ & 460 mJ). Increasing the length of time is an obvious first step in achieving the retro-Deils Alder reaction, however the main application in mind here was the teaching lab experiment for the synthesis of ferrocene. The current method of heating **87** is able to achieve workable amounts of **88** after 3 hours. Further work is underway in coating the surface of the VFD tube in a mesoporous silica, functionalised with catalytic properties for the retro-Deils Alder.

Further to the synthesis of ferrocene, the VFD mediated oxidation to ferrocenium was briefly studied. It was hypothesised that shear forces would facilitate the stretching of Fe-C bonds in ferrocene (Figure 86). This mechanical energy imparted into the molecule would contribute to the energy barrier in transforming ferrocene into the ferrocenium ion. This would effectively lower the activation energy, allowing for the use of more mild oxidants – such as air.

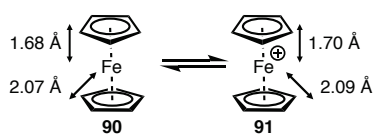
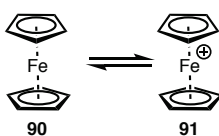


**Figure 86.** The  $\text{Fc}/\text{Fc}^+$  redox couple. Shown are the bond lengths.<sup>106</sup>

To study the effect of the VFD on the oxidation of ferrocene (**90**), comparisons were made across VFD rotational speeds between 4 – 9 krpm and compared to a magnetically stirred sample (batch). Initially, this was performed in a biphasic solution of **90** in toluene (1 M) and water (Table 17). This did not reveal any conversion to **90**, as determined by a lack of blue colour in the aqueous phase.

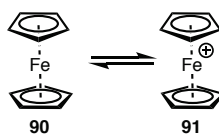


**Table 17.** Studying oxidation of Fc (**90**) to form Fc<sup>+</sup> (**91**) in the VFD vs batch. The biphasic system of **90** in toluene (1 M) and water was operated under various mixing conditions. Presence of **91** determined from blue colour in the aqueous phase.



Entry	[1 M] <b>90</b> (mL)	Water (mL)	Vessel	Atmosphere	2 hours	12 hours
1	1	0.5	Batch	air	×	×
2	1	0.5	VFD 4 krpm	air	×	×
3	1	0.5	VFD 5 krpm	air	×	×
4	1	0.5	VFD 6 krpm	air	×	×
5	1	0.5	VFD 7 krpm	air	×	×
6	1	0.5	VFD 8 krpm	air	×	×
7	1	0.5	VFD 9 krpm	air	×	×

It was thought that [H<sup>+</sup>] in neutral water was too low to allow the H<sup>+</sup>/H<sub>2</sub> and the O<sub>2</sub>/H<sub>2</sub>O couples to be reduced by Fc. To account for this, the pH was raised. This was achieved by using a biphasic system of **90** in toluene (1 M) and HCl (1 M, aq.) (Table 18). The presence of **91** was determined by a blue colour in the aqueous phase. This was found to occur after 12 hours, but not within 2 hours. A promising preliminary experiment showed the production of **91** after 2 hours in the VFD at 9 krpm (entry 7). However, this was not found to be reproducible.



Entry	[1 M] <b>90</b> (mL)	[1 M] HCl (mL)	Vessel	Atmosphere	2 hours	12 hours
1	1	0.5	Batch	air	×	✓
2	1	0.5	VFD 4 krpm	air	×	✓
3	1	0.5	VFD 5 krpm	air	×	✓
4	1	0.5	VFD 6 krpm	air	×	✓
5	1	0.5	VFD 7 krpm	air	×	✓
6	1	0.5	VFD 8 krpm	air	×	✓
7	1	0.5	VFD 9 krpm	air	×*	✓

\* A single replicate showed the blue colour after 2 hours, but this was not reproducible

**Table 18.** Studying oxidation of Fc (**90**) to form Fc<sup>+</sup> (**91**) in the VFD vs batch. The biphasic system of **90** in toluene (1 M) and HCl (1 M, aq.) was operated under various mixing conditions. Presence of **91** determined from blue colour in the aqueous phase.

It was thought that the reduction potential of Fc<sup>+</sup>/Fc couple was too high for a reaction to occur over manageable timescales for high throughput analysis (> 5 minutes, < 1 hour). To increase the reaction rate, a new oxidising agent was sought after. Initially, Fe<sup>(III)</sup>/Fe<sup>(II)</sup> (E<sup>0</sup> = 0.77 V vs SHE) was trialed, however it was found that as soon as the aqueous Fe<sup>(III)</sup>Cl<sub>2</sub> solution made contact with the hydrophobic **90** in toluene (1 M) (Table 19. Entries 1 & 2). A redox couple with a reduction potential closer to that of Fc<sup>+</sup>/Fc was sought after, and for this [Fe<sup>(III)</sup>(CN)<sub>6</sub>]<sup>3+</sup>/[Fe<sup>(II)</sup>(CN)<sub>6</sub>]<sup>2+</sup> (E<sup>0</sup> = 0.38 V vs SHE). This is close to the estimated E<sup>0</sup> of Fc<sup>+</sup>/Fc (0.3 – 0.5 V vs SHE), though due to the insolubility of **90** in water, this value cannot be determined. However, again entries 3 & 4 show that a blue colour was formed at the moment of contact. This is too fast to be implemented

into a real-time monitoring set-up, required to monitor the formation of **91** and make quantitative comparisons between VFD and batch.

**Table 19.** Studying oxidation of **90** to form **91** in the VFD vs batch. The biphasic system of **90** in toluene (1 M) and an oxidant (Ox = Fe<sup>(III)</sup> or [Fe<sup>(III)</sup>(CN)<sub>6</sub>]<sup>3+</sup> (1 M, aq.) was operated in batch and in the VFD at 7 krpm. Presence of **91** determined from blue colour in the aqueous phase.

<i>Entry</i>	<i>Ox</i>	<i>Vessel</i>	<i>Atmosphere</i>	<i>&lt; 1 second</i>	<i>12 hours</i>
<b>1</b>	Fe <sup>(III)</sup>	Batch	N <sub>2</sub>	✓	✓
<b>2</b>	Fe <sup>(III)</sup>	VFD 7 krpm	N <sub>2</sub>	✓	✓
<b>3</b>	[Fe <sup>(III)</sup> (CN) <sub>6</sub> ] <sup>3+</sup>	Batch	N <sub>2</sub>	✓	✓
<b>4</b>	[Fe <sup>(III)</sup> (CN) <sub>6</sub> ] <sup>3+</sup>	VFD 7 krpm	N <sub>2</sub>	✓	✓

Some evidence that hints that the shear is indeed lowering the activation energy barrier to forming the ferrocene. However, despite attempting several rotational speeds. No benefit in the oxidation of **90** was conclusively shown here. Real time methods, such as UV-Vis spectroscopy is promising for ascertaining whether or not the oxidation of **90** is effected by the shear stress in the VFD.

An interesting result was noted during the oxidation of ferrocene (**90**), it was observed that as evaporation decreased the extent of the solvent front in the VFD, the ferrocene would crystallise at the interface. This would either result in crystals that were rods or cubic in appearance. XRD experiments suggested that different crystal phases were present between these visually different crystals. The rods correspond to the most common form of ferrocene, but the cubes do not match the expected XRD pattern for **90**. These unique cubes were only observed at an operating speed of 9 krpm.

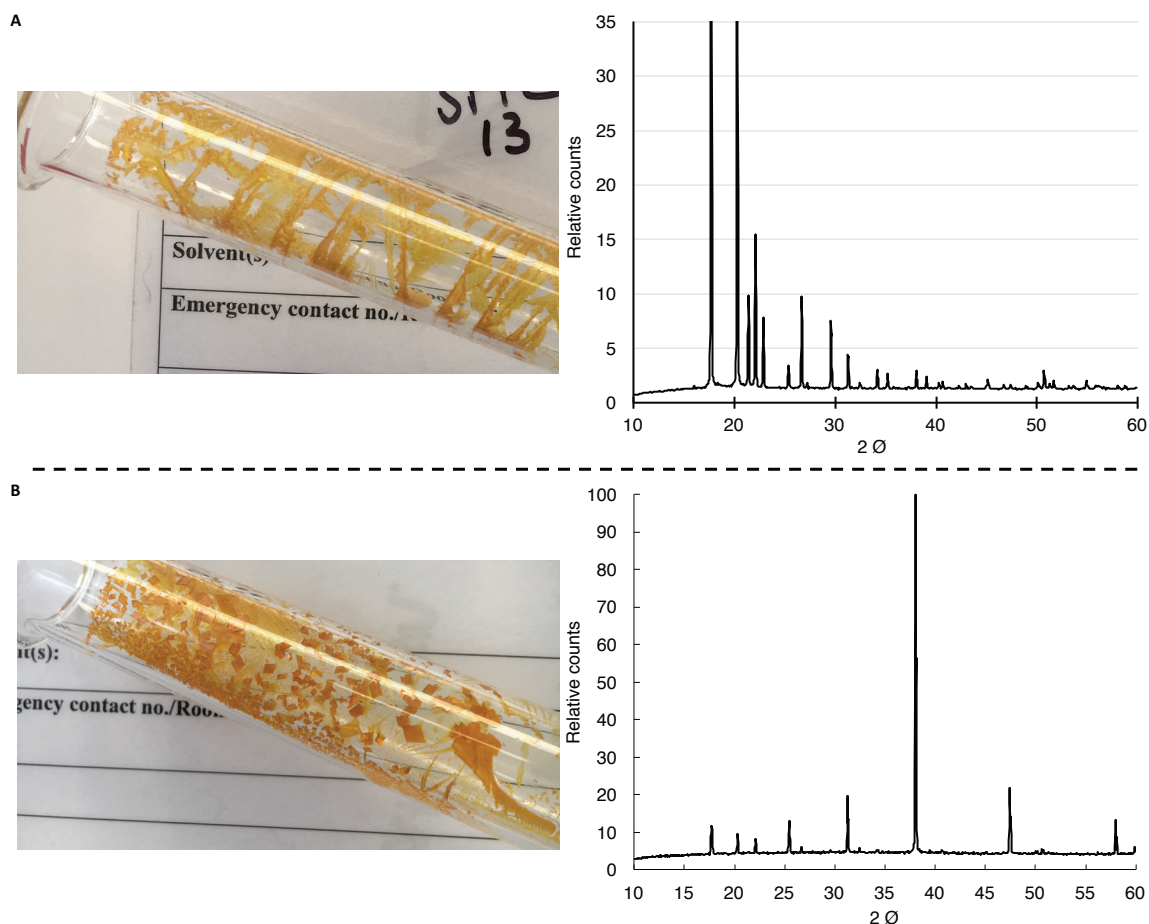


**Figure 87.** Ferrocene crystals obtained in the VFD. **(A)** Crystals typically obtained in the VFD are rods, with corresponding XRD pattern expected for ferrocene. **(B)** cubic crystals sometimes obtained at 9 krpm, with unique XRD pattern.

IR studies were performed to check if water was being incorporated into the structure, which could account for this anomalous crystal phase. As can be seen, there is no water present in either the IR of the bulk crystals (rods or cubes). When these cubes were attempted to be reproduced with solvents purified by distillation, no cubes could be obtained. It is possible that impurities in the solvent led to these crystals, in which case co-crystals were being observed, explaining the different XRD patterns. Further work is required to determine the exact nature of forming these cubic crystals.

It is inconclusive whether or not the VFD can control the formation of different crystal phases of materials, but it does not look possible to achieve this for ferrocene. The anomalous crystal structures observed are likely due to impurities in solvents. Further work is required to identify what impurities caused these anomalous crystals.

## 7.2 - Oscillation Reactions

Oscillation reactions are reactions that undergo periodic - often drastic - changes on their way to achieving equilibrium. In general, a product will be formed slowly increasing the concentration until a critical point is reached, favouring a new reaction, consuming the new compound. These equilibria compete with each other, going back and forth in regular time intervals. This oscillation occurs several times until an equilibrium is eventually reached.

Here at Flinders University, a common 2<sup>nd</sup> year chemistry practical is the oscillation of cerium/malonic acid. This results in a sharp change in pH which can be visualised by the pH indicator ferroin (**92**, Figure 88). Performed at concentrations specified, this reaction oscillates from red to blue and back approximately every 7 seconds. It was hypothesised that the unique conditions in the VFD may be able to alter the rate of kinetics observed for this oscillation. A possible effect would be that of shear stress acting to aid in the removal of the solvation sphere around the cerous metal centre. Any partial removal of the solvation sphere would possibly lower the required energy for a successful reaction collision of the malonic acid to the metal centre.

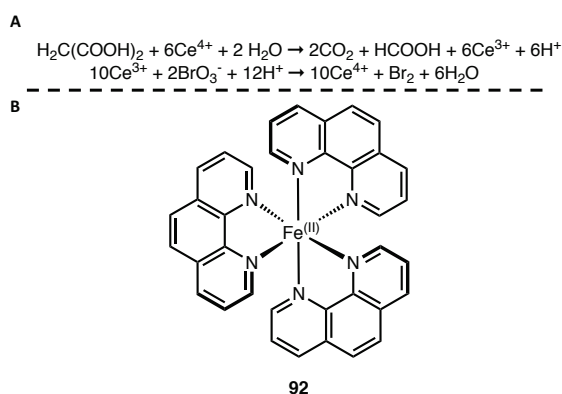


**Figure 88.** (A) The competing reactions in the cerium/malonic acid oscillator. (B) the pH indicator ferroin used to visualise this oscillation.

This reaction was to be monitored by UV-Vis spectroscopy. Firstly, the wavelength maxima of the resting state (red) of the solution was found to be 512 nm (Figure 89A). Using this wavelength, the oscillation was then monitored over time (Figure 89B). As can be observed, the absorbance at 512 nm increases, and then is rapidly decreased to a baseline absorbance, before slowly building up again to repeat this process. This is observed visually from a build-up of a red colour, before rapidly turning blue. Interestingly, the maximum absorbance reached increases with each period.

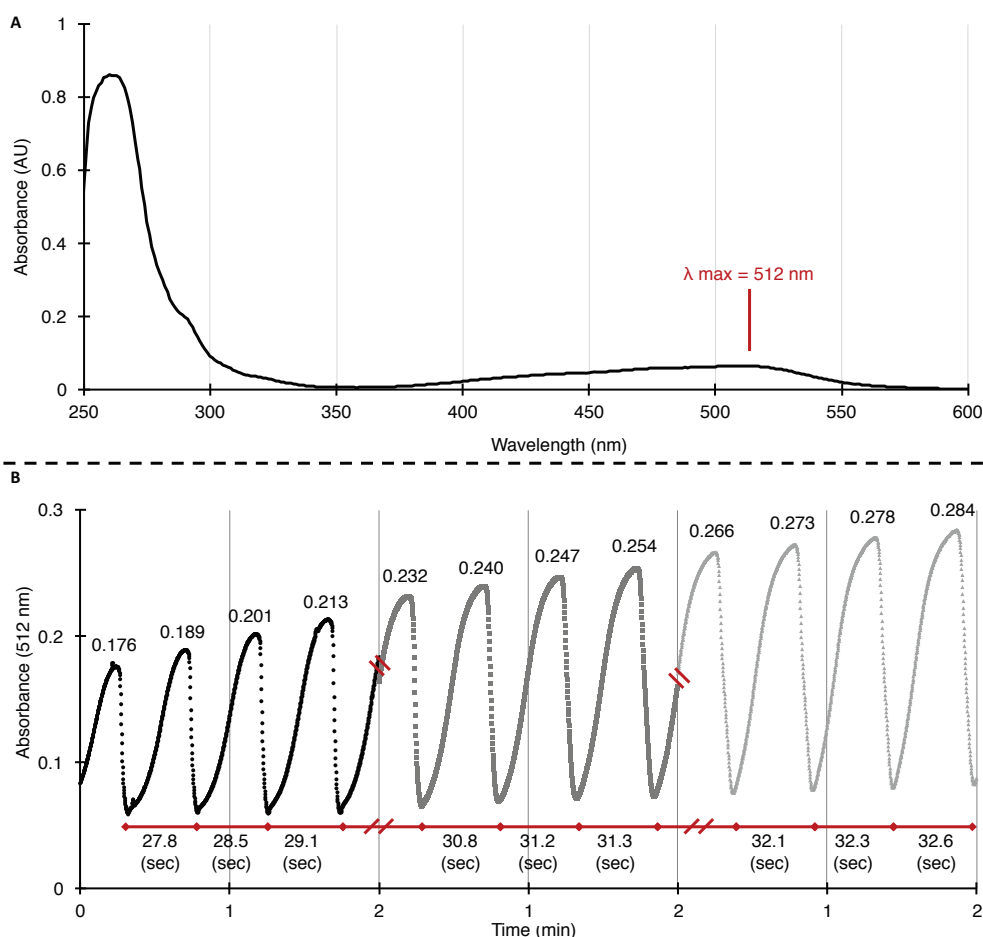


**Figure 89.** (A) Absorbance of the cerium/malonic acid oscillator upon reaching the resting state, highlighting the  $\lambda_{max}$  at 512 nm. (B) monitoring the wavelength 512 nm over time of the cerium/malonic acid oscillation in an unstirred cuvette – visualised by ferrocene pH indicator (92). Note that the instrument was only able to measure consecutively for 2 minutes. After this, it had to be manually reset ( $\approx 30 \text{ sec}$ ) This is indicated by breaks in the spectra and new colour shading

Monitoring the oscillation in this way allows quantitation of the time taken between each oscillation. For each 2-minute monitoring interval, it can be observed that the time between each interval increases in a linear fashion (average linear  $R^2 = 0.96$ , Figure 90A). The slope of this linear increase should be compared to that of batch to obtain a direct comparison between batch vs VFD processing. Interestingly, the absorbance maxima reached at each oscillation increases in a linear fashion (average linear  $R^2 = 1.0$ , Figure 90B). This can thus be used to identify an oscillation period in terms of how many oscillations have taken place. This is an important factor in comparing the effected rate in the VFD vs batch, as the oscillation time intervals must be compared over the same range of oscillation periods.

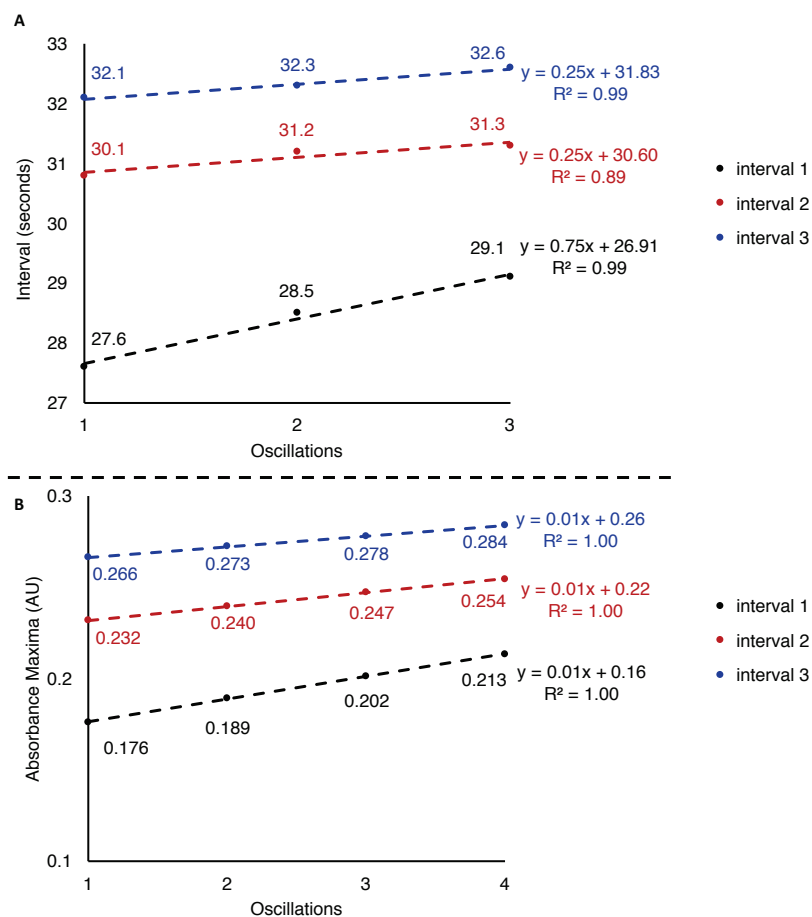


**Figure 90.** Plotting the (A) time intervals between each oscillation and the (B) maximum absorbance reached in each oscillation (Figure 89). Intervals indicate the 2-minute monitoring time. Shown are the linear trend-lines, their equations and the linear  $R^2$  values.

Unfortunately, monitoring this reaction in real-time in the VFD was ultimately unsuccessful. The shorter path-lengths of the thin film and the less sensitive hardware did not allow for spectra to be obtained. Concentrations were increased, however too much ferriin indicator (**92**) appeared to shut down the oscillations, and no concentration trailed gave anything but noise. More sensitive real-time UV-Vis hardware is required to achieve monitoring of this reaction in the VFD. Due to this, another oscillator system was sought after.

Since the previous attempted oscillator was unsuccessfully monitored in the VFD, a new approach was needed. The luminol oscillator is a clear colourless solution that periodically produces the bright blue glow of luminol. It was thought that a regular camera would then be able to film the VFD in a dark box to observe the periodical blue glow. After attempting a few different conditions, no oscillation was able to be achieved, and no blue glow could be observed when filming the VFD in a dark box. Recommended future works involves the development of a more sensitive UV-Vis real time detector for the VFD to be able to monitor the cerium/malonic acid oscillator (or similar oscillating reaction). It may also be possible to get conditions that produce a brighter luminol oscillation for video monitoring in dark box. On top of these, there is also the possibility of a different real-time measurement that will monitor any of the numerous known oscillating reactions. Currently in development is a real-time Raman attachment for the VFD. This may prove effective for monitoring oscillating reactions over time. This Raman attachment may be of use for the cerium/malonic acid oscillator described herein. The Raman spectrum of  $\text{CeO}_2$  has been described at length.<sup>288</sup> Combined with the use of Raman to

describe  $\text{Ce}^{3+}/\text{Ce}^{4+}$  in nanoparticles may be of use to applying Raman monitoring to this  $\text{Ce}^{3+}/\text{Ce}^{4+}$  oscillation.<sup>289, 290</sup>

Although all the avenues explored here were largely inconclusive, it is still worthwhile to overcome the highlighted obstacles and observe the effect of the VFD on the kinetics of the reactions, real-time in the VFD. This has applications in fine tuning parameters, and high-throughput data collection towards optimising reactions in general. It may also shed light on the behaviour of metal/ligand complexes and the role of shear (or other factors) in the VFD.

### 7.3 - Oil degumming

Production of biodiesel is an area of research that has seen a large amount of interest. There are many methods reported that have been able to produce biodiesel from renewable sources. This is highly promising as producing transport fuel from renewable sources would alleviate the reliance on fossil fuel sources. Many routes have been reported to produce biofuel from sources such as plant oils (olive, canola, coconut ect.) and also from microbes (algae & certain fungal species). The VFD has previously reported the formation of biodiesel from both these sources.<sup>93, 291</sup>

A major problem with bio-sourced fuels is that, depending on the processing and on the source, the fuel may “gum” up engines. “Gumming” refers to clogging that occurs from residual solids or liquids from the combustion that do not leave the engine through the exhaust systems. This poses a large problem for uptake of biofuels. Residual phospholipid groups are largely (but not solely) responsible for this gumming. Many methods have been developed to counter this gumming problem, and a large portion of these methods aim to remove these phosphates from the biofuel. Due to this, it is common to measure the amount of phosphorus in the biofuel as the benchmark test for how successful a degumming method is.

A common degumming method is to simply mix the biofuel with hot water. This hot water is more effective at removing these phosphate groups. This is often combined with washes with hot basic water, in an attempt to de-protonate the phosphate groups increasing the hydrophilicity. However, this runs the risk of hydrolysing esters, destroying the biofuel and re-forming the starting plant/microbial oil.

The VFD was proposed to be a great platform for mixing biofuels with pH neutral water, in a continuous manor - removing the gumming agents and increasing the performance of the fuels. It was also thought that due to the enhanced mixing capabilities, it could be performed at room temperature. This reduces the risk of hydrolysing the esters. A method for the complete digestion of the biofuel for ICP-OES analysis of the phosphorus was developed.

Firstly, a method for finding the phosphorous content of the oil was developed. This used a microwave assisted acid digestion of the oil, before ICP-OES analysis of the phosphorous content. This method was then used to compare batch vs VFD processing (Table 20) As can be seen, no discernible difference in phosphorous content was identified.

**Table 20.** Comparisons of the phosphorous content (P) in mustard seed oil (entry 1) to that of attempted de-gumming in batch and VFD processing. P determined by microwave assisted acid digestion for ICP-OES analysis.

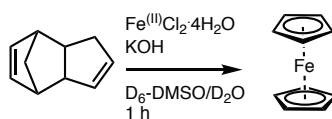
Entry	Mustard seed oil (mL)	Water (mL)	Vessel	Temperature	Time	P (mg/Kg)
1	0.5		-	-	-	13
2	3	2	batch	room	2 hours	15
3	3	2	VFD 5 krpm	room	2 hours	14

Since these preliminary results did not appear to be promising, the project was not continued. Further work in this area should include the development of a model for the SA:V of immiscible liquids in the VFD is currently underway (pg. 170), which may assist in finding optimal conditions in the VFD for the degumming of oils for biodiesel production.

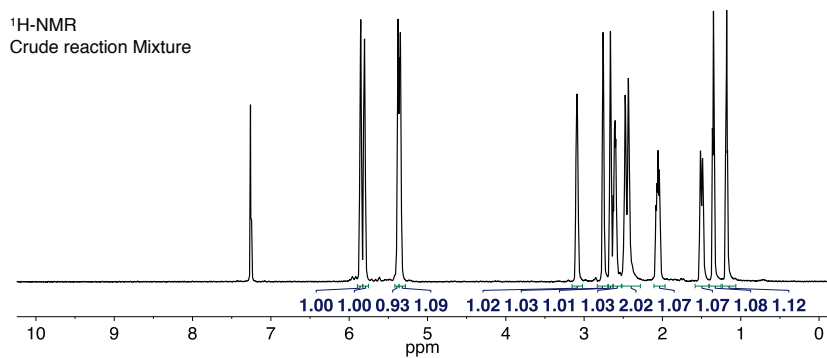


## 7.4 - Experimental Details and Spectra

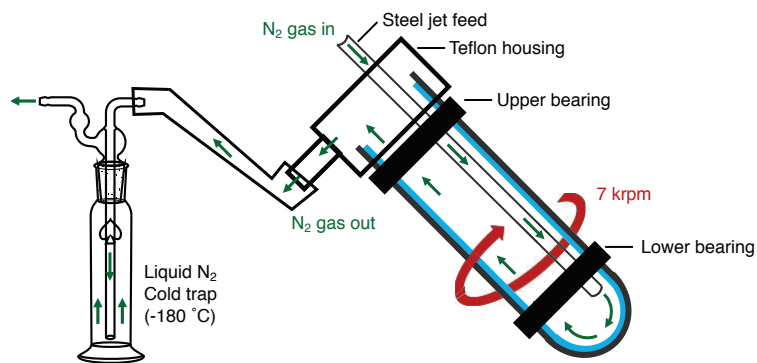
### 7.4.1 - VFD One-Pot Synthesis of Ferrocene



The following is a general procedure for the attempted one-pot synthesis of ferrocene. This was performed at room temperature, 80 °C, room temperature with a pulsed laser (1000 nm, 650 mJ), room temperature with a pulsed laser (1000 nm, 460 mJ). To a VFD tube, 87 (159 mg, 1.2 mmol),  $\text{Fe}^{(III)}\text{Cl}_2 \cdot 4\text{H}_2\text{O}$  (119 mg, 0.6 mmol) and KOH (34 mg, 0.6 mmol) were dissolved in  $\text{D}_6\text{-DMSO}$  (1.5 mL) and  $\text{D}_2\text{O}$  (0.5 mL). This was then operated in the VFD at 7 krpm for 1 hour. After 1 hour had passed, a small aliquot of the liquid was taken and diluted in  $\text{CDCl}_3$  for  $^1\text{H-NMR}$  analysis. This was repeated in a VFD tube that was then stirred with a magnetic stirrer bar. A typical  $^1\text{H-NMR}$  spectrum can be found below.

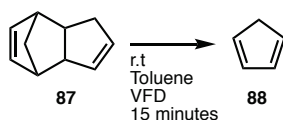


#### 7.4.2 – Attempted Cracking of Dicyclopentadiene in VFD with Carrier Gas

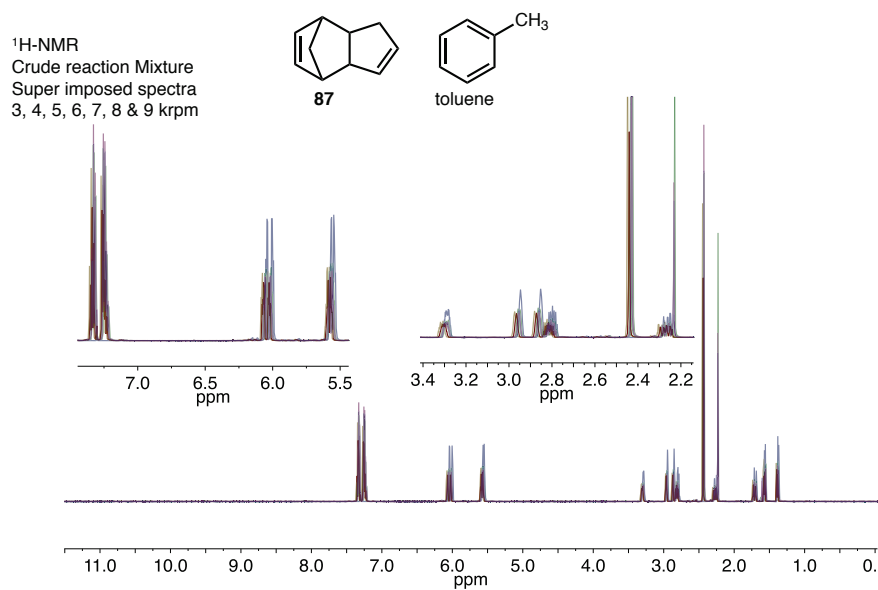


The following experiment was performed to achieve room temperature cracking of **87**, and collect the resulting **88** separately in a flow of carrier gas. For this, the **87** (2 g, 15.1 mmol) was placed in a VFD and operated at 7 krpm. During operation, a gentle stream of N<sub>2</sub> gas was passed over the rotating surface, delivered to the base of the tube by a stainless-steel jet-feed. This gas flow then exited the VFD through the Teflon housing unit of the VFD (all other exits were sealed). This gas flow then passed through silica tubing into a glass receptacle placed in a liquid N<sub>2</sub> bath. This was performed for 3 hours. After this time, no material was found in the cold trap, and only trace **87** remained in the VFD tube.

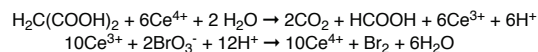
### 7.4.3 - Attempted Cracking of Dicyclopentadiene in VFD (Sealed)



The following experiment was performed in a sealed tube to observe the if 87 would crack in the VFD at room temperature. To a VFD tube, **87** (1 g, 7.6 mmol) and toluene (250  $\mu\text{L}$ ) were added. This was then sealed with a rubber septum. The VFD was then operated for 15 minutes. This was repeated for speeds of 3, 4, 5, 6, 7, 8 & 9 krpm. After the 15 minutes had elapsed, the rotation was halted and a small aliquot ( $\approx 500 \mu\text{L}$ ) was diluted in  $\text{CDCl}_3$  for  $^1\text{H-NMR}$  analysis. The spectra of which can be found below.



#### 7.4.4 - Oscillation Details



For all cerium/malonic acid oscillating reactions, the following stock solutions were used. Cerous Nitrate (0.1 M, aq.), malonic acid (1.375 M, aq.), potassium bromate (0.3125 M, aq.), ferroin indicator (**92**) (0.025, aq.). For a typical reaction of 10 mL volume, the following amounts and order of addition was used. To a vial, water (1.5 mL) was mixed with cerous nitrate (0.1 M, 2.5 mL), followed by potassium bromate (0.3125 M, 2.5 mL), then malonic acid (1.375 M, 2.5 mL), then H<sub>2</sub>SO<sub>4</sub> (18.7 M, 1 mL) followed by the ferroin indicator (0.025 M, 75 μL). This results in 10.075 mL, with the following concentrations: cerous nitrate (2.5 mM), potassium bromate (78 mM), malonic acid (344 mM), H<sub>2</sub>SO<sub>4</sub> (1.875 M). The oscillation begins immediately. Note that the order of addition is important.

#### 7.4.5 - Oil Degumming Details

Firstly, a method for finding the phosphorous content of the oil was developed. Adapting methods from the literature, the following procedure was employed. An aliquot of the sample (500 mg) was digested with HNO<sub>3</sub> (4 mL, 30 % aq.) and HCl (1 mL, 37 % aq.). This was then subject to microwave radiation for 1 hour. Following this, each sample was diluted to 25 mL in water for analysis by ICP-OES (LOQ = 1 mg/Kg). This was analysed in duplicate, reporting the average value.

## Chapter 8 – Summary and Outlook

This candidature explored a wide variety of projects in great detail. Although these projects differ vastly from one another, they are linked in attempting to answer one principle question – what are the *Synthetic Applications of Vortex Thin Film Microfluidics*. The broad nature of the question makes it difficult to provide an answer. However, the diverse array of work described here has highlighted several benefits of vortex fluidics. Despite these discoveries, further work into vortex fluidic processing is required. In the first instance, a model for predicting the outcome of chemical transformations would be vastly beneficial for the VFD to find widespread uptake. This requires an understanding of the fundamental fluid dynamics occurring in this complex and dynamic environment. This work has contributed progress to this goal in many ways.

Firstly, the importance of surface area plays a key role in many important transformations. The VFD shows increased surface area, which enhances mass- and heat-transfer abilities. Achieving enhanced mass-transfer in a scalable continuous flow process here has shown great potential for the utilisation of green reagents for organic oxidations. This work showed that common bleach ( $\text{NaOCl} + \text{HOCl}$ ), or hydrogen peroxide are viable reagents for biphasic systems, made possible by the VFD. These reagents are highly desirable as they are cheap, readily available and produce benign compounds upon use. Hydrogen peroxide more so, as water is the only degradation product. Bleach degrades to form both water and sodium chloride, which is usually not a problem. However, further care must be taken as bleach can cause unwanted chlorination – the outcome of which can be toxic.<sup>147</sup> Regardless, both these oxidation reagents are highly desirable compared to the typical text-book organic oxidants, which are often expensive and extremely toxic.<sup>108-112</sup> Although hydrogen peroxide and bleach are more desirable, they must be overlooked in most applications for solubility reasons – neither are active in hydrophobic media. The VFD was shown to facilitate their mass-transfer across liquid-liquid phase boundaries, and both of reagents were found to successfully oxidise a variety of hydrophobic compounds. Furthermore, the enhanced heat-transfer properties were shown to avoid run away exotherms, which not only drastically effect the yield and stereo-selective outcomes, they are incredibly dangerous. Such run away exotherms in industrial scales have resulted in the tragic loss of life.<sup>245</sup> Thus this work finds relevance broadly in any biphasic, and/or exothermic process. Work performed here into imaging the behaviour of biphasic systems in the VFD has also progress work towards achieving a predictive model describing the surface-area-to-volume (SA:V). A large series of neutron images of  $\text{D}_2\text{O}$  and toluene were obtained at various ratios, performed in the VFD at all 50 rpm increments between 1 – 9 krpm rotational speeds. This large database of images is being worked on by other members of the Raston research group, and will provide experimental values for the relative thickness of each liquid phase as the rotational speed is altered – essential for describing the SA:V. This will be essential when engineering any biphasic application of the VFD.

The same principle of increasing the SA:V for enhanced reactivity across a liquid-liquid phase boundary was demonstrated across liquid-gas phase boundaries. Specifically, the ability for the VFD to enhance the aerobic oxidation of N-acetyl-L-cysteine to form the resulting disulphide. This was shown to be vastly beneficial in the VFD compared to batch, especially when scaling up. Only when scaling up liquid-gas reactions does the VFD find its use. This was further demonstrated by studies into utilising  $\text{CO}_2$  for polycarbonate and cyclic carbonate synthesis, and also for the ethenolysis reaction. At small scales where the mass transfer is not

limiting, the VFD was shown to provide no benefit. However, since any profitable application needs to be at large scales, the VFD is highly promising device for mediating such processes. If considering large-scale applications for either polymerisation or ethenolysis, confidence can be instilled from work reported herein that any existing method can be implemented into a VFD process without altering the outcome of the reaction. This is important to establish as the VFD has altered the outcome of many other reactions in unpredictable ways.<sup>82</sup>

A further unexpected outcome as a result of VFD processing was also found in this work. That is, that the oxidative sulphytolysis of oxytocin is vastly improved in the VFD. The VFD enabled this reaction at all pH levels trialled (pH 9 – 10.5), well below what is required in stirred vials (pH 10.5). This enhancement was found to correlate to an increase in operational rotation speed. Unfortunately, the exact underpinning cause for this was not able to be described – as is the case with much work regarding the complexities of vortex fluidics. However, the work into oxidative sulphytolysis provides key pieces of information for achieving the goal of a predictive model for VFD processing. The work in this field also may provide key evidence for the fundamental mechanistic explanation of the oxidative sulphytolysis reaction, in that the sulphide was shown to be the limiting reagent, and not the tetrathionate.

The reported enhancement to aerobic oxidation was further studied, as a means to favourably alter the outcome of olefin metathesis (OM) reactions. This was rationalised through the effective scavenging of phosphine ligands from Grubbs-type ruthenium complexes – increasing the presence of the active catalyst. From this a clear result was achieved, demonstrating the enhancement of the activity of such catalyst bearing one phosphine ( $-P(Cy)_3$ ) and one N-heterocyclic carbene (NHC, IMes). However, the exact extent of the aerobic oxidation was not able to be elucidated, and it is suspected that other contributing factors cause this shocking phenomenon. In exploring OM, a novel quenching and scavenging method was developed. This is using a saturated solution of N-acetyl-L-cysteine in MeCN ( $\approx 20$  mg/mL, 0.12 M). This was demonstrated for a wide variety of ruthenium OM catalysts, and for an array of reactive substrates. This method avoids the formation of unwanted bond-migration isomerisation that can occur with many quenching methods.<sup>226</sup> Not only is the activity of the catalyst immediately halted, the chromatographic retention factor of the resulting ruthenium complex is vastly altered – a property that will be useful for purifications of OM processes in general, and will find use beyond VFD applications.

## Bibliography

1. J. S. L. Philpot, *Trans. Faraday Soc.*, 1940, **35**, 38-46.
2. K. Geyer, J. D. C. Codée and P. H. Seeberger, *Chem.: Eur. J.*, 2006, **12**, 8434-8442.
3. G. M. Whitesides, *Lab Chip*, 2013, **13**, 11-13.
4. K. S. Elvira, X. C. i Solvas, R. C. R. Wootton and A. J. deMello, *Nat. Chem.*, 2013, **5**, 905.
5. D. E. Fitzpatrick and S. V. Ley, *Tetrahedron*, 2018, **74**, 3087-3100.
6. R. L. Hartman, J. P. McMullen and K. F. Jensen, *Angew. Chem. Int. Ed.*, 2011, **50**, 7502-7519.
7. M. B. Plutschack, B. Pieber, K. Gilmore and P. H. Seeberger, *Chem. Rev.*, 2017, **117**, 11796-11893.
8. B. P. Mason, K. E. Price, J. L. Steinbacher, A. R. Bogdan and D. T. McQuade, *Chem. Rev.*, 2007, **107**, 2300-2318.
9. S. G. Newman and K. F. Jensen, *Green Chem.*, 2013, **15**, 1456-1472.
10. L. Rogers and K. F. Jensen, *Green Chem.*, 2019, **21**, 3481-3498.
11. R. A. Sheldon, *Chem. Soc. Rev.*, 2012, **41**, 1437-1451.
12. J. Britton and C. L. Raston, *Chem. Soc. Rev.*, 2017, **46**, 1250-1271.
13. D. Webb and T. F. Jamison, *Chem. Sci.*, 2010, **1**, 675-680.
14. T. W. G. F. Solomons, Craig B, *Organic Chemistry*, John Wiley & Sons, 2011.
15. J. G. Clayden, Nick, Warren, Stuart, *Organic Chemistry*, Oxford University Press, 2001.
16. K. Omura and D. Swern, *Tetrahedron*, 1978, **34**, 1651-1660.
17. M. Movsisyan, E. I. P. Delbeke, J. K. E. T. Berton, C. Battilocchio, S. V. Ley and C. V. Stevens, *Chem. Soc. Rev.*, 2016, **45**, 4892-4928.
18. O. Bleie, M. F. Roberto, T. I. Dearing, C. W. Branham, O. M. Kvalheim and B. J. Marquardt, *J. Flow. Chem.*, 2015, **5**, 183-189.
19. J. R. McConnell, J. E. Hitt, E. D. Daus and T. A. Rey, *Org. Process Res. Dev.*, 2008, **12**, 940-945.
20. P. J. Nieuwland, K. Koch, N. van Harskamp, R. Wehrens, J. C. M. van Hest and F. P. J. T. Rutjes, *Chem. - Asian J.*, 2010, **5**, 799-805.
21. J. J. M. van der Linden, P. W. Hilberink, C. M. P. Kronenburg and G. J. Kemperman, *Org. Process Res. Dev.*, 2008, **12**, 911-920.
22. T. Kawaguchi, H. Miyata, K. Ataka, K. Mae and J.-i. Yoshida, *Angew. Chem. Int. Ed.*, 2005, **44**, 2413-2416.
23. J.-i. Yoshida, Y. Takahashi and A. Nagaki, *Chem. Commun.*, 2013, **49**, 9896-9904.
24. S. S. Gambhir, *Nat. Rev. Cancer*, 2002, **2**, 683-693.
25. J. N. Liu, W. B. Bu and J. L. Shi, *Chem. Rev.*, 2017, **117**, 6160-6224.
26. A. Y. Louie, *Chem. Rev.*, 2010, **110**, 3146-3195.
27. H. Audrain, *Angew. Chem. Int. Ed.*, 2007, **46**, 1772-1775.
28. H. H. Coenen and J. Ermert, *J. Clin. Transl. Imaging*, 2018, **6**, 169-193.
29. A. Günther and K. F. Jensen, *Lab Chip*, 2006, **6**, 1487-1503.
30. C. J. Mallia and I. R. Baxendale, *Org. Process Res. Dev.*, 2016, **20**, 327-360.
31. K. Skowerski, S. J. Czarnocki and P. Knapkiewicz, *ChemSusChem*, 2014, **7**, 536-542.
32. P. I. Dalko and L. Moisan, *Angew. Chem. Int. Ed.*, 2004, **43**, 5138-5175.
33. S. Shirakawa and K. Maruoka, *Angew. Chem. Int. Ed.*, 2013, **52**, 4312-4348.
34. F. Bures, *Top. Curr. Chem.*, 2019, **377**, 21.
35. A. Woitalka, S. Kuhn and K. F. Jensen, *Chem. Eng. Sci.*, 2014, **116**, 1-8.
36. J. Delgado, *Heat Mass Transf.*, 2006, **42**, 279-310.
37. R. Munirathinam, J. Huskens and W. Verboom, *Adv. Synth. Catal.*, 2015, **357**, 1093-1123.
38. D. C. Bailey and S. H. Langer, *Chem. Rev.*, 1981, **81**, 109-148.
39. R. DiCosimo, J. McAuliffe, A. J. Poulouse and G. Bohlmann, *Chem. Soc. Rev.*, 2013, **42**, 6437-6474.
40. M. B. Gawande, P. S. Branco and R. S. Varma, *Chem. Soc. Rev.*, 2013, **42**, 3371-3393.
41. G. A. Price, D. Mallik and M. G. Organ, *J. Flow. Chem.*, 2017, **7**, 82-86.
42. S. Bordawekar, A. Chanda, A. M. Daly, A. W. Garrett, J. P. Higgins, M. A. LaPack, T. D. Maloney, J. Morgado, S. Mukherjee, J. D. Orr, G. L. Reid, B.-S. Yang and H. W. Ward, *Org. Process Res. Dev.*, 2015, **19**, 1174-1185.
43. J. P. McMullen and K. F. Jensen, *Annu. Rev. Anal. Chem.*, 2010, **3**, 19-42.
44. A. Chanda, A. M. Daly, D. A. Foley, M. A. LaPack, S. Mukherjee, J. D. Orr, G. L. Reid, D. R. Thompson and H. W. Ward, *Org. Process Res. Dev.*, 2015, **19**, 63-83.
45. V. Sans, L. Porwol, V. Dragone and L. Cronin, *Chem. Sci.*, 2015, **6**, 1258-1264.
46. K. Singh and B. Blumich, *Trac-Trends Anal. Chem.*, 2016, **83**, 12-26.
47. M. V. Gomez and A. de la Hoz, *Beilstein J. Org. Chem.*, 2017, **13**, 285-300.
48. D. T. Ahneman, J. G. Estrada, S. Lin, S. D. Dreher and A. G. Doyle, *Science*, 2018, **360**, 186.
49. B. J. Reizman, Y.-M. Wang, S. L. Buchwald and K. F. Jensen, *React. Chem. Eng.*, 2016, **1**, 658-666.
50. P. C. Ashok, B. B. Praveen and K. Dholakia, *Opt. Express*, 2011, **19**, 22982-22992.
51. A. J. Harvie, J. O. Herrington and J. C. deMello, *React. Chem. Eng.*, 2019, **4**, 1579-1588.
52. H. Lange, C. F. Carter, M. D. Hopkin, A. Burke, J. G. Goode, I. R. Baxendale and S. V. Ley, *Chem. Sci.*, 2011, **2**, 765-769.
53. J. A. Medrano, N. C. A. de Nooijer, F. Gallucci and M. V. Annaland, *Sensors*, 2016, **16**, 18.
54. K. Thurmond, Z. Loparo, W. Partridge and S. S. Vasu, *Appl. Spectrosc.*, 2016, **70**, 962-971.
55. G. Chaplain, S. J. Haswell, P. D. I. Fletcher, S. M. Kelly and A. Mansfield, *Aust. J. chem.*, 2013, **66**, 208-212.



56. S. Mozharov, A. Nordon, D. Littlejohn, C. Wiles, P. Watts, P. Dallin and J. M. Girkin, *J. Am. Chem. Soc.*, 2011, **133**, 3601-3608.
57. S. Carter, A. Fisher, R. Garcia, B. Gibson, S. Lancaster, J. Marshall and I. Whiteside, *J. Anal. At. Spectrom.*, 2015, **30**, 2249-2294.
58. P. Norouzi, M. R. Ganjali, A. A. Moosavi-Movahedi and B. Larijani, *Talanta*, 2007, **73**, 54-61.
59. A.-C. Bédard, A. Adamo, K. C. Aroh, M. G. Russell, A. A. Bedermann, J. Torosian, B. Yue, K. F. Jensen and T. F. Jamison, *Science*, 2018, **361**, 1220.
60. M. C. Brothers, M. DeBrosse, C. C. Grigsby, R. R. Naik, S. M. Hussain, J. Heikenfeld and S. S. Kim, *Accounts Chem. Res.*, 2019, **52**, 297-306.
61. M. Brzozowski, M. O'Brien, S. V. Ley and A. Polyzos, *Accounts Chem. Res.*, 2015, **48**, 349-362.
62. C. W. Coley, D. A. Thomas, J. A. M. Lummiss, J. N. Jaworski, C. P. Breen, V. Schultz, T. Hart, J. S. Fishman, L. Rogers, H. Gao, R. W. Hicklin, P. P. Plehiers, J. Byington, J. S. Piotti, W. H. Green, A. J. Hart, T. F. Jamison and K. F. Jensen, *Science*, 2019, **365**, eaax1566.
63. R. J. Ingham, C. Battilocchio, D. E. Fitzpatrick, E. Sliwinski, J. M. Hawkins and S. V. Ley, *Angew. Chem. Int. Ed.*, 2015, **54**, 144-148.
64. C. Mateos, M. J. Nieves-Remacha and J. A. Rincon, *React. Chem. Eng.*, 2019, **4**, 1536-1544.
65. N. Pamme, *Lab Chip*, 2007, **7**, 1644-1659.
66. P. Sagmeister, J. D. Williams, C. A. Hone and C. O. Kappe, *React. Chem. Eng.*, 2019, **4**, 1571-1578.
67. C. Waldron, A. Pankajakshan, M. Quaglio, E. Cao, F. Galvanin and A. Gavriilidis, *React. Chem. Eng.*, 2019, **4**, 1623-1636.
68. B. M. Wyvratt, J. P. McMullen and S. T. Grosser, *React. Chem. Eng.*, 2019, **4**, 1637-1645.
69. K. Shibatomi, K. Kitahara, N. Sasaki, Y. Kawasaki, I. Fujisawa and S. Iwasa, *Nat. Commun.*, 2017, **8**, 15600.
70. M. Singer Hobbs, E. V. Sackville, A. J. Smith, K. J. Edler and U. Hintermair, *ChemCatChem*, 2019, **0**.
71. J. W. Sawicki, A. R. Bogdan, P. A. Searle, N. Talaty and S. W. Djuric, *React. Chem. Eng.*, 2019, **4**, 1589-1594.
72. M. Christensen, F. Adedeji, S. Grosser, K. Zawatzky, Y. Ji, J. Liu, J. A. Jurica, J. R. Naber and J. E. Hein, *React. Chem. Eng.*, 2019, **4**, 1555-1558.
73. C. A. Hone, A. Boyd, A. O'Kearney-McMullan, R. A. Bourne and F. L. Muller, *React. Chem. Eng.*, 2019, **4**, 1565-1570.
74. R. A. Bourne, K. K. Hii and B. J. Reizman, *React. Chem. Eng.*, 2019, **4**, 1504-1505.
75. K. Molga, E. P. Gajewska, S. Szymkuć and B. A. Grzybowski, *React. Chem. Eng.*, 2019, **4**, 1506-1521.
76. S. V. Ley, D. E. Fitzpatrick, R. J. Ingham and R. M. Myers, *Angew. Chem. Int. Ed.*, 2015, **54**, 3449-3464.
77. T. L. Tzou, D. W. Edwards, P. W. H. Chung, Icheme and Icheme, *An explosion accident - Causes and safety information management lessons to be learned*, Inst Chemical Engineers, Rugby, 2003.
78. C. L. Schreiber and B. D. Smith, *Nat. Rev. Chem.*, 2019, **3**, 393-400.
79. M. Arslan, G. Acik and M. A. Tasdelen, *Polym. Chem.*, 2019, **10**, 3806-3821.
80. H. C. Kolb, M. G. Finn and K. B. Sharpless, *Angew. Chem. Int. Ed.*, 2001, **40**, 2004-2021.
81. D. Cantillo, B. Gutmann and C. Oliver Kappe, *Org. Biomol. Chem.*, 2016, **14**, 853-857.
82. J. Britton, K. A. Stubbs, G. A. Weiss and C. L. Raston, *Chem. Eur. J.*, 2017, **23**, 13270-13278.
83. L. Yasmin, X. Chen, K. A. Stubbs and C. L. Raston, *Scientific Reports*, 2013, **3**, 2282.
84. J. Britton, K. A. Stubbs, G. A. Weiss and C. L. Raston, *Chem. Eur. J.*, 2017, DOI: 10.1002/chem.201700888, n/a-n/a.
85. J. Britton, J. M. Chalker and C. L. Raston, *Chem. Eur. J.*, 2015, **21**, 10660-10665.
86. T. Z. Yuan, C. F. G. Ormonde, S. T. Kudlacek, S. Kunche, J. N. Smith, W. A. Brown, K. M. Pugliese, T. J. Olsen, M. Iftikhar, C. L. Raston and G. A. Weiss, *ChemBioChem*, 2015, **16**, 393-396.
87. J. Britton, L. M. Meneghini, C. L. Raston and G. A. Weiss, *Angew. Chem. Int. Ed.*, 2016, DOI: 10.1002/anie.201604014.
88. K. Vimalanathan, J. R. Gascooke, I. Suarez-Martinez, N. A. Marks, H. Kumari, C. J. Garvey, J. L. Atwood, W. D. Lawrance and C. L. Raston, *Sci. Rep.*, 2016, **6**, 22865.
89. K. Vimalanathan, J. R. Gascooke, I. Suarez-Martinez, N. A. Marks, H. Kumari, C. J. Garvey, J. L. Atwood, W. D. Lawrance and C. L. Raston, *Sci. Rep.*, 2016, **6**.
90. K. E. Moore, D. N. Mangos, A. D. Slattery, C. L. Raston and R. A. Boulous, *RSC Adv.*, 2016, **6**, 20095-20101.
91. J. Mo, P. K. Eggers, X. Chen, M. R. H. Ahamed, T. Becker, L. Y. Lim and C. L. Raston, *Sci. Rep.*, 2015, **5**.
92. Y. A. Goh, X. Chen, F. M. Yasin, P. K. Eggers, R. A. Boulous, X. Wang, H. T. Chua and C. L. Raston, *Chem. Comm.*, 2013, **49**, 5171-5173.
93. J. Britton and C. L. Raston, *RSC Adv.*, 2015, **5**, 2276-2280.
94. J. Britton, J. M. Chalker and C. L. Raston, *Angew. Chem. Int. Ed.*, 2015, **21**, 10660-10665.
95. J. Britton and C. L. Raston, *RSC Adv.*, 2014, **4**, 49850-49854.
96. L. Yasmin, X. Chen, K. A. Stubbs and C. L. Raston, *Sci. Rep.*, 2013, **3**.
97. J. Britton, C. L. Raston and G. A. Weiss, *Chem. Commun.*, 2016, **52**, 10159-10162.
98. J. Britton, S. B. Dalziel and C. L. Raston, *Green Chem.*, 2016, **18**, 2193-2200.
99. J. Britton, L. M. Meneghini, C. L. Raston and G. A. Weiss, *Angew. Chem. Int. Ed.*, 2016, **55**, 11387-11391.
100. L. A. Ho, C. L. Raston and K. A. Stubbs, *Eur. J. Org. Chem.*, 2016, **2016**, 5957-5963.
101. I. K. Alsulami, T. M. D. Alharbi, D. P. Harvey, C. T. Gibson and C. L. Raston, *Chem. Commun.*, 2018, **54**, 7896-7899.
102. S. J. Pye, S. J. Dalgarno, J. M. Chalker and C. L. Raston, *Green Chem.*, 2018, **20**, 118-124.
103. P. Anastas and N. Eghbali, *Chem. Soc. Rev.*, 2010, **39**, 301-312.
104. R. A. Sheldon, *Green Chem.*, 2007, **9**, 1273-1283.

105. G.-J. ten Brink, I. W. C. E. Arends and R. A. Sheldon, *Science*, 2000, **287**, 1636-1639.
106. M. Namazian, C. Y. Lin and M. L. Coote, *J. Chem. Theory Comput.*, 2010, **6**, 2721-2725.
107. S. K. Ritter, *Chem. Eng. News*, 2016, **94**, 22 - 25.
108. G. Cainelli and G. Cardillo, *Chromium Oxidants in Organic Chemistry*, Springer, Berlin, 1984.
109. H. Tohma and Y. Kita, *Adv. Synth. Catal.*, 2004, **346**, 111-124.
110. B. M. Trost, *Science*, 1991, **254**, 1471-1477.
111. B. M. Trost, *Angew. Chem. Int. Ed.*, 1995, **34**, 259-281.
112. Y.-S. Duh, X. H. Wu and C.-S. Kao, *Process Saf. Prog.*, 2008, **27**, 89-99.
113. N. Gunasekaran, *Adv. Synth. Catal.*, 2015, **357**, 1990-2010.
114. S. S. Stahl, *Science*, **309**, 1824-1826.
115. P. L. Anelli, C. Biffi, F. Montanari and S. Quici, *J. Org. Chem.*, 1987, **52**, 2559-2562.
116. C. W. Jones, *Applications of Hydrogen Peroxide and Derivatives*, Royal Society of Chemistry, Cambridge, 1999.
117. B. Martin, J. Sedelmeier, A. Bouisseau, P. Fernandez-Rodriguez, J. Haber, F. Kleinbeck, S. Kamptmann, F. Susanne, P. Hoehn, M. Lanz, L. Pellegatti, F. Venturoni, J. Robertson, M. C. Willis and B. Schenkel, *Green Chem.*, 2017, **19**, 1439-1448.
118. D. J. C. Constable, P. J. Dunn, J. D. Hayler, G. R. Humphrey, J. J. L. Leazer, R. J. Linderman, K. Lorenz, J. Manley, B. A. Pearlman, A. Wells, A. Zaks and T. Y. Zhang, *Green Chem.*, 2007, **9**, 411-420.
119. H. P. L. Gemoets, Y. Su, M. Shang, V. Hessel, R. Luque and T. Noel, *Chem. Soc. Rev.*, 2016, **45**, 83-117.
120. A. Gavriilidis, A. Constantinou, K. Hellgardt, K. K. Hii, G. J. Hutchings, G. L. Brett, S. Kuhn and S. P. Marsden, *React. Chem. Eng.*, 2016, **1**, 595-612.
121. R. L. Hartman, J. R. Naber, N. Zaborenko, S. L. Buchwald and K. F. Jensen, *Org. Process Res. Dev.*, 2010, **14**, 1347-1357.
122. M. Schoenitz, L. Grundemann, W. Augustin and S. Scholl, *Chem. Commun.*, 2015, **51**, 8213-8228.
123. R. K. Shah, H. C. Shum, A. C. Rowat, D. Lee, J. J. Agresti, A. S. Utada, L.-Y. Chu, J.-W. Kim, A. Fernandez-Nieves, C. J. Martinez and D. A. Weitz, *Mater. Today*, 2008, **11**, 18-27.
124. J. Jovanović, E. V. Rebrov, T. A. Nijhuis, V. Hessel and J. C. Schouten, *Ind. Eng. Chem. Res.*, 2010, **49**, 2681-2687.
125. P. M. Osterberg, J. K. Niemeier, C. J. Welch, J. M. Hawkins, J. R. Martinelli, T. E. Johnson, T. W. Root and S. S. Stahl, *Org. Process Res. Dev.*, 2015, **19**, 1537-1543.
126. L. Vanoye, J. Wang, M. Pablos, R. Philippe, C. d. Bellefon and A. Favre-Réguillon, *Org. Process Res. Dev.*, 2016, **20**, 90-94.
127. C. A. Hone, D. M. Roberge and C. O. Kappe, *ChemSusChem*, 2017, **10**, 32-41.
128. D. Givol, F. Delorenzo, R. F. Goldberger and C. B. Anfinsen, *Proc. Natl. Acad. Sci. USA*, 1965, **53**, 676-684.
129. W. J. Wedemeyer, E. Welker, M. Narayan and H. A. Scheraga, *Biochemistry*, 2000, **39**, 4207-4216.
130. I. V. Koval, *Russ. Chem. Rev.*, 1994, **63**, 735-750.
131. M. Akcan and D. J. Craik, in *Peptide Synthesis and Applications*, eds. K. J. Jensen, P. Tofteng Shelton and S. L. Pedersen, 2013, pp. 89-101.
132. D. C. M. Albanese, F. Foschi and M. Penso, *Org. Process Res. Dev.*, 2016, **20**, 129-139.
133. J. H. Ramsden, R. S. Drago and R. Riley, *J. Am. Chem. Soc.*, 1989, **111**, 3958-3961.
134. N. Fukuda and T. Ikemoto, *J. Org. Chem.*, 2010, **75**, 4629-4631.
135. D. A. Evans and G. C. Andrews, *Accounts Chem. Res.*, 1974, **7**, 147-155.
136. B. M. Trost, N. R. Schmuft and M. J. Miller, *J. Am. Chem. Soc.*, 1980, **102**, 5979-5981.
137. N. S. Simpkins, *Sulphones in Organic Synthesis*, Pergamon, New York, 1993.
138. J. Clayden and M. Julia, *J. Chem. Soc., Chem. Commun.*, 1994, 1905-1906.
139. K. Deng, C. J., A. Yang and T. Cohen, *Org. Lett.*, 2005, **7**, 3637-3640.
140. J. M. Chalker, *Aust. J. Chem.*, 2015, **68**, 1801-1809.
141. T. Okada, H. Matsumuro, a. Kitagawa, o. Iwai, K. Yamazaki, Y. Kinoshita, Y. Kimura and M. Kiriara, *Synlett*, 2015, **26**, 2547-2552.
142. C.-N. Hsiao and H. Shechter, *J. Org. Chem.*, 1988, **53**, 2688-2699.
143. A. Jonczyk and T. Radwan-Pytlewski, *Pol. J. Chem.*, 1995, **69**, 1422-1427.
144. X. Luo, P. Smith, C. L. Raston and W. Zhang, *ACS Sustainable Chemistry and Engineering*, 2016, **4**, 3905-3911.
145. E. Weitz and A. Scheffer, *Chem. Ber.*, 1921, **54**, 2327-2344.
146. J. Britton, J. M. Chalker and C. L. Raston, *Chemistry (Weinheim an der Bergstrasse, Germany)*, 2015, **21**, 10660-10665.
147. T. T. Schug, R. Abagyan, B. Blumberg, T. J. Collins, D. Crews, P. L. DeFur, S. M. Dickerson, T. M. Edwards, A. C. Gore, L. J. Guillet, T. Hayes, J. J. Heindel, A. Moores, H. B. Patisaul, T. L. Tal, K. A. Thayer, L. N. Vandenberg, J. C. Warner, C. S. Watson, F. S. vom Saal, R. T. Zoeller, K. P. O'Brien and J. P. Myers, *Green Chem.*, 2013, **15**, 181-198.
148. H. Clavier, K. Grela, A. Kirschning, M. Mauduit and S. P. Nolan, *Angew. Chem. Int. Ed.*, 2007, **46**, 6786-6801.
149. R. H. Grubbs, *Tetrahedron*, 2004, **60**, 7117-7140.
150. A. H. Hoveyda and A. R. Zhugralin, *Nature*, 2007, **450**, 243.
151. T. P. J. Montgomery, Adam M.; Grubbs, Robert H., *Catalysts*, 2017, **7**, 2073-4344.
152. O. M. Ogba, N. C. Warner, D. J. O'Leary and R. H. Grubbs, *Chem. Soc. Rev.*, 2018, **47**, 4510-4544.
153. X. Shen, T. T. Nguyen, M. J. Koh, D. M. Xu, A. W. H. Speed, R. R. Schrock and A. H. Hoveyda, *Nature*, 2017, **541**, 380-+.
154. C. S. Higman, J. A. M. Lummiss and D. E. Fogg, *Angew. Chem. Int. Ed.*, 2016, **55**, 3552-3565.
155. D. Hughes, P. Wheeler and D. Ene, *Org. Process Res. Dev.*, 2017, **21**, 1938-1962.

156. K. C. Nicolaou, P. G. Bulger and D. Sarlah, *Angew. Chem. Int. Ed.*, 2005, **44**, 4490-4527.
157. F. Sinclair, M. Alkattan, J. Prunet and M. P. Shaver, *Polym. Chem.*, 2017, **8**, 3385-3398.
158. M. R. Becker, R. B. Watson and C. S. Schindler, *Chem. Soc. Rev.*, 2018, **47**, 7867-7881.
159. L. Ravindar, R. Lekkala, K. P. Rakesh, A. M. Asiri, H. M. Marwani and H.-L. Qin, *Org. Chem. Front.*, 2018, **5**, 1381-1391.
160. J. Bidange, C. Fischmeister and C. Bruneau, *Chem. – Eur. J.*, 2016, **22**, 12226-12244.
161. J. Spekrijse, J. P. M. Sanders, J. H. Bitter and E. L. Scott, *ChemSusChem*, 2017, **10**, 470-482.
162. S. L. Mangold and R. H. Grubbs, *Chem. Sci.*, 2015, **6**, 4561-4569.
163. S. C. Marinescu, D. S. Levine, Y. Zhao, R. R. Schrock and A. H. Hoveyda, *J. Am. Chem. Soc.*, 2011, **133**, 11512-11514.
164. V. M. Marx, M. B. Herbert, B. K. Keitz and R. H. Grubbs, *J. Am. Chem. Soc.*, 2013, **135**, 94-97.
165. H. Miyazaki, M. B. Herbert, P. Liu, X. Dong, X. Xu, B. K. Keitz, T. Ung, G. Mkrtumyan, K. N. Houk and R. H. Grubbs, *J. Am. Chem. Soc.*, 2013, **135**, 5848-5858.
166. K. A. Burdett, L. D. Harris, P. Margl, B. R. Maughon, T. Mokhtar-Zadeh, P. C. Saucier and E. P. Wasserman, *Organometallics*, 2004, **23**, 2027-2047.
167. L. M. de Espinosa and M. A. R. Meier, in *Organometallics and Renewables*, eds. M. A. R. Meier, B. M. Weckhuysen and P. C. A. Bruijninx, Springer Berlin Heidelberg, Berlin, Heidelberg, 2012, DOI: 10.1007/978-3-642-28288-1\_1, pp. 1-44.
168. R. W. Jenkins, L. A. Sargeant, F. M. Whiffin, F. Santomauro, D. Kaloudis, P. Mozzanega, C. D. Bannister, S. Baena and C. J. Chuck, *ACS Sustainable Chem. Eng.*, 2015, **3**, 1526-1535.
169. B. B. Marvey, *Int J Mol Sci*, 2008, **9**, 1393-1406.
170. M. A. R. Meier, J. O. Metzger and U. S. Schubert, *Chem. Soc. Rev.*, 2007, **36**, 1788-1802.
171. J. C. Mol, *Top. Curr. Chem.*, 2004, **27**, 97-104.
172. A. Nickel, T. Ung, G. Mkrtumyan, J. Uy, C. W. Lee, D. Stoianova, J. Papazian, W.-H. Wei, A. Mallari, Y. Schrodi and R. L. Pederson, *Top. Curr. Chem.*, 2012, **55**, 518-523.
173. J. Spekrijse, J. Le Nôtre, J. van Haveren, E. L. Scott and J. P. M. Sanders, *Green Chem.*, 2012, **14**, 2747-2751.
174. S. Wolf and H. Plenio, *Green Chem.*, 2011, **13**, 2008-2012.
175. A.-M. Aguirre, A. Bassi and P. Saxena, *Crit. Rev. Biotechnol.*, 2013, **33**, 293-308.
176. Y. J. Su, K. H. Song, P. D. Zhang, Y. Q. Su, J. Cheng and X. Chen, *Renew. Sust. Energ. Rev.*, 2017, **74**, 402-411.
177. J. Esteban and M. Ladero, *J. Food Sci. Technol.*, 2018, **53**, 1095-1108.
178. D. R. Anderson, T. Ung, G. Mkrtumyan, G. Bertrand, R. H. Grubbs and Y. Schrodi, *Organometallics*, 2008, **27**, 563-566.
179. N. W. Awang, K. Tsutsumi, B. Huštáková, S. F. M. Yusoff, K. Nomura and B. M. Yamin, *RSC Adv.*, 2016, **6**, 100925-100930.
180. A. K. Chatterjee, T.-L. Choi, D. P. Sanders and R. H. Grubbs, *J. Am. Chem. Soc.*, 2003, **125**, 11360-11370.
181. S. Gutierras, S. M. Vargas and M. A. Tlenkopatchev, *J. Chem. Thermodynamics*, 2004, **36**, 29-36.
182. L. M. Kustov and D. B. Furman, *J. Organomet. Chem.*, 2018, **867**, 261-265.
183. M. S. Sanford, J. A. Love and R. H. Grubbs, *J. Am. Chem. Soc.*, 2001, **123**, 6543-6554.
184. R. M. Thomas, B. K. Keitz, T. M. Champagne and R. H. Grubbs, *J. Am. Chem. Soc.*, 2011, **133**, 7490-7496.
185. P. Wyřbek, P. Małeckı, A. Sytniczuk, W. Kořnik, A. Gawin, J. Kostrzewa, A. Kajetanowicz and K. Grela, *ACS Omega*, 2018, **3**, 18481-18488.
186. P. S. Engl, C. B. Santiago, C. P. Gordon, W.-C. Liao, A. Fedorov, C. Copéret, M. S. Sigman and A. Togni, *J. Am. Chem. Soc.*, 2017, **139**, 13117-13125.
187. G. S. Forman, R. M. Bellabarba, R. P. Tooze, A. M. Z. Slawin, R. Karch and R. Winde, *J. Organomet. Chem.*, 2006, **691**, 5513-5516.
188. J. Julis, S. A. Bartlett, S. Baader, N. Beresford, E. J. Routledge, C. S. J. Cazin and D. J. Cole-Hamilton, *Green Chem.*, 2014, **16**, 2846-2856.
189. R. Kadyrov, C. Azap, S. Weidlich and D. Wolf, *Top. Curr. Chem.*, 2012, **55**, 538-542.
190. R. Kadyrov, C. Azap, S. Weidlich and D. Wolf, *Top. Catal.*, 2012, **55**, 538-542.
191. D. Mandelli, M. J. D. M. Jannini, R. Buffon and U. Schuchardt, *J. Am. Oil Chem. Soc.*, 1996, **73**, 229-232.
192. S. C. Marinescu, R. R. Schrock, P. Müller and A. H. Hoveyda, *J. Am. Chem. Soc.*, 2009, **131**, 10840-10841.
193. V. M. Marx, A. H. Sullivan, M. Melaimi, S. C. Virgil, B. K. Keitz, D. S. Weinberger, G. Bertrand and R. H. Grubbs, *Angew. Chem. Int. Ed.*, 2015, **54**, 1919-1923.
194. Y. Schrodi, T. Ung, A. Vargas, G. Mkrtumyan, C. W. Lee, T. M. Champagne, R. L. Pederson and S. H. Hong, *Clean*, 2008, **36**, 669-673.
195. B. Gutmann, D. Cantillo and C. O. Kappe, *Angew. Chem. Int. Ed.*, 2015, **54**, 6688-6728.
196. K. A. Alexander, E. A. Paulhus, G. M. L. Lazarus and N. E. Leadbeater, *J. Organomet. Chem.*, 2016, **812**, 74-80.
197. S. Monfette, M. Eyholzer, D. M. Roberge and D. E. Fogg, *Chem. – Eur. J.*, 2010, **16**, 11720-11725.
198. C. P. Park, M. M. Van Wingerden, S.-Y. Han, D.-P. Kim and R. H. Grubbs, *Organic Letters*, 2011, **13**, 2398-2401.
199. C. P. Park, M. M. Van Wingerden, S.-Y. Han, D.-P. Kim and R. H. Grubbs, *Org. Lett.*, 2011, **13**, 2398-2401.
200. C. Schotten, D. Plaza, S. Manzini, S. P. Nolan, S. V. Ley, D. L. Browne and A. Lapkin, *ACS Sustain. Chem. Eng.*, 2015, **3**, 1453-1459.
201. C. Thurier, C. Fischmeister, C. Bruneau, H. Olivier-Bourbigou and P. H. Dixneuf, *ChemSusChem*, 2008, **1**, 118-122.
202. N. A. Lundquist, M. J. Sweetman, K. R. Scroggie, M. J. H. Worthington, L. J. Esdaile, S. F. K. Alboaiji, S. E. Plush, J. D. Hayball and J. M. Chalker, *ACS Sustainable Chem. Eng.*, 2019, **7**, 11044-11049.

203. M. J. H. Worthington, C. J. Shearer, L. J. Esdaile, J. A. Campbell, C. T. Gibson, S. K. Legg, Y. Yin, N. A. Lundquist, J. R. Gascooke, I. S. Albuquerque, J. G. Shapter, G. G. Andersson, D. A. Lewis, G. J. L. Bernardes and J. M. Chalker, *Adv. Sustainable Syst.*, 2018, **2**, 1800024.
204. N. A. Lundquist, M. J. H. Worthington, N. Adamson, C. T. Gibson, M. R. Johnston, A. V. Ellis and J. M. Chalker, *RSC Adv.*, 2018, **8**, 1232-1236.
205. E. K. Sitepu, K. Corbin, X. Luo, S. J. Pye, Y. Tang, S. C. Leterme, K. Heimann, C. L. Raston and W. Zhang, *Bioresour. Technol.*, 2018, **266**, 488-497.
206. J. Britton and C. L. Raston, *RSC Advances*, 2015, **5**, 2276-2280.
207. L. A. Arrua, B. J. McCoy and J. M. Smith, *Chem. Eng. Process.*, 1990, **36**, 1768-1772.
208. Y. M. Ahn, K. Yang and G. I. Georg, *Org. Lett.*, 2001, **3**, 1411-1413.
209. J. H. Cho and B. M. Kim, *Org. Lett.*, 2003, **5**, 531-533.
210. B. R. Galan, K. P. Kalbarczyk, S. Szczepankiewicz, J. B. Keister and S. T. Diver, *Org. Lett.*, 2007, **9**, 1203-1206.
211. P. G. Gassman and T. H. Johnson, *J. Am. Chem. Soc.*, 1976, **98**, 6055-6057.
212. W. Liu, P. J. Nichols and N. Smith, *Tetrahedron Lett.*, 2009, **50**, 6103-6105.
213. K. McEleney, D. P. Allen, A. E. Holliday and C. M. Crudden, *Org. Lett.*, 2006, **8**, 2663-2666.
214. L. A. Paquette, J. D. Schloss, I. Efremov, F. Fabris, F. Gallou, J. Méndez-Andino and J. Yang, *Org. Lett.*, 2000, **2**, 1259-1261.
215. G. Szczepaniak, A. Ruszczynska, K. Kosiński, E. Bulska and K. Grela, *Green Chem.*, 2018, **20**, 1280-1289.
216. J. R. O. Filho, W. C. Silva, J. C. M. Pereira and D. W. Franco, *Inorg. Chim. Acta*, 2006, **359**, 2888-2895.
217. N. M. Giles, A. B. Watts, G. I. Giles, F. H. Fry, J. A. Littlechild and C. Jacob, *Chem. Biol.*, 2003, **10**, 677-693.
218. J. M. Chalker, C. S. C. Wood and B. G. Davis, *J. Am. Chem. Soc.*, 2009, **131**, 16346-16347.
219. J. M. Chalker, *Aust. J. Chem.*, 2015, **68**, 1801-1809.
220. J. M. Chalker, Y. A. Lin, O. Boutureira and B. G. Davis, *Chem. Commun.*, 2009, DOI: 10.1039/B908004J, 3714-3716.
221. Y. A. Lin, J. M. Chalker and B. G. Davis, *ChemBioChem*, 2009, **10**, 959-969.
222. Y. A. Lin, J. M. Chalker and B. G. Davis, *J. Am. Chem. Soc.*, 2010, **132**, 16805-16811.
223. Y. A. Lin, J. M. Chalker, N. Floyd, G. J. L. Bernardes and B. G. Davis, *J. Am. Chem. Soc.*, 2008, **130**, 9642-9643.
224. G. A. Edwards, P. A. Culp and J. M. Chalker, *Chem. Commun.*, 2015, **51**, 515-518.
225. H. Wang, H. Matsushashi, B. D. Doan, S. N. Goodman, X. Ouyang and W. M. Clark, *Tetrahedron*, 2009, **65**, 6291-6303.
226. S. H. Hong, D. P. Sanders, C. W. Lee and R. H. Grubbs, *J. Am. Chem. Soc.*, 2005, **127**, 17160-17161.
227. S. Krompiec, N. Kuźnik, M. Krompiec, R. Penczek, J. Mrzigod and A. Tórz, *J. Mol. Catal. A Chem.*, 2006, **253**, 132-146.
228. B. Schmidt, *Eur. J. Org. Chem*, 2004, **2004**, 1865-1880.
229. S. E. Clapham, A. Hadzovic and R. H. Morris, *Coord. Chem. Rev.*, 2004, **248**, 2201-2237.
230. G. C. Vougioukalakis, *Chem.-Eur. J.*, 2012, **18**, 8868-8880.
231. P. Wheeler, J. H. Phillips and R. L. Pederson, *Org. Process Res. Dev.*, 2016, **20**, 1182-1190.
232. R. Duque, E. Öchsner, H. Clavier, F. Cajo, S. P. Nolan, M. Mauduit and D. J. Cole-Hamilton, *Green Chem.*, 2011, **13**, 1187-1195.
233. M. R. Buchmeiser, *New J. Chem.*, 2004, **28**, 549-557.
234. J. Gmeiner, M. Seibicke, C. Lang, U. Gärtner and O. Trapp, *Adv. Synth. Catal.*, 2014, **356**, 2081-2087.
235. Z. J. Wang, W. R. Jackson and A. J. Robinson, *Green Chem.*, 2015, **17**, 3407-3414.
236. J. M. Phillips, M. Ahamed, X. Duan, R. N. Lamb, X. Qu, K. Zheng, J. Zou, J. M. Chalker and C. L. Raston, *ACS Appl. Bio Mater.*, 2019, **2**, 488-494.
237. S. Hübner, J. G. de Vries and V. Farina, *Adv. Synth. Catal.*, 2016, **358**, 3-25.
238. K. Skowerski, J. Białocki, A. Tracz and T. K. Olszewski, *Green Chem.*, 2014, **16**, 1125-1130.
239. L. Yasmin, K. A. Stubbs and C. L. Raston, *Tetrahedron Lett.*, 2014, **55**, 2246-2248.
240. J. Britton, S. B. Dalziel and C. L. Raston, *RSC Adv.*, 2015, **5**, 1655-1660.
241. M. N. Gandy, C. L. Raston and K. A. Stubbs, *Chem. Commun.*, 2015, **51**, 11041-11044.
242. L. Yasmin, P. K. Eggers, B. W. Skelton, K. A. Stubbs and C. L. Raston, *Green Chem.*, 2014, **16**, 3450-3453.
243. X. Chen, R. A. Boulos, P. K. Eggers and C. L. Raston, *Chem. Commun.*, 2012, **48**, 11407-11409.
244. X. Chen, J. F. Dobson and C. L. Raston, *Chem. Commun.*, 2012, **48**, 3703-3705.
245. M. Fujita, Y.-i. Izato, Y. Iizuka and A. Miyake, *Process Saf. Environ. Prot.*, 2019, **129**, 339-347.
246. J.-F. Tremblay, *Journal*, 2012, **90**.
247. X. Luo, A. H. M. Al-Antaki, D. P. Harvey, Y. Ruan, S. He, W. Zhang and C. L. Raston, *ACS Appl. Mater. Interfaces*, 2018, **10**, 27224-27232.
248. S. J. Liu and X. H. Wang, *Curr. Opin. Green Sustain. Chem.*, 2017, **3**, 61-66.
249. M. Taherimehr and P. P. Pescarmona, *J. Appl. Polym. Sci.*, 2014, **131**, 17.
250. L. F. Xiao, F. W. Li and C. G. Xia, *Prog. Chem.*, 2005, **17**, 706-715.
251. R. R. Ang, L. T. Sin, S. T. Bee, T. T. Tee, A. A. H. Kadhum, A. R. Rahmat and B. A. Wasmii, *J. Clean Prod.*, 2015, **102**, 1-17.
252. S. Fukuoka, I. Fukawa, T. Adachi, H. Fujita, N. Sugiyama and T. Sawa, *Org. Process Res. Dev.*, 2019, **23**, 145-169.
253. S. J. Poland and D. J. Darensbourg, *Green Chem.*, 2017, **19**, 4990-5011.
254. Y. Y. Wang and D. J. Darensbourg, *Coord. Chem. Rev.*, 2018, **372**, 85-100.
255. P. Izák, F. D. Bobbink, M. Hulla, M. Klepic, K. Friess, Š. Hovorka and P. J. Dyson, *ChemPlusChem*, 2018, **83**, 7-18.

256. A. Barthel, Y. Saih, M. Gimenez, J. D. A. Pelletier, F. E. Kühn, V. D'Elia and J.-M. Basset, *Green Chem.*, 2016, **18**, 3116-3123.
257. M. North, R. Pasquale and C. Young, *Green Chem.*, 2010, **12**, 1514-1539.
258. Y. Chen and T. Mu, *Green Chem.*, 2019, **21**, 2544-2574.
259. H. Yang, Y. Gu, Y. Deng and F. Shi, *Chem. Commun.*, 2002, DOI: 10.1039/B108451H, 274-275.
260. T. Junkers, *J. Flow. Chem.*, 2017, **7**, 106-110.
261. L. S. Mendez-Portillo, C. Dubois and P. A. Tanguy, *Chem. Eng. J.*, 2014, **256**, 212-221.
262. A. Natalello, J. Morsbach, A. Friedel, A. Alkan, C. Tonhauser, A. H. E. Muller and H. Frey, *Org. Process. Res. Dev.*, 2014, **18**, 1408-1412.
263. L. Wang, C. Xu, Q. Han, X. Tang, P. Zhou, R. Zhang, G. Gao, B. Xu, W. Qin and W. Liu, *Chem. Commun.*, 2018, **54**, 2212-2215.
264. P. W. Morgan and S. L. Kwolek, *J. Chem. Educ.*, 1959, **36**, 182.
265. M. Eriksen, S. Mason, S. Wilson, C. Box, A. Zellers, W. Edwards, H. Farley and S. Amato, *Marine Pollution Bulletin*, 2013, **77**, 177-182.
266. J. M. Swan, *Nature*, 1957, **180**, 643-645.
267. J. L. Bailey and R. D. Cole, *J. Biol. Chem.*, 1959, **234**, 1733-1739.
268. N. K. D. Kella and J. E. Kinsella, *J. Biochem. Biophys. Meth.*, 1985, **11**, 251-263.
269. D. J. Cowley and R. B. Mackin, *FEBS Lett*, 1997, **402**, 124-130.
270. C. Peralta, A. Melatos, M. Giacobello and A. Ooi, *J. Fluid Mech.*, 2008, **609**, 221-274.
271. T. E. Solheim, F. Salvemini, S. B. Dalziel and C. L. Raston, *Sci. Rep.*, 2019, **9**, 2817.
272. U. Garbe, T. Randall and C. Hughes, *Nuclear Instruments and Methods in Physics Research Section A: Accelerators, Spectrometers, Detectors and Associated Equipment*, 2011, **651**, 42-46.
273. S. P. Newman, P. G. D. Pellow and S. W. Clarke, *Clinical Physics and Physiological Measurement*, 1986, **7**, 139-146.
274. S. Banerjee, E. Gnanamani, X. Yan and R. N. Zare, *Analyst*, 2017, **142**, 1399-1402.
275. X. Yan, R. M. Bain and R. G. Cooks, *Angew. Chem. Int. Ed.*, 2016, **55**, 12960-12972.
276. X. Yan, Y.-H. Lai and R. N. Zare, *Chem. Sci.*, 2018, **9**, 5207-5211.
277. X. Luo, P. Smith, C. L. Raston and W. Zhang, *ACS Sustain. Chem. Eng.*, 2016, **4**, 3905-3911.
278. X. Luo, P. Smith, C. L. Raston and W. Zhang, *ACS Sustainable Chem. Eng.*, 2016, **4**, 3905-3911.
279. C. W. Coley, L. Rogers, W. H. Green and K. F. Jensen, *ACS Cent. Sci.*, 2017, **3**, 1237-1245.
280. A. Cook, A. P. Johnson, J. Law, M. Mirzazadeh, O. Ravitz and A. Simon, *WIREs Comput. Mol. Sci.*, 2012, **2**, 79-107.
281. T. Klucznik, B. Mikulak-Klucznik, M. P. McCormack, H. Lima, S. Szymkuć, M. Bhowmick, K. Molga, Y. Zhou, L. Rickershauser, E. P. Gajewska, A. Toutchkine, P. Dittwald, M. P. Startek, G. J. Kirkovits, R. Roszak, A. Adamski, B. Sieredzińska, M. Mrksich, S. L. J. Trice and B. A. Grzybowski, *Chem*, 2018, **4**, 522-532.
282. W. A. Warr, *Mol. Inf.*, 2014, **33**, 469-476.
283. S. Szymkuć, E. P. Gajewska, T. Klucznik, K. Molga, P. Dittwald, M. Startek, M. Bajczyk and B. A. Grzybowski, *Angew. Chem. Int. Ed.*, 2016, **55**, 5904-5937.
284. J. C. Gilbert and S. A. Monti, *J. Chem. Edu.*, 1973, **50**, 369.
285. G. B. Kauffman, *J. Chem. Edu.*, 1983, **60**, 185.
286. G. C. Vogel and W. D. Perry, *J. Chem. Edu.*, 1991, **68**, 607-608.
287. K. Vimalanathan, J. R. Gascooke, I. Suarez-Martinez, N. A. Marks, H. Kumari, C. J. Garvey, J. L. Atwood, W. D. Lawrance and C. L. Raston, *Scientific Reports*, 2016, **6**.
288. W. H. Weber, K. C. Hass and J. R. McBride, *Phys. Rev. B*, 1993, **48**, 178-185.
289. M. Fernández-García, A. Martínez-Arias, J. C. Hanson and J. A. Rodriguez, *Chem. Rev.*, 2004, **104**, 4063-4104.
290. D. W. Wheeler and I. Khan, *Vib. Spectrosc.*, 2014, **70**, 200-206.
291. E. K. Sitepu, K. Corbin, X. Luo, S. J. Pye, Y. Tang, S. C. Leterme, K. Heimann, C. L. Raston and W. Zhang, *Bioresour. Tech.*, 2018, **266**, 488-497.